FAT AND SKELETAL METASTASIS

EDITED BY: Guanwu Li, Yongsheng Chen and DongMei Wu
PUBLISHED IN: Frontiers in Endocrinology

frontiers Research Topics

ISSN 1664-8714
ISBN 978-2-83250-378-2
DOI 10.3389/978-2-83250-378-2

About Frontiers

Frontiers is more than just an open-access publisher of scholarly articles: it is a pioneering approach to the world of academia, radically improving the way scholarly research is managed. The grand vision of Frontiers is a world where all people have an equal opportunity to seek, share and generate knowledge. Frontiers provides immediate and permanent online open access to all its publications, but this alone is not enough to realize our grand goals.

Frontiers Journal Series

The Frontiers Journal Series is a multi-tier and interdisciplinary set of open-access, online journals, promising a paradigm shift from the current review, selection and dissemination processes in academic publishing. All Frontiers journals are driven by researchers for researchers; therefore, they constitute a service to the scholarly community. At the same time, the Frontiers Journal Series operates on a revolutionary invention, the tiered publishing system, initially addressing specific communities of scholars, and gradually climbing up to broader public understanding, thus serving the interests of the lay society, too.

Dedication to Quality

Each Frontiers article is a landmark of the highest quality, thanks to genuinely collaborative interactions between authors and review editors, who include some of the world's best academicians. Research must be certified by peers before entering a stream of knowledge that may eventually reach the public - and shape society; therefore, Frontiers only applies the most rigorous and unbiased reviews.
Frontiers revolutionizes research publishing by freely delivering the most outstanding research, evaluated with no bias from both the academic and social point of view. By applying the most advanced information technologies, Frontiers is catapulting scholarly publishing into a new generation.

What are Frontiers Research Topics?

Frontiers Research Topics are very popular trademarks of the Frontiers Journals Series: they are collections of at least ten articles, all centered on a particular subject. With their unique mix of varied contributions from Original Research to Review Articles, Frontiers Research Topics unify the most influential researchers, the latest key findings and historical advances in a hot research area! Find out more on how to host your own Frontiers Research Topic or contribute to one as an author by contacting the Frontiers Editorial Office: frontiersin.org/about/contact

FAT AND SKELETAL METASTASIS

Topic Editors:
Guanwu Li, Shanghai University of Traditional Chinese Medicine, China
Yongsheng Chen, Wayne State University, United States
DongMei Wu, East China Normal University, China

Citation: Li, G., Chen, Y., Wu, D., eds. (2022). Fat and Skeletal Metastasis. Lausanne: Frontiers Media SA. doi: 10.3389/978-2-83250-378-2

Table of Contents

frontiers in Endocrinology

ORIGINAL RESEARCH
published: 01 November 2021
doi: 10.3389/fendo.2021.763349

IDH1 R132C and ERC2 L309I Mutations Contribute to the Development of Maffucci's Syndrome

Peng Cheng[1], *Kun Chen*[2], *Shu Zhang*[3], *Ke-tao Mu*[4], *Shuang Liang*[1] *and Ying Zhang*[5]*

[1] Department of Orthopedics, Tongji Hospital of Tongji Medical College, Huazhong University of Science and Technology, Wuhan, China, [2] Department of Orthopedics, The First Affiliated Hospital of University of Science and Technology of China, Hefei, China, [3] The Center for Biomedical Research, Key Laboratory of Organ Transplantation, Ministry of Education and Chinese Academy of Medical Sciences, NHC Key Laboratory of Organ Transplantation, Huazhong University of Science and Technology, Wuhan, China, [4] Department of Radiology, Tongji Hospital of Tongji Medical College, Huazhong University of Science and Technology, Wuhan, China, [5] Department of Nephrology, Tongji Hospital of Tongji Medical College, Huazhong University of Science and Technology, Wuhan, China

OPEN ACCESS

Edited by:
Guanwu Li,
Shanghai University of Traditional Chinese Medicine, China

Reviewed by:
Nathan Hall,
GMDx, Australia
Linqiang Tian,
The Third Affiliated Hospital of Xinxiang Medical University, China

***Correspondence:**
Ying Zhang
zhangying19880914@163.com

Specialty section:
This article was submitted to Bone Research, a section of the journal Frontiers in Endocrinology

Received: *23 August 2021*
Accepted: *11 October 2021*
Published: *01 November 2021*

Citation:
Cheng P, Chen K, Zhang S, Mu K-t, Liang S and Zhang Y (2021) IDH1 R132C and ERC2 L309I Mutations Contribute to the Development of Maffucci's Syndrome. Front. Endocrinol. 12:763349. doi: 10.3389/fendo.2021.763349

Background: Maffucci's syndrome is characterized by the coexistence of multiple enchondromas and soft-tissue hemangiomas. It has been clear that somatic mosaic isocitrate dehydrogenase type 1 (IDH1) or isocitrate dehydrogenase type 2 (IDH2) mutations are associated with Maffucci's syndrome and Ollier disease, but the mechanisms underlying hemangiomas of the Maffucci's syndrome is still obscure. This study aimed to determine the mechanism of hemangiomas in Maffucci's syndrome.

Methods: We received a 26-year-old female patient with typical Maffucci's syndrome, and exome sequencing was conducted using DNA from her peripheral blood and enchondroma tissues. Somatic mutations were characterized by a comparative analysis of exome sequences and further confirmed by the sequencing of PCR products derived from original blood and tissue samples. The mutations of an additional 69 patients with Ollier disease were further tested. The functional impacts of these somatic mutations on Maffucci's syndrome, especially the development of hemangiomas, were evaluated.

Results: We reported a typical case of Maffucci's syndrome, which was confirmed by both imaging findings and pathology. Through exome sequencing of this patient's DNA samples, we identified an R132C mutation in the isocitrate dehydrogenase type 1 (IDH1) gene and an L309I mutation in the ELKS/RAB6-interacting/CAST family member 2 (ERC2) gene in this patient. Approximately 33.3% of the clones were positive for the IDH1 R132C mutation, and 19.0% of the clones were positive for the ECR2 L309I mutation. The IDH1 R132C mutation was detected in most of the patients with Ollier disease (51/69 patients), and the mean frequency of this mutation was 63.3% in total sequence readouts, but the ECR2 L309I mutation was absent in all of the patients with Ollier disease. *In vitro* experiments confirmed that the IDH1 R132C mutation promotes chondrocyte proliferation, and the ERC2 L309I mutation enhances angiogenesis.

Conclusions: Our results suggest that while IDH1 is a known pathogenic gene in enchondromatosis, ERC2 is a novel gene identified in Maffucci's syndrome. The somatic L309I mutation of ERC2 contributes to the pathogenesis of hypervascularization to facilitate the development of hemangiomas in Maffucci's syndrome. The combination of the IDH1 R132C and ERC2 L309I mutations contributes to the development of Maffucci's syndrome, and these results may enable further research on the pathogenesis of Maffucci's syndrome.

Keywords: hemangiomas, Maffucci's syndrome, ERC2 mutation, IDH1 mutation, multiple enchondromas

INTRODUCTION

Enchondromatosis is a rare, nonhereditary skeletal disorder with two common clinical subtypes, Maffucci's syndrome and Ollier disease (1–3). Maffucci's syndrome is characterized by the coexistence of multiple enchondromas and soft-tissue hemangiomas and has an incidence rate of 23% in cases of malignant tumors (4, 5), while Ollier disease shares the same characteristics of multiple enchondromas but does not involve hemangiomas. The estimated prevalence of Ollier disease is approximately 1/100,000, which is much more common than Maffucci's syndrome (6–8).

It is clear that somatic mosaic isocitrate dehydrogenase type 1 (IDH1) and isocitrate dehydrogenase type 2 (IDH2) mutations are associated with Maffucci's syndrome and Ollier disease (8, 9). Heterozygous mutations in IDH1 and IDH2 have also been detected in gliomas/glioblastomas (9, 10) and acute myeloid leukemia (AML) (11–13). IDH1 mutations usually occur at R132, and IDH2 mutations are generally found at R172, a residue analogous to R132 in IDH1 (14–16). However, an additional IDH2 mutation site, R140, has also been reported (17–19). The above somatic mutations render IDH1 or IDH2 unable to convert isocitrate to α-ketoglutarate but promote D-2-hydroxyglutarate accumulation, the levels of which strongly correlate with tumorigenesis (13, 20, 21). Other IDH1/IDH2 mutations have also been found, but the detailed functional relevance has not been described.

A monoallelic point mutation of IDH1 is believed to be strongly correlated with tumorigenesis, which explains the development of multiple enchondromas, but the mechanisms underlying hemangiomas in Maffucci's syndrome have yet to be elucidated. We recently received a young female patient with Maffucci's syndrome. To identify the possible pathogenic genes, we collected peripheral blood DNA and enchondroma DNA and conducted a comparative exome sequence analysis of the above DNA samples. We identified an R132C mutation in the IDH1 gene and an L309I mutation in the ELKS/RAB6-interacting/CAST family member 2 (ERC2) gene. We also obtained evidence suggesting that the IDH1 R132C mutation is likely the primary mutation responsible for the pathogenesis of multiple enchondromas, while the ERC2 L309I mutation may be the causative factor underlying hemangiomas by enhancing the intracellular calcium concentration in endothelial cells. Collectively, our data suggest that somatic mutations in these two genes synergistically contribute to the development of Maffucci's syndrome.

MATERIALS AND METHODS

Exome Sequencing and Somatic Mutation Analysis

Genomic DNA was isolated from the enchondroma tissues in right-hand finger bones and peripheral blood of the patient. Exome was captured and sequenced to 100× by BGI (Shenzhen Guangdong, China) using the Illumina HiSeq™ 2000 Sequencing Systems. The resulting sequences were first compared with published reference sequences (https://www.globus.org/) to exclude normal polymorphisms. Variants between enchondromas and peripheral blood DNA were analyzed by BGI to characterize somatic mutations with reads above 10% in the 100× readouts (22, 23). The mutations and frequencies were confirmed by randomly sequencing 21 PCR clones with a pMD®18-T vector (Takara Biotechnology, Dalian, China).

Cell Culture

ATDC5 and HUVECs cells were purchased from the Chinese Academy of Cell Bank. ATDC5 cells were cultured with DMEM/F12 medium at 37°C with 5% CO_2 in a humidified incubator. For chondrocyte induction, ATDC5 cells were cultured with CDM (chondrogenic differentiation medium) (Cyagen Biosciences Inc., China) at 37°C with 5% CO_2 in a humidified incubator. HUVECs were cultured in 2% FBS EBM-2 endothelial cell basic medium at 37°C for 24 h under a 5% CO_2 atmosphere.

Lentivirus Vector Construction and Cell Infection

The coding sequence of the target gene (IDH1, IDH1 with R132C mutation, ERC2 and ERC2 with L309I mutation) was PCR amplified from the GV287 target gene using primers with AgeI/AgeI overhangs and cloned into pTZ58 (Fermentas, Vilnus, Lithuania). The AgeI/AgeI fragment was then subcloned into pUbi (AgeI/AgeI) and pEGFP-C1 (Clontech, Mountain View, CA) (AgeI/AgeI) to generate Ubi-GENE-3FLAG-SV40-EGFP encoding plasmids, respectively. To produce lentivirus, the pBABE-puro plasmids were coinfected along with the helper

plasmids into 293T cells, and the medium was harvested 36 h and 72 h after infection (24). ATDC5 or HUVEC infection was performed by incubating the cells in virus-enriched medium for 12 h, which included 4 μg/ml polybrene. Transduced cells were identified for EGFP expression under a fluorescence microscope.

Proliferation Assay

The cells (mouse chondrogenic cell line ATDC5 or HUVECs) were seeded in 96-well plates at a density of 2×10^4 cells/well. For chondrocyte induction, 10 μg/ml bovine insulin (Wako Pure Chemical, Osaka, Japan) was added after 12 h of culture under a 5% CO_2 atmosphere (21). After an additional 24 h of culture, 10 μl of WST-8 mixture (Dojindo, Shanghai, China) was added to each well and cultured for another 2 h. After washing, the cells were subjected to the measurement of absorbance under a microplate reader at a wavelength of 450 nm.

Migration Assay

ATDC5 cells were seeded in a 24-well plate at a density of 8×10^4 cells/well, and the cells were induced into chondrocytes as described above. A scratch was next created using a sterile yellow tip, the detached cells were removed, and the scratches were monitored for 48 h under culture conditions without any bovine insulin. Each set of experiments was performed in triplicate, and photographs were taken at the indicated time points.

Transwell Invasion Assay

ATDC5 cells or HUVECs were placed on the upper layer of culture medium inserted with a permeable membrane, and BD Matrigel (BD Biosciences, San Jose, CA) was placed below the cell permeable membrane. After 12 h of incubation, the ATDC5 cells that migrated through the membrane were stained with crystal violet solution and then counted under a light microscope, while the migrated HUVECs were analyzed under a fluorescence microscope.

Cell Cycle Analysis

The transduced ATDC5 cells were first induced to chondrocytes as described earlier and then synchronized to the G_0/G_1 phase by 24 h of serum starvation, and 10% FBS was added to the cultures. After another 24 h of culture, the cells were harvested for cell cycle analysis. Briefly, after washing, the cells were stained with propidium iodide, and the cell cycle distribution for each culture was analyzed by flow cytometry.

Tube Formation Assay

To examine tube formation, growth factor-reduced Matrigel (BD Bioscience, San Jose, CA) was placed in 96-well tissue culture plates (100 μL/well) and allowed to form a gel at 37°C for at least 30 min. HUVECs (2×10^4 cells) after 24 h of transduction were added into each well and incubated in 2% FBS EBM-2 endothelial cell basic medium at 37°C for 24 h under a 5% CO_2 atmosphere. Endothelial tubes were then examined under a fluorescence microscope by inspecting the overall tube length and branch points.

Intracellular Free Calcium Assay

The transduced HUVECs were seeded in a 24-well plate at a density of 2×10^4 cells/well. After 12 h of culture, cell-permeant acetoxymethyl (AM) esters of X-Rhod-1 were loaded into the cultures. After another 4 h of culture, the cells were subjected to analysis of intracellular calcium concentration under an Olympus IX73 fluorescence microscope at 550 nm excitation and 600 nm emission. Images were taken at 100X magnification.

Statistical Analysis

For pairwise comparisons, the data were analyzed using Student's t-test. A comparison between multiple experimental groups was accomplished by one-way ANOVA using SPS 11.5 for windows. All experiments were conducted with at least 3 independent replications. All data are presented as the mean ± SEM. In both cases, $p < 0.05$ was considered to be statistically significant.

RESULTS

Clinical Report

The patient here we report is a 26-year-old young woman who had typical multiple enchondromas but had no family members with disease history. Physical exams revealed that her 3-year-old daughter was also normal. The patient had abnormal protrusion in her right-hand fingers when she was 1 year old. Unfortunately, no medical examination was conducted at that time because of her family's financial problems. The patient presented when she was 26 years old; by then, all of her limbs could still move but were affected by deformities. The right hand had dangerous tumor-like deformities, fingers in this hand displayed deformity shape of the visible nodular and soft spherical bulge in light blue (**Figure 1A**), and the right upper arm was shortening (**Figure 1B**), but her left hand showed healthy appearance (**Figure 1C**). The right knee showed strong varus, and the left knee displayed valgus; both feet and ankles displayed deformities (data not shown). Palpable subcutaneous nodules could be found around the bones of these deformity areas, but no tenderness was characterized.

Ultrasound examinations revealed that her liver, gallbladder, spleen, pancreas, pancreatic duct, kidneys, and bladder were healthy. MR examinations showed that the phalanges of the fingers are circular or ovoid, with multi-locular, well-defined chondromatoid lesions and the soft tissue around the phalanx of the finger presents dilatative, well-bounded hyperintensity on T2WI.(**Figure 1D**). X-ray examinations demonstrated that the bones of the right palm, fingers of the right hand, right ulna, both radius (**Figure 1B**), humerus, scapulas, head of the right seventh rib (**Figure 1E**) and metatarsals of both feet (**Figure 1F**) were characterized by irregular swelling and morphological abnormalities. Cortical bones of these parts were markedly thinned, and multiple cystic-like lucent and dotted calcification areas can be noted around these parts. Bones in the cranial and maxillofacial regions, however, had no apparent abnormalities (**Figure 1G**). These asymmetrically distributed enchondroma

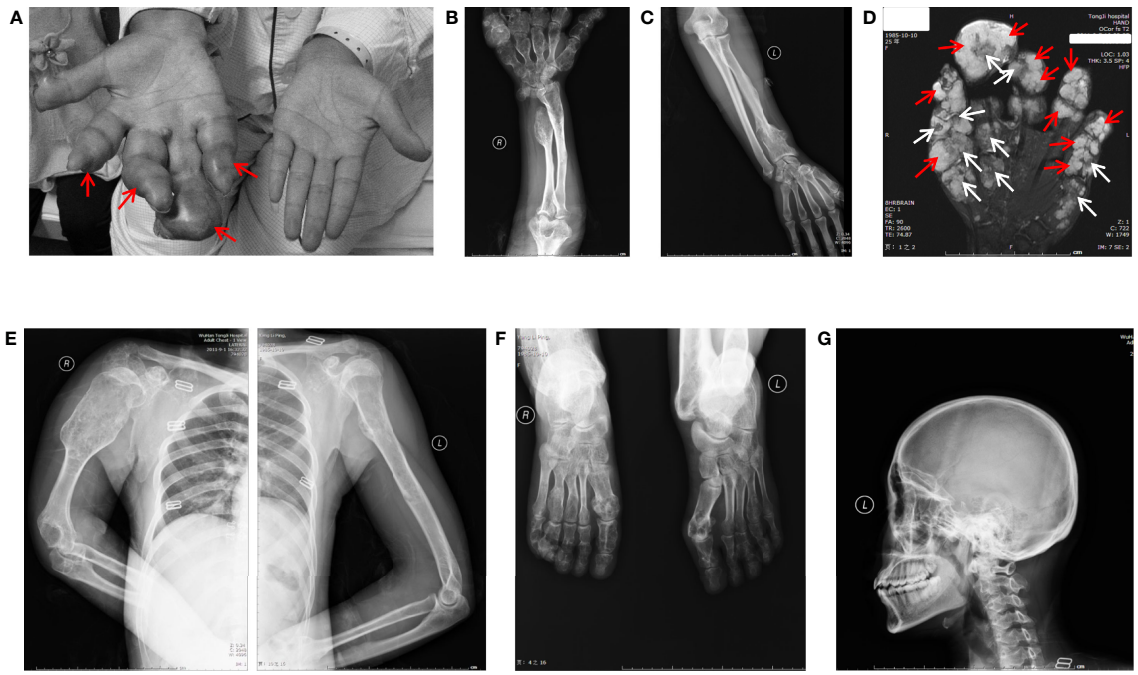

FIGURE 1 | General view and radiographic imaging of the lesion. **(A)** The right hand of the patient with Maffucci's syndrome showed deformities due to multiple enchondromas and a superficial hemangioma. The red arrows show hemangioma as a soft spherical bulge in light blue. **(B)** X-ray images of the right ulnar and radial bones and multiple metacarpophalangeal bones of the right hand show multiple reduced bone densities and partial expansive bone destruction **(C)**. The X-ray shows a relatively normal bone mass in the left arm. **(D)** MR results of the patient's right hand showed the phalanges are circular or oval, multilocular, well-defined, iso-intensity and hyperintensity on T2WI (white arrows) and the soft tissue around the phalanx presents dilatative, well-bounded hyperintensity on T2WI (red arrows). **(E)** X-ray images of the patient's upper body and enlarged right arm are shown in the film. **(F)** X-ray images of the patient's feet have the same radiographic appearance as those of the upper limbs. **(G)** X-ray image of cranial and maxillofacial bones showed no apparent abnormalities.

bone destruction and surrounding soft tissue hemangioma malformations are typical imaging features of Maffucci's syndrome.

These lesions seriously affected the function of the patient's hands, and the patient was very concerned that these lesions may be malignant. In order to further clarify the disease and nature, biopsy was necessary. Histological analysis indicated typical enchondroma changes in sections originating from right finger bones (**Figures 2A, B**), and cavernous hemangioma changes were noted in the enchondroma tissues from the same finger (**Figures 2C, D**).

According to these typical clinical manifestations, radiological data, and histological analysis by the authoritative pathologist, the diagnosis of Maffucci's syndrome was clear.

Exome Sequencing and Characterization of Somatic Mutations in the IDH1 and ERC2 Genes in Maffucci's Syndrome

Exome sequencing was next conducted using the patient's DNA samples originating from her peripheral blood and enchondroma tissues with 100x coverage. Comparative analysis of her enchondroma exome sequences with the sequences of 1000 standard human specimens in the public database Globus (https://www.globus.org/) revealed more than 65,000 variations, more than 99% of which are likely DNA polymorphisms between individuals. We thus first excluded those common polymorphisms identified through the public database and then aligned her enchondroma exome sequences with her peripheral blood exome sequences, *via* which we identified 90 mutations that cause amino acid changes. In general, somatic mutations in the enchondroma tissues are likely mosaic because of normal cell contamination or very low frequencies (only a proportion of tumor cells carry the same somatic mutation). By exclusion of those possibilities, the differences were limited to two mutations: the C394T mutation of IDH1 (NM_005896) in exon 4, which causes arginine to cysteine at position 132 (R132C), and the frequency of this mutation is 38.7% in total sequence readouts; and the C925A mutation of ERC2 (NM_015576) in exon 3, which mutates leucine to isoleucine at position 309 (L309I), and the ratio of this mutation is 23.8% in total sequence readouts.

To confirm the above sequencing data, we next PCR amplified the two regions (IDH1-c. C394T and ECR2-c. C925A) from her peripheral blood DNA and enchondroma DNA, respectively. The resulting PCR products were cloned into a TA vector, followed by sequencing analysis of 21 randomly selected clones. Indeed, these mutations were absent in the blood DNA, while approximately 33.3% of the clones were positive for the IDH1 R132C mutation (**Figure 3A**), and 19.0% of the clones were positive for the ECR2 L309I mutation

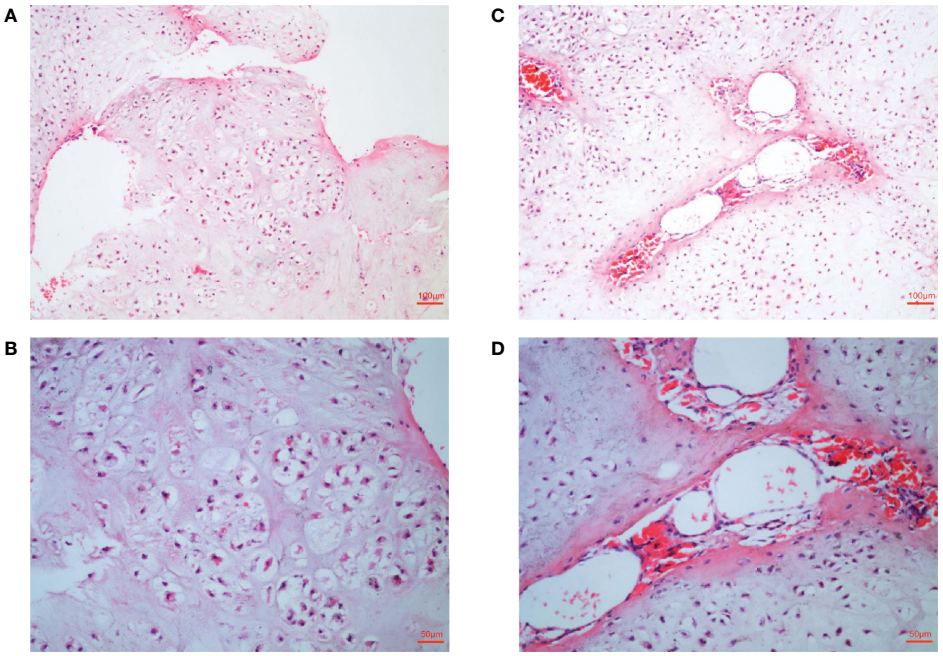

FIGURE 2 | Histological examination of lesions. **(A, B)** Histological examination manifesting typical enchondroma in the patient's right-hand finger bones. The specific manifestation was microscopic appearance of lobular hyaline cartilage with uniform chondrocytes, heaps of chondrocytes, uniform nuclear size and not deep staining **(C, D)**. Samples were collected from patient's right-hand finger bones displaying cavernous hemangioma in the enchondroma tissues. Microscopically, a large number of neoplastic vascular tissues can be seen in the middle of cartilage tissue. The blood vessels are thin-walled and dilated and filled with red blood cells.

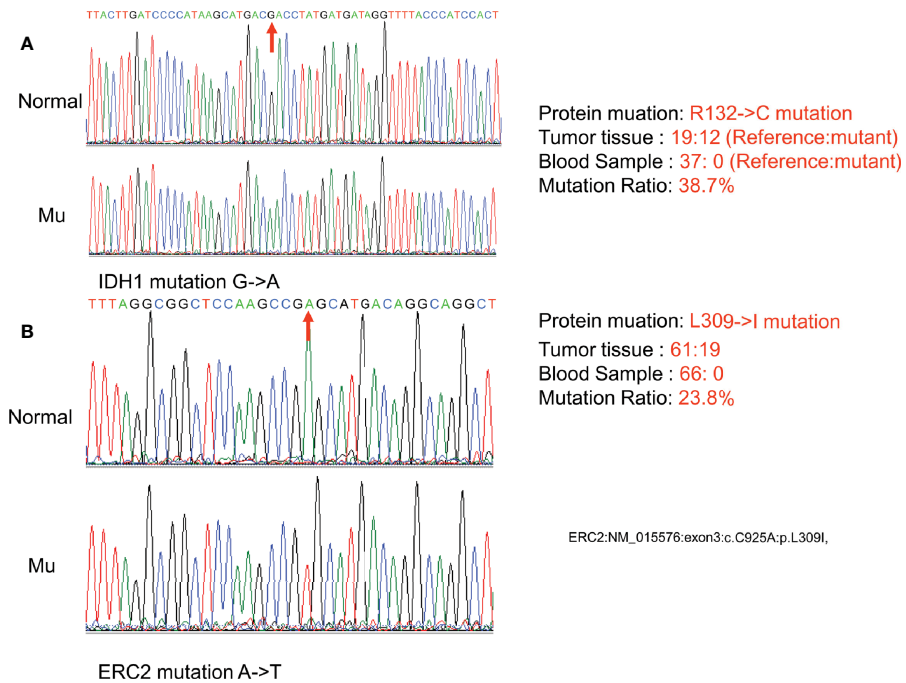

FIGURE 3 | Confirmation of somatic nonsynonymous mutation of IDH1 (c. C394T) **(A)** and ERC2 (c. C925A) **(B)** by sequencing PCR clones. The fragment flanking the mutated nucleotide was amplified by PCR and then cloned into a pMD18-T vector. Twenty-one clones were randomly sequenced to confirm the mutations and their frequency. (Normal:Normal; Mu:Mutation).

(**Figure 3B**). To exclude the possibility that those mutations are also present in healthy individuals, we genotyped 500 healthy individuals, and none of the subjects detected those two mutations.

IDH1 R132C Mutation Is in Both Subtypes of Enchondromatosis, While ERC2 L309I Mutation May Only Be in Maffucci's Syndrome

The foregoing case of Maffucci's syndrome demonstrates that there may be two gene mutations of IDH1 and ERC2 in Maffucci's syndrome. To demonstrate additional evidence of these two mutations in disease pathobiology, we genotyped 69 patients with Ollier disease using DNAs extracted from enchondroma tissues after dissection of embedded paraffin blocks. Excitingly, the IDH1 R132C mutation was detected in most of the patients with Ollier disease (51/69 patients), and the mean frequency of this mutation was 63.3% in total sequence readouts, but the ECR2 L309I mutation was absent in all of the patients with Ollier disease (**Figure 4**). Unfortunately, we were unable to identify additional patients with Maffucci's syndrome for the analysis of the ECR2 L309I mutation.

The IDH1 R132C Mutation Promotes Chondrocyte Proliferation, and the ERC2 L309I Mutation Enhances Angiogenesis

Given that the ECR2 L309I mutation is absent in patients with Ollier disease (with multiple chondromas only), while Maffucci's syndrome is characterized by the coexistence of multiple chondromas and hemangiomas, we thus hypothesized that the IDH1 R132C mutation causes multiple chondromas, while the ERC2 L309I mutation is responsible for the development of hemangiomas. To test this hypothesis, we conducted studies in chondrocytes, in which we induced a mouse chondrogenic cell line, ATDC5, into chondrocytes after transduction with lentiviruses expressing wild-type IDH1 (IDH1-wt) or the R132C mutant (IDH1-mu) (22, 23). As expected, chondrocytes transduced with the IDH1-mu viruses exhibited significantly higher migration capacity (**Figure 5**) and proliferation capability (**Figure 6A**). Cell cycle analysis revealed that the R132C mutation significantly promoted the G1-S phase transition (**Figures 6B, C**).

To demonstrate the impact of the ERC2 L309I mutation on the development of hemangiomas, we checked its role in angiogenesis, as hemangiomas are characterized by excessive vessel formation. For this purpose, we transduced HUVECs with lentiviruses expressing wild-type ERC2 (ERC2-wt) and the L309I mutant (ERC2-mu). Interestingly, the transduction of ERC2-mu viruses potently enhanced the capacity of HUVECs for angiogenesis, as evidenced by the higher capability for proliferation (**Figure 7A**), tubular formation (**Figures 7B, C**) and migration (**Figures 7D, E**). Collectively, these data suggest that the IDH1 R132C mutation combines with the ERC2 L309I mutation to cause the development of Maffucci's syndrome.

The ERC2 L309I Mutation Increases the Concentration of Intracellular Calcium

Given that CAST/ERC2 has been noted to modulate neurotransmitter release in nerve terminals by regulating intracellular Ca^{2+} concentrations (24), we then examined the effect of the L309I mutation of ERC2 on the intracellular calcium concentration in HUVECs by staining with Fura-2/AM (Invitrogen, OR, USA), a dye used to measure intracellular free calcium. HUVECs transduced with ERC2-mu displayed significantly higher intracellular free calcium concentrations than cells transduced with ERC2-wt (**Figure 8**).

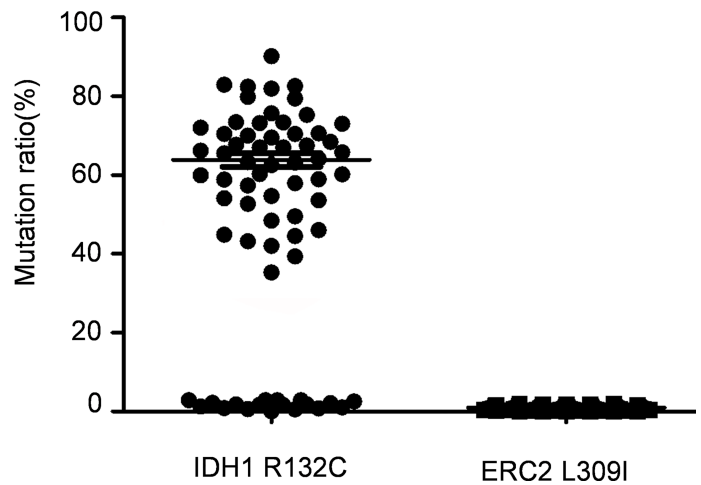

FIGURE 4 | The IDH1 R132C mutation is in Ollier disease, while the ERC2 L309I mutation is absent. The IDH1 R132C mutation was detected in most of the patients with Ollier disease (51/69 patients), and the mean frequency of this mutation was 63.3% in total sequence readouts, but the ECR2 L309I mutation was absent in all patients with Ollier disease examined.

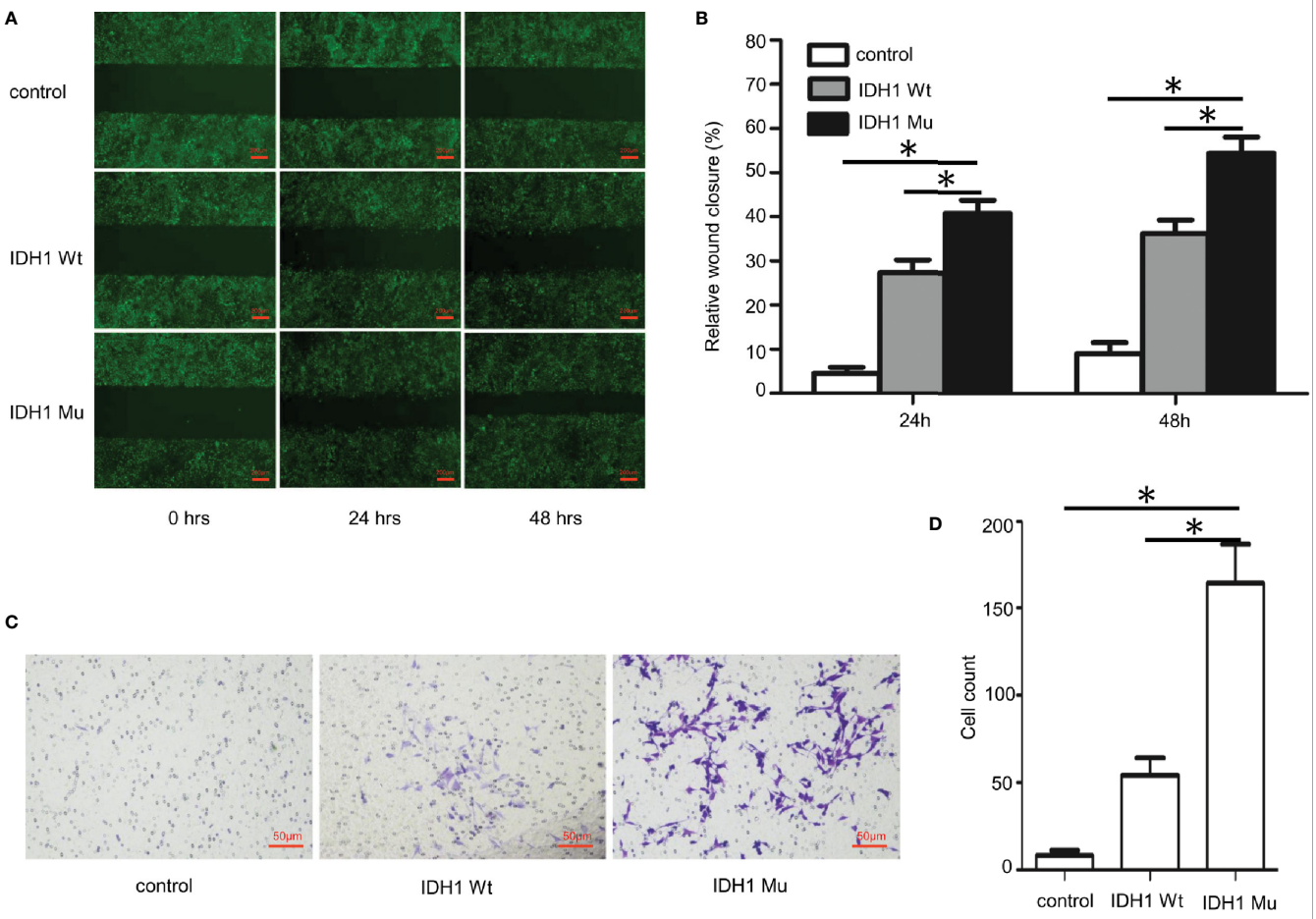

FIGURE 5 | Impact of the IDH1 R132C mutation on chondrocyte migration. The mouse chondrogenic ATDC5 cells were transduced with IDH1 wt and IDH1 mu (R132C) lentiviruses and then induced into chondrocytes as described. ATDC5 cells transduced with empty lentiviruses served as a control. **(A)** Representative images of each group from typical scratch migration assays. **(B)** A bar graphic figure shows the results of 5 independent scratch migration assays conducted. **(C)** Representative images of each group from transwell migration assays. **(D)** A bar graph shows data collected from 3 independent transwell migration assays. (*P<0.05).

DISCUSSION

Maffucci's syndrome is characterized by the coexistence of multiple enchondromas and soft-tissue hemangiomas (4, 5). Multiple enchondromas are characterized by irregular distribution of multiple benign cartilaginous lesions within the bones (7, 25). The phalanges, femur, and tibia are most commonly affected, with a tendency towards unilateral involvement (8, 26). As this patient showed, there is typical deformity in a limb or multiple painless bony lesions in the right hands, and the deformity is asymmetrically distributed. Radiographs typically show multiple well-defined lytic lesions within the medullary canal with a thin overlying cortex. Calcification can also be seen within the lesion, and the bone is enlarged, shortened, and deformed (4). Histological analysis indicated typical enchondroma changes, and cavernous hemangioma changes were noted in sections derived from the right palm. Therefore, the patient's diagnosis of Maffucci's syndrome was correct.

Maffucci's syndrome has a 23% incidence of a malignant tumor (8). It has been reported that somatic mosaic isocitrate dehydrogenase type 1 (IDH1) or isocitrate dehydrogenase type 2 (IDH2) mutations are associated with Maffucci's syndrome (10, 27). R132 of IDH1 is a hotspot somatic mutation site that has been reported to be the leading cause of chondrosarcoma/chondromas (10, 28), gliomas/glioblastomas (29) and some type of AML (30). Indeed, epigenetic studies suggest that this mutation was sufficient to establish the glioma hypermethylation phenotype in a cell model (29). In this patient, R132 was mutated to cysteine (R132C), and we confirmed that it was the primary mutation responsible for the development of multiple enchondromas.

In contrast, the ERC2 (L309I) mutation was a novel discovery, and its impact on the pathogenesis of Maffucci's syndrome is entirely unknown. The function of ERC2 is more reported in the release of neurotransmitters. In nerve terminals, CAST/ERC2 forms a protein complex with other active zone proteins and is thought to play an organizational and functional

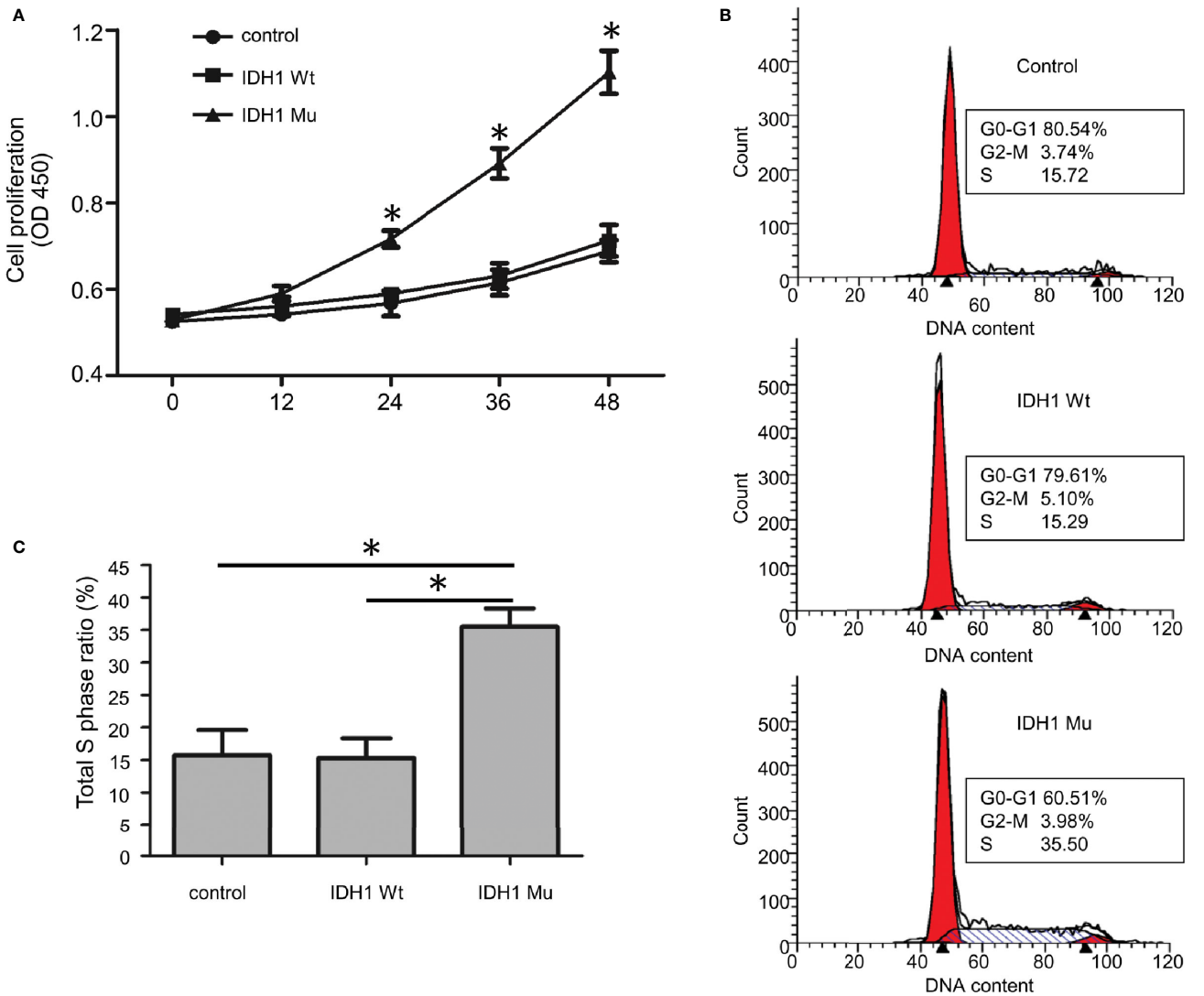

FIGURE 6 | The effect of the IDH1 R132C mutation on chondrocyte growth. **(A)** Proliferation results of chondrocytes after staining with WST-8 (n = 3). **(B)** Representative results of each group for cell cycle analysis. **(C)** A bar graphic figure shows the results collected from 3 independent replications. The IDH1 mu transduced cells manifested a significantly higher capacity for G1-S phase transition. (*P<0.05).

role in neurotransmitter release (31–33). Studies have also reported that genetic aberrations of ERC2 accelerate tumor formation in the body, such as kidney cancer and pancreatic cancer (34). Our results demonstrate the impact of the ERC2 L309I mutation on the development of hemangiomas, which may be an essential factor in the transformation of enchondromatosis into Maffucci's syndrome.

After further study, we found higher intracellular free calcium concentrations in HUVECs transduced with ERC2-mu. This result indicates that the L309I mutation rendered HUVECs with higher potency to regulate intracellular calcium influx (35). Since intracellular Ca^{2+} is known to be a second messenger for signal transduction closely related to cell proliferation, migration, apoptosis, and survival (36–39), our data suggest that the ECR2 L309I mutation probably contributes to the development of hemangiomas by enhancing intracellular calcium concentrations in endothelial cells.

In summary, by a comparative analysis of exome sequences between peripheral blood DNA and enchondroma DNA in a patient with Maffucci's syndrome, we identified an R132C mutation in the IDH1 gene and an L309I mutation in the ERC2 gene. Initial functional studies suggest that the IDH1 R132C mutation is likely the primary mutation responsible for the development of enchondromas, while the ERC2 L309I mutation is probably a causative mutation underlying the pathogenesis of hemangiomas. Therefore, our results suggest that the R132C mutation in IDH1 and the L309I mutation in ERC2 are probably the causative factors contributing to the development of Maffucci's syndrome. These data may promote further research on the pathogenesis of Maffucci's syndrome.

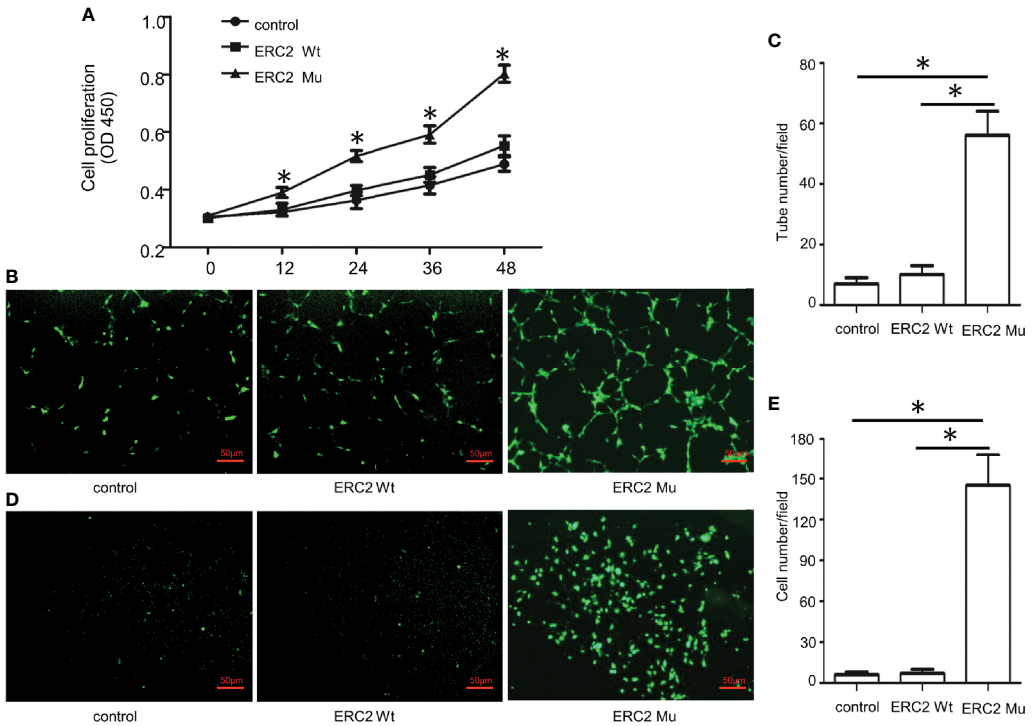

FIGURE 7 | The effects of the ERC2 L309I mutation on endothelial angiogenesis. HUVECs were transfected with ERC2 wt and ERC2 mu (L309I) lentiviruses and then subjected to angiogenesis analysis. **(A)** Proliferation results by analysis of WST-8 fluorescence (n = 3). **(B)** Representative images for analysis of tubular formation. **(C)** Quantitative results for capillary-like tube formation (n = 3). **(D)** Representative images for transwell migration assays. **(E)** A bar graph displaying the data from 3 independent transwell migration assays. (*P<0.05).

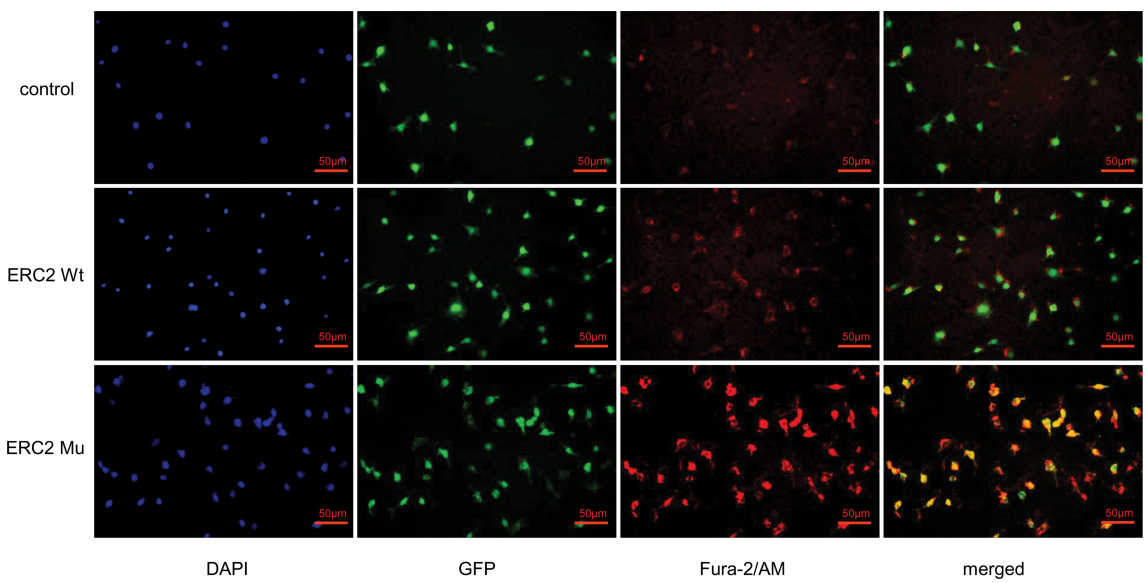

FIGURE 8 | ERC2 L309I mutation enhances endothelial intracellular calcium concentration. HUVECs were transduced with ERC2 wt and ERC2 mu (L309I) lentiviruses. HUVECs transduced with empty lentiviruses served as a control. Fura-2/AM was next applied to the cultures, and the intracellular free calcium concentration was then assessed for red fluorescence after washing under a fluorescence microscope.

DATA AVAILABILITY STATEMENT

The original contributions presented in the study are included in the article/supplementary material. Further inquiries can be directed to the corresponding author.

ETHICS STATEMENT

The studies involving human participants were reviewed and approved by Ethics Committee of Tongji Hospital Affiliated to Tongji Medical College (TJMC). The patients/participants provided their written informed consent to participate in this study. Written informed consent was obtained from the individual(s) for the publication of any potentially identifiable images or data included in this article.

AUTHOR CONTRIBUTIONS

YZ designed experiments and edited the manuscript. PC and KC conducted most of the experiments, analyzed the data and wrote the draft. YZ collected the biopsy samples and did pathological analysis. SZ and SL conducted mutation analysis. PC followed up the patient and obtained the clinical data. K-tM collected imaging data and provided professional advice. All authors contributed to the article and approved the submitted version.

FUNDING

This work was supported by the Hubei Province health and family planning scientific research project (Grant number WJ2019Q028) and Natural Science Foundation of Hubei Province of China (Grant No. 2020CFB216).

ACKNOWLEDGMENTS

The authors would like to thank the patients for their involvement in the present study.

REFERENCES

1. Jurik AG. Multiple Hereditary Exostoses and Enchondromatosis. *Best Pract Res CL RH* (2020) 34:101505. doi: 10.1016/j.berh.2020.101505
2. Silve C, Juppner H. Ollier Disease. *Orphanet J Rare Dis* (2006) 1:37. doi: 10.1186/1750-1172-1-37
3. Ben-Itzhak I, Denolf FA, Versfeld GA, Noll BJ. The Maffucci Syndrome. *J Pediatr Orthop* (1988) 8:345–8. doi: 10.1097/01241398-198805000-00018
4. Ghembaza MEA, Lounici A. Maffucci Syndrome With Multiple Hand Calcifications. *Joint Bone Spine* (2017) 84:621–1. doi: 10.1016/j.jbspin.2016.11.007
5. Maione V, Stinco G, Errichetti E. Multiple Enchondromas and Skin Angiomas: Maffucci Syndrome. *Lancet* (2016) 388:905–5. doi: 10.1016/S0140-6736(16)00088-X
6. Wang J, Xu Z, Bao Z, Dai X, Ma L, Yao N, et al. Ollier Disease: Two Case Reports and a Review of the Literature. *Am J Transl Res* (2018) 10:3818–26. doi: 10.1943/AJTR0076533
7. Tejada Gallego J, Martinez-Gonzalez C. Multiple Enchondromatosis, Ollier Disease. *Anales pediatria (Barcelona Spain: 2003)* (2017) 87:176–7. doi: 10.1016/j.anpedi.2016.04.011
8. Tsao Y, Tsai C, Chen W. Maffucci Syndrome. *J Rheumatol* (2015) 42:2434–5. doi: 10.3899/jrheum.150216
9. Zhu GG, Nafa K, Agaram N, Zehir A, Benayed R, Sadowska J, et al. Genomic Profiling Identifies Association of IDH1/IDH2 Mutation With Longer Relapse-Free and Metastasis-Free Survival in High-Grade Chondrosarcoma. *Clin Cancer Res* (2020) 26:419–27. doi: 10.1158/1078-0432.CCR-18-4212
10. Saiji E, Pause FG, Lascombes P, Biderbost CC, Marq NL, Berczy M, et al. IDH1 Immunohistochemistry Reactivity and Mosaic IDH1 or IDH2 Somatic Mutations in Pediatric Sporadic Enchondroma and Enchondromatosis. *Virchows Arch* (2019) 475:625–36. doi: 10.1007/s00428-019-02606-9
11. van Noorden CJF, Khurshed M, Hira VVV, Molenaar RJ. Mechanisms of the IDH1/2 Mutations and Its Association With Contradictory Survival of Glioblastoma Patients *Versus* AML Patients. *FASEB J* (2018) 32S:40.10. doi: 10.1096/fasebj.2018.32.1_supplement.40.10
12. Molenaar RJ, Radivoyevitch T, Nagata Y, Przychodzen BP, Makishima H, Carraway HE, et al. IDH1/2 -Mutated Acute Myeloid Leukemia Has Impaired DNA Damage Response and Is Sensitive to Monotherapy With the PARP Inhibitior Olaparib. *Blood* (2017) 1301:568. doi: 10.1182/blood-2017-101342
13. Reitman ZJ, Sinenko SA, Spana EP, Yan H. Genetic Dissection of Leukemia-Associated IDH1 and IDH2 Mutants and D-2-Hydroxyglutarate in Drosophila. *Blood* (2015) 125:336–45. doi: 10.1182/blood-2014-05-577940
14. Largeaud L, Bertoli S, Berard E, Dufrechou S, Prade N, Gadaud N, et al. Outcome of Relapsed/Refractory AML Patients With IDH1(R132) Mutations in Real Life Before the Era of IDH1 Inhibitors. *Leukemia Lymphoma* (2020) 61:473–6. doi: 10.1080/10428194.2019.1668937
15. Knepper TC, Deutsch YE, Bhagat CK, Watts JM, Bradley TJ, Samra W, et al. Increased Frequency of IDH1/2 Mutations in Extramedullary Acute Myeloid Leuke. *Blood* (2018) 1321:1542. doi: 10.1182/blood-2018-99-113088
16. Badur MG, Muthusamy T, Parker SJ, Ma S, McBrayer SK, Cordes T, et al. Oncogenic R132 IDH1 Mutations Limit NADPH for *De Novo* Lipogenesis Through (D)2-Hydroxyglutarate Production in Fibrosarcoma Sells. *Cell Rep* (2018) 25:1018–+. doi: 10.1016/j.celrep.2018.09.074
17. Gonzalez-Romero E, Roson-Burgo B, Liquori A, Ibanez M, Boluda-Navarro M, Morote-Faubel M, et al. Transcriptomical Analysis and Modeling in C.Elegans of the IDH2 R140 R172 Mutation. *Haematologica* (2019) 1043:69–70. doi: 10.0390/s3-co-087
18. Luem N, Szankasi P, Kelley T, Patel JL. IDH2 R172 Mutated Myeloid Malignancies Show Distinct Mutational Profiles Compared to Cases With IDH1 and IDH2 R140 Mutations. *Lab Invest* (2018) 981:536–6. doi: 10.1530/98-s1-1505
19. Meggendorfer M, Cappelli L, Haferlach C, Kern W, Falini B, Haferlach T. IDH1R132, IDH2R140 and IDH2R172 in AML: Different Genetic Landscapes Correlate With Outcome and May Influence Targeted Treatment Strategies. *Blood* (2018) 32:1249–53. doi: 10.1038/s41375-018-0026-z
20. Chang S, Yim S, Park H. The Cancer Driver Genes IDH1/2, JARID1C/KDM5C, and UTX/KDM6A: Crosstalk Between Histone Demethylation and Hypoxic Reprogramming in Cancer Metabolism. *Exp Mol Med* (2019) 51:1–17. doi: 10.1038/s12276-019-0230-6
21. Komotar RJ, Starke RM, Sisti MB, Connolly ES. IDH1 and IDH2 Mutations in Gliomas and the Associated Induction of Hypoxia-Inducible Factor and Production of 2-Hydroxyglutarate. *Neurosurgery* (2010) 66:N20–1. doi: 10.1227/01.neu.0000369899.41915.67
22. Di Dalmazi G, Altieri B, Scholz C, Sbiera S, Luconi M, Waldman J, et al. RNA Sequencing and Somatic Mutation Status of Adrenocortical Tumors: Novel Pathogenetic Insights. *J Clin Endocrinol Metab* (2020) 105:e4459–73. doi: 10.1210/clinem/dgaa616
23. Zhang M, Zhang L, Li Y, Sun F, Fang Y, Zhang R, et al. Exome Sequencing Identifies Somatic Mutations in Novel Driver Genes in Non-Small Cell Lung Cancer. *Aging-Us* (2020) 12:13701–15. doi: 10.18632/aging.103500
24. Cheng P, Sun X, Yin D, Xu F, Yang K, Qin L, et al. Nanog Down-Regulates the Wnt Signaling Pathway *via* Beta-Catenin Phosphorylation During Epidermal Stem Cell Proliferation and Differentiation. *Cell Biosci* (2015) 5:5. doi: 10.1186/2045-3701-5-5
25. Kadar A, Kleinstern G, Morsy M, Soreide E, Moran SL. Multiple Enchondromas of the Hand in Children: Long-Term Follow-Up of Mean

15.4 Years. *J Pediatr Orthoped* (2018) 38:543–8. doi: 10.1097/BPO.0000000000000869
26. Ngai C, Ding DY, Rapp TB. Maffucci Syndrome an Interesting Case and A Review of the Literature. *Bull of Hosp for Joint Dis* (2015) 73:282–5. doi: 10.2328/BHJD26630472
27. Amary MF, Damato S, Halai D, Eskandarpour M, Berisha F, Bonar F, et al. Ollier Disease and Maffucci Syndrome Are Caused by Somatic Mosaic Mutations of IDH1 and IDH2. *Nat Genet* (2011) 43:1262–5. doi: 10.1038/ng.994
28. Hirabayashi S, Seki M, Hasegawa D, Kato M, Hyakuna N, Shuo T, et al. Constitutional Abnormalities Ofidh1 Combined With Secondary Mutations Predispose a Patient With Maffucci Syndrome to Acute Lymphoblastic Leukemia. *Pediatr Blood Cancer* (2017) 64:e26647. doi: 10.1002/pbc.26647
29. Turcan S, Rohle D, Goenka A, Walsh LA, Fang F, Yilmaz E, et al. IDH1 Mutation Is Sufficient to Establish the Glioma Hypermethylator Phenotype. *Nature* (2012) 483:479–83. doi: 10.1038/nature10866
30. DiNardo CD, Propert KJ, Loren AW, Paietta E, Sun Z, Levine RL, et al. Serum 2-Hydroxyglutarate Levels Predict Isocitrate Dehydrogenase Mutations and Clinical Outcome in Acute Myeloid Leukemia. *Blood* (2013) 121:4917–24. doi: 10.1182/blood-2013-03-493197
31. Arancibia D, Lira M, Cruz Y, Barrera DP, Montenegro-Venegas C, Godoy JA, et al. Serine-Arginine Protein Kinase SRPK2 Modulates the Assembly of the Active Zone Scaffolding Protein Cast1/Erc2. *Cells-Basel* (2019) 8:1333. doi: 10.3390/cells8111333
32. Hagiwara A, Kitahara Y, Grabner CP, Vogl C, Abe M, Kitta R, et al. Cytomatrix Proteins CAST and ELKS Regulate Retinal Photoreceptor Development and Maintenance. *J Cell Biol* (2018) 217:3993–4006. doi: 10.1083/jcb.201704076
33. Sigrist S, Ohtsuka T. The Presynaptic Active Zone: Molecules, Plasticity, and Diseases. *Neurosci Res* (2018) 127:1–2. doi: 10.1016/j.neures.2018.01.004
34. Mochida S, Hida Y, Tanifuji S, Hagiwara A, Hamada S, Abe M, et al. SAD-B Phosphorylation of CAST Controls Active Zone Vesicle Recycling for Synaptic Depression. *Cell Rep* (2016) 16:2901–13. doi: 10.1016/j.celrep.2016.08.020
35. Dong W, Radulovic T, Goral RO, Thomas C, Montesinos MS, Guerrero-Given D, et al. CAST/ELKS Proteins Control Voltage-Gated Ca2+ Channel Density and Synaptic Release Probability at a Mammalian Central Synapse. *Cell Rep* (2018) 24:284–+. doi: 10.1016/j.celrep.2018.06.024
36. Tajada S, Villalobos C. Calcium Permeable Channels in Cancer Hallmarks. *Front Pharmacol* (2020) 11:968. doi: 10.3389/fphar.2020.00968
37. Marchetti C, Gavazzo P, Burlando B. Epigallocatechin-3-Gallate Mobilizes Intracellular Ca2+ in Prostate Cancer Cells Through Combined Ca2+ Entry and Ca2+-Induced Ca(2+)release. *Life Sci* (2020) 258:118232. doi: 10.1016/j.lfs.2020.118232
38. Terrie E, Coronas V, Constantin B. Role of the Calcium Toolkit in Cancer Stem Cells. *Cell Calcium* (2019) 80:141–51. doi: 10.1016/j.ceca.2019.05.001
39. Visa A, Sallan MC, Maiques O, Alza L, Talavera E, Lopez-Ortega R, et al. T-Type Ca(v)3.1 Channels Mediate Progression and Chemotherapeutic Resistance in Glioblastoma. *Cancer Res* (2019) 79:1857–68. doi: 10.1158/0008-5472.CAN-18-1924

Conflict of Interest: The authors declare that the research was conducted in the absence of any commercial or financial relationships that could be construed as a potential conflict of interest.

Publisher's Note: All claims expressed in this article are solely those of the authors and do not necessarily represent those of their affiliated organizations, or those of the publisher, the editors and the reviewers. Any product that may be evaluated in this article, or claim that may be made by its manufacturer, is not guaranteed or endorsed by the publisher.

frontiers in Endocrinology

ORIGINAL RESEARCH
published: 20 January 2022
doi: 10.3389/fendo.2021.778019

Brown Adipose Tissue Rescues Bone Loss Induced by Cold Exposure

Jingke Du[1,2†], Zihao He[1,3†], Mingming Xu[1†], Xinhua Qu[4], Junqi Cui[5], Shuangyan Zhang[1], Shuhong Zhang[1], Hanjun Li[1] and Zhifeng Yu[1*]*

[1] Shanghai Key Laboratory of Orthopedic Implants, Department of Orthopedic Surgery, Shanghai Ninth People's Hospital, Shanghai Jiao Tong University School of Medicine, Shanghai, China, [2] Knee Surgery Department of the Institute of Sports Medicine, Beijing Key Laboratory of Sports Injuries, Peking University Third Hospital, Beijing, China, [3] Arthritis Clinic and Research Center, Peking University People's Hospital, Peking University, Beijing, China, [4] Department of Bone and Joint Surgery, Renji Hospital, School of Medicine, Shanghai Jiao Tong University, Shanghai, China, [5] Department of Pathology, Shanghai Ninth People's Hospital, Shanghai Jiao Tong University School of Medicine, Shanghai, China

OPEN ACCESS

Edited by:
Guanwu Li, Shanghai University of Traditional Chinese Medicine, China

Reviewed by:
Peng Cheng, Huazhong University of Science and Technology, China
Gemma Di Pompo, Rizzoli Orthopedic Institute (IRCCS), Italy

***Correspondence:**
Zhifeng Yu
zfyu@outlook.com
Hanjun Li
hanjun_li@aliyun.com

†These authors have contributed equally to this work and share first authorship

Specialty section:
This article was submitted to Bone Research, a section of the journal Frontiers in Endocrinology

Received: *16 September 2021*
Accepted: *27 December 2021*
Published: *20 January 2022*

Citation:
Du J, He Z, Xu M, Qu X, Cui J, Zhang S, Zhang S, Li H and Yu Z (2022) Brown Adipose Tissue Rescues Bone Loss Induced by Cold Exposure. Front. Endocrinol. 12:778019. doi: 10.3389/fendo.2021.778019

Cold temperature activates the sympathetic nervous system (SNS) to induce bone loss by altering bone remodeling. Brown adipose tissue (BAT) is influenced by the SNS in cold environments. Many studies have confirmed a positive relationship between BAT volume and bone mass, but the influence and mechanism of BAT on bone *in vivo* and *in vitro* is still unknown. Two-month-old C57/BL6j male mice were exposed to cold temperature (4°C) to induce BAT generation. BAT volume, bone remodeling and microstructure were assessed after 1 day, 14 days and 28 days of cold exposure. CTX-1, P1NP and IL-6 levels were detected in the serum by ELISA. To determine the effect of BAT on osteoclasts and osteoblasts *in vitro*, brown adipocyte conditional medium (BAT CM) was collected and added to the differentiation medium of bone marrow-derived macrophages (BMMs) and bone marrow mesenchymal stem cells (BMSCs). Micro-CT results showed that the bone volume fraction (BV/TV, %) significantly decreased after 14 days of exposure to cold temperature but recovered after 28 days. Double labeling and TRAP staining *in vivo* showed that bone remodeling was altered during cold exposure. BAT volume enlarged after 14 days of cold stimulation, and IL-6 increased. BAT CM promoted BMSC mineralization by increasing osteocalcin (Ocn), RUNX family transcription factor 2 (Runx2) and alkaline phosphatase (Alp) expression, while bone absorption was inhibited by BAT CM. In conclusion, restoration of bone volume after cold exposure may be attributed to enlarged BAT. BAT has a beneficial effect on bone mass by facilitating osteogenesis and suppressing osteoclastogenesis.

Keywords: cold exposure, bone remodeling, osteoblast, osteoclast, interleukin-6

INTRODUCTION

The body's metabolism can be affected by many factors, such as food intake (1, 2), exercise (3, 4), stress state (5, 6), and environmental temperature (7). Low-temperature exposure can affect the activity of the nervous system (8–10), endocrine system (11, 12), musculoskeletal system (13–15) and so on (7, 16). All of these factors influence the expression levels of cytokines *in vivo*. The

relationship between temperature and bone mass has triggered researchers' interest in recent years, but the effects of cold exposure on bone have not been well illustrated. Some results declared that cold leads to increased bone mass (13), while other studies indicated that cold has negative effects on bone volume (14, 17). Studies have shown that cold exposure affects the generation and release of neurotransmitters, which play a role in skeletal metabolism and endocrinology (10, 18). Wee, N.K.Y., et al. confirmed that neuropeptide Y (NPY) plays a significant role in the increase in energy expenditure, UCP1 expression, and bone loss in response to cold exposure (10). Low temperature-activated sympathetic nerves lead to the activation of β adrenergic receptors and subsequently initiate osteoclast-related bone resorption (19, 20). In addition, activated sympathetic nerves can influence bone mass in indirect ways by affecting the expression levels of bone morphogenetic protein 8b (BMP8b) and PTH (20, 21).

In addition to its effects on bone mass, cold stimulation also promotes the generation of brown adipose tissue (BAT) and increased UCP1 expression levels (22, 23), which is essential for brown adipocytes. Similar to white adipose tissue, BAT can be considered an endocrine organ that secretes many factors under both physiological and pathological conditions (24, 25). These adipose cytokines have widespread functions. In addition to its influence on lipid metabolism, BAT releases fibroblast growth factor 21 (FGF21), interleukin-6 (IL-6) (26), and neuregulin 4 (Nrg4) to influence metabolism (27, 28). Reports have shown that brown adipokines, such as BMP8b and Nrg4, influence the remodeling of the neurovascular network and alleviate liver steatosis (29, 30). Enlarged BAT *via* hypertrophy and hyperplasia (31) increases energy consumption and leads to increased bone mass (32).

The positive relationship between BAT and bone mass has been previously confirmed (33). Bredella, M. A. et al. found that BAT has a positive effect on bone mass and that BAT is a positive predictor of femoral bone structure (34). Bone formation ability was attenuated in BAT-deficient mice (*Misty* mice) (35). Correlation analyses in humans showed that BAT is an independent predictor of bone mass (13, 16). In this study, we aimed to investigate the effect and mechanism of BAT on bone metabolism, which could help to elucidate the functions and applications of BAT.

MATERIALS AND METHODS

Animals

Male C57BL/6J mice at two months of age were purchased from Shanghai SLAC Laboratory Animal Company (Shanghai, China), and this study was approved by the animal ethics committee of Shanghai Ninth People's Hospital. The mice were fed commercial food and water under specific aseptic (SPF) conditions. For cold stimulation, thirty mice were randomly divided into two groups, cold stimulation (cold) and room temperature (normal), with fifteen mice per group. Briefly, mice in the cold group grew in incubators (Fuyilian, FYL-YS-280 L) at 4°C, while mice in the normal group were in the same type of incubators at room temperature (23°C) (36). Mice were euthanized after being exposed to cold/normal temperature for 1 d, 14 d and 28 d, and tibias were then collected.

Calcein and Alizarin Red Double Labeling

To calculate dynamic bone histomorphometry, animals were injected with 30 mg/kg calcein (Sigma) and alizarin red (Sigma) 10 and 3 days before euthanasia. Nondecalcified tibiae were embedded in methyl methacrylate and sectioned.

After imaging with a confocal microscope, histomorphometric examination was confined to the consistent cortical region and was performed using BIOQUANT OSTEO 2019 (v19.6.60). The mineral apposition rate (MAR) and bone formation rate per bone surface (BFR/BS) were analyzed at 40× magnification from 6 representative fields per bone sample (37).

Microcomputed Tomography Scanning

At the end of each experiment, the tibias of the mice were fixed in 4% paraformaldehyde. Samples were scanned using micro-CT (μCT 80; Scanco, Zurich, Switzerland) as previously described (38). The micro-CT parameters were as follows: voltage, 70 kV; electric current, 114 μA; and resolution, 10 μm per pixel. Three-dimensional structural parameters, including bone volume fraction (BV/TV), trabecular number (Tb.N), trabecular thickness (Tb.Th) and trabecular separation (Tb.Sp), were analyzed (38, 39).

In Vivo Brown Adipose Volume Analysis

Perkin Elmer micro-CT was applied to analyze brown adipose tissue as described in previous studies (40, 41). Briefly, mice were anesthetized with 30 mg/kg pentobarbital sodium and then scanned in the machine to measure BAT volume in the scapula. The data were analyzed using Analyze 12.0 according to the instructions to determine the BAT volume.

Fat Mass and Lean Mass Measurement

Mice were scanned by dual-emission X-ray absorptiometry (DXA, Hologic Discovery A) through animal models to obtain the lean mass, %lean, fat mass, %fat and whole-body weight.

Enzyme-Linked Immunosorbent Assay (ELISA)

Interleukin-6 (IL-6) (70-EK206/3-96, Multisciences), P1NP (Lengton, Shanghai), and CTX-1 (Lengton, Shanghai) ELISA kits were used to detect the expression levels of IL-6, P1NP, and CTX-1 in the serum, according to the manufacturer's instructions. A microplate reader (Bioteck, Arcugnano [Vicenza], Italy) was used to determine the optical density (OD) of each well at 450 nm.

TRAP Staining

After decalcification in 10% ethylenediaminetetraacetic acid (EDTA) for 3 weeks, samples were embedded in paraffin. To observe the microstructure of the samples, 4-μm-thick sagittal

sections of the medial compartment of the knee joint were cut. After TRAP staining was performed, OC surface/bone surface (Oc.N/BS) was calculated using a Bioquant system.

In Vitro Differentiation of BAT

BAT was isolated and cultured following previously described methods (42). Briefly, 4-week-old C57BL/6 mice were euthanized. Interscapular BAT was collected, minced, and digested in collagenase digestion buffer (DMEM, 1 mg/ml collagenase I, 1% FBS). Preadipocyte cells were collected by filtering through 70 μm membranes and centrifuging. Preadipocytes were cultured to 80%-90% confluence in DMEM supplemented with 10 ng/ml bFGF (Pepro Tech), 10% fetal bovine serum (Gibco) and pen/strep (Life Technologies). Cells were subcultured every 3 days and used from passages 3 to 5. Then, preadipocytes were differentiated with DMEM containing 10% fetal bovine serum (Gibco), 10 μg/ml insulin (Sigma), 1 μM dexamethasone (Sigma), 0.5 mM 3-isobutyl-1-methylxanthine, phosphodiesterase inhibitor (IBMX, Sigma), 5 μM rosiglitazone (Sigma), and 1 nM T3 (Sigma) for 6 days until brown adipocyte formation.

Preparation of BAT CM

To obtain conditioned medium (BAT CM), DMEM with 10% exosome-free FBS was used to culture brown adipocytes, which were collected after 48 hours. The conditioned medium was centrifuged at 300 × g for 10 min to discard cells and further centrifuged at 2,000 × g for 10 min and at 10,000 × g for 30 min to remove cellular debris and large vesicles, respectively (43, 44). After filtration through a 0.22 μm filter, conditioned medium was used to culture BMMs and BMSCs.

In Vitro Osteoclastogenesis

To obtain bone marrow macrophages (BMMs), 4-week-old C57BL/6J mice were sacrificed, and their femurs and tibias were separated under sterile conditions. Bone marrow was flushed from the mouse femurs and tibias using complete a-MEM, which contained macrophage-colony stimulating factor (M-CSF, 30 ng/mL). After resuspension, bone marrow cells were cultured in a 10-cm dish at 37°C in 5% CO_2. The medium was changed after 3 and 7 days to remove nonadherent cells. When the cellular density reached 80% confluence, BMMs were washed three times with phosphate buffered saline (PBS) and collected using 0.25% trypsin for subsequent experiments. Bone mesenchymal stem cells (BMSCs) were obtained through the same procedure but were cultured without M-CSF (45). For osteoclastogenesis, BMMs were seeded into 24-well plates (10^5 cells/well) or 96-well plates (10^4 cells/well) and then treated with osteoclastogenesis medium, which consisted of complete a-MEM, receptor activator of nuclear factor kappa-B ligand (RANKL, 50 ng/mL) and M-CSF (30 ng/mL). BAT CM was added or not to the osteoclastogenesis medium for 7 days until osteoclasts were formed (46). After fixing the cells in 4% paraformaldehyde for 30 min, TRAP-positive cells were stained using a TRAP staining kit (Sigma-Aldrich, 387A-1KT). ImageJ software (Media Cybernetics Bethesda, MD, United States) was used to calculate the number of multinuclear (n≥3) TRAP-positive cells in each well. To determine the bone resorption ability, BMMs were differentiated in an osteoassay stripwell plates for 8 days. Then, the cells were washed with 4% sodium hypochlorite for 10 minutes followed by three washes with double distilled water. The resorption area was calculated using ImageJ software (Media Cybernetics Bethesda, MD, United States).

In Vitro Osteogenesis

BMSCs were seeded into 24-well plates and cultured until the they reached 80% confluence. Then, the medium was replaced with an osteogenesis assay kit (MUBMX-90021, Cyagen, CA, United States) with or without BAT conditioned medium (1:1) at 37°C in humidified air with 5% CO_2 for 21 days to induce osteogenesis. Bone formation was detected using alkaline phosphatase (ALP) or alizarin red staining on days 14 and 21. ALP staining was performed as follows: after washing three times with PBS and fixation in 4% paraformaldehyde for 10 min at room temperature, cultured cells were stained using the BCIP/NBT Alkaline Phosphatase Color Development Kit (Beyotime Institute of Biotechnology, Shanghai, China). All steps were strictly in accordance with the manufacturer's instructions. After 21 days of culture, alizarin red staining was performed. Briefly, the cultured cells were washed with PBS and fixed in 4% paraformaldehyde for 30 min, and then 500 μL alizarin red dye (contained in the MUBMX-90021 kit) was added to each well and incubated at room temperature for 10 min. After washing five times with PBS, 10% cetylpyridinium chloride (500 μL) (H811089, Macklin, CA, United States) was added to each well for semiquantitative analysis. Then, the absorbance of the supernatant at 562 nm was detected after incubation for 30 min at room temperature.

Quantitative Reverse-Transcription Polymerase Chain Reaction (qRT-PCR)

TRIzol reagent (Thermo Scientific, US) was used to extract total RNA. After the concentration was measured, the total RNA was converted to complementary DNA using a Quant script RT Kit (Promega, Madison, WI, USA). To detect messenger RNA (mRNA) levels, cDNA and SYBR Premix Ex Taq Mix (Selleck) PCR in 10 μL PCRs were performed in the Real-Time PCR System (Light Cycler 2.0; Roche Diagnostics GmbH, Mannheim, Germany). The primer sequences are shown in **Table 1**.

Statistical Analysis

GraphPad Prism 5.0 (GraphPad Software Inc., CA, United States) was used for statistical analysis of data. Each experiment was repeated at least three times. For animal studies, each group had at least three mice. All quantitative values are presented as the mean ± standard deviation (SD). Two−way analysis of variance (ANOVA) or Student's t-test was used for analysis of differences. Bonferroni correction was performed for multiple comparisons. $P < 0.05$ was considered statistically significant.

TABLE 1 | Primer sequences for the quantitative reverse-transcription polymerase chain reaction.

Target genes	Forward (5'-3')	Reverse (5'-3')
Gapdh	AGGTCGGTGTGAACGGATTTG	TGTAGACCATGTAGTTGAGGTCA
Ocn	CTGACCTCACAGATCCCAAGC	TGGTCTGATAGCTCGTCACAAG
Runx2	CCGGGAATGATGAGAACTA	ACCGTCCACTGTCACTTT
Alp	CCAACTCTTTTGTGCCAGAGA	GGCTACATTGGTGTTGAGCTTTT
Traf6	AAAGCGAGAGATTCTTTCCCTG	ACTGGGGACAATTCACTAGAGC
Ctsk	GAAGAAGACTCACCAGAAGCAG	TCCAGGTTATGGGCAGAGATT
Atp6a3	CACAGGGTCTGCTTACAACTG	CGTCTACCACGAAGCGTCTC
Dcst	GGGGACTTATGTGTTTCCACG	ACAAAGCAACAGACTCCCAAAT
UCP1	AGGCTTCCAGTACCATTAGGT	CTGAGTGAGGCAAAGCTGATTT
Pgc1α	TATGGAGTGACATAGAGTGTGCT	CCACTTCAATCCACCCAGAAAG
Cidea	TGACATTCATGGGATTGCAGAC	GGCCAGTTGTGATGACTAAGAC
Prdm16	CCAAGGCAAGGGCGAAGAA	AGTCTGGTGGGATTGGAATGT

RESULTS

Cold Exposure Influences Bone Mass in a Time-Dependent Manner

After being exposed to 4°C for different times, mice exhibited fluctuations in bone microstructure (**Figure 1A**). As shown in **Figure 1B**, BV/TV and Tb.Th decreased at 14 days but recovered after 28 days of exposure. Tb.Sp in both groups increased after 28 days of exposure, but it was higher in the cold-treated group. Tb.N in both groups decreased with prolonged time and was lower in the cold-treated group.

Cold Exposure Affects Bone Remodeling

Calcein and alizarin red double labeling were performed to determine the bone formation rate (**Figure 2A**). As shown in **Figure 2C**, the bone formation rate/bone surface (BFR/BS)

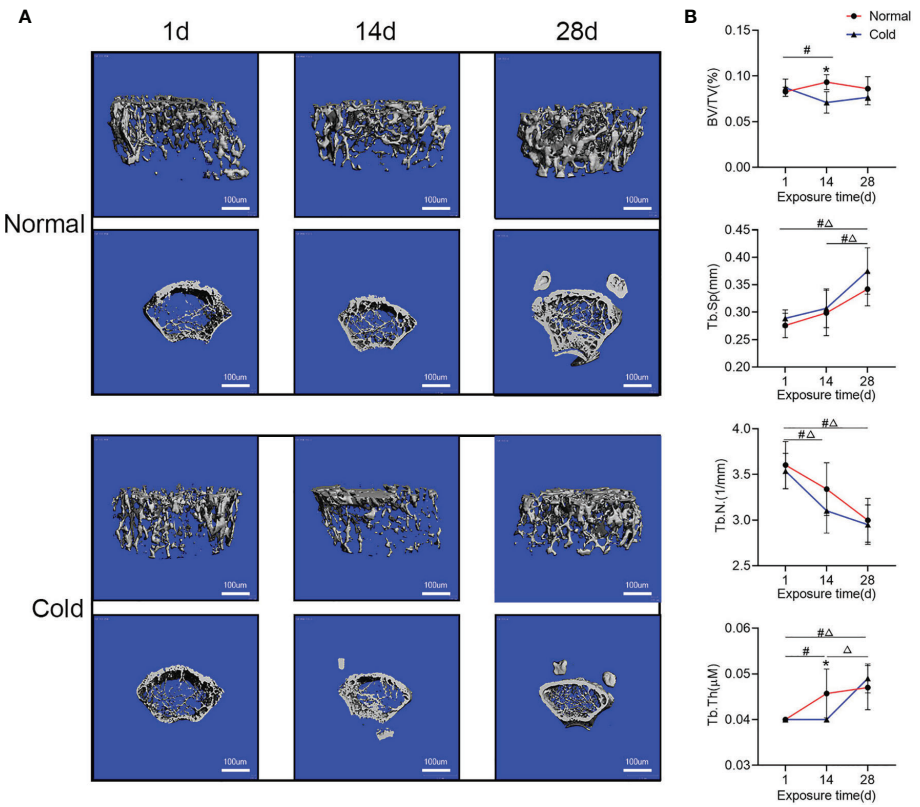

FIGURE 1 | Bone mass fluctuates with increased time. **(A)** Representative images of micro-CT are shown. **(B)** Trabecular bone microarchitecture of tibias showing bone volume/total volume (BV/TV), trabecular number (Tb.N), trabecular separation (Tb.Sp), and trabecular thickness (Tb.Th). Data are shown as the mean ± SD (n=5 per group). Significance (p-value) was calculated using two-way ANOVA, *$p < 0.05$, cold group *vs.* normal group; $^{\#}p < 0.05$, difference at different time points in the normal group; $^{\Delta}p < 0.05$, difference at different time points in the cold group; 1 day (1 d), 14 days (14 d), 28 days (28 d), Normal: mice at room temperature (23°C), Cold: mice at 4°C.

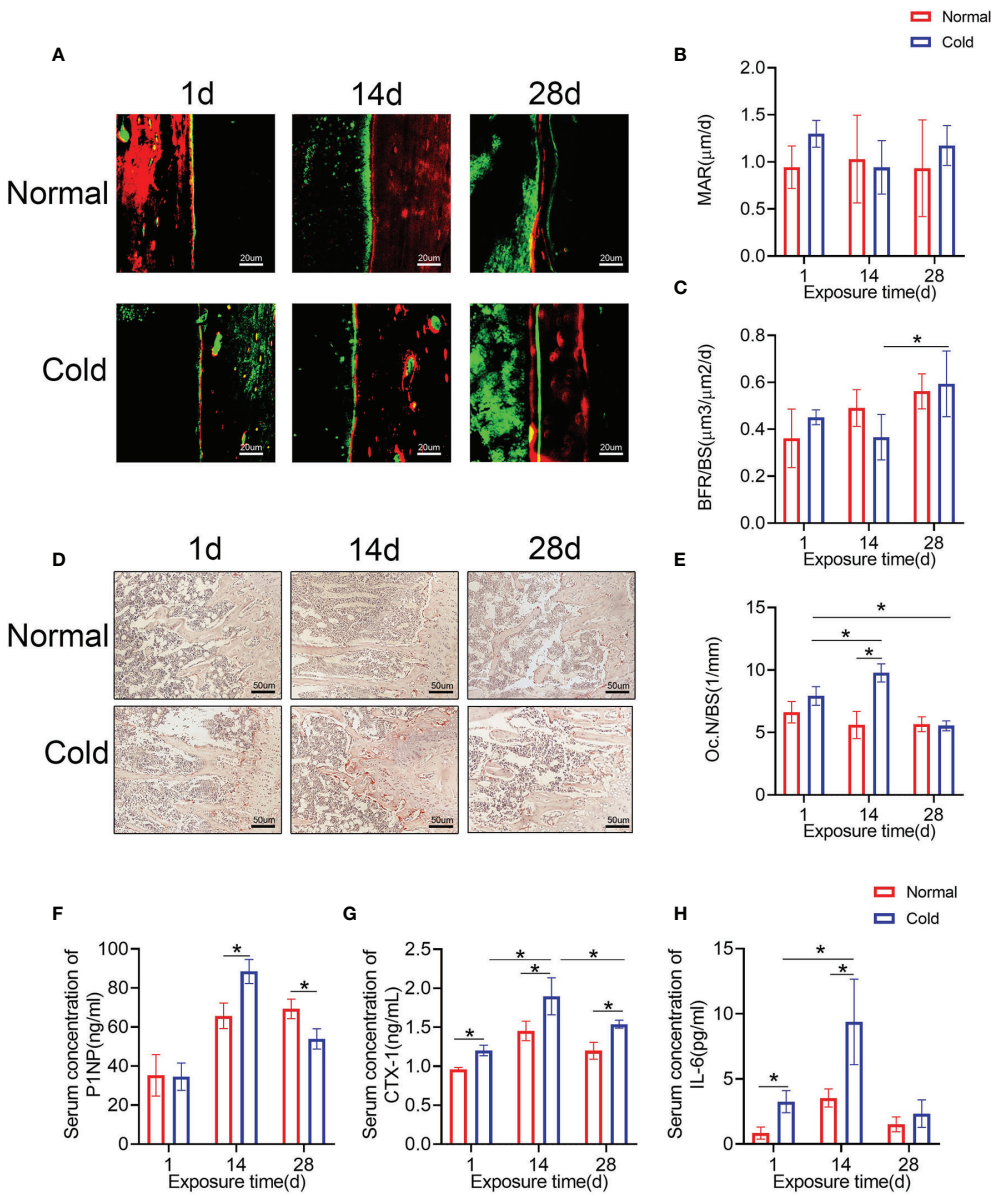

FIGURE 2 | Bone remodeling is influenced by temperature. **(A)** Calcium and alizarin red double labeling were performed to determine the bone formation rate. **(B, C)** BFR/BS and MAR shown in A were calculated. **(D)** Representative TRAP staining of femur bone sections. **(E)** Histomorphometric quantification of Oc.N/BS in femur bone. **(F–H)** CTX-1, P1NP and IL-6 in the serum were detected by ELISA. Black arrows: TRAP positive cells. Data are shown as the mean ± SD (n=5 per group). Significance (p-value) was calculated using two-way ANOVA, *p < 0.05; 1 day (1 d), 14 days (14 d), 28 days (28 d), Normal: mice at room temperature (23°C), Cold: mice at 4°C.

decreased dramatically after 14 days of cold stimulation and increased at 28 days, but there were no significant changes in the mineral appositional rates (MARs) (**Figure 2B**). Osteoclast numbers were calculated using TRAP staining (**Figure 2D**), and increased osteoclast number/bone surface (Oc.N/BS) of the cold group was observed at 14 days (**Figure 2E**), which was recovered even lower than the baseline after 28 days of exposure. Levels of P1NP in the cold group, a marker of bone formation, were higher at 14 days and lower at 28 days than that in the control group (**Figure 2F**). CTX-1 was detected in the same way to confirm bone resorption ability. Expression levels of CTX-1 in the cold group were higher than that in the control group and reached their highest level at 14 days (**Figure 2G**). In addition, cold promoted the expression of IL-6, one of the most important factors induced by BAT (26), at 1 and 14 days (**Figure 2H**).

Brown Adipose Tissue Accumulates in a Cold Environment *In Vivo*

To observe the effect of cold on BAT, BAT in the interscapular region of mice was scanned and calculated. As shown in **Figures 3A, C**, brown adipose volume was stimulated by cold temperature, which increased in 14 days and was maintained until 28 days. Concordantly, the lean mass in both groups was higher on day 14 than on day 1, while the cold group exhibited a higher lean mass on day 28 (**Figure 3D**). Other results calculated by DXA, such as body weight, fat mass, %lean and %fat, did not change significantly (**Figures 3B**, **E–G**).

Brown Adipocytes Affect Osteogenesis and Osteoclastogenesis *In Vitro*

Brown adipose tissue cells in the stromal vascular fraction (BAT svf, BS) were cultivated *in vitro*. Oil red O staining was performed to test whether BAT SVF cells were differentiated into brown adipocytes (BB) (**Figure 4A**), which produce scattered lipid droplets. Western blot analysis showed that UCP1 expression was increased in the BB group (**Figure 4B**). Furthermore, brown adipocyte gene markers were dramatically increased in the differentiated group (**Figure 4C**).

Brown adipocyte conditional medium (BAT CM) was added to the osteogenesis differentiation medium of BMSCs. Staining assays showed that BAT CM strengthened ALP and alizarin red staining in BMSCs (**Figure 4D**). Semiquantitative analysis of alizarin red is shown in **Figure 4E**, which confirmed improved bone formation in the BAT CM group. Moreover, Alp, Ocn, and Runx2 levels were upregulated by BAT CM compared to the corresponding control treatments (**Figure 4F**).

To determine the effects of BAT CM on osteoclastogenesis, we added BAT CM to the differentiation medium of BMMs, and TRAP staining (**Figure 4G**) revealed reduced multinuclear osteoclastogenesis after 6 days of cultivation (**Figure 4I**). Meanwhile, resorption ability was assessed using the osteoassay stripwell, and the resorption area was smaller in the BAT CM group (**Figure 4J**). Additionally, Ctsk, Dcst, and Traf6 were downregulated by BAT CM (**Figure 4H**).

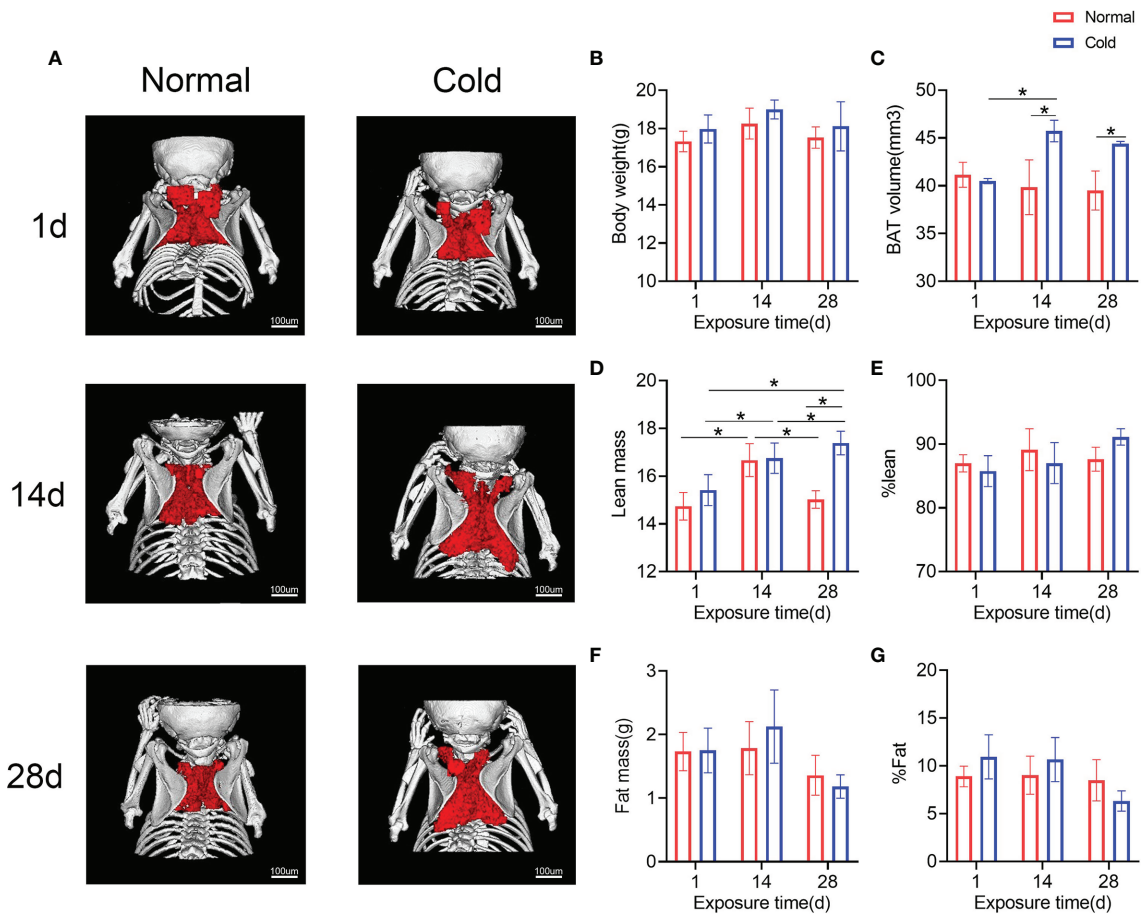

FIGURE 3 | Brown adipose tissue in the interscapula enlarges in response to cold exposure. **(A)** Reconstruction images of the micro-CT are shown, brown adipose reconstructs with red and bone with white. **(B–G)** Body weight, brown adipose volume (BAT volume), lean mass, %lean, fat mass and %fat were calculated. Data are shown as the mean ± SD (n=5 per group). Significance (p-value) was calculated using two-way ANOVA, *p < 0.05; 1 day (1 d), 14 days (14 d), 28 days (28 d), Normal: mice at room temperature (23°C), Cold: mice at 4°C.

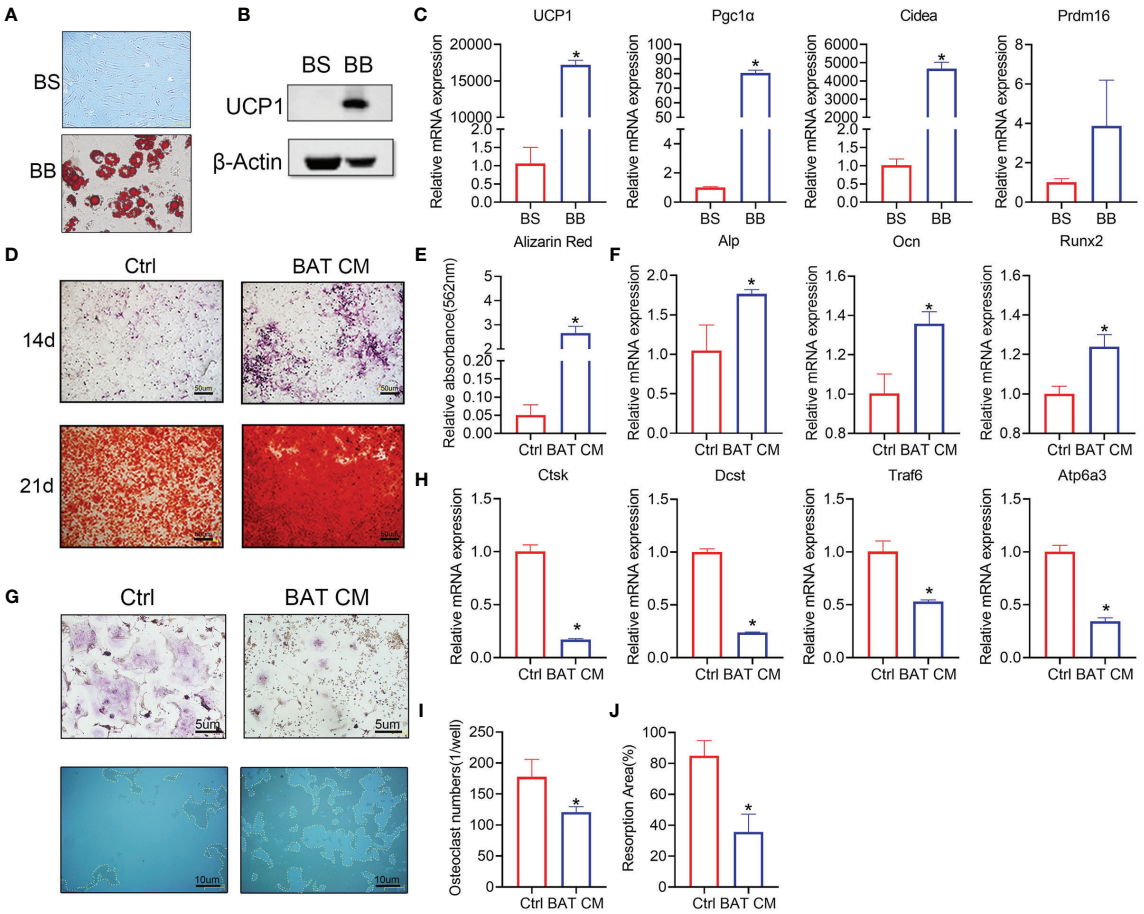

FIGURE 4 | Brown adipocytes affect bone remodeling *in vitro*. **(A)** Oil red O staining was performed to show the distribution of lipid droplets in brown adipocytes. **(B)** Western blot analysis showed that UCP1 expression was higher in the differentiation group. **(C)** RT-PCR shows the relative mRNA expression levels of the two groups. **(D)** ALP and alizarin red staining were performed at 14 and 21 days. **(E)** Semiquantitative analysis of alizarin red staining. **(F)** Alp, Ocn and Runx2 expression levels are shown. **(G)** TRAP staining (top) and bone resorption ability (below) in the hydroxyapatite covered plate are shown. Absorbed areas are circled with yellow dotted lines. **(H)** Relative expression levels of Ctsk, Dcst, Traf6, and Atp6a3 were detected by RT-PCR. **(I)** Osteoclast numbers in each well are calculated. **(J)** The osteoclast resorption area in the osteoassay stripwell plate was computed. Data are shown as the mean ± SD (n≥3 per group). Significance (p-value) was calculated using Student's t-test, *p < 0.05; 1 day (1 d), 14 days (14 d), 28 days (28 d), Normal: mice at room temperature (23°C), Cold: mice at 4°C.

DISCUSSION

In this research, fluctuating bone mass was observed in response to the extension of cold exposure time, decreased at 14 days, and increased at 28 days. Further detection revealed that there was increased bone formation and osteoclast numbers at 14 days. Studies *in vitro* showed that BAT CM promoted osteogenesis and impaired osteoclastogenesis.

Cold-induced bone loss after 14 days of exposure is consistent with research showing that low temperature is negatively correlated with bone mass. Robbins et al. found that cool nursed mice exhibited reduced bone mass but higher UCP1 expression at 20°C versus 26°C (17). Similarly, growing C57BL/6J and C3H/HeJ mice nursing at 22°C resulted in premature cancellous bone loss (14, 47). In addition, Serrat et al. excluded the effect of tissue perfusion on extremity elongation in mice and attributed shorter hindlimbs to alterations in chondrocyte proliferation and extracellular matrix volume in the cold environment (48). Other study concluded that cold has positive effect on bone mass. They performed their studies in anorexia nervosa people and cold stimulation was used as a tool to select people with brown adipose, and then the positive relationship between brown adipose volume and bone mass was concluded (13). In our study, cold induced bone loss after 14 days of exposure, which is consistent with research showing that low temperature is negatively correlated with bone mass.

As the regulator of bone remodeling, the sympathetic nervous system can be activated by exercise, cold, and emotion (19, 20). The negative relationship between the activation of sympathetic nerves and bone mass has been confirmed (49). As a sympathetic nerve enrichment organ (50, 51), cold-induced enlargement of BAT is well defined (28). Recently, Moser C et al. reported that

cold promotes the generation of BAT after 1 week of exposure, which is consistent with our results (52). It is generally acknowledged that brown adipocytes consume energy and have a wide range of functions (24, 25, 31). An important role of BAT in bone remodeling has been confirmed in FoxC2(AD) (+/Tg) mice, which exhibit enhanced bone remodeling ability and increased bone mass (37). In another study, Katherine J Motyl et al. raised *Misty* mice, brown adipose barren mice, in a cold (4°C) environment and concluded that a short period of cold stimulation decreases RUNX2 and increases RANKL expression levels (35). In addition, brown adipocytes play a role in BMP-2-induced heterotopic ossification in muscle (53).

Besides, BAT can secrete cytokines, such as leptin, fibroblast growth factor 21(FGF21), IL-6, and neuregulin 4, all of them could influence bone remodeling (27, 54). Leptin, a well-studied protein, has direct anabolic effect on osteoblast (55), and BMSCs rich in leptin receptor (LepR) are the main source of bone formation (56). Studies in healthy adults found a positive association between plasma FGF21 levels and BMD in women (57), while Ruo-Han Hao et al. observed that FGF21 is negatively related to regional BMD in humans (58). Inconsistent results were also reported in animal studies (59, 60). So, it is reasonable to assume that these adipokines play a role in the changes of bone mass under cold stress. Similarly, IL-6 may play a role in the process of bone mass fluctuation during cold exposure. Reports have confirmed that mice are under stress in cold environments (61, 62), which leads to the release of IL-6 by BAT (26). All of these findings indicate that low temperature may accelerate bone renewal by promoting osteogenesis and osteoclastogenesis. As a well-defined cytokine, IL-6 is a type of interleukin that can be produced by fibroblasts, macrophages, T lymphocytes, B lymphocytes, endotheliocytes, keratinocytes, and a variety of tumor cells (63) and has a wide range of functions *in vivo (*64). In terms of its effects on bone remodeling, it is believed that IL-6 enhances osteoclast differentiation (65, 66), but it does not promote osteoclastogenesis in a direct way, even in osteoclasts or their progenitor cells expressing the IL-6 receptor (67). In contrast, like many other cytokines and hormones, IL-6 indirectly promotes osteoclast formation and bone resorption by promoting RANKL expression (64). For example, IL-6 promotes expression of RANKL in osteoblast cell lines *in vivo (*68, 69), thereby activating osteoclasts to promote bone resorption. Studies *in vivo* found that ovariectomy-induced bone loss can be alleviated by inhibiting the activity of IL-6, indicating the obvious effect of IL-6 on the activity of osteoclasts (70). In our study, IL-6 expression levels were markedly increased on day 14 of cold stimulation but gradually decreased with the extension of exposure time, accompanied by changes in the number of osteoclasts, which increased on day 14 and decreased on day 28. Therefore, it can be speculated that bone loss caused by a low-temperature environment after 14 days is closely related to IL-6 and controlling the expression level of IL-6 may represent a potential target for osteoporosis treatment. Considering the significant effects of cytokines mentioned above, BAT may promote osteogenesis *in vivo and vitro* by secreting cytokines or extracellular vesicles.

In recent years, increasing attention has been given to the role of small extracellular vesicles in information transmission. It has been reported that fibroblasts of young human donors alleviate certain senescence biomarkers of cells derived from old donors (71). Similarly, small extracellular vesicles derived from osteoclasts or tumor cells can influence bone formation or resorption (72, 73). Furthermore, miRNAs have been found to be secreted extracellularly in exosomes and to have a wide range of functions (74). For example, miRNA-5106 in M2 macrophage-derived exosomes accelerates fracture healing *in vivo (*75). In addition, miRNA-21 and miRNA-217 can transmit senescence signals to neighboring endothelial cells (76). Moreover, studies found that brown adipose depletion impairs bone remodeling *in vivo (*35), while brown adipocyte-derived exosomes alleviate metabolic syndrome in high-fat diet mice (77). Therefore, we postulate that the bone rescue ability of BAT CM is attributed to the exosomes contained in it, and further, some microRNAs may be identified as promoting these effects.

In conclusion, the changes in bone mass that occur in low temperature conditions may be the result of a combination of temperature and BAT. The exact mechanism may be complicated, but it is clear that BAT secretes a number of factors that influence bone mass. The striking influence of BAT CM on bone formation and osteoclastogenesis indicates that further studies should be performed to detect the important factors in this process, which could represent an important treatment for osteoporosis. In summary, the functional cytokines or extracellular vesicles in BAT CM need further investigation.

DATA AVAILABILITY STATEMENT

The raw data supporting the conclusions of this article will be made available by the authors, without undue reservation.

ETHICS STATEMENT

The animal study was reviewed and approved by Animal Ethics Committee of Shanghai Ninth People's Hospital.

AUTHOR CONTRIBUTIONS

All authors listed have made a substantial, direct, and intellectual contribution to the work, and approved it for publication.

FUNDING

This work was supported by grants from the National Natural Science Foundation of China (Nos. 11572197, 11872251, 81802679) and the National Key R&D Program (grant no. 2016YFC1102100).

REFERENCES

1. Woods SC, Ramsay DS. Food Intake, Metabolism and Homeostasis. *Physiol Behav* (2011) 104(1):4–7. doi: 10.1016/j.physbeh.2011.04.026
2. Abreu-Vieira G, Xiao C, Gavrilova O, Reitman ML. Integration of Body Temperature Into the Analysis of Energy Expenditure in the Mouse. *Mol Metab* (2015) 4(6):461–70. doi: 10.1016/j.molmet.2015.03.001
3. Moghetti P, Bacchi E, Brangani C, Donà S, Negri C. Metabolic Effects of Exercise. *Front Horm Res* (2016) 47:44–57. doi: 10.1159/000445156
4. Ozcivici E, Luu YK, Adler B, Qin YX, Rubin J, Judex S, et al. Mechanical Signals as Anabolic Agents in Bone. *Nat Rev Rheumatol* (2010) 6(1):50–9. doi: 10.1038/nrrheum.2009.239
5. Glaser R, Kiecolt-Glaser JK. Stress-Induced Immune Dysfunction: Implications for Health. *Nat Rev Immunol* (2005) 5(3):243–51. doi: 10.1038/nri1571
6. Umamaheswaran S, Dasari SK, Yang P, Lutgendorf SK, Sood AK. Stress, Inflammation, and Eicosanoids: An Emerging Perspective. *Cancer Metastasis Rev* (2018) 37(2-3):203–11. doi: 10.1007/s10555-018-9741-1
7. Steinberg B, Singh IJ, Mitchell OG. The Effects of Cold-Stress. Hibernation, and Prolonged Inactivity on Bone Dynamics in the Golden Hamster, Mesocricetus Auratus. *J Morphol* (1981) 167(1):43–51. doi: 10.1002/jmor.1051670105
8. Shevchuk NA. Adapted Cold Shower as a Potential Treatment for Depression. *Med Hypotheses* (2008) 70(5):995–1001. doi: 10.1016/j.mehy.2007.04.052
9. Smits ES, Duraku LS, Niehof SP, Daanen HA, Hovius SE, Selles RW, et al. Cold-Induced Vasodilatation in Cold-Intolerant Rats After Nerve Injury. *J Plast Reconstr Aesthet Surg* (2013) 66(9):1279–86. doi: 10.1016/j.bjps.2013.04.004
10. Wee NKY, Nguyen AD, Enriquez RF, Zhang L, Herzog H, Baldock PA. Neuropeptide Y Regulation of Energy Partitioning and Bone Mass During Cold Exposure. *Calcif Tissue Int* (2020) 107(5):510–23. doi: 10.1007/s00223-020-00745-9
11. Davis SL. Environmental Modulation of the Immune System *via* the Endocrine System. *Domest Anim Endocrinol* (1998) 15(5):283–9. doi: 10.1016/s0739-7240(98)00034-4
12. Kramer B, Buffenstein R. The Pancreas of the Naked Mole-Rat (Heterocephalus Glaber): An Ultrastructural and Immunocytochemical Study of the Endocrine Component of Thermoneutral and Cold Acclimated Animals. *Gen Comp Endocrinol* (2004) 139(3):206–14. doi: 10.1016/j.ygcen.2004.09.006
13. Bredella MA, Fazeli PK, Freedman LM, Calder G, Lee H, Rosen CJ, et al. Young Women With Cold-Activated Brown Adipose Tissue Have Higher Bone Mineral Density and Lower Pref-1 Than Women Without Brown Adipose Tissue: A Study in Women With Anorexia Nervosa, Women Recovered From Anorexia Nervosa, and Normal-Weight Women. *J Clin Endocrinol Metab* (2012) 97(4):E584–90. doi: 10.1210/jc.2011-2246
14. Iwaniec UT, Philbrick KA, Wong CP, Gordon JL, Kahler-Quesada AM, Olson DA, et al. Room Temperature Housing Results in Premature Cancellous Bone Loss in Growing Female Mice: Implications for the Mouse as a Preclinical Model for Age-Related Bone Loss. *Osteoporos Int* (2016) 27(10):3091–101. doi: 10.1007/s00198-016-3634-3
15. Serrat MA. Environmental Temperature Impact on Bone and Cartilage Growth. *Compr Physiol* (2014) 4(2):621–55. doi: 10.1002/cphy.c130023
16. Lee P, Brychta RJ, Collins MT, Linderman J, Smith S, Herscovitch P, et al. Cold-Activated Brown Adipose Tissue is an Independent Predictor of Higher Bone Mineral Density in Women. *Osteoporos Int* (2013) 24(4):1513–8. doi: 10.1007/s00198-012-2110-y
17. Robbins A, Tom C, Cosman MN, Moursi C, Shipp L, Spencer TM, et al. Low Temperature Decreases Bone Mass in Mice: Implications for Humans. *Am J Phys Anthropol* (2018) 167(3):557–68. doi: 10.1002/ajpa.23684
18. Lau J, Shi YC, Herzog H. Temperature Dependence of the Control of Energy Homeostasis Requires CART Signaling. *Neuropeptides* (2016) 59:97–109. doi: 10.1016/j.npep.2016.03.006
19. Chen H, Hu B, Lv X, Zhu S, Zhen G, Wan M, et al. Prostaglandin E2 Mediates Sensory Nerve Regulation of Bone Homeostasis. *Nat Commun* (2019) 10 (1):181. doi: 10.1038/s41467-018-08097-7
20. Elefteriou F. Impact of the Autonomic Nervous System on the Skeleton. *Physiol Rev* (2018) 98(3):1083–112. doi: 10.1152/physrev.00014.2017
21. Elefteriou F, Ahn JD, Takeda S, Starbuck M, Yang X, Liu X, et al. Leptin Regulation of Bone Resorption by the Sympathetic Nervous System and CART. *Nature* (2005) 434(7032):514–20. doi: 10.1038/nature03398
22. Tian Q, Zhao J, Yang Q, Wang B, Deavila JM, Zhu MJ, et al. Dietary Alpha-Ketoglutarate Promotes Beige Adipogenesis and Prevents Obesity in Middle-Aged Mice. *Aging Cell* (2020) 19(1):e13059. doi: 10.1111/acel.13059
23. Marlatt KL, Ravussin E. Brown Adipose Tissue: An Update on Recent Findings. *Curr Obes Rep* (2017) 6(4):389–96. doi: 10.1007/s13679-017-0283-6
24. Scheja L, Heeren J. The Endocrine Function of Adipose Tissues in Health and Cardiometabolic Disease. *Nat Rev Endocrinol* (2019) 15(9):507–24. doi: 10.1038/s41574-019-0230-6
25. Villarroya J, Cereijo R, Gavaldà-Navarro A, Peyrou M, Giralt M, Villarroya F. New Insights Into the Secretory Functions of Brown Adipose Tissue. *J Endocrinol* (2019) 243(2):R19–27. doi: 10.1530/joe-19-0295
26. Qing H, Desrouleaux R, Israni-Winger K, Mineur YS, Fogelman N, Zhang C, et al. Origin and Function of Stress-Induced IL-6 in Murine Models. *Cell* (2020) 182(2):372–87.e14. doi: 10.1016/j.cell.2020.05.054
27. Villarroya F, Cereijo R, Villarroya J, Giralt M. Brown Adipose Tissue as a Secretory Organ. *Nat Rev Endocrinol* (2017) 13(1):26–35. doi: 10.1038/nrendo.2016.136
28. Heeren J, Scheja L. Brown Adipose Tissue and Lipid Metabolism. *Curr Opin Lipidol* (2018) 29(3):180–5. doi: 10.1097/mol.0000000000000504
29. Pellegrinelli V, Peirce VJ, Howard L, Virtue S, Türei D, Senzacqua M, et al. Adipocyte-Secreted BMP8b Mediates Adrenergic-Induced Remodeling of the Neuro-Vascular Network in Adipose Tissue. *Nat Commun* (2018) 9(1):4974. doi: 10.1038/s41467-018-07453-x
30. Wang GX, Zhao XY, Meng ZX, Kern M, Dietrich A, Chen Z, et al. The Brown Fat-Enriched Secreted Factor Nrg4 Preserves Metabolic Homeostasis Through Attenuation of Hepatic Lipogenesis. *Nat Med* (2014) 20(12):1436–43. doi: 10.1038/nm.3713
31. Cannon B, Nedergaard J. Brown Adipose Tissue: Function and Physiological Significance. *Physiol Rev* (2004) 84(1):277–359. doi: 10.1152/physrev.00015.2003
32. Nguyen AD, Lee NJ, Wee NKY, Zhang L, Enriquez RF, Khor EC, et al. Uncoupling Protein-1 is Protective of Bone Mass Under Mild Cold Stress Conditions. *Bone* (2018) 106:167–78. doi: 10.1016/j.bone.2015.05.037
33. Lidell ME, Enerbäck S. Brown Adipose Tissue and Bone. *Int J Obes Suppl* (2015) 5(Suppl 1):S23–7. doi: 10.1038/ijosup.2015.7
34. Bredella MA, Gill CM, Rosen CJ, Klibanski A, Torriani M. Positive Effects of Brown Adipose Tissue on Femoral Bone Structure. *Bone* (2014) 58:55–8. doi: 10.1016/j.bone.2013.10.007
35. Motyl KJ, Bishop KA, DeMambro VE, Bornstein SA, Le P, Kawai M, et al. Altered Thermogenesis and Impaired Bone Remodeling in Misty Mice. *J Bone Miner Res* (2013) 28(9):1885–97. doi: 10.1002/jbmr.1943
36. Lim S, Honek J, Xue Y, Seki T, Cao Z, Andersson P, et al. Cold-Induced Activation of Brown Adipose Tissue and Adipose Angiogenesis in Mice. *Nat Protoc* (2012) 7(3):606–15. doi: 10.1038/nprot.2012.013
37. Rahman S, Lu Y, Czernik PJ, Rosen CJ, Enerback S, Lecka-Czernik B. Inducible Brown Adipose Tissue, or Beige Fat, is Anabolic for the Skeleton. *Endocrinology* (2013) 154(8):2687–701. doi: 10.1210/en.2012-2162
38. Zhou F, Mei J, Yuan K, Han X, Qiao H, Tang T. Isorhamnetin Attenuates Osteoarthritis by Inhibiting Osteoclastogenesis and Protecting Chondrocytes Through Modulating Reactive Oxygen Species Homeostasis. *J Cell Mol Med* (2019) 23(6):4395–407. doi: 10.1111/jcmm.14333
39. He Z, Chu L, Liu X, Han X, Zhang K, Yan M, et al. Differences in Subchondral Trabecular Bone Microstructure and Finite Element Analysis-Based Biomechanical Properties Between Osteoporosis and Osteoarthritis. *J Orthop Translat* (2020) 24:39–45. doi: 10.1016/j.jot.2020.05.006
40. Zhang X, Kuo C, Moore A, Ran C. Cerenkov Luminescence Imaging of Interscapular Brown Adipose Tissue. *J Vis Exp* (2014) 92):e51790. doi: 10.3791/51790
41. Mrzilkova J, Michenka P, Seremeta M, Kremen J, Dudak J, Zemlicka J, et al. Morphology of the Vasculature and Blood Supply of the Brown Adipose Tissue Examined in an Animal Model by Micro-CT. *BioMed Res Int* (2020) 2020:7502578. doi: 10.1155/2020/7502578
42. Ingram JR, Dougan M, Rashidian M, Knoll M, Keliher EJ, Garrett S, et al. PD-L1 is an Activation-Independent Marker of Brown Adipocytes. *Nat Commun* (2017) 8(1):647. doi: 10.1038/s41467-017-00799-8

43. Cianciaruso C, Beltraminelli T, Duval F, Nassiri S, Hamelin R, Mozes A, et al. Molecular Profiling and Functional Analysis of Macrophage-Derived Tumor Extracellular Vesicles. *Cell Rep* (2019) 27(10):3062–80.e11. doi: 10.1016/j.celrep.2019.05.008
44. Song L, Tang S, Han X, Jiang Z, Dong L, Liu C, et al. KIBRA Controls Exosome Secretion *via* Inhibiting the Proteasomal Degradation of Rab27a. *Nat Commun* (2019) 10(1):1639. doi: 10.1038/s41467-019-09720-x
45. Hu Y, Wu H, Xu T, Wang Y, Qin H, Yao Z, et al. Defactinib Attenuates Osteoarthritis by Inhibiting Positive Feedback Loop Between H-Type Vessels and MSCs in Subchondral Bone. *J Orthop Translat* (2020) 24:12–22. doi: 10.1016/j.jot.2020.04.008
46. Song C, Yang X, Lei Y, Zhang Z, Smith W, Yan J, et al. Evaluation of Efficacy on RANKL Induced Osteoclast From RAW264.7 Cells. *J Cell Physiol* (2019) 234(7):11969–75. doi: 10.1002/jcp.27852
47. Martin SA, Philbrick KA, Wong CP, Olson DA, Branscum AJ, Jump DB, et al. Thermoneutral Housing Attenuates Premature Cancellous Bone Loss in Male C57BL/6J Mice. *Endocr Connect* (2019) 8(11):1455–67. doi: 10.1530/ec-19-0359
48. Serrat MA, King D, Lovejoy CO. Temperature Regulates Limb Length in Homeotherms by Directly Modulating Cartilage Growth. *Proc Natl Acad Sci USA* (2008) 105(49):19348–53. doi: 10.1073/pnas.0803319105
49. Takeda S, Elefteriou F, Levasseur R, Liu X, Zhao L, Parker KL, et al. Leptin Regulates Bone Formation *via* the Sympathetic Nervous System. *Cell* (2002) 111(3):305–17. doi: 10.1016/s0092-8674(02)01049-8
50. Bartness TJ, Vaughan CH, Song CK. Sympathetic and Sensory Innervation of Brown Adipose Tissue. *Int J Obes (Lond)* (2010) 34 Suppl 1(0 1):S36–42. doi: 10.1038/ijo.2010.182
51. Morrison SF, Madden CJ, Tupone D. Central Neural Regulation of Brown Adipose Tissue Thermogenesis and Energy Expenditure. *Cell Metab* (2014) 19(5):741–56. doi: 10.1016/j.cmet.2014.02.007
52. Moser C, Straub LG, Rachamin Y, Dapito DH, Kulenkampff E, Ding L, et al. Quantification of Adipocyte Numbers Following Adipose Tissue Remodeling. *Cell Rep* (2021) 35(4):109023. doi: 10.1016/j.celrep.2021.109023
53. Olmsted-Davis E, Gannon FH, Ozen M, Ittmann MM, Gugala Z, Hipp JA, et al. Hypoxic Adipocytes Pattern Early Heterotopic Bone Formation. *Am J Pathol* (2007) 170(2):620–32. doi: 10.2353/ajpath.2007.060692
54. Wang GX, Zhao XY, Lin JD. The Brown Fat Secretome: Metabolic Functions Beyond Thermogenesis. *Trends Endocrinol Metab* (2015) 26(5):231–7. doi: 10.1016/j.tem.2015.03.002
55. Reid IR, Baldock PA, Cornish J. Effects of Leptin on the Skeleton. *Endocr Rev* (2018) 39(6):938–59. doi: 10.1210/er.2017-00226
56. Zhou BO, Yue R, Murphy MM, Peyer JG, Morrison SJ. Leptin-Receptor-Expressing Mesenchymal Stromal Cells Represent the Main Source of Bone Formed by Adult Bone Marrow. *Cell Stem Cell* (2014) 15(2):154–68. doi: 10.1016/j.stem.2014.06.008
57. Lee P, Linderman J, Smith S, Brychta RJ, Perron R, Idelson C, et al. Fibroblast Growth Factor 21 (FGF21) and Bone: Is There a Relationship in Humans? *Osteoporos Int* (2013) 24(12):3053–7. doi: 10.1007/s00198-013-2464-9
58. Hao RH, Gao JL, Li M, Huang W, Zhu DL, Thynn HN, et al. Association Between Fibroblast Growth Factor 21 and Bone Mineral Density in Adults. *Endocrine* (2018) 59(2):296–303. doi: 10.1007/s12020-017-1507-y
59. Li H, Sun H, Qian B, Feng W, Carney D, Miller J, et al. Increased Expression of FGF-21 Negatively Affects Bone Homeostasis in Dystrophin/Utrophin Double Knockout Mice. *J Bone Miner Res* (2020) 35(4):738–52. doi: 10.1002/jbmr.3932
60. Yang S, Guo Y, Zhang W, Zhang J, Zhang Y, Xu P. Effect of FGF-21 on Implant Bone Defects Through Hepatocyte Growth Factor (HGF)-Mediated PI3K/AKT Signaling Pathway. *BioMed Pharmacother* (2019) 109:1259–67. doi: 10.1016/j.biopha.2018.10.150
61. Castellani JW, Tipton MJ. Cold Stress Effects on Exposure Tolerance and Exercise Performance. *Compr Physiol* (2015) 6(1):443–69. doi: 10.1002/cphy.c140081
62. Albertos P, Wagner K, Poppenberger B. Cold Stress Signalling in Female Reproductive Tissues. *Plant Cell Environ* (2019) 42(3):846–53. doi: 10.1111/pce.13408
63. Kishimoto T. IL-6: From its Discovery to Clinical Applications. *Int Immunol* (2010) 22(5):347–52. doi: 10.1093/intimm/dxq030
64. Sims NA. Cell-Specific Paracrine Actions of IL-6 Family Cytokines From Bone, Marrow and Muscle That Control Bone Formation and Resorption. *Int J Biochem Cell Biol* (2016) 79:14–23. doi: 10.1016/j.biocel.2016.08.003
65. Silva RAB, Sousa-Pereira AP, Lucisano MP, Romualdo PC, Paula-Silva FWG, Consolaro A, et al. Alendronate Inhibits Osteocyte Apoptosis and Inflammation *via* IL-6, Inhibiting Bone Resorption in Periapical Lesions of Ovariectomized Rats. *Int Endod J* (2020) 53(1):84–96. doi: 10.1111/iej.13206
66. Wu Q, Zhou X, Huang D, Ji Y, Kang F. IL-6 Enhances Osteocyte-Mediated Osteoclastogenesis by Promoting JAK2 and RANKL Activity *In Vitro*. *Cell Physiol Biochem* (2017) 41(4):1360–9. doi: 10.1159/000465455
67. Gao Y, Morita I, Maruo N, Kubota T, Murota S, Aso T. Expression of IL-6 Receptor and GP130 in Mouse Bone Marrow Cells During Osteoclast Differentiation. *Bone* (1998) 22(5):487–93. doi: 10.1016/s8756-3282(98)00040-4
68. Tamura T, Udagawa N, Takahashi N, Miyaura C, Tanaka S, Yamada Y, et al. Soluble Interleukin-6 Receptor Triggers Osteoclast Formation by Interleukin 6. *Proc Natl Acad Sci USA* (1993) 90(24):11924–8. doi: 10.1073/pnas.90.24.11924
69. Palmqvist P, Persson E, Conaway HH, Lerner UH. IL-6, Leukemia Inhibitory Factor, and Oncostatin M Stimulate Bone Resorption and Regulate the Expression of Receptor Activator of NF-Kappa B Ligand, Osteoprotegerin, and Receptor Activator of NF-Kappa B in Mouse Calvariae. *J Immunol* (2002) 169(6):3353–62. doi: 10.4049/jimmunol.169.6.3353
70. Lazzaro L, Tonkin BA, Poulton IJ, McGregor NE, Ferlin W, Sims NA. IL-6 Trans-Signalling Mediates Trabecular, But Not Cortical, Bone Loss After Ovariectomy. *Bone* (2018) 112:120–7. doi: 10.1016/j.bone.2018.04.015
71. Fafián-Labora JA, Rodríguez-Navarro JA, O'Loghlen A. Small Extracellular Vesicles Have GST Activity and Ameliorate Senescence-Related Tissue Damage. *Cell Metab* (2020) 32(1):71–86.e5. doi: 10.1016/j.cmet.2020.06.004
72. Liang M, Yin X, Zhang S, Ai H, Luo F, Xu J, et al. Osteoclast-Derived Small Extracellular Vesicles Induce Osteogenic Differentiation *via* Inhibiting ARHGAP1. *Mol Ther Nucleic Acids* (2021) 23:1191–203. doi: 10.1016/j.omtn.2021.01.031
73. Yu L, Sui B, Fan W, Lei L, Zhou L, Yang L, et al. Exosomes Derived From Osteogenic Tumor Activate Osteoclast Differentiation and Concurrently Inhibit Osteogenesis by Transferring COL1A1-Targeting miRNA-92a-1-5p. *J Extracell Vesicles* (2021) 10(3):e12056. doi: 10.1002/jev2.12056
74. Frank AC, Ebersberger S, Fink AF, Lampe S, Weigert A, Schmid T, et al. Apoptotic Tumor Cell-Derived microRNA-375 Uses CD36 to Alter the Tumor-Associated Macrophage Phenotype. *Nat Commun* (2019) 10(1):1135. doi: 10.1038/s41467-019-08989-2
75. Xiong Y, Chen L, Yan C, Zhou W, Yu T, Sun Y, et al. M2 Macrophagy-Derived Exosomal miRNA-5106 Induces Bone Mesenchymal Stem Cells Towards Osteoblastic Fate by Targeting Salt-Inducible Kinase 2 and 3. *J Nanobiotechnol* (2020) 18(1):66. doi: 10.1186/s12951-020-00622-5
76. Mensà E, Guescini M, Giuliani A, Bacalini MG, Ramini D, Corleone G, et al. Small Extracellular Vesicles Deliver miR-21 and miR-217 as Pro-Senescence Effectors to Endothelial Cells. *J Extracell Vesicles* (2020) 9(1):1725285. doi: 10.1080/20013078.2020.1725285
77. Zhou X, Li Z, Qi M, Zhao P, Duan Y, Yang G, et al. Brown Adipose Tissue-Derived Exosomes Mitigate the Metabolic Syndrome in High Fat Diet Mice. *Theranostics* (2020) 10(18):8197–210. doi: 10.7150/thno.43968

Conflict of Interest: The authors declare that the research was conducted in the absence of any commercial or financial relationships that could be construed as a potential conflict of interest.

frontiers in Endocrinology

ORIGINAL RESEARCH
published: 25 January 2022
doi: 10.3389/fendo.2022.829867

Associations of Fat Mass and Fat Distribution With Bone Mineral Density in Non-Obese Postmenopausal Chinese Women Over 60 Years Old

Jingzheng Fan[1], *Yuyan Jiang*[2], *Junlian Qiang*[1], *Bin Han*[1] *and Qiang Zhang*[1,3]*

[1] Department of Geriatrics, Tianjin Medical University General Hospital, Tianjin, China, [2] Department of Nuclear Medicine, Tianjin Medical University General Hospital, Tianjin, China, [3] Institute of Tianjin Geriatrics, Tianjin Medical University General Hospital, Tianjin, China

OPEN ACCESS

Edited by:
Guanwu Li,
Shanghai University of Traditional Chinese Medicine, China

Reviewed by:
Yingchao Han,
Shanghai JiaoTong University, China

***Correspondence:**
Qiang Zhang
zhangqiangyulv@163.com

Specialty section:
This article was submitted to Bone Research, a section of the journal Frontiers in Endocrinology

Received: *06 December 2021*
Accepted: *03 January 2022*
Published: *25 January 2022*

Citation:
Fan J, Jiang Y, Qiang J, Han B and Zhang Q (2022) Associations of Fat Mass and Fat Distribution With Bone Mineral Density in Non-Obese Postmenopausal Chinese Women Over 60 Years Old. Front. Endocrinol. 13:829867. doi: 10.3389/fendo.2022.829867

Background: Bone mineral density (BMD) loss is a major complication of menopause, and this loss is closely associated with Fat mass (FM). The relationship between FM, fat distribution (FD), and BMD in postmenopausal women, however, remains incompletely understood. The present study was thus developed to explore these associations between body fat accumulation, FD, and BMD among non-obese postmenopausal women over the age of 60.

Methods: This was a cross-sectional analysis of 357 healthy postmenopausal women between the ages of 60.2 and 86.7 years. Dual-energy X-ray absorptiometry (DXA) was utilized to measure total and regional BMD as well as fat-related parameters including total FM, android and gynoid fat, body fat percentage (BF%), and total lean mass (LM) for all subjects. The android-to-gynoid fat ratio (AOI) was used to assess FD. Pearson's correlation testing and multiple regression analyses were used to explore relationships among AOI, LM, FM, and BMD.

Results: Both LM and FM were positively correlated with total and regional BMD in univariate analysis (all $P < 0.01$), whereas BMD was not significantly associated with AOI in any analyzed site other than the head. Multivariate linear regression models corrected for age, height, and years post-menopause, revealed a sustained independent positive relationship between FM and BMD (standard β range: 0.141 – 0.343, $P < 0.01$). The relationship between FM and BMD was unaffected by adjustment for LM (standard β range: 0.132 – 0.258, $P < 0.01$), whereas AOI had an adverse impact on BMD at most analyzed skeletal sites (total body, hip, femoral neck, arm, leg, and head) (standard β range: –0.093 to –0.232, $P < 0.05$). These findings were unaffected by using BF% in place of FM (standard β range: –0.100 to –0.232, $P < 0.05$).

Conclusions: In this cohort of non-obese postmenopausal women over the age of 60 from China, total FM was positively associated with BMD, while AOI was negatively correlated with BMD. As such, a combination of proper weight gain and the control of central obesity may benefit the overall bone health of women after menopause.

Keywords: bone mineral density, fat distribution, fat mass, lean mass, postmenopausal

INTRODUCTION

Osteoporosis is a prevalent and often asymptomatic condition that commonly develops in women after menopause, contributing to significant reductions in quality of life over time. The diagnosis of osteoporosis is primarily made through measurements of bone mineral density (BMD) (1), which is in turn closely tied to body composition-related parameters including lean mass (LM) and fat mass (FM) (2). The relative degree to which LM and FM contribute to BMD, however, remains controversial. Some reports have found LM and FM to equally contribute to increases in bone mass among postmenopausal women (3–6). In contrast, other studies have suggested that FM has a significantly more pronounced beneficial impact on BMD relative to LM (7–10), while others have reported the exact opposite finding (11–13).

After menopause, woman commonly exhibit changes in body composition consisting of a reduction in gynoid fat together with an increase in central fat in the android region (14, 15). The android-to-gynoid fat ratio (AOI) has thus been reported to be a valuable indicator of central (visceral) fat accumulation that is correlated with BMD, but studies have yielded inconsistent findings regarding such a relationship (16–20). Shao et al., for example, found central fat accumulation to be negatively correlated with BMD (18), whereas Kapus et al. observed the opposite relationship (19). These contrasting results underscore the complex interplay between FM, fat distribution (FD), and BMD in postmenopausal women.

Most studies to date have either focused primarily on obese individual or have enrolled postmenopausal women without regard for their body weight, whereas few works have been selectively performed on healthy subjects with a body mass index (BMI) within non-obese limits (20–22). There have also been few studies to date exploring the relationships between FM, AOI, and BMD at different skeletal sites among elderly postmenopausal women (7). As such, this study was developed to examine the associations between FM, central FD, and total or regional BMD among non-obese postmenopausal Chinese women over the age of 60.

METHODS

Subjects

In total, 357 non-obese ($18.5 < BMI < 30$ kg/m^2) women 60 years of age or older were selected as a random sample from among patients at the Department of Geriatric Health Check-Up Centre, Tianjin Medical University General Hospital between January 2020 and August 2021. Participants were excluded from this study if they exhibited blood diseases, chronic renal diseases, pituitary disorders, thyroid diseases, a history of pathological fractures, known malignancies, rheumatoid arthritis, hypogonadism or were taking medicine with the potential to impact fat, lean mass, or bone metabolism (including calcium, vitamin D, hormone replacement therapy, oral contraceptives, anticonvulsants, diuretics, corticosteroid-containing asthma medications, oral anticoagulants, immunosuppressive drugs, or nonsteroidal ant-inflammatory drugs). None of the participants were heavy drinkers.

The Ethics Committee of the Tianjin Medical University General Hospital study approved the present study. With all subjects having provided written informed consent to participate.

Data Collection

Data collected from patients through self-reported questionnaires and standardized interviews included: age (in years) and years since menopause (YSM). Participants were considered postmenopausal when they reported having experienced amenorrhea for 12 consecutive months.

Standard approaches were used to gather anthropometric data. Standing height (cm) was measured using a stadiometer accurate to within 0.1 cm accuracy, while body weight (kg) was measured using a portable electronic beam scale accurate to within 0.1 kg while participants were wearing only light clothing without shoes. Both parameters were measured twice. BMI was determined as follow: body weight (kg)/height^2 (m^2).

Body Composition Analyses

FM, LM, body fat percentage (BF%), gynoid fat, android fat, and both total and regional BMD were assessed *via* whole-body DXA scanning (Software Version enCORE 13.40.038; Lunar Prodigy, GE Healthcare, USA). BF% was calculated as follows: BF%=total FM/total body weight x 100. Gynoid and android regions of interest (ROIs) were determined using the provided software base on the manufacturer's instructions. The android ROI height was 20% of the distance from the pelvic horizontal cut line to the neck cut line, with the arm cut lines serving as lateral boundaries. The gynoid ROI height was two times that of the android ROI, with the leg cut lines serving as lateral boundaries, and the upper boundary being beneath the pelvic horizontal cut lines by 1.5 times the android ROI height (**Figure 1**). AOI was calculated by dividing the android FM by the gynoid FM. Regional BMD values were assessed for body regions including the head, ribs, legs, arms, lumbar spine, femoral neck, hip, and trunk. Prior to each measurement, densitometer standardization was

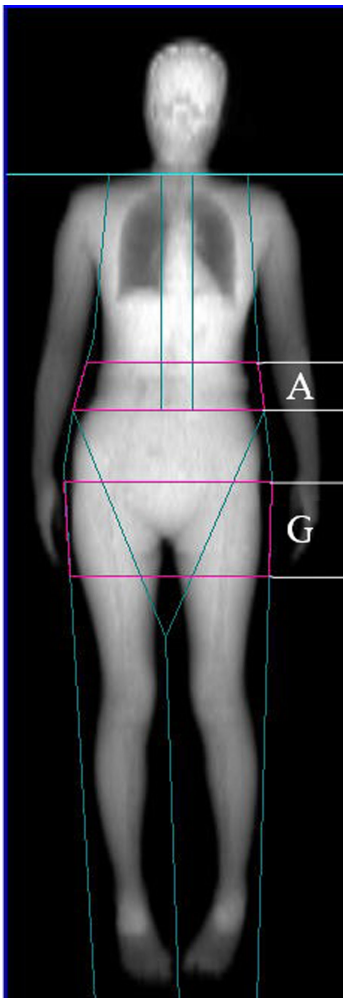

FIGURE 1 | Dual-energy X-ray absorptiometry-based body composition measurement (A: android fat distribution ROI, G: gynoid fat distribution ROI).

performed. The absorptiometry machine was subject to daily quality control analysis. All DXA measurements were performed by a single trained technologist, yielding excellent precision for all measured parameters. The *in vivo* precision of such DXA-based body composition analyses has been demonstrated in prior reports, with coefficient of variation value of < 2% for all total and regional BMD measurements and < 3% for all body composition analyses. These measures were established using duplicate measures of the study cohort as in prior reports (18).

Statistical Analysis

The Shapiro-Wilk test was used to assess the normality of data distributions. Continuous data are given as means ± standard deviation (SD). Pearson's correlation analyses were used to explore relationships among different study variables, while multivariate linear regression models were utilized to evaluate relationships among BMD and AOI, LM, and FM, with age, height, and YSM serving as fixed covariates. In Model 1, the relationships between FM and AOI with total and regional BMD were assessed. Model 2 additionally explored the relationships between LM and total and regional BMD in a model incorporating FM and AOI. These regression analyses were then repeated, with BF% in place of FM. The results of these analyses are given as standardized regression coefficients. $P < 0.05$ was the threshold of significance, and data were analyzed using SPSS v16 (SPSS Inc., IL, USA).

RESULTS

Descriptive Statistics

In total, 357 healthy, non-obese (BMI: 18.5 – 30) postmenopausal women were enrolled in the present study. Their demographic characteristics, anthropometric parameters, body composition-related findings, and BMD (total and regional) are compiled in **Table 1**. These participants had an average age of 69.1 years (range: 60.2 – 86.7 years). The mean number of years since menopause for these subjects was 18.6 (range: 6.1 – 38.7 years). The average FM of the overall study cohort was 20.36 kg, accounting for 34.7% of total body weight.

The Relationships Among Anthropometric, Body Composition, and BMD Parameters

In univariate analyses, higher LM, FM, and BF% were associated with increases in both total and regional BMD (total body, head, ribs, legs, arms, spine, lumbar spine, femoral neck, hips) (r = 0.199–0.499, all $P < 0.01$). In contrast, AOI was not significantly associated with total or regional BMD among postmenopausal

TABLE 1 | Baseline characteristics of subjects.

Parameters	Mean ± SD	Range
Age (years)	69.12 ± 5.17	60.2-86.7
YSM (years)	18.61 ± 5.67	6.1-38.7
Height (cm)	157.57 ± 6.13	140-178
Body weight (kg)	58.26 ± 7.61	41-82
BMI (kg/m^2)	23.45 ± 2.67	18.6-30
Body composition measures (kg)		
Total LM	35.45 ± 4.64	15.9-58.66
Total FM	20.36 ± 5.06	6.71-33.27
BF%	34.67 ± 5.76	11.77-51.58
Android fat	2.02 ± 0.59	0.22-3.89
Gynoid fat	3.28 ± 0.82	0.70-5.65
AOI	0.63 ± 0.16	0.22-1.34
Bone mineral density (g/cm^2)		
Total body	1.006 ± 0.091	0.756-1.315
Total hip	0.833 ± 0.120	0.500-1.236
Femoral neck	0.773 ± 0.119	0.410-1.221
Lumbar spine	0.986 ± 0.171	0.426-1.586
Spine	0.928 ± 0.125	0.650-1.312
Arm	0.719 ± 0.090	0.537-1.107
Leg	1.043 ± 0.118	0.641-1.368
Trunk	0.803 ± 0.083	0.607-1.335
Rib	0.578 ± 0.052	0.453-0.764
Head	1.935 ± 0.281	1.315-3.401

YSM, years since menopause; BMI, body mass index; FM, fat mass; BF%, body fat percentage; LM, lean mass; AOI, android to gynoid fat ratio.

women with the exception of head BMD ($r = -0.140$, $P < 0.01$). Both increased age and YSM were significantly negatively correlated with total and regional BMD values (all $P < 0.05$; **Table 2**). In contrast, height, body weight, and BMI were positively correlated with total and regional BMD values (all $P < 0.05$).

Correlations between anthropometrics parameters and soft tissue-related variables are compiled in **Table 3**. These analyses revealed LM and FM to be positively correlated with the height, body weight, and BMI of postmenopausal women (all $P < 0.001$). While AOI was positively correlated with BMI and body weight, it was negatively correlated with height in this study cohort (all $P < 0.05$). BF% was positively associated with both body weight and BMI (all $P < 0.001$). Age or YSM were not correlated with FM, LM, AOI, or BF%.

Multivariate Analyses

Next, multivariate linear regression analyses were conducted to more fully explore the relationships among these different study variables (**Table 4**). Model 1 revealed a significant positive correlation between FM and both total and regional BMD values (total body, head, ribs, legs, arms, spine, lumbar spine, femoral neck, and hips) (standard β range: 0.141 to 0.343, all $P < 0.001$), while AOI was not significantly associated with any BMD parameters other than head BMD (r = -0.156, $P < 0.01$). Following adjustment for LM in Model 2, the positive correlations between FM and BMD remained significant (standard β range: 0.132 to 0.258, all $P < 0.01$). In addition, a significant relationship between LM and BMD was detected for all body regions (all $P < 0.01$), whereas AOI was significantly negatively correlated with head, leg, arm, femoral neck, hip, and total body BMD (standard β range: −0.093 to −0.232, all $P < 0.05$). When these analyses were repeated with BF% in place of FM, the results were largely the same (see **Table 5**), with BF% being significantly correlated with BMD. Following adjustment for LM, no change in the relationship between BF% and BMD was observed (standard β range: −0.100 to −0.232, all $P < 0.05$). A significant negative association between LM and BMD was also observed, while AOI was negatively correlated with head, femoral neck, arm, leg, hip, and total body BMD (standard β range: −0.100 to −0.232, $P < 0.05$).

DISCUSSION

These analyzes revealed total FM to be positively correlated with BMD for all analyzed skeletal regions, whereas AOI, serving as a readout for central FD, was negatively correlated with BMD for most skeletal regions following adjustment for age, height, YSM, total FM, and total LM among non-obese postmenopausal Chinese women over 60 years of age.

Consistent with our expectations, we found that most analyzed anthropometric parameters such as age and YSM were strongly correlated with BMD, both of which were negatively correlated with total and regional BMD values. In contrast, these BMD indices were positively correlated with the height, body weight, and BMI of study participants, although these relationships became less clear upon in-depth analyses of the relationships between anthropometric variables and soft tissue parameters. While some soft tissue parameters were positively correlated with height, weight, and BMI, others were negatively correlated with these variables or not clearly related to them. This suggests that the interplay between FD, anthropometric factors,

TABLE 2 | Correlations between subject characteristics, body composition and total body. and regional BMD measurements.

	Total BMD	Hip BMD	FN BMD	LS BMD	Spine BMD	Arm BMD	Leg BMD	Trunk BMD	Rib BMD	Head BMD
Age (years)	-0.179[b]	-0.195[c]	-0.222[c]	-0.104[c]	-0.115[a]	-0.195[c]	-0.197[c]	-0.119[a]	-0.111[a]	-0.142[b]
YSM (years)	-0.183[b]	-0.207[c]	-0.227[c]	-0.116[c]	-0.106[a]	-0.206[c]	-0.199[c]	-0.135[a]	-0.114[a]	-0.124[b]
Height (cm)	0.329[b]	0.249[b]	0.346[c]	0.183[c]	0.211[c]	0.301[c]	0.322[c]	0.313[c]	0.260[c]	0.216[c]
BW (kg)	0.475[c]	0.373[b]	0.432[c]	0.368[c]	0.459[c]	0.418[c]	0.492[c]	0.558[c]	0.611[c]	0.282[b]
BMI (kg/m^2)	0.305[b]	0.256[b]	0.252[c]	0.268[c]	0.360[c]	0.262[c]	0.328[c]	0.409[c]	0.497[c]	0.171[b]
LM (kg)	0.460[b]	0.320[b]	0.418[c]	0.369[c]	0.413[c]	0.421[c]	0.451[c]	0.499[c]	0.521[c]	0.282[c]
FM (kg)	0.315[b]	0.303[b]	0.300[c]	0.267[c]	0.357[c]	0.313[c]	0.410[c]	0.403[c]	0.499[c]	0.199[c]
BF%	0.157[b]	0.198[b]	0.156[b]	0.147[b]	0.215[c]	0.171[a]	0.275[c]	0.227[c]	0.328[c]	0.100[a]
AOI	-0.066	-0.031	-0.061	0.041	0.084	-0.036	0.010	0.023	0.102	-0.140[b]

[a]$P < 0.05$, [b]$P < 0.01$, [c]$P < 0.001$.

YSM, years since menopause; BW, body weight; BMI, body mass index; BMD, bone mineral density; FN, femoral neck; FM, fat mass; LS, Lumbar spine; BF%, body fat percentage; LM, lean mass; AOI, android to gynoid fat ratio.

TABLE 3 | Correlation of soft tissue components with anthropometric parameters.

	Age (years)	YSM (years)	Height (cm)	Body weight (kg)	BMI (kg/m2)
Total LM (kg)	-0.005	-0.001	0.599[c]	0.719[c]	0.405[c]
Total FM (kg)	-0.065	-0.097	0.192[c]	0.787[c]	0.779[c]
BF%	-0.045	-0.084	-0.035	0.487[c]	0.601[c]
AOI	-0.025	0.001	-0.105[a]	0.174[b]	0.273[c]

[a]$P < 0.05$, [b]$P < 0.01$, [c]$P < 0.001$.

YSM, years since menopause; BMI, body mass index; FM, fat mass; BF%, body fat percentage; LM, lean mass; AOI, android to gynoid fat ratio.

TABLE 4 | Regression analysis of FM, AOI, and LM with total body and regional BMD.

	Total BMD (g/cm^2)			Hip BMD (g/cm^2)			FN BMD (g/cm^2)			LS BMD (g/cm^2)			Spine BMD (g/cm^2)		
	Sβ	*t*	*P*	Sβ	*t*	*P*	Sβ	*t*	*P*	Sβ	*t*	*P*	Sβ	*t*	*P*
Model 1: Without adjustment for LM															
FM (kg)	**0.244**	**5.074**	**<0.001**	**0.263**	**5.309**	**<0.001**	**0.227**	**4.759**	**<0.001**	**0.244**	**4.780**	**<0.001**	**0.322**	**6.503**	**<0.001**
AOI	-0.085	-1.750	0.081	-0.072	-1.440	0.151	-0.083	-1.711	0.088	0.012	0.238	0.812	0.049	0.981	0.327
Model 2: With adjustment for LM															
LM (kg)	**0.385**	**7.827**	**<0.001**	**0.210**	**4.038**	**<0.001**	**0.338**	**6.794**	**<0.001**	**0.275**	**5.238**	**<0.001**	**0.294**	**5.834**	**<0.001**
FM (kg)	**0.198**	**4.027**	**<0.001**	**0.245**	**4.721**	**<0.001**	**0.195**	**3.926**	**<0.001**	**0.182**	**3.469**	**0.001**	**0.248**	**4.904**	**<0.001**
AOI	**-0.184**	**-3.913**	**<0.001**	**-0.128**	**-2.566**	**0.005**	**-0.174**	**-3.664**	**<0.001**	-0.057	-1.119	0.264	-0.024	-0.485	0.628
	Arm BMD (g/cm^2)			Leg BMD (g/cm^2)			Trunk BMD (g/cm^2)			Rib BMD (g/cm^2)			Head BMD (g/cm^2)		
	Sβ	*t*	*P*	Sβ	*t*	*P*	Sβ	*t*	*P*	Sβ	*t*	*P*	Sβ	*t*	*P*
Model 1: Without adjustment for LM															
FM (kg)	**0.141**	**4.569**	**<0.001**	**0.343**	**7.396**	**<0.001**	**0.261**	**5.539**	**<0.001**	**0.293**	**5.754**	**<0.001**	**0.206**	**3.946**	**<0.001**
AOI	0.013	0.267	0.790	0.008	0.169	0.866	0.001	0.010	0.992	-0.061	1.177	0.240	**-0.181**	**-3.506**	**0.001**
Model 2: With adjustment for LM															
LM (kg)	**0.452**	**9.293**	**<0.001**	**0.437**	**9.410**	**<0.001**	**0.192**	**2.997**	**0.003**	**0.195**	**3.690**	**<0.001**	**0.204**	**3.814**	**<0.001**
FM (kg)	**0.132**	**2.717**	**0.007**	**0.258**	**5.563**	**<0.001**	**0.214**	**5.539**	**<0.001**	**-0.246**	**4.663**	**<0.001**	**0.170**	**3.186**	**0.002**
AOI	**-0.093**	**-2.008**	**0.045**	**-0.093**	**-2.103**	**0.036**	0.001	0.010	0.992	-0.015	-0.284	0.777	**-0.232**	**-4.543**	**<0.001**

Models were adjusted for age, YSM, and height in postmenopausal women.
BMD, bone mineral density; FN, femoral neck; FM, fat mass; LS, Lumbar spine; LM, lean mass; AOI, android to gynoid fat ratio; Sβ, standardized coefficients β.
All significant values are shown in bold.

and body fat accumulation has the potential to be beneficial or harmful with respect to BMD. It is thus vital that these anthropometric parameters be controlled for when evaluating relationships between bone mass and fat. However, prior studies have indicated that using body weight or BMI to correct for the effects of LM or FM on BMD has the potential to result in incorrect conclusions given that both LM and FM are tightly correlated with overall body weight (with correlation coefficients of 0.79 and 0.72 for FM vs. body weight and LM vs. body weight, respectively) (23). The incorporation of both total FM and body weight into a regression model has the potential to lead to inaccurate conclusions as a consequence of mathematical coupling (24–26). In contrast, height has been shown to be a more appropriate readout to use when seeking to control for body size (3). LM also has the potential to be leveraged as a variable for adjustment when assessing relationships between fat and bone mass (26). In the present analysis, we thus utilized age, height, and YSM as fixed covariates and total LM as an additional covariate for adjustment in our multivariate linear regression analyses exploring the associations between FM and BMD.

TABLE 5 | Regression analysis of BF%, AOI, and LM with total body and regional BMD.

	Total BMD (g/cm^2)			Hip BMD (g/cm^2)			FN BMD (g/cm^2)			LS BMD (g/cm^2)			Spine BMD (g/cm^2)		
	Sβ	*t*	*P*	Sβ	*t*	*P*	Sβ	*t*	*P*	Sβ	*t*	*P*	Sβ	*t*	*P*
Model 1: Without adjustment for LM															
BF%	**0.123**	**2.519**	**0.012**	**0.191**	**3.834**	**<0.001**	**0.138**	**2.868**	**0.004**	**0.153**	**2.971**	**0.003**	**0.200**	**3.931**	**<0.001**
AOI	-0.050	-1.016	0.310	-0.045	-0.889	0.374	-0.054	-1.109	0.268	0.040	0.767	0.443	0.086	1.667	0.096
Model 2: With adjustment for LM															
LM (kg)	**0.454**	**9.600**	**<0.001**	**0.298**	**5.968**	**<0.001**	**0.317**	**4.901**	**<0.001**	**0.339**	**6.843**	**<0.001**	**0.381**	**7.946**	**<0.001**
BF%	**0.121**	**2.578**	**0.010**	**0.191**	**3.851**	**<0.001**	**0.143**	**3.014**	**0.003**	**0.131**	**2.648**	**0.008**	**0.173**	**3.595**	**<0.001**
AOI	**-0.182**	**-3.779**	**<0.001**	**-0.132**	**-2.604**	**0.010**	**-0.143**	**-2.821**	**0.005**	-0.059	-1.142	0.254	-0.025	-0.494	0.621
	Arm BMD (g/cm^2)			Leg BMD (g/cm^2)			Trunk BMD (g/cm^2)			Rib BMD (g/cm^2)			Head BMD (g/cm^2)		
	Sβ	*t*	*P*	Sβ	*t*	*P*	Sβ	*t*	*P*	Sβ	*t*	*P*	Sβ	*t*	*P*
Model 1: Without adjustment for LM															
BF%	**0.139**	**2.807**	**0.005**	**0.268**	**5.670**	**<0.001**	**0.104**	**2.074**	**0.039**	**0.169**	**3.263**	**0.001**	**0.118**	**2.278**	**0.023**
AOI	0.039	0.778	0.437	0.008	0.169	0.866	0.040	0.790	0.430	-0.095	1.819	0.070	**-0.156**	**-3.016**	**0.003**
Model 2: With adjustment for LM															
LM (kg)	**0.500**	**10.843**	**<0.001**	**0.531**	**12.095**	**<0.001**	**0.229**	**3.634**	**<0.001**	**0.282**	**5.590**	**<0.001**	**0.264**	**5.159**	**<0.001**
BF%	**0.127**	**2.768**	**0.006**	**0.249**	**5.703**	**<0.001**	**0.196**	**3.979**	**<0.001**	**0.154**	**3.048**	**0.002**	**0.113**	**2.216**	**0.027**
AOI	**-0.100**	**-2.136**	**0.033**	**-0.106**	**-2.387**	**0.018**	-0.038	-0.714	0.476	-0.018	0.337	0.736	**-0.232**	**-4.462**	**<0.001**

Models were adjusted for age, YSM, and height in postmenopausal women.
BMD, bone mineral density; FN, femoral neck; FM, fat mass; LS, Lumbar spine; BF%, body fat percentage; LM, lean mass; AOI, android to gynoid fat ratio; Sβ, standardized coefficients β.
All significant values are shown in bold.

We observe a positive relationship between BMD and total FM among postmenopausal women, in line with prior reports (3, 7, 9). This relationship may be attributable to the elevated gravitational force associated with increased weight, in turn contributing to improvements in BMD (26). However, given that total FM accounts for a relatively small fraction of overall body weight, such gravitational forces are unlikely to fully explain the interplay between FM and BMD. Other research suggests that adipocytes can produce hormones including adiponectin, leptin, insulin, and adipocytic estrogens, all of which can impact bone metabolism *via* the endocrine pathway, thus potentially contributing to these results (27–30). These hormones may play a protective role, stimulating osteoblastogenesis and inhibiting the resorption of established bone tissue mediated by osteoclasts (31).

While increases in bone mass were observed with rising total FM in this analysis, BMD values for most analyzed regions were negatively correlated with central fat accumulation, as measured based on AOI, in non-obese postmenopausal elderly women. These findings are consistent with those from other studies suggesting that DXA-based AOI values are negatively correlated with bone health (16–18). This result may be attributable to a few underlying mechanisms. For one, adipose tissue sources can release high levels of inflammatory cytokines such as TNF-α or IL-6, thus contributing to bone loss and decreased BMD (32–34). Secondly, free fatty acid secretion from the visceral adipose tissue can inhibit insulin receptor expression, thereby contributing to the incidence of insulin resistance (35). Third, the osteoblastic and adipocytic differentiation of mesenchymal stem cells (MSCs) have been shown to be negatively correlated (36). The same mechanisms that are active in the bone marrow may thus be ties to the interplay between bone and central fat deposits.

In this study, we additionally observed strong positive correlations between LM and BMD in all analyzed body sites, with these correlations generally being stronger than those observed for FM. This suggests that muscle-mediated mechanical loads have a more robust beneficial impact on BMD as compared to FM in postmenopausal women (3, 9, 11, 12).

There are multiple strengths to the present study. For one, our research subjects were recruited from among a single well-defined population of individuals over 60 years of age of a specific ethnicity. Second, this study is among the few to have explored the association between central FD and BMD among non-obese postmenopausal women. Third, we assessed both total BMD and the regional BMD at multiple sites including the head, spine, lumbar spine, arms, legs, trunk, ribs, hips, and femoral neck, and we utilized DXA-based AOI as a measure for central FD rather than using alternative metrics such as the waist-to-thigh or waist-to-hip ratio.

There are a number of limitations to the present study. For one, this study was cross-sectional in design, thus precluding our ability to draw causal inferences pertaining to the relationships between FM, AOI, LM, and BMD. Secondly, no premenopausal women were included in this study, and all study participants were Chinese, thus limiting the degree to which these data are generalizable. Third, while we adjusted for age, height, and YSM when assessing the relationships between FM, FD, and BMD, we did not take other potential confounding variables such as serum sex hormone levels, vitamin D levels, dietary composition, smoking, or socioeconomic status into consideration when conducting multivariable regression analyses.

In conclusion, the results of this analysis suggest that FD and FM are associated with BMD among postmenopausal Chinese woman over the age of 60, even after adjusting for age, height, YSM, and LM. AOI can serve as an indicator of central FD, and was found to be negatively associated with both total and regional BMD, whereas total FM exhibit a positive relationship with BMD at all analyzed body sites, suggesting that it may serve as a protective factor. Total LM exhibited results consistent with total FM, thus suggesting that proper weight gain with appropriate control of central obesity may be beneficial to bone health among postmenopausal women. These data emphasize the important of regular physical activity, which can reduce central obesity even in the absence of weight loss while also reducing age-related muscle atrophy and increasing mechanical loading of the skeletal system (37).

DATA AVAILABILITY STATEMENT

The original contributions presented in the study are included in the article/supplementary material. Further inquiries can be directed to the corresponding author.

ETHICS STATEMENT

The studies involving human participants were reviewed and approved by the Ethics Committee of the Tianjin Medical University General Hospital. The patients/participants provided their written informed consent to participate in this study. Written informed consent was obtained from the individual(s) for the publication of any potentially identifiable images or data included in this article.

AUTHOR CONTRIBUTIONS

JF and YJ contributed equally to this work and share first authorship. JF and YJ designed the investigation. JQ and BH conducted the investigation and collected data. YJ performed the statistics. QZ wrote the main manuscript. All authors contributed to the article and approved the submitted version.

FUNDING

This work was funded by the National Natural Science Foundation of China (Grant No. 92163213, 81970085 and 82000844), and Science and Technology Talent Cultivation Project of Tianjin Municipal Health Commission (Grant No. KJ20216), and the Tianjin science and sechnology plan project (Grant No. 17ZXMFSY00080).

REFERENCES

1. Ho-Pham LT, Nguyen UD, Nguyen TV. Association Between Lean Mass, Fat Mass, and Bone Mineral Density: A Meta-Analysis. *J Clin Endocrinol Metam* (2014) 99:30–8. doi: 10.1210/jc.2013-3190
2. Hannan MT, Felson DT, Anderson JJ. Bone Mineral Density in Elderly Men and Women: Results From the Framingham Osteoporosis Study. *J Bone Miner Res* (1992) 7:547–53. doi: 10.1002/jbmr.5650070511
3. Ho-Pham LT, Nguyen ND, Lai TQ, Nguyen TV. Contributions of Lean Mass and Fat Mass to Bone Mineral Density: A Study in Postmenopausal Women. *BMC Musculoskelet Disord* (1992) 11:59. doi: 10.1186/1471-2474-11-59
4. Cheng Q, Zhu YX, Zhang MX, Li LH, Du PY, Zhu MH. Age and Sex Effects on the Association Between Body Composition and Bone Mineral Density in Healthy Chinese Men and Women. *Menopause* (2012) 19:448–55. doi: 10.1097/gme.0b013e31823a40ba
5. Fu X, Ma X, Lu H, He W, Wang Z, Zhu S. Associations of Fat Mass and Fat Distribution With Bone Mineral Density in Pre- and Postmenopausal Chinese Women. *Osteoporos Int* (2011) 22:113–9. doi: 10.1007/s00198-010-1210-9
6. Dytfeld J, Ignaszak-Szczepaniak M, Gowin E, Michalak M, Horst-Sikorska W. Influence of Lean and Fat Mass on Bone Mineral Density (BMD) in Postmenopausal Women With Osteoporosis. *Arch Gerontol Geriatr* (2011) 53:e237–42. doi: 10.1016/j.archger.2011.01.002
7. Hosseini SA, Hosseini SR, Ghadimi R, Noreddini H, Bijani A. Association Between Body Fat and Bone Mineral Density in non-Obese Post-Menopausal Women Over 60 Years Old. *Caspian J Intern Med* (2021) 12:200–6. doi: 10.22088/cjim.12.2.200
8. Chain A, Crivelli M, Faerstein E, Bezerra FF. Association Between Fat Mass and Bone Mineral Density Among Brazilian Women Differs by Menopausal Status: The Pro-Saude Study. *Nutrition* (2017) 33:14–9. doi: 10.1016/j.nut.2016.08.001
9. Namwongprom S, Rojanasthien S, Mangklabruks A, Soontrapa S, Wongboontan C, Ongphiphadhanakul B. Effect of Fat Mass and Lean Mass on Bone Mineral Density in Postmenopausal and Perimenopausal Thai Women. *Int J Womens Health* (2013) 5:87–92. doi: 10.2147/IJWH.S41884
10. Kim HY, Kim SS, Kim JS, Jung JG, Yoon SJ, Jo YH. Association Between Abdominal Obesity and Lumbar Bone Mineral Density According to the Postmenopausal Period in Korean Women. *J Of Obes Metab Syndrome* (2017) 26:210–6. doi: 10.7570/jomes.2017.26.3.210
11. Marin-Mio RV, Moreira L, Camargo M, Perigo N, Cerondoglo MS, Lazaretti-Castro M. : Lean Mass as a Determinant of Bone Mineral Density of Proximal Femur in Postmenopausal Women. *Arch Endocrinol Metab* (2018) 62:431–7. doi: 10.20945/2359-3997000000059
12. Ilesanmi-Oyelere BL, Coad J, Roy N, Kruger MC. Lean Body Mass in the Prediction of Bone Mineral Density in Postmenopausal Women. *Biores Open Access* (2018) 7:150–8. doi: 10.1089/biores.2018.0025
13. Kim JH, Choi HJ, Kim MJ, Shin CS, Cho NH. Fat Mass is Negatively Associated With Bone Mineral Content in Koreans. *Osteoporos Int* (2012) 23:2009–16. doi: 10.1007/s00198-011-1808-6
14. Anagnostis P, Paschou SA, Katsiki N, Krikidis D, Lambrinoudaki I, Goulis DG. Menopausal Hormone Therapy and Cardiovascular Risk: Where are We Now? *Curr Vasc Pharmacol* (2019) 17:564–72. doi: 10.2174/1570161116666180709095348
15. Liu X, Shi H. Regulation of Estrogen Receptor Alpha Expression in the Hypothalamus by Sex Steroids: Implication in the Regulation of Energy Homeostasis. *Int J Endocrinol* (2019) 2015:949085. doi: 10.1155/2015/949085
16. Xiao Z, Tan Z, Shang J, Cheng Y, Tang Y, Guo B, et al. Sex-Specific and Age-Specific Characteristics of Body Composition and its Effect on Bone Mineral Density in Adults in Southern China: A Cross-Sectional Study. *BMJ Open* (2020) 10:e32268. doi: 10.1136/bmjopen-2019-032268
17. Xiao Z, Xu H. Gender-Specific Body Composition Relationships Between Adipose Tissue Distribution and Peak Bone Mineral Density in Young Chinese Adults. *BioMed Res Int* (2020) 2020:6724749. doi: 10.1155/2020/6724749
18. Shao HD, Li GW, Liu Y, Qiu YY, Yao JH, Tang GY. Contributions of Fat Mass and Fat Distribution to Hip Bone Strength in Healthy Postmenopausal Chinese Women. *J Bone Miner Metab* (2015) 33:507–15. doi: 10.1007/s00774-014-0613-7
19. Kapus O, Gaba A, Lehnert M. Relationships Between Bone Mineral Density, Body Composition, and Isokinetic Strength in Postmenopausal Women. *Bone Rep* (2020) 12:100255. doi: 10.1016/j.bonr.2020.100255
20. Namwongprom S, Rojanasthien S, Wongboontan C, Mangklabruks A. Contribution of Android and Gynoid Adiposity to Bone Mineral Density in Healthy Postmenopausal Thai Women. *J Clin Densitom* (2019) 22:346–50. doi: 10.1016/j.jocd.2018.05.037
21. Bouchi R, Nakano Y, Ohara N, Takeuchi T, Murakami M, Asakawa M, et al. Clinical Relevance of Dual-Energy X-Ray Absorptiometry (DXA) as a Simultaneous Evaluation of Fatty Liver Disease and Atherosclerosis in Patients With Type 2 Diabetes. *Cardiovasc Diabetol* (2016) 15:64. doi: 10.1186/s12933-016-0384-7
22. Kim DH, Lim H, Chang S, Kim JN, Roh YK, Cho MK. Association Between Body Fat and Bone Mineral Density in Normal-Weight Middle-Aged Koreans. *Korean J Fam Med* (2019) 40:100–5. doi: 10.4082/kjfm.17.0082
23. Cole TJ, Fewtrell MS, Prentice A. The Fallacy of Using Percentage Body Fat as a Measure of Adiposity. *Am J Clin Nutr* (2008) 87:1959–60. doi: 10.1093/ajcn/87.6.1959
24. Gilthorpe MS, Tu YK. Mathematical Coupling: A Multilevel Approach. *Int J Epidemiol* (2004) 33:1399–400. doi: 10.1093/ije/dyh302
25. Tu YK, Clerehugh V, Gilthorpe MS. Ratio Variables in Regression Analysis can Give Rise to Spurious Results: Illustration From Two Studies in Periodontology. *J Dent* (2004) 32:143–51. doi: 10.1016/j.jdent.2003.09.004
26. Reid IR. Relationships Between Fat and Bone. *Osteoporos Int* (2008) 19:595–606. doi: 10.1007/s00198-007-0492-z
27. McTernan PG, Anderson LA, Anwar AJ, Eggo MC, Crocker J, Barnett AH, et al. Glucocorticoid Regulation of P450 Aromatase Activity in Human Adipose Tissue: Gender and Site Differences. *J Clin Endocrinol Metab* (2002) 87:1327–36. doi: 10.1210/jcem.87.3.8288
28. Faloni AP, Sasso-Cerri E, Rocha FR, Katchburian E, Cerri PS. Structural and Functional Changes in the Alveolar Bone Osteoclasts of Estrogen-Treated Rats. *J Anat* (2012) 220:77–85. doi: 10.1111/j.1469-7580.2011.01449.x
29. Williams GA, Wang Y, Callon KE, Watson M, Lin JM, Lam JB, et al. *In Vitro* and *In Vivo* Effects of Adiponectin on Bone. *Endocrinology* (2009) 150:3603–10. doi: 10.1210/en.2008-1639
30. Tu Q, Zhang J, Dong LQ, Saunders E, Luo E, Tang J, et al. Adiponectin Inhibits Osteoclastogenesis and Bone Resorption *via* APPL1-Mediated Suppression of Akt1. *J Biol Chem* (2011) 286:12542–53. doi: 10.1074/jbc.M110.152405
31. Pollock NK. Childhood Obesity, Bone Development, and Cardiometabolic Risk Factors. *Mol Cell Endocrinol* (2015) 410:52–63. doi: 10.1016/j.mce.2015.03.016
32. Cartier A, Lemieux I, Almeras N, Tremblay A, Bergeron J, Despres JP. Visceral Obesity and Plasma Glucose-Insulin Homeostasis: Contributions of Interleukin-6 and Tumor Necrosis Factor-Alpha in Men. *J Clin Endocrinol Metab* (2008) 93:1931–8. doi: 10.1210/jc.2007-2191
33. Pou KM, Massaro JM, Hoffmann U, Vasan RS, Maurovich-Horvat P, Larson MG, et al. Visceral and Subcutaneous Adipose Tissue Volumes are Cross-Sectionally Related to Markers of Inflammation and Oxidative Stress: The Framingham Heart Study. *Circulation* (2007) 116:1234–41. doi: 10.1161/CIRCULATIONAHA.107.710509
34. Wood IS, Wang B, Jenkins JR, Trayhurn P. The Pro-Inflammatory Cytokine IL-18 is Expressed in Human Adipose Tissue and Strongly Upregulated by TNFalpha in Human Adipocytes. *Biochem Biophys Res Commun* (2005) 337:422–9. doi: 10.1016/j.bbrc.2005.09.068
35. Rokoff LB, Rifas-Shiman SL, Switkowski KM, Young JG, Rosen CJ, Oken E, et al. Body Composition and Bone Mineral Density in Childhood. *Bone* (2019) 121:9–15. doi: 10.1016/j.bone.2018.12.009
36. Gimble JM, Zvonic S, Floyd ZE, Kassem M, Nuttall ME. Playing With Bone and Fat. *J Cell Biochem* (2006) 98:251–66. doi: 10.1002/jcb.20777
37. Ross R, Janssen I, Dawson J, Kungl AM, Kuk JL, Wong SL, et al. Exercise-Induced Reduction in Obesity and Insulin Resistance in Women: A Randomized Controlled Trial. *Obes Res* (2004) 12:789–98. doi: 10.1038/oby.2004.95

Conflict of Interest: The authors declare that the research was conducted in the absence of any commercial or financial relationships that could be construed as a potential conflict of interest.

this article, or claim that may be made by its manufacturer, is not guaranteed or endorsed by the publisher.

frontiers | Frontiers in Endocrinology

ORIGINAL RESEARCH
published: 14 April 2022
doi: 10.3389/fendo.2022.874904

Associations Between Vertebral Marrow Proton Density Fat Fraction and Risk of Prostate Cancer

*Shaojun Li[1], Bo Wang[2], Wenwen Liang[2], Qi Chen[1], Wei Wang[1], Jiangjun Mei[3], He Zhang[4], Qianqian Liu[5] and Mingyuan Yuan[1]**

[1] Department of Radiology, Shanghai University of Medicine & Health Sciences Affiliated Zhoupu Hospital, Shanghai, China, [2] Department of Radiology, Gongli Hospital of Shanghai Pudong New Area, Shanghai, China, [3] Department of Ultrasound Medicine, Shanghai University of Medicine & Health Sciences Affiliated Zhoupu Hospital, Shanghai, China, [4] Department of Urology, Gongli Hospital of Shanghai Pudong New Area, Shanghai, China, [5] Department of Laboratory Medicine, Gongli Hospital of Shanghai Pudong New Area, Shanghai, China

Bone marrow adipocytes may be responsible for cancer progression. Although marrow adipogenesis is suspected to be involved in prostate carcinogenesis, an association between marrow adiposity and prostate cancer risk has not been clearly established *in vivo*. This work included 115 newly diagnosed cases of histologically confirmed prostate cancer (range, 48–79 years) and 87 age-matched healthy controls. Marrow proton density fat fraction (PDFF) was measured by 3.0-T MR spectroscopy at the spine lumbar. Associations between marrow PDFF and risk of prostate cancer by stage of disease and grade sub-types were performed using multivariable polytomous logistic regression. There were no significant group differences in the vertebral marrow PDFF, despite prostate cancer patients having 6.6% higher marrow PDFF compared to the healthy controls (61.7 ± 9.8% vs. 57.9 ± 6.5%; t = 1.429, p = 0.161). After adjusting for various clinical and demographic characteristics, we found that elevated marrow PDFF was related to an increased risk of high-grade prostate cancer [odds ratios (OR) = 1.31; 95% confidence interval (CI), 1.08–1.57; p = 0.003]. Likewise, increased marrow PDFF had a significantly positive correlation with aggressive prostate cancer risk (OR = 1.54; 95% CI, 1.13–1.92; p <0.001). There were no associations between marrow PDFF and low-grade (p = 0.314) or non-aggressive (p = 0.435) prostate cancer risk. The data support the hypothesis that marrow adiposity was correlated with increased risk of aggressive prostate cancer, supporting a link between adipogenesis and prostate cancer risk.

Keywords: prostate cancer risk, bone marrow, adipocyte, proton density fat fraction, MR spectroscopy

OPEN ACCESS

Edited by:
DongMei Wu,
East China Normal University, China

Reviewed by:
Jingzheng Fan,
Tianjin Medical University General Hospital, China
Yongming Dai,
Shanghai United Imaging Healthcare Co., Ltd., China

***Correspondence:**
Mingyuan Yuan
doctorme476@163.com

Specialty section:
This article was submitted to Bone Research, a section of the journal Frontiers in Endocrinology

Received: *13 February 2022*
Accepted: *15 March 2022*
Published: *14 April 2022*

Citation:
Li S, Wang B, Liang W, Chen Q, Wang W, Mei J, Zhang H, Liu Q and Yuan M (2022) Associations Between Vertebral Marrow Proton Density Fat Fraction and Risk of Prostate Cancer. Front. Endocrinol. 13:874904. doi: 10.3389/fendo.2022.874904

INTRODUCTION

Marrow adipocytes are derived from multipotent bone marrow mesenchymal stem cells that can differentiate into various cell types, including myocytes, osteoblasts, chondrocytes, and adipocytes (1). Adipocytes within the bone marrow niche carry out diverse functions that are capable of secreting inflammatory mediators, growth factors, and adipokines, which play an active role in

regulating the function and behavior of neighboring cells, and have potentials to dysregulate normal bone homeostasis (2–4).

The unique features of the bone marrow niche make it a favorable metastatic site of cancers, including multiple myeloma, prostate, and breast cancer bone metastasis (4–6). The positive feedback loops initiated by tumor cells within the bone marrow niche also induce these cancer cells to metastasize and to grow within the bone marrow but not in other anatomical sites (7). Mechanisms resulting in the homing of prostate cancer cells to bone marrow remain poorly understood. Several studies have demonstrated that marrow fat tissue fuels and supports the growth of solid tumor metastasis, such as breast and prostate cancer bone metastasis, by serving as plenty of source of lipids and signaling molecules (4, 8). As a powerful tool to reveal novel mechanistic targets of cancer-related bone-metastatic diseases treatments, understanding the prominent role of marrow adiposity in adaptation and survival of tumor cells in the bone is of great clinical implication. Skeletal metastases are a major cause of morbidity and mortality in prostate cancer.

Skeletal metastasis remains the most common and the deadliest complication of advanced prostate cancer. The role of marrow fat cells in the bone metastatic process of prostate cancer cells is well established (9, 10). *Ex vivo* human primary marrow adipocyte secretions may support prostate-cancer-directed migration in a chemokine receptor CCR3-dependent manner (5), whereas the number and depth of *in vivo* analyses in patients are limited. We hypothesized that an increase in marrow proton density fat fraction measured by magnetic resonance spectroscopy (MRS) in spinal vertebral bodies may be correlated with increased prostate cancer risk, both overall and subgroup according to stage and grade. If this is the case, marrow adiposity may present a promising therapeutic option for aggressive prostate cancer.

MATERIALS AND METHODS

Study Population

This study includes 115 newly diagnosed, histologically confirmed, primary prostate cancer (range, 48–79 years) identified by the Pathology Department between December 2017 and November 2021. We also recruited 87 age-matched healthy controls (range, 49–78 years) from the community on the basis of the participant's age at the date of the diagnosis. Prostate cancer patients were classified into localized (stage T1 or T2; NXM0) or advanced stage (stage T3 or T4) according to the tumor–node–metastasis (TNM) clinical staging system and into low grade (Gleason score <7) and high grade (Gleason sum ≥7) according to Gleason scores following review of histological material, as previously described (11). Aggressive disease was classified by TNM stage III–IV and/or Gleason sum 7 or higher. Non-aggressive disease was defined as Gleason score <7 and stage I/II at diagnosis (12).

At enrollment, all patients completed self-administered questionnaires about demographics, general risk factors, smoking status, and medical history, family history of prostate cancer, and lifestyle factors (e.g., physical activity, history of smoking, and alcohol consumption). Cigarette smoking at baseline was classified as current, former, or never. Physical activity was determined by using the International Physical Activity Questionnaire short form, with data reported as Metabolic Equivalent of Task hours per week (6). Height was measured to the nearest 0.5 cm with a metric rule attached to the wall and a right angled wood block. Body weight was measured to the nearest 0.1 kg with a balance beam scale after participants removed footwear and excess clothing. Body mass index was calculated as the weight (in kilograms) divided by the square of the height (in meters). Participants also had an overnight fasting blood sample collected. Participants were excluded in the following cases: (1) previous cancer or another history of chronic illness such as diabetes mellitus, hypothalamic or pituitary disorders, or impaired renal function; (2) use of medications known to influence bone metabolism such as bisphosphonates, steroids, hormone replacement therapy, or any medications that affect bone metabolism; (3) previous history of lumbar spinal surgery or irradiation; and (4) any contraindication to MR examinations. The study protocols conformed to the Declaration of Helsinki. The study was approved by the Institutional Review Board of Shanghai University of Medicine & Health Sciences Affiliated Zhoupu Hospital, and all participants signed a letter of informed consent for the scientific evaluation of their data.

Biochemical Analyses

All blood samples were obtained before 8 a.m. after an 8-h overnight fast and were analyzed on the same day as collection. The plasma concentration of glucose was determined using an automatic biochemical analyzer (ADVIA Chemistry XPT System, Siemens Healthcare, Erlangen, Germany). Prostate-specific antigen, total cholesterol, triglycerides, high- and low-density lipoprotein cholesterol, and total cholesterol were measured with a Cobas 8000 (Roche Diagnostics, Basel, Switzerland) using chemiluminescence immunoassay.

MRI Examinations

For marrow proton density fat fraction (PDFF) measurements of the L3 vertebra, the participants underwent spine ^{1}H-magnetic resonance spectroscopy (^{1}H-MRS) in a 3-T MRI instrument (Siemens Skyra, Siemens Medical Systems, Erlangen, Germany), as previously described (13, 14). Briefly, the participants were positioned head first in the magnet bore in the prone position. A phased-array coil was positioned over the lumbar region. To exclude any confounders such as silent compression fractures, vertebral hemangiomas, and wedging of vertebrae, the standard protocols including sagittal T1- and T2-weighted images were used for anatomical and morphological evaluations of the lumbar spine. Before the MR spectroscopy acquisition, coronal, sagittal, and axial scout T2-weighted fast spin echo sequence were used as a reference for the spectral acquisition box.

A single voxel T2-corrected multi-echo MR spectroscopy sequence was performed by placing a voxel measuring 1.5 mm × 1.5 mm × 1.5 mm (3.4 ml) within the L3 vertebral body using a

stimulated echo acquisition mode with five echo times (12, 24, 36, 48, and 72 ms) and 3,000 ms repetition time. Spectral data were acquired in 1,024 data points with a 2,000 Hz receiver bandwidth, 90° flip angle without water suppression, and a total acquisition time of 17 s. For each voxel placement, automated procedures were performed to optimize the gradient shimming and transmit and receive gain. An example of the fat spectral and water peaks at a specific echo time and the automatically calculated fat fraction from the high-speed T2-corrected multi-echo scan are displayed in **Figure 1**.

Statistical Analysis

Data are expressed as the mean ± standard deviation, median (interquartile range), or frequencies and percentages where appropriate. Differences in baseline demographic and clinical characteristics between cases and healthy controls were evaluated using *t*-test or Wilcoxon rank sum test (for continuous variables) and chi-squared tests (for categorical variables). Differences in the PDFF values among the controls and low- and high-grade prostate cancer, and among the controls and aggressive and non-aggressive prostate cancer were assessed using analysis of covariance (ANCOVA) followed by Bonferroni *post-hoc* multiple comparisons when controlling for covariates. Multivariable polytomous logistic regression was used to estimate odds ratios (ORs) and 95% confidence intervals (CIs) for the associations of marrow PDFF with prostate cancer risk by stage and grade sub-types, in which two separate sets of analyses were ran. The potential confounding factors that are hypothesized or known to be associated with prostate cancer were included in the multivariable models including age, body mass index (BMI), physical activity, alcohol consumption, smoking status, levels of prostate specific antigen and blood lipids, and family history of prostate cancer (15, 16). These statistical analyses were performed using IBM SPSS statistical software version 20 (SPSS Inc., Chicago, IL, USA). All statistical tests were two sided, and *p*-values were considered to be significant if <0.05.

RESULTS

General Outcomes

The demographic and clinical characteristics of the prostate cancer patients and healthy controls are presented in **Table 1**. Among the total 115 prostate cancer, 60 (52.2%) were classified as aggressive prostate cancer, and 52 (45.2%) had a Gleason score ≥7. Cases and healthy controls did not differ markedly in demographic characteristics. Prostate cancer patients had higher levels of prostate-specific antigen than healthy controls (median, 10.2 vs. 2.1 ng/ml; $p < 0.001$) and were more likely to have hypercholesterolemia. There were no other differences between groups in family history of prostate cancer, smoking status, alcohol intake, and levels of physical activity. There were no significant group differences in the marrow PDFF at the spine lumbar, despite prostate cancer patients having 6.6% higher marrow PDFF compared to the healthy controls (61.7 ± 9.8% vs. 57.9 ± 6.5%; $t = 1.429$, $p = 0.161$) (**Table 1**).

Differences in PDFF Among the Controls and Low- and High-Grade Prostate Cancer, and Among the Controls and Aggressive and Non-aggressive Prostate Cancer

Figure 2 summarizes the marrow PDFF results from the healthy controls, low- and high-grade prostate cancer, and aggressive and non-aggressive prostate cancer. In the unadjusted models, lumbar spine PDFF was higher in the high-grade prostate cancer patients (67.3 ± 9.2%) than those in health controls (57.9 ± 6.5%, $p < 0.001$) or low-grade prostate cancer (56.1 ± 6.9%, $p < 0.001$), and these differences remained statistically significant even after controlling for various clinical and demographic characteristics including age, body mass index, smoking status, alcohol intake, physical activity, prostate specific antigen levels, levels of blood lipids, and family history of prostate cancer. Similar results were observed between the healthy controls (57.9 ± 6.5%) and aggressive prostate cancer patients (68.3 ± 7.4%, $p < 0.001$), and between the non-aggressive

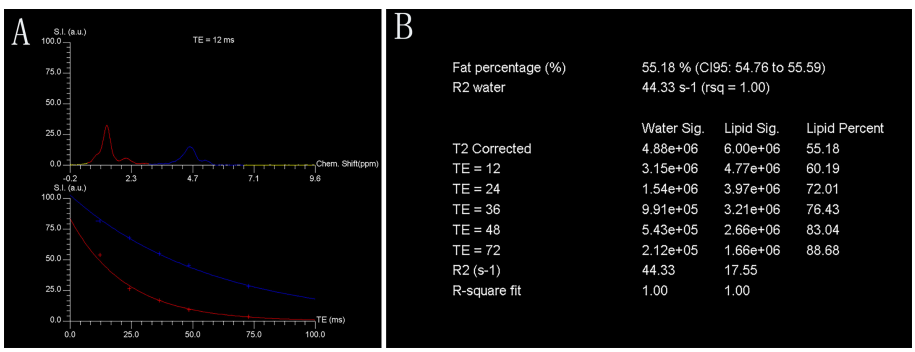

FIGURE 1 | Representative single-voxel T2-corrected multi-echo magnetic resonance spectroscopy. Fat and water spectral peaks at echo time of 12 ms are presented. Red curve denotes fat spectrum (bulk methylene protons at 1.30 ppm), and blue curve denotes water spectrum (H_2O at 4.7 ppm) **(A)**. Each fat and water integral at five echoes (echo time = 12, 24, 36, 48, and 72 ms, respectively) with estimated marrow PDFF of 55.18% **(B)**. Chem., chemical; CI, confidence interval; FF, fat fraction; rsq, r-squared; S.I. (a.u.), signal intensity (arbitrary units); TE, echo time.

TABLE 1 | Baseline characteristics of the study population.

	Prostate cancer (n = 115)	Healthy controls (n = 87)
Age, years	61.6 ± 8.8	62.5 ± 8.6
Height, cm	170.5 ± 7.1	171.0 ± 8.5
Weight, kg	62.9 ± 8.9	63.1 ± 9.0
BMI, kg/m^2	23.9 ± 4.2	23.5 ± 3.9
Family history of prostate cancer, n (%)	6 (5.2)	2 (2.3)
Smoking status, n (%)		
Never	75 (65.2)	60 (69.0)
Former smoker	25 (21.7)	17 (19.5)
Current smoker	15 (13.0)	10 (11.5)
Alcohol intake, n (%)		
None	87 (75.7)	68 (78.2)
≤7 units per week	19 (16.5)	13 (14.9)
>7 units per week	9 (7.8)	6 (6.9)
Prostate-specific antigen, ng/ml	10.2 (6.1, 28.5)	2.1 (1.0, 7.6) [a]
Histologic grade, n (%)		
Low (Gleason sum: 2–6)	63 (54.8)	NA
High (Gleason sum: ≥7)	52 (45.2)	NA
Stage of disease, n (%)		
I/II	79 (68.7)	NA
III/IV	36 (31.3)	NA
Physical activity, METs/week	9 (4, 16)	10 (4, 18)
Total cholesterol, mmol/L	4.62 (4.28, 4.96)	4.11 (3.98, 4.33) [a]
Triglyceride, mmol/L	1.29 (1.24, 1.34)	1.26 (1.19, 1.30)
HDL cholesterol, mmol/L	1.27 (1.23, 1.31)	1.28 (1.25, 1.34)
LDL cholesterol, mmol/L	2.97 (2.83, 3.12)	2.82 (2.68, 3.23)
PDFF, %	61.7 ± 9.8	57.9 ± 6.5 [b]

Data are expressed as mean ± SD, median (IQR), or n (%) as appropriate.
BMI, body mass index; HDL, high-density lipoprotein; IQR, interquartile range Q1-Q3; LDL, low-density lipoprotein; METs, metabolic equivalent of tasks; NA, not applicable; SD, standard deviation; PDFF, proton density fat fraction.
To detect difference between the two groups.
[a]p value by Wilcoxon rank sum test.
[b]p value by independent-sample t-test (all p<0.05).

(55.0 ± 7.2%, $p < 0.001$) and aggressive prostate cancer patients (68.3 ± 7.4%, $p < 0.001$) (**Figure 2**).

Relationships Between Proton Density Fat Fraction and Prostate Cancer Risk

Table 2 gives multivariable-adjusted associations of marrow PDFF with risk of low- and high-grade prostate cancer and non-aggressive and aggressive prostate cancer, respectively. When stratified by Gleason scores, there were significant associations between elevated marrow PDFF and risk of low- or high-grade prostate cancer in the univariable analysis (all $p < 0.05$). Similar findings were observed in non-aggressive and aggressive disease.

In multivariable analysis adjusted for aforementioned covariates, increased marrow PDFF was correlated with an increased risk of high-grade prostate cancer (OR = 1.31; 95% CI, 1.08–1.57; $p = 0.003$), but this relationship did not reach significance in risk of low-grade prostate cancer (OR = 1.19; 95% CI, 0.88–1.49; $p = 0.314$). Similar results were found in aggressive prostate cancer risk (OR = 1.54; 95% CI, 1.13–1.92; $p < 0.001$) but not in non-aggressive prostate cancer risk (**Table 2**).

DISCUSSION

Bone marrow niche is dynamic and complex. The functional role of bone marrow fat cells in the development and progression, phenotype, and survival of skeletal tumor cells remains elusive. Adipocyte-enriched microenvironments is a preferred site for prostate cancer bone metastasis, and several studies have focused on the cellular and molecular mechanisms of this tropism, indicating that a complex interaction occurs between neoplastic cells and the cells directly responsible for skeletal remodeling, namely, osteoclasts and osteoblasts in modulating the microenvironment of bone marrow (17). Expansion of marrow adiposity has shown to be related with both osteoblastic and osteolytic disease (9, 18). We found that prostate cancer patients were more likely to have a higher marrow PDFF. Our data in the present study may provide *in vivo* imaging evidence supporting previous *in vitro* studies, indicating that in multiple myeloma, breast, and prostate cancer, crosstalk of adipocytes–tumor cells is one of the important mediators for implantation and propagation of the migrating metastatic cells and may serve as an emerging facilitator of therapy evasion (19, 20). Therapeutic approaches that modulate the balance between osteogenesis and

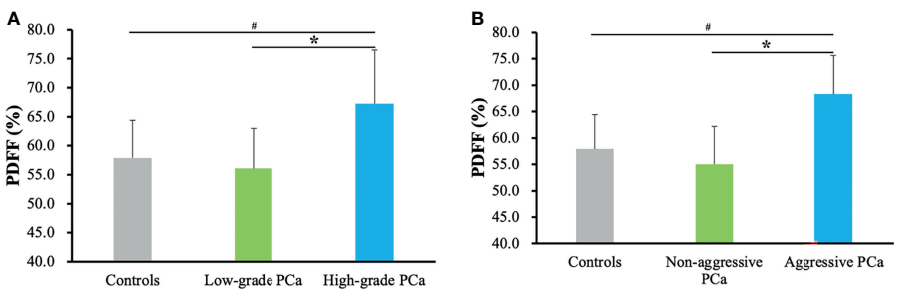

FIGURE 2 | Marrow PDFF results from the healthy controls, low- and high-grade prostate cancer **(A)**, and aggressive and non-aggressive prostate cancer **(B)**. Data are expressed as mean ± SD. $^{\#}p < 0.001$ and $^{*}p < 0.001$ were calculated by ANCOVA followed by Bonferroni *post-hoc* multiple comparisons after adjusting for age, body mass index, alcohol intake, smoking status, physical activity, prostate specific antigen levels, levels of blood lipids, and family history of prostate cancer. PCa, prostate cancer; PDFF, proton density fat fraction.

TABLE 2 | Association between marrow proton density fat fraction and prostate cancer risk.

	Unadjusted		Multivariable adjusted*	
	OR (95% CI)	*p*-value	OR (95% CI)	*p*-value
Low-grade prostate cancer	1.35 (1.09–1.55)	0.017	1.19 (0.88–1.49)	0.314
High-grade prostate cancer	1.47 (1.16–1.80)	<0.001	1.31 (1.08–1.57)	0.003
Non-aggressive prostate cancer	1.40 (1.08–1.69)	0.021	1.29 (0.90–1.77)	0.435
Aggressive prostate cancer	1.61 (1.20–2.04)	<0.001	1.54 (1.13–1.92)	<0.001

Low-grade was classified by Gleason score <7, and high-grade was classified by Gleason sum ≥7 according to Gleason scores. Aggressive disease was classified by Gleason grade ≥ 7 and/or stage III–IV, and non-aggressive disease was defined as Gleason score <7 and stage I/II at diagnosis.

**Multivariable adjusted for age, body mass index, smoking status, alcohol use, physical activity, prostate specific antigen, levels of blood lipids, and family history of prostate cancer. OR, odds ratio; CI, confidence interval.*

adipogenesis may be one of the most effective ways to maintain healthy skeletal integrity, thus preventing and treating cancer infiltration.

Overall, in this large retrospective study, we reported an odds ratio of 1.31–1.54 for marrow fat fraction to predict high-grade or aggressive prostate cancer on multivariable analysis, suggesting a possible link between expansion of marrow fat and greater risk of high-grade disease. Several mechanisms could explain the associations of marrow adiposity with prostate cancer risk. The representative mechanisms include the secretion of adipocytokines and lipid transfer (21). Previous studies have shown that prostate cancers cells are attracted to a rich source of lipids stored within adipocytes in the bone marrow (22). In the bone marrow, fat cells are indeed active cells because these cells actively not only store free fatty acids but also secrete chemokines, adipokines, growth factors, and inflammatory mediators such as interleukin 1 beta, interleukin 6, and tumor necrosis factor alpha, which affect bone remodeling, insulin metabolism, and energy regulation (23, 24). Increased marrow adiposity is tightly linked to marrow inflammation. In various physiological conditions, inflammatory pathways may maintain normal bone metabolism but are significantly altered in condition of marrow fat expansion (10). For example, bone marrow fat cells secrete significant and regulated levels of IL-6, which promotes metastasis of tumor cells through the JAK2/STAT3 signaling pathway (24, 25). Upregulated expression of interleukin 6 in malignant cells was found to promote osteoclastogenesis. Similarly, several studies have linked marrow fat cells-derived CXCL1 and CXCL2 chemokines with prostate tumor progression and the effects of osteolysis in metastatic prostate cancer (9, 10, 26).

Furthermore, adipocytes' impact on the tumor cell behavior may attribute to the regulation of cancer cell metabolism *via* lipid transfer and lipolysis (4). The number of marrow adipocytes was increased in a metastatic bone marrow niche at the early phase; interestingly, during tumor progression, the number of fat cells with abundant lipid droplets was decreased (21, 27). These data provide *in vivo* evidence supporting the essential role of adipocytes in the lipid transfer from marrow fat cells to tumor cells. Previous *ex vivo* and *in vivo* studies also have shown that lipid chaperone fatty acid-binding protein 4 and interleukin 1 beta expression in metastatic prostate carcinoma cells are markedly induced by the exposure to bone marrow adipocytes in a functional crosstalk (8, 10). Diedrich et al. provided evidence that marrow adipocytes are able to induce the glycolytic phenotypes in prostate cancer cells by paracrine regulation of glycolytic enzymes, increasing lactate production and decreasing mitochondrial oxidative phosphorylation (28). They also found that fat cells are capable of driving metabolic reprogramming of metastatic prostate tumors through oxygen-independent mechanism of activating hypoxia-inducible factor 1 alpha signaling that can be reversed by hypoxia-inducible factor 1 alpha downregulation. Based on these data, targeting lipid metabolism of marrow fat cells combined with standard therapeutic agents may present unique therapeutic protocols for some cancers that thrive in adipocyte-rich metabolically active red bone marrow.

There are several strengths in our study, including its primary strength, its relatively large sample size, which allowed us to determine associations with low- and high-grade prostate cancer risk. Second, we uniformly used the Gleason scoring system to assess all tumors, which minimizes the large intra-rater variability in assigning clinical grade. Third, the precise marrow fat content at spinal vertebral bodies was obtained by using MR spectroscopy *in vivo*. The limitations of our study also must be acknowledged. First, the cross-sectional design of the study indicates that causality cannot be established for the outcomes assessed. Second, our study consisted of only Chinese men, which may limit the generalizability of our findings to men in other racial/ethnic groups. Future studies should focus on the relationship in other populations. Furthermore, although detailed evaluations of several lifestyle factors enabled controlling for confounding factors, residual or unmeasured confounding factors such as individual bone mineral density, caffeine or tea intake, and calcium and vitamin D supplementation cannot be ruled out.

In conclusion, our findings showed a close link between marrow adiposity and an increased risk of high-grade or aggressive prostate cancer but did not support an association between marrow adiposity and risk of low-grade or non-aggressive prostate cancer. MRI plays a critical role in the non-invasive assessment of bone marrow composition. Measures of marrow fat content may be predictive of prostate cancer risk. Future studies should specifically assess the associations of the

diversity and complexity of bone marrow adipocytes with risk of prostate cancer, peculiarly prostate cancer bone metastasis.

DATA AVAILABILITY STATEMENT

The original contributions presented in the study are included in the article/supplementary material, further inquiries can be directed to the corresponding author.

ETHICS STATEMENT

The studies involving human participants were reviewed and approved by the Institutional Review Board of Shanghai University of Medicine & Health Sciences Affiliated Zhoupu Hospital. The patients/participants provided their written informed consent to participate in this study.

AUTHOR CONTRIBUTIONS

Study design: SL, BW, and MY. Study conduct: JM, HZ, and QL. Data collection: WL, QC, and WW. Data analysis: SL, QC, and JM. Data interpretation: SL, BW, WL, QL, and MY. Drafting manuscript: SL, BW, and WL. All authors contributed to the article and approved the submitted version.

FUNDING

This work was supported by the funds for Training Project of Academic Leaders of Health System in Pudong New Area of Shanghai (No. PWRd2021-07) and 2020 New Interdisciplinary Construction Project of Shanghai Pudong New Area Health (No. PWXx2020-06).

REFERENCES

1. Zayzafoon M, Gathings WE, McDonald JM. Modeled Microgravity Inhibits Osteogenic Differentiation of Human Mesenchymal Stem Cells and Increases Adipogenesis. *Endocrinology* (2004) 145:2421–32. doi: 10.1210/en.2003-1156
2. Pierce JL, Begun DL, Westendorf JJ, McGee-Lawrence ME. Defining Osteoblast and Adipocyte Lineages in the Bone Marrow. *Bone* (2018) 118:2–7. doi: 10.1016/j.bone.2018.05.019
3. Wang H, Leng Y, Gong Y. Bone Marrow Fat and Hematopoiesis. *Front Endocrinol (Lausanne)* (2018) 9:694. doi: 10.3389/fendo.2018.00694
4. Herroon MK, Diedrich JD, Podgorski I. New 3D-Culture Approaches to Study Interactions of Bone Marrow Adipocytes With Metastatic Prostate Cancer Cells. *Front Endocrinol (Lausanne)* (2016) 7:84. doi: 10.3389/fendo.2016.00084
5. Guerard A, Laurent V, Fromont G, Esteve D, Gilhodes J, Bonnelye E, et al. The Chemokine Receptor CCR3 Is Potentially Involved in the Homing of Prostate Cancer Cells to Bone: Implication of Bone-Marrow Adipocytes. *Int J Mol Sci* (2021) 22(4):1994 doi: 10.3390/ijms22041994
6. Li G, Xu Z, Zhuang A, Chang S, Hou L, Chen Y, et al. Magnetic Resonance Spectroscopy-Detected Change in Marrow Adiposity Is Strongly Correlated to Postmenopausal Breast Cancer Risk. *Clin Breast Cancer* (2017) 17:239–44. doi: 10.1016/j.clbc.2017.01.004
7. Reagan MR, Rosen CJ. Navigating the Bone Marrow Niche: Translational Insights and Cancer-Driven Dysfunction. *Nat Rev Rheumatol* (2016) 12:154–68. doi: 10.1038/nrrheum.2015.160
8. Herroon MK, Diedrich JD, Rajagurubandara E, Martin C, Maddipati KR, Kim S, et al. Prostate Tumor Cell-Derived IL-1β Induces an Inflammatory Phenotype in Bone Marrow Adipocytes and Reduces Sensitivity to Docetaxel *via* Lipolysis-Dependent Mechanisms. *Mol Cancer Res* (2019) 17:2508–21. doi: 10.1158/1541-7786.MCR-19-0540
9. Hardaway AL, Herroon MK, Rajagurubandara E, Podgorski I. Marrow Adipocyte-Derived CXCL1 and CXCL2 Contribute to Osteolysis in Metastatic Prostate Cancer. *Clin Exp Metastasis* (2015) 32:353–68. doi: 10.1007/s10585-015-9714-5
10. Hardaway AL, Herroon MK, Rajagurubandara E, Podgorski I. Bone Marrow Fat: Linking Adipocyte-Induced Inflammation With Skeletal Metastases. *Cancer Metastasis Rev* (2014) 33:527–43. doi: 10.1007/s10555-013-9484-y
11. Zuccolo L, Lewis SJ, Donovan JL, Hamdy FC, Neal DE, Smith GD. Alcohol Consumption and PSA-Detected Prostate Cancer Risk–A Case-Control Nested in the ProtecT Study. *Int J Cancer* (2013) 132:2176–85. doi: 10.1002/ijc.27877
12. Bonn SE, Barnett MJ, Thornquist M, Goodman G, Neuhouser ML. Body Mass Index and Prostate Cancer Risk in the Carotene and Retinol Efficacy Trial. *Eur J Cancer Prev* (2019) 28:212–9. doi: 10.1097/cej.0000000000000438
13. Li G, Xu Z, Lin H, Chen Y, Li X, Chang S. Association Between Insulin Resistance and the Magnetic Resonance Spectroscopy-Determined Marrow Fat Fraction in Nondiabetic Postmenopausal Women. *Menopause* (2018) 25:676–82. doi: 10.1097/GME.0000000000001063
14. Moorthi RN, Fadel W, Eckert GJ, Ponsler-Sipes K, Moe SM, Lin C. Bone Marrow Fat is Increased in Chronic Kidney Disease by Magnetic Resonance Spectroscopy. *Osteoporos Int* (2015) 26:1801–7. doi: 10.1007/s00198-015-3064-7
15. Mondul AM, Weinstein SJ, Bosworth T, Remaley AT, Virtamo J, Albanes D. Circulating Thyroxine, Thyroid-Stimulating Hormone, and Hypothyroid Status and the Risk of Prostate Cancer. *PloS One* (2012) 7:e47730. doi: 10.1371/journal.pone.0047730
16. Jamnagerwalla J, Howard LE, Allott EH, Vidal AC, Moreira DM, Castro-Santamaria R, et al. Serum Cholesterol and Risk of High-Grade Prostate Cancer: Results From the REDUCE Study. *Prostate Cancer Prostatic Dis* (2018) 21:252–9. doi: 10.1038/s41391-017-0030-9
17. Vičić I, Belev B. The Pathogenesis of Bone Metastasis in Solid Tumors: A Review. *Croatian Med J* (2021) 62:270–82. doi: 10.3325/cmj.2021.62.270
18. Singh L, Brennan TA, Russell E, Kim JH, Chen Q, Brad Johnson F, et al. Aging Alters Bone-Fat Reciprocity by Shifting *In Vivo* Mesenchymal Precursor Cell Fate Towards an Adipogenic Lineage. *Bone* (2016) 85:29–36. doi: 10.1016/j.bone.2016.01.014
19. Fraczak E, Olbromski M, Piotrowska A, Glatzel-Plucinska N, Dziegiel P, Dybko J, et al. Bone Marrow Adipocytes in Haematological Malignancies. *Acta Histochem* (2018) 120:22–7. doi: 10.1016/j.acthis.2017.10.010
20. Nieman KM, Kenny HA, Penicka CV, Ladanyi A, Buell-Gutbrod R, Zillhardt MR, et al. Adipocytes Promote Ovarian Cancer Metastasis and Provide Energy for Rapid Tumor Growth. *Nat Med* (2011) 17:1498–503. doi: 10.1038/nm.2492
21. Cha YJ, Koo JS. Roles of Omental and Bone Marrow Adipocytes in Tumor Biology. *Adipocyte* (2019) 8:304–17. doi: 10.1080/21623945.2019.1643189
22. Gazi E, Gardner P, Lockyer NP, Hart CA, Brown MD, Clarke NW. Direct Evidence of Lipid Translocation Between Adipocytes and Prostate Cancer Cells With Imaging FTIR Microspectroscopy. *J Lipid Res* (2007) 48:1846–56. doi: 10.1194/jlr.M700131-JLR200
23. Wang D, Haile A, Jones LC. Dexamethasone-Induced Lipolysis Increases the Adverse Effect of Adipocytes on Osteoblasts Using Cells Derived From Human Mesenchymal Stem Cells. *Bone* (2013) 53:520–30. doi: 10.1016/j.bone.2013.01.009

24. Laharrague P, Fontanilles AM, Tkaczuk J, Corberand JX, Pénicaud L, Casteilla L. Inflammatory/Haematopoietic Cytokine Production by Human Bone Marrow Adipocytes. *Eur Cytokine Netw* (2000) 11:634–9.
25. Wang L, Cao L, Wang H, Liu B, Zhang Q, Meng Z, et al. Cancer-Associated Fibroblasts Enhance Metastatic Potential of Lung Cancer Cells Through IL-6/STAT3 Signaling Pathway. *Oncotarget* (2017) 8:76116–28. doi: 10.18632/oncotarget.18814
26. Kim SS, Kim KS, Han IH, Kim Y, Bang SS, Kim JH, et al. Proliferation of Mouse Prostate Cancer Cells Inflamed by Trichomonas vaginalis. *Korean J Parasitol* (2021) 59:547–56. doi: 10.3347/kjp.2021.59.6.54
27. Wang J, Chen GL, Cao S, Zhao MC, Liu YQ, Chen XX, et al. Adipogenic Niches for Melanoma Cell Colonization and Growth in Bone Marrow. *Lab Invest* (2017) 97:737–45. doi: 10.1038/labinvest.2017.14
28. Diedrich JD, Rajagurubandara E, Herroon MK, Mahapatra G, Huttemann M, Podgorski I. Bone Marrow Adipocytes Promote the Warburg Phenotype in Metastatic Prostate Tumors *via* HIF-1alpha Activation. *Oncotarget* (2016) 7:64854–77. doi: 10.18632/oncotarget.11712

Conflict of Interest: The authors declare that the research was conducted in the absence of any commercial or financial relationships that could be construed as a potential conflict of interest.

frontiers | Frontiers in Endocrinology

ORIGINAL RESEARCH
published: 27 April 2022
doi: 10.3389/fendo.2022.815835

Gender- and Age-Associated Differences in Bone Marrow Adipose Tissue and Bone Marrow Fat Unsaturation Throughout the Skeleton, Quantified Using Chemical Shift Encoding-Based Water–Fat MRI

*Kerensa M. Beekman[1,2], Martine Regenboog[1,3], Aart J. Nederveen[1], Nathalie Bravenboer[4,5], Martin den Heijer[2], Peter H. Bisschop[3], Carla E. Hollak[3], Erik M. Akkerman[1] and Mario Maas[1]**

[1] Department of Radiology and Nuclear Medicine, Amsterdam University Medical Centers, Amsterdam Movement Sciences, University of Amsterdam, Amsterdam, Netherlands, [2] Department of Endocrinology, Amsterdam University Medical Centers, Amsterdam Movement Sciences, Vrije Universiteit University, Amsterdam, Netherlands, [3] Department of Endocrinology and Metabolism, Amsterdam University Medical Centers, Amsterdam Movement Sciences, University of Amsterdam, Amsterdam, Netherlands, [4] Department of Clinical Chemistry, Research Laboratory Bone and Calcium Metabolism, Amsterdam University Medical Centers, Amsterdam Movement Sciences, Vrije Universiteit University, Amsterdam, Netherlands, [5] Department of Internal Medicine, Leiden University Medical Center, Leiden, Netherlands

Bone marrow adipose tissue (BMAT) is a dynamic tissue which is associated with osteoporosis, bone metastasis, and primary bone tumors. The aim of this study is to determine region-specific variations and age- and gender-specific differences in BMAT and BMAT composition in healthy subjects. In this cross-sectional study, we included 40 healthy subjects (26 male: mean age 49 years, range 22–75 years; 14 female: mean age 50 years, range 29–71) and determined the bone marrow signal fat fraction and bone marrow unsaturation in the spine (C3-L5), pelvis, femora, and tibiae using chemical shift encoding-based water–fat imaging (WFI) with multiple gradient echoes (mGRE). Regions of interest covered the individual vertebral bodies, pelvis and proximal epimetaphysis, diaphysis, and distal epimetaphysis of the femur and tibia. The spinal fat fraction increased from cervical to lumbar vertebral bodies (mean fat fraction (± SD or (IQR): cervical spine 0.37 ± 0.1; thoracic spine 0.41 ± 0.08. lumbar spine 0.46 ± 0.01; $p < 0.001$). The femoral fat fraction increased from proximal to distal (proximal 0.78 ± 0.09; diaphysis 0.86 (0.15); distal 0.93 ± 0.02; $p < 0.001$), while within the tibia the fat fraction decreased from proximal to distal (proximal 0.92 ± 0.01; diaphysis 0.91 (0.02); distal 0.90 ± 0.01; $p < 0.001$). In female subjects, age was associated with fat fraction in the spine, pelvis, and proximal femur ($\rho = 0.88$ $p < 0.001$; $\rho = 0.87$ $p < 0.001$; $\rho = 0.63$ $p = 0.02$; $\rho = 0.74$ $p =$

OPEN ACCESS

Edited by:
DongMei Wu,
East China Normal University, China

Reviewed by:
Ziru Li,
University of Michigan, United States
Thomas Baum,
Technical University of Munich, Germany
Samantha Costa,
Maine Medical Center Research Institute, United States
Guanwu Li,
Shanghai University of Traditional Chinese Medicine, China

***Correspondence:**
Mario Maas
m.maas@amsterdamumc.nl

Specialty section:
This article was submitted to Bone Research, a section of the journal Frontiers in Endocrinology

Received: *15 November 2021*
Accepted: *17 March 2022*
Published: *27 April 2022*

Citation:
Beekman KM, Regenboog M, Nederveen AJ, Bravenboer N, den Heijer M, Bisschop PH, Hollak CE, Akkerman EM and Maas M (2022) Gender- and Age-Associated Differences in Bone Marrow Adipose Tissue and Bone Marrow Fat Unsaturation Throughout the Skeleton, Quantified Using Chemical Shift Encoding-Based Water–Fat MRI. Front. Endocrinol. 13:815835. doi: 10.3389/fendo.2022.815835

0.002, respectively), while in male subjects age was only associated with spinal fat fraction (ρ = 0.40 p = 0.04). Fat fraction and unsaturation were negatively associated within the spine (r = -0.40 p = 0.01), while in the extremities fat fraction and unsaturation were positively associated (distal femur: r = 0.42 p = 0.01; proximal tibia: r = 0.47, p = 0.002; distal tibia: r = 0.35 p = 0.03), both independent of age and gender. In conclusion, we confirm the distinct, age- and gender-dependent, distribution of BMAT throughout the human skeleton and we show that, contradicting previous animal studies, bone marrow unsaturation in human subjects is highest within the axial skeleton compared to the appendicular skeleton. Furthermore, we show that BMAT unsaturation was negatively correlated with BMAT within the spine, while in the appendicular skeleton, BMAT and BMAT unsaturation were positively associated.

Keywords: bone marrow adipose tissue, bone marrow fat unsaturation, bone marrow adipose tissue distribution, healthy subjects, water–fat MR imaging

INTRODUCTION

Bone marrow adipose tissue (BMAT) is associated with different diseases like osteoporosis (1–3) and primary bone malignancies (4); furthermore, the bone marrow is a frequent metastatic site. BMAT is associated with bone metabolism (5, 6) and serves as a lipid source for proliferation and infiltration of malignant cells (7, 8), and tumor cells can affect the secretion of free fatty acids by bone marrow adipocytes (9). Furthermore, lower BMAT unsaturation and higher BMAT saturation appear to be associated with fractures (10).

Traditionally, the bone marrow is divided into red (or hematopoietic) and yellow (or fatty) marrow (11). After birth, conversion of the red marrow into yellow marrow starts in the appendicular skeleton in a centripetal way (12), and BMAT increases by approximately 6%–7.5% per decade (13–16). In situations of increased hematological demands, reconversion of yellow marrow to red marrow may occur. Furthermore, there are gender-associated differences in BMAT (13–15, 17).

Little is known about the region-specific variation bone marrow fatty acid composition in humans. Animal studies suggest that there are two distinct types of BMAT: regulated and constitutive BMAT (rBMAT and cBMAT) (18). In animals, rBMAT contains more saturated fatty acids, is located proximally within long bones, develops throughout life, and responds to BMAT-inducing stimuli. cBMAT contains more unsaturated fatty acids, is located distally in long bones, develops in early life, and does not respond to BMAT-inducing stimuli (18).

The gold standard for BMAT and BMAT fatty acid composition is single-voxel proton magnetic resonance spectroscopy (^{1}H-MRS) (19). However, ^{1}H-MRS availability is limited and the sampling area within the skeleton small, due to long acquisition times. Chemical shift encoding-based water–fat imaging (WFI) is widely used for quantification of BMAT (19). WFI with multiple gradient echoes (WFI-mGRE) is able to quantify both bone marrow fat fraction and BMAT unsaturation from the same MRI images, with fast acquisition times. Furthermore, WFI-mGRE shows good agreement with ^{1}H-MRS (20–24).

Insight in the normal variation of BMAT and BMAT fatty acid composition throughout the skeleton is necessary to further evaluate the interaction between BMAT, bone metabolism, and skeletal malignancies. Therefore, we aimed to determine region-specific variation and age- and gender-specific differences in BMAT and BMAT composition using WFI-mGRE, in healthy subjects.

Abbreviations: BMAT, bone marrow adipose tissue; S_{FF}, signal fat fraction; WFI, chemical shift encoding-based water–fat imaging; mGRE, multiple gradient echoes; rBMAT, regulated BMAT; cBMAT, constitutive BMAT; ^{1}H-MRS, single-voxel proton magnetic resonance spectroscopy; ROIs, regions of interest; CL, average fatty acid chain length; *ndb*, number of double bonds; *nmidb*, methylene-interrupted double bonds.

METHODS

Subjects

In this cross-sectional study, we quantified the bone marrow signal fat fraction in 40 healthy subjects within the spine (C3-L5), pelvis, femora, and tibia. All subjects were recruited as part of a different study (25) (trial nr. NTR5056). The main inclusion criterion was age >18 years, and subjects with a history of bone marrow disease were excluded. Subjects had no hematologic or metabolic disorders. One subject used vitamin D supplementation, and two subjects used oral contraceptives.

We included 26 male subjects and 14 female subjects. The mean age was 49 years for male subjects (range 22–75 years) and 50 years (range 29–71) for the female subjects (p = 0.84). Seven out of the 14 female subjects were postmenopausal. Subject characteristics are shown in **Table 1**. Male subjects were taller compared to female subjects (mean height: male 182 ± 8 cm, female 170 ± 7 cm; p < 0.001) and were heavier (mean weight: male 84 ± 13 kg; female 68 ± 12 kg; p < 0.001). BMI was not significantly different between male and female subjects (mean BMI male: 25.5 ± 0.6; female: 23.6 ± 0.5; p = 0.16).

TABLE 1 | Subject characteristics, mean ± SD.

	Male	Female
N	26	14
Age (years)	49 (range 22–75)	50 (range 29–71)
Postmenopausal		7 out of 14
Height (cm)	182 ± 8	170 ± 7
Weight (kg)	84 ± 14	68 ± 12
BMI (kg/m^2)	25.5 ± 3.4	23.6 ± 4.4
Hb	9.3 ± 0.6	8.3 ± 0.5

Scans were acquired between July 2014 and August 2015 at the Amsterdam University Medical Centers/University of Amsterdam. The local ethics committee of the Amsterdam University Medical Centers/University of Amsterdam approved the protocol, and all subjects gave their written informed consent. This study was carried out in compliance with the World Medical Association Declaration of Helsinki—Ethical Principles for Medical Research Involving Human Subjects.

Image Acquisition

From the previous study with trial number NTR5056, we used a coronal whole-body and a sagittal whole-spine data set. All images were acquired on a 1.5-T MRI (Siemens Avanto, Siemens AG, Erlangen, Germany). All patients were placed in the scanner in supine position. Both datasets consisted of magnitude and phase images, enabling complex valued analysis. Both datasets were acquired using a standard 2D multi-echo spoiled gradient echo sequence, with 12 echoes, TE = 0.99–16.5 ms and an echo spacing of 1.41 ms. Slice thickness was 7.5 mm, with a 7.5-mm gap. The flip angle was 20°, and the acquisition matrix was 256 × 96.

The whole-body data set was acquired with 8 to 9 stations of 15 to 21 slices, a repetition time of 301 ms, and a field of view of 250 × 500 mm. Acquisition time is 17.8 s per station (breath-hold for the thorax and abdominal stations). The spine data set was acquired with 3 to 5 stations of 15 slices, a repetition time of 333 ms, and a field of view of 280 × 280 mm. Acquisition time is 19.7 s per station.

Region of Interest

Regions of interest (ROIs) were always drawn within the data of one station, since phase information from different stations does not match. The fitted parameters from different ROIs were averaged when necessary. In the spine, usually one mid-sagittal ROI per vertebral body was drawn. For the pelvis, several ROIs in 3 slices where the pelvis bone marrow was manifestly visible, both right and left, were drawn. For both the femora and tibiae, right as well as left, three ROIs were drawn: the proximal epimetaphysis, the diaphysis, and the distal epimetaphysis, again in the image where the bone marrow was most clearly visible. Examples of the ROIs covering the spine, pelvis, femora, and tibiae are shown in **Supplemental Figure 1**.

Analysis of the ROIs

The multi-echo data were fitted to a fat–water signal function, based on the fat characterization model by (26).

$$S(TE) = e^{i(\varphi_0+\omega_0 TE)} \cdot S_0 \cdot \left\{ (1 - S_{FF}) \; e^{-TE/T_{2,W}^{*}} + S_{FF} \; e^{-TE/T_{2,f}^{*}} \sum_{n-1}^{9} e^{-i \; \omega_n TE} v_n(CL, dnb, nmidb) \right\}$$

The model includes nine fat peaks, each with its own frequency with respect to the water peak, ωn, and weighting factor, vn, which in its turn depends on the average fatty acid chain length (*CL*), the number of double bonds per fat molecule (*ndb*), and the number of direct double-bond neighbor pairs (methylene-interrupted double bonds, *nmidb*). The weighting factors were scaled so that their sum equaled one. It turned out that our data were not sufficient enough to fit all three parameters reliably, so we fixed the *CL* to 17.45, being the average chain length in human fat (20), thus leaving *ndb* and *nmidb* as free parameters to characterize the fat composition.

Further free parameters are as follows: $\varphi 0$, the excitation phase offset, $\omega 0$, the frequency contribution of $B0$ inhomogeneities, $S0$, the signal magnitude at t = 0, S_{FF}, the signal fat fraction, $T2,w^{*}$, the water relaxation time, and $T2,f^{*}$, the fat relaxation time, which is taken to be equal for all fat peaks. Our data set did not contain information to correct for differences in $T1$, which would require additional acquisitions, therefore measuring the signal fat fraction, rather than the actual proton density fat fraction. In the tibiae and femora, a pixel-by-pixel fit could be performed. In the spine and pelvis, we first estimated an averaged signal over the ROI. This estimation was done for the signal magnitude and phase separately. **Figure 1** shows an example of a dataset and the corresponding fit.

Statistical Analysis

The statistical analysis was performed with IBM SPSS Statistics for Windows (version 26; SPSS Inc., Chicago, IL, USA). Graphs were created using GraphPad Prism (Version 8.2.1 for Windows, GraphPad Software, La Jolla, CA, USA). The mean and standard deviation (reported as " ± SD") or the median and interquartile ranges (reported as "(IQR)") are reported, depending on the distribution. To compare male and female subject characteristics, we used Student's t-test or the Mann–Whitney U test, depending on the distribution of the data. Within-subject differences in BMAT distribution and unsaturation linear mixed models (LMM) were used. A covariance structure was chosen based on Akaike's information criterion (AIC) and Schwarz's Bayesian criterion (BIC). We used Pearson (r) and Spearman's (ρ) tests to determine correlations between variables depending on the distribution of the data. To estimate the effects of age, gender, and unsaturation (*ndb*) and their interactions on BMAT (fat fraction), multiple linear regression models were used. BMAT was included as the outcome variable, and the age and number of double bonds and their interactions were included as predictors.

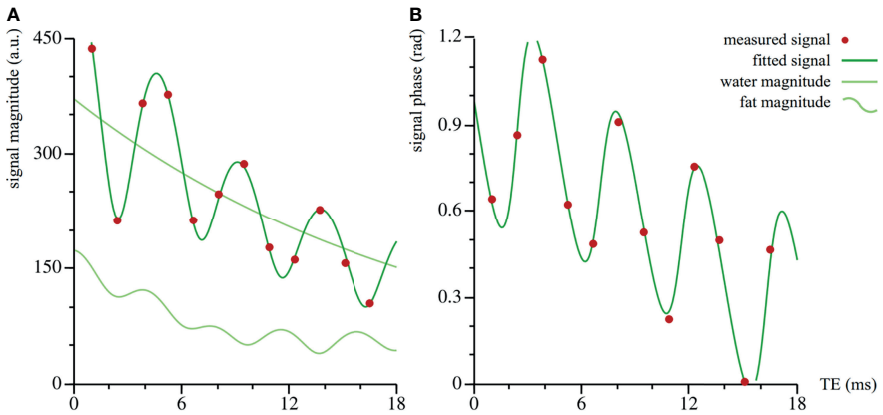

FIGURE 1 | Dataset and corresponding fit of vertebra Th11 of volunteer #20. The fit is performed on the complex valued data: the magnitude (arbitrary units) in **(A)**, the phase (radians) in **(B)**. The amplitude in the total signal magnitude is larger than in the fat component only, because of the interference of the fat and water signals.

In case assumptions were violated (normally distributed residuals, equal variances), the outcome variable was rank transformed. All statistical tests were two-sided, and a p-value of 0.05 was considered significant. For the *post-hoc* analysis of the LMM, a Bonferroni correction was applied, making $p < 0.008$ significant for the comparison between the spine, pelvis, femur, and tibia and $p < 0.016$ for the comparisons within the spine, femur, and tibia.

RESULTS

Distribution of Bone Marrow Adipose Tissue and Bone Marrow Fat Composition

When analyzing all subjects collectively, the bone marrow fat fraction increased from cranial to caudal, with the spine having the lowest fat fraction and the tibia the highest (spine 0.41 ± 0.09; pelvis 0.56 ± 0.1; femur 0.86 (0.08); tibia 0.91 (0.02) $p < 0.001$; **Figure 2A**). Similarly, within the spine the fat fraction increased from cranial to caudal (**Figure 3A**), with the cervical spine having a significantly lower fat fraction compared to the thoracic and lumbar spine (cervical spine 0.37 ± 0.1; thoracic spine 0.41 ± 0.08; lumbar spine 0.46 ± 0.01; $p < 0.001$). Within the femur, the fat fraction increased from proximal to distal (proximal 0.78 ± 0.09; diaphysis 0.86 (0.15); distal 0.93 ± 0.02; $p < 0.001$; **Figure 3B**), while within the tibia the fat fraction showed a small, but significant decrease from proximal to distal (proximal 0.92 ± 0.01; diaphysis 0.91 (0.02); distal 0.90 ± 0.01; $p < 0.001$; **Figure 3C**). Throughout our data, the resulting fitted values of methylene-interrupted double bonds *(nmidb)* were close to zero. Consequently, we cannot draw any conclusions from this parameter, and we only present the values for *ndb* as a measure for bone marrow fat unsaturation. Unsaturation was highest in the pelvis, second highest in the spine, and lowest in the tibia (spine 2.71 ± 0.35; pelvis 2.82 (0.56); femur 2.22 ± 0.14; tibia 2.03 ± 0.16; $p < 0.001$; **Figure 2B**). Unsaturation was not significantly different when comparing the cervical spine, the thoracic spine, and the lumbar spine (cervical spine 2.89 ± 1.04; thoracic spine 2.74 ± 0.50; lumbar spine 2.56 ± 0.53, $p = 0.13$); **Figure 3D**). Within both the femur and the tibia, unsaturation was highest within the diaphysis (femur: proximal 2.16 ± 0.19; diaphysis 2.31 ± 0.13; distal 2.2 ± 0.15; $p < 0.001$; **Figure 3E** and

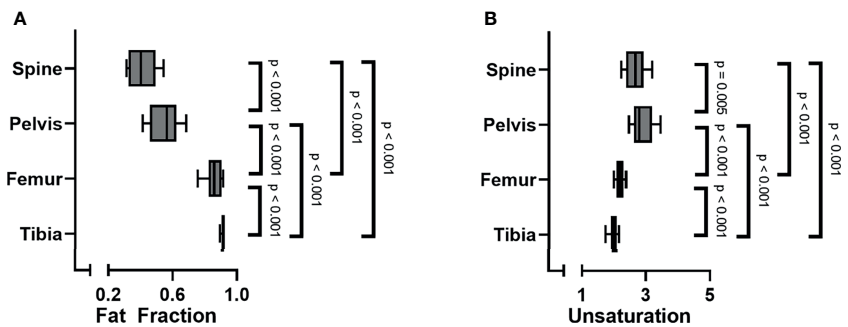

FIGURE 2 | **(A)** Bone marrow fat fraction increased from cranial to caudal (linear mixed model (LMM): $p < 0.001$). **(B)** Unsaturation (number of double bonds, *ndb*) was highest within the pelvis, followed by the spine, and lowest within the tibia (LMM: $p < 0.001$).

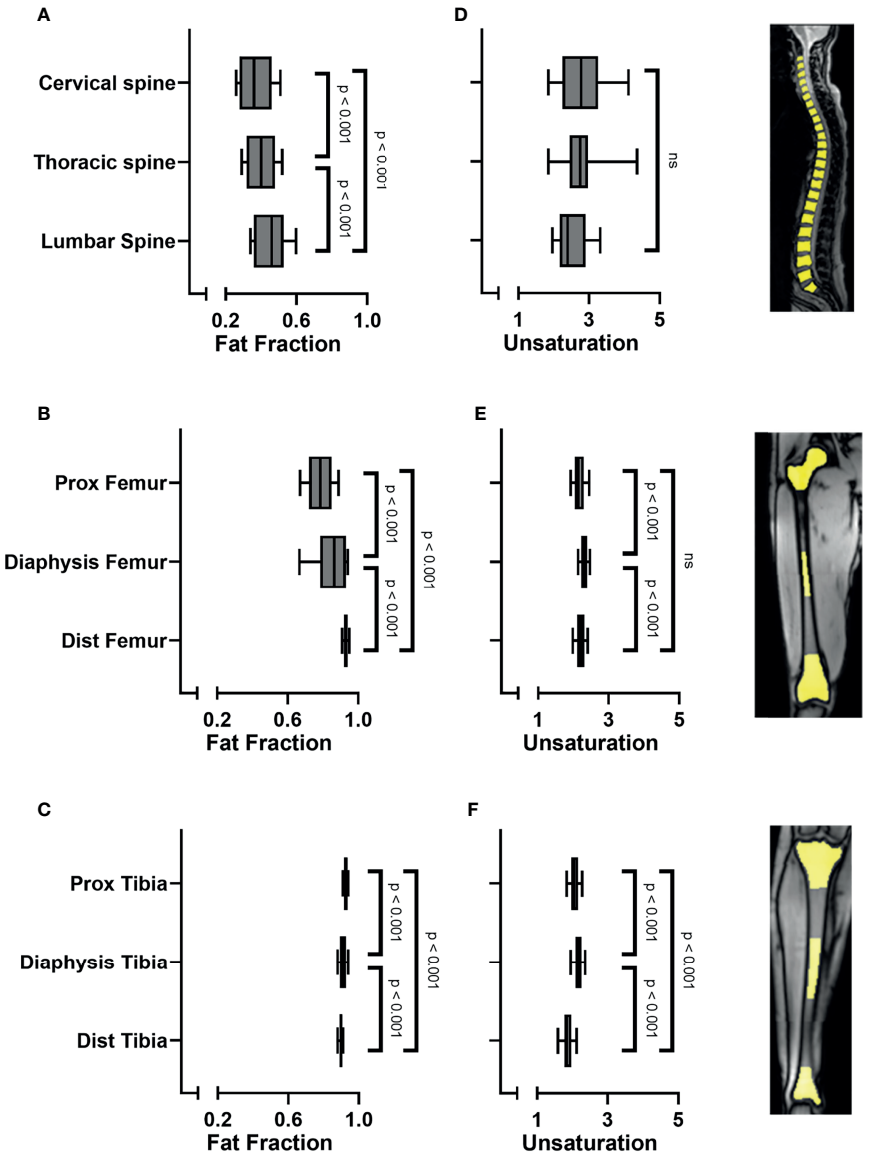

FIGURE 3 | **(A)** Bone marrow fat fraction increased from cranial to caudal within the spine (linear mixed model (LMM): $p < 0.001$). **(B)** Fat fraction increased in the femur from proximal to distal (LMM: $p < 0.001$). **(C)** Fat fraction decreased in the tibia from proximal to distal (LMM: $p < 0.001$). **(D)** Unsaturation (number of double bonds, *ndb*) was similar when comparing the cervical spine, thoracic spine, and the lumbar spine (LMM: $p = 0.09$; ns). **(E)** Unsaturation was highest within the diaphysis of the femur ($p < 0.001$) and **(F)** within the diaphysis of the tibia (LMM: $p < 0.001$), compared to the proximal and distal sites. Images on the right side show representative images of ROI placement in the vertebral bodies of the spine, in the proximal epimetaphysis, the diaphysis and the distal epimetaphysis of the femora and tibiae. ns, non-significant.

tibia: proximal 2.06 ± 0.16; diaphysis 2.17 ± 0.15; distal 1.85 ± 0.20; $p < 0.001$; **Figure 3F**) . No significant correlations were found between unsaturation and age, neither in female nor in male subjects; results are shown in **Supplemental Figure 2**.

Age- and Gender-Related Differences in Bone Marrow Adipose Tissue

When analyzing all subjects collectively, the bone marrow fat fraction increased with age in the spine and pelvis (spine: $r = 0.64$ and $p < 0.001$; pelvis: $r = 0.56$ and $p < 0.001$; data not shown). Within the extremities, the fat fraction of the femur tended to correlate with age, based on a positive correlation between the fat fraction of the proximal femur and age (femur: $\rho = 0.27$, $p = 0.09$; proximal femur: $r = 0.41$, $p = 0.01$; tibia $\rho = -0.23$, $p = 0.16$; data not shown). Within female subjects, bone marrow fat fraction and age were positively correlated within the spine, pelvis, femur, and proximal femur (spine: $\rho = 0.88$, $p < 0.001$; pelvis: ρ 0.87, $p < 0.001$; femur: $\rho = 0.63$, $p = 0.02$; proximal femur: $\rho = 0.74$, $p = 0.002$; **Figures 4A–D**), while in male subjects fat fraction and age were only correlated within the spine, and not within the pelvis,

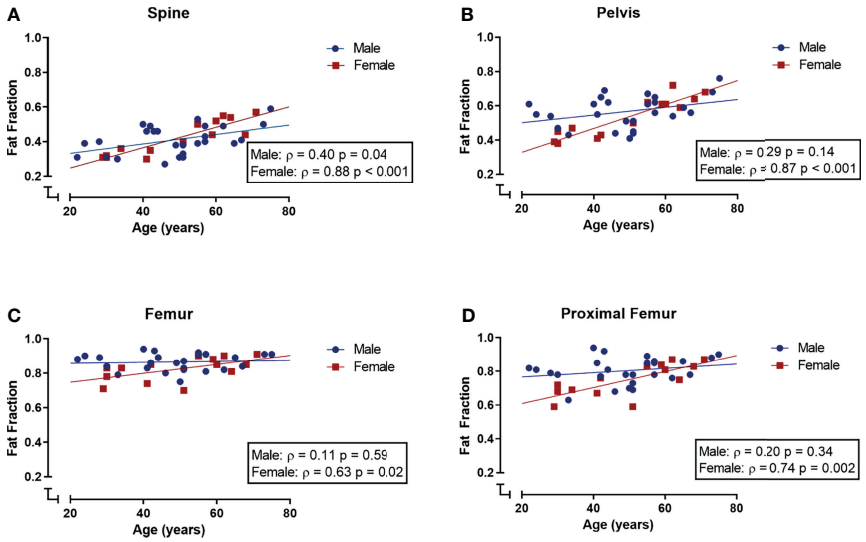

FIGURE 4 | Correlations (Spearman's rank correlation coefficient) between age and bone marrow fat fraction (S_{FF}) in male (blue) and female (red) subjects. **(A)** Spinal fat fraction and age were positively correlated in both male and female subjects. **(B–D)** Within the pelvis, femur, and proximal femur fat fraction and age were positively correlated in female subjects but not in male subjects.

femur, proximal femur, and tibia (spine: ρ = 0.40, p = 0.04; pelvis: ρ = 0.29, p = 0.14; femur: ρ = 0.11, p = 0.59; proximal femur: ρ = 0.20, p = 0.34 (**Figures 4A–D**); tibia ρ = -0.29, p = 0.16; data not shown). Multiple linear regression models were applied to estimate the effect of age, gender, and their interaction on the bone marrow fat fraction. Within the spine, only age was a significant predictor of fat fraction ($p < 0.001$, $R^2 = 0.40$). Within the pelvis, age, gender, and their interaction term were significant predictors of the fat fraction (age: $p < 0.001$; gender p = 0.01; age*gender p = 0.02; $R^2 = 0.41$). Within the femur, only gender was a significant predictor of the fat fraction (p = 0.025; R^2 0.19); no significant interaction between age and gender was found within the total femur. Within the proximal femur, age, gender, and the interaction term were significant predictors of the fat fraction (age: p = 0.001; gender p = 0.01; age*gender p = 0.05; $R^2 = 0.34$). Regression lines are shown in **Figure 4**.

The Association Between BMAT Amount and BMAT Composition

Despite age and gender being significant predictors of fat fraction, we previously showed that there were no significant correlations between age, gender, and unsaturation (Section 3.1; **Supplemental Figure 2**). Therefore, we decided to combine our subjects to evaluate bone marrow fat fractions and unsaturation. Within the spine, there was a negative correlation between bone marrow fat fraction and unsaturation (r = -0.40, p = 0.01; **Figure 5A**). While in the distal femur, the total tibia and in the proximal and distal tibia fat fraction and unsaturation were positively correlated (distal femur: r = 0.42, p = 0.01, **Figure 5B**; total tibia: ρ = 0.52, p = 0.05, data not shown; proximal tibia: r = 0.47 p = 0.002, **Figure 5C**; distal tibia: r = 0.35, p = 0.03 **Figure 5D**). No correlation between fat fraction and unsaturation was found at the other skeletal sites (pelvis: r = 0.16, p = 0.31; femur: ρ = -0.26 p = 0.37; proximal femur: -0.01, p = 0.95; diaphysis of the femur: ρ -0.16, p = 0.58; and the diaphysis of the tibia: r = 0.13, p = 0.43; data not shown).

A multiple linear regression model was used to predict the outcome variable (fat fraction/S_{FF}) based on unsaturation, age, and gender and their interaction terms. Within the spine, age and unsaturation were significant predictors of the fat fraction (age: $p < 0.001$; *ndb* p = 0.02; R^2 of 0.50); gender and interaction terms were not significant predictors for the fat fraction in the spine. In the distal femur, the total tibia, and the proximal and distal tibia, only unsaturation was a significant predictor of the fat fraction while gender, age, or interaction terms were not (*ndb*: distal femur: p = 0.005, R^2 0.23; total tibia: p = 0.03, R^2 0.19; proximal tibia: p = 0.002, R^2 0.24; distal tibia: p = 0.02, R^2 0.18).

DISCUSSION

To our knowledge, we are the first to report both BMAT distribution and BMAT unsaturation, and the association between BMAT and BMAT unsaturation, quantified simultaneously with WFI-mGRE, in a large part of the skeleton in a group of healthy subjects.

We show that BMAT increases from spine to tibia, from the cervical to the lumbar spine, and from proximal to distal in femora, while we show a small but significant decrease within tibia. These patterns are consistent with literature (13–15, 27–31). Furthermore, we confirm differences in the age-associated increase in BMAT between male and female subjects (15, 29, 31). BMAT within the femur and tibia does not increase with age in male subjects, while in female subjects femoral BMAT does

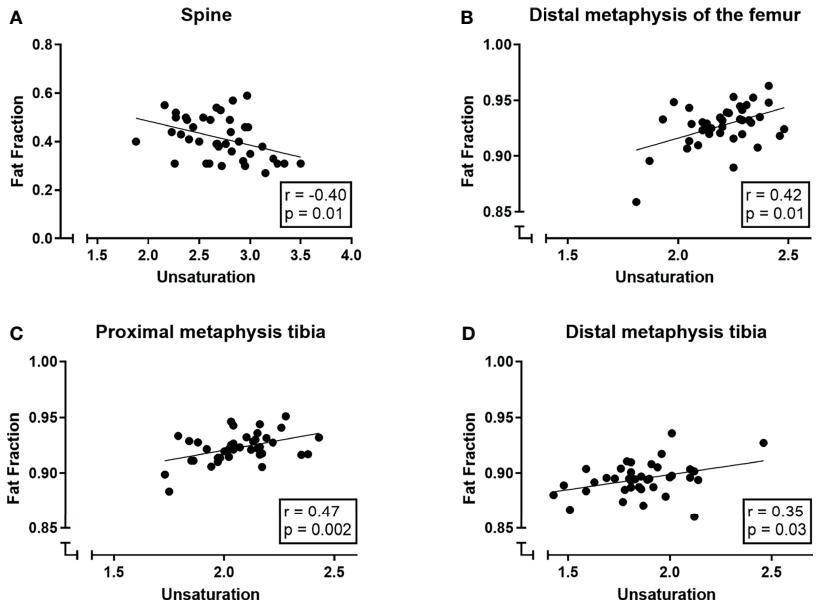

FIGURE 5 | Correlations (Pearson correlation coefficient) between bone marrow signal fat fractions (S_{FF}) and unsaturation (number of double bonds *ndb*) in **(A)** the spine, **(B)** the distal femur, **(C)** the proximal tibia and **(D)** the distal tibia.

increase with age. This could indicate that BMAT in the axial and appendicular skeleton is differently regulated in female and male subjects and suggests a role for sex steroids, as it is known that exogenous estradiol can decrease BMAT (32, 33), and low endogenous testosterone is associated with high BMAT in older men (34). Changes in sex steroids with aging, and especially during menopause in female subjects, could explain these gender differences observed in femoral BMAT. Another explanation for the gender difference at a younger age could be increased hematopoietic demands in premenopausal women due to blood loss during menstrual periods, as BMAT is also potentially linked to erythropoiesis (35).

We show higher BMAT unsaturation within the axial skeleton compared to the appendicular skeleton. Our results are inconsistent with animal studies (18, 36), showing higher unsaturation in areas of yellow bone marrow compared to red bone marrow. However, few studies have quantified BMAT unsaturation in both the axial and appendicular skeleton in human subjects. Our results are consistent with a small study by Badr and coworkers which showed higher unsaturation within the pelvis compared to the proximal femur in young female subjects, quantified by ^{1}H-MRS (37). This could imply that BMAT unsaturation in areas red bone marrow in the axial skeleton and yellow bone marrow of the appendicular skeleton might differ between human subjects and these animal models. We showed that BMAT unsaturation was higher within the femur compared to the tibia and that BMAT unsaturation was higher within the diaphysis of the tibia and femur compared to the proximal or distal metaphysis, but we found no gender- or age-associated differences in BMAT unsaturation. Our results are comparable to a study by Bao who reported higher BMAT unsaturation within the distal femur compared to the proximal tibia, and no differences in BMAT unsaturation between young male and female subjects (38). Our results partially differ from the study by Scheller and coworkers in 5 young female subjects, as they report higher BMAT unsaturation, measured using ^{1}H-MRS, within the tibia compared to the femur. However, unsaturation was higher within the diaphysis of the tibia and femur, although not significantly in the study by Scheller and coworkers. The difference could be due to the sample size, or age and gender differences, as Scheller and coworkers included only 5 young, female subjects, and we included both male and female subjects with a larger age range (18). Other studies that quantified BMAT unsaturation in proximal and distal skeletal sites in human subjects show conflicting results, possibly due to small sample sizes, and differences in age and gender of the subject (39–41). To the best of our knowledge, there are no other studies quantifying BMAT composition in both the axial and appendicular skeleton in human subjects. Due to heterogeneity in used imaging techniques, in scanner vendors, and in study populations, results from different studies are hard to compare. The negative correlation we found between BMAT and unsaturation in the spine, consistent with a previous study (42), opposed to the positive correlation between BMAT and unsaturation we found within the appendicular skeleton (distal femur, and proximal and distal tibia), could support the existence of different types of BMAT in the axial versus appendicular skeleton, also referred to as regulated and constitutive BMAT, as reviewed by Craft et al. (43), with a distinct fatty acid composition and with different effects on bone metabolism (44–48) and on skeletal

metastasis. Another potential explanation for the difference in unsaturation between the axial and appendicular skeleton in healthy subjects could be glucose metabolism as a recent study by Suchacki and coworkers showed that BMAT glucose uptake was higher within the axial skeleton compared to BMAT glucose uptake within long bones (49).

Patients with osteoporosis and subjects with fractures have lower unsaturation and higher saturation of their BMAT compared to healthy subjects or subjects without fractures (10, 42). *In vitro* research has shown that saturated fatty acids can increase osteoclast differentiation, decrease osteoblastic differentiation, and induce a pro-inflammatory response, while unsaturated fatty acids could prevent these effects (50). Furthermore, BMAT could serve as an energy depot for bone metabolism and bone metastasis. Although most tumors depend on glycolysis for their energy supply, β-oxidation of fatty acids can serve as a main source of energy for some types of cancers (9). Tumor cells can stimulate lipolysis and the secretion of free fatty acids by bone marrow adipocytes (51) and overexpress lipid transporters to increase lipid uptake (52–54). Furthermore, multiple enzymes of the desaturase pathway are overexpressed in tumor cells of metastatic prostate cancer and multiple myeloma; however, in the hypoxic environment of the bone marrow the function of the enzyme stearoyl-CoA desaturase is compromised and therefore the synthesis of monounsaturated fatty acids. Under these hypoxic conditions, tumor cells can switch to collecting unsaturated fatty acids from the microenvironment (9), and it could be proposed that, although highly speculative, the increased unsaturated fatty acids we show within the spine and pelvis compared to the femora and tibia might be a part of the explanation why skeletal metastases are preferentially located within the axial skeleton (55). Furthermore, it could be postulated, again highly speculatively, that the gender-associated differences in BMAT within the spine, pelvis, and proximal femur, i.e., areas containing red bone marrow, could be part of the explanation for the observation that female patients are less likely to have skeletal metastasis (56) and more likely to develop osteoporosis. Future research on the interaction between BMAT and bone metabolism or skeletal metastasis should take these differences between the axial and appendicular skeleton into consideration, as results on BMAT acquired from the iliac crest might provide different results compared to BMAT acquired from the proximal femur.

Our study has limitations. First, we did not compare the WFI-mGRE to a reference method, like gas chromatography or ^{1}H-MRS. As subjects were included as part of a different study protocol, data of the gradient echo MRI images were analyzed retrospectively. Nevertheless, previous studies have demonstrated good agreement between WFI-mGRE and ^{1}H-MRS (20, 22). A second limitation is that we measure the bone marrow fat signal fraction instead of the corrected proton density fat fraction (PDFF). Although we did use a multipeak fat spectrum for the fit and corrected for T2* decay, we did not correct for T1 bias. The relatively short T1 of fat compared to water could cause higher fat fractions in areas where fat is less than water or lower fat fractions when fat is higher than water (57). Therefore, our results within the appendicular skeleton, where fat is much higher than water, likely underestimate the actual PDFF. Fat and water fractions within the spine and pelvis are more balanced, i.e., fat fractions closer to 50%, causing less T1 bias. Therefore, our results of the spine and pelvis are more comparable to the actual PDFF. T1 bias increases with larger flip angles. As we used a flip angle of 20° in our retrospective analysis, T1 bias could be further reduced by using a smaller flip angle in future studies. Last, our sample size is relatively small; therefore, our subanalyses are likely subject to power issues. For example, only 14, both premenopausal and postmenopausal, women were included, which potentially influenced our results. Due to the retrospective nature of our study, it was not powered for these analyses. Therefore, future research should reproduce our data.

To conclude, we show that off-shelf GRE sequences can be used to quantify BMAT and BMAT composition simultaneously, in large parts of the skeleton. We describe the distribution of BMAT and BMAT unsaturation within a group of healthy subjects and report age- and gender-associated differences. Contradicting previous animal studies, we show higher unsaturation within the axial skeleton (i.e., red marrow) compared to the appendicular skeleton (i.e., yellow marrow) and we show opposing correlations between BMAT and BMAT unsaturation when comparing the spine to the femur and tibia; this could support the existence of two distinct types of BMAT within the axial versus appendicular skeleton, potentially with different interactions with its environment. Our results supply a useful ground for future research on the interaction between BMAT and different (patho)physiological processes like bone metabolism and skeletal metastasis.

DATA AVAILABILITY STATEMENT

The raw data supporting the conclusions of this article will be made available by the authors, without undue reservation.

ETHICS STATEMENT

The studies involving human participants were reviewed and approved by the Ethics Committee of the Amsterdam University Medical Centers/University of Amsterdam. The patients/participants provided their written informed consent to participate in this study.

AUTHOR CONTRIBUTIONS

Study design: KB, MR, CH, PB, MM. Study conduct: MR, EA, and CH. Data collection: MR, EA. Data analysis: KB, EA, and AN. Data interpretation: KB, EA, AN, NB, PB, MH, and MM. Drafting of the manuscript: KB, EA and MM. All authors critically revised the manuscript and approved the final version of the manuscript to be submitted.

FUNDING

KMB is supported by an Alliance grant provided by Amsterdam University Medical Centers/VU University/University of Amsterdam (2013–01).

SUPPLEMENTARY MATERIAL

The Supplementary Material for this article can be found online at: https://www.frontiersin.org/articles/10.3389/fendo.2022.815835/full#supplementary-material

REFERENCES

1. Griffith JF, Yeung DKW, Antonio GE, Wong SYS, Kwok TCY, Woo J, et al. Vertebral Marrow Fat Content and Diffusion and Perfusion Indexes in Women With Varying Bone Density: MR Evaluation. *Radiology* (2006) 241:831–8. doi: 10.1148/radiol.2413051858
2. Justesen J, Stenderup K, Ebbesen EN, Mosekilde L, Steiniche T, Kassem M. Adipocyte Tissue Volume in Bone Marrow is Increased With Aging and in Patients With Osteoporosis. *Biogerontology* (2001) 2:165–71. doi: 10.1023/A:1011513223894
3. Meunier P, Aaron J, Edouard C, Vignon G. Osteoporosis and the Replacement of Cell Populations of the Marrow by Adipose Tissue. A Quantitative Study of 84 Iliac Bone Biopsies. *Clin ortho related Res* (1971) 80:147–54. doi: 10.1097/00003086-197110000-00021
4. Rosen BR, Fleming DM, Kushner DC, Zaner KS, Buxton RB, Bennet WP, et al. Hematologic Bone Marrow Disorders: Quantitative Chemical Shift MR Imaging. *Radiology* (1988) 169:799–804. doi: 10.1148/radiology.169.3.3187003
5. Li Z, Hardij J, Bagchi DP, Scheller EL, MacDougald OA. Development, Regulation, Metabolism and Function of Bone Marrow Adipose Tissues. *Bone* (2018) 110:134-40. doi: 10.1016/j.bone.2018.01.008
6. Tencerova M, Ferencakova M, Kassem M. Bone Marrow Adipose Tissue: Role in Bone Remodeling and Energy Metabolism. *Best Pract Res Clin Endocrinol Metab* (2021) 35:1–15. doi: 10.1016/j.beem.2021.101545
7. Morris E v., Edwards CM. Bone Marrow Adipose Tissue: A New Player in Cancer Metastasis to Bone. *Front Endocrinol* (2016) 7:90. doi: 10.3389/fendo.2016.00090
8. Cha YJ, Koo JS. Roles of Omental and Bone Marrow Adipocytes in Tumor Biology. *Adipocyte* (2019) 8:304–17. doi: 10.1080/21623945.2019.1643189
9. Diedrich JD, Herroon MK, Rajagurubandara E, Podgorski I. The Lipid Side of Bone Marrow Adipocytes: How Tumor Cells Adapt and Survive in Bone. *Curr Osteo Rep* (2018) 16:443–57. doi: 10.1007/s11914-018-0453-9
10. Patsch JM, Li X, Baum T, Yap SP, Karampinos DC, Schwartz A v, et al. Bone Marrow Fat Composition as a Novel Imaging Biomarker in Postmenopausal Women With Prevalent Fragility Fractures. *J Bone Min Res* (2013) 28:1721–8. doi: 10.1002/jbmr.1950
11. Piney A. The Anatomy of the Bone Marrow: With Special Reference to the Distribution of the Red Marrow. *Br J Med* (1922) 2:792–5.
12. Cristy M. Active Bone Marrow Distribution as a Function of Age in Humans. *Phys Med Biol* (1981) 26:389–400. doi: 10.1088/0031-9155/26/3/003
13. Kugel H, Jung C, Schulte O, Heindel W. Age- and Sex-Specific Differences in the 1H-Spectrum of Vertebral Bone Marrow. *J Magn Reson Imag: JMRI* (2001) 13:263–8. doi: 10.1002/1522-2586(200102)13:2<263::AID-JMRI1038>3.0.CO;2-M
14. Ishijima H, Ishizaka H, Horikoshi H, Sakurai M. Water Fraction of Lumbar Vertebral Bone Marrow Estimated From Chemical Shift Misregistration on MR Imaging: Normal Variations With Age and Sex. *AJR Am J Roentgenol* (1996) 167:355–8. doi: 10.2214/ajr.167.2.8686603
15. Griffith JF, Yeung DKW, Ma HT, Leung JCS, Kwok TCY, Leung PC. Bone Marrow Fat Content in the Elderly: A Reversal of Sex Difference Seen in Younger Subjects. *J Magnet Reson Imaging* (2012) 36:225–30. doi: 10.1002/jmri.23619
16. van Dussen L, Akkerman EM, Hollak CEM, Nederveen AJ, Maas M. Evaluation of an Imaging Biomarker, Dixon Quantitative Chemical Shift Imaging, in Gaucher Disease: Lessons Learned. *J Inherit Metab Dis* (2014) 37:1003–11. doi: 10.1007/s10545-014-9726-3
17. Aoki T, Yamaguchi S, Kinoshita S, Hayashida Y, Korogi Y. Quantification of Bone Marrow Fat Content Using Iterative Decomposition of Water and Fat With Echo Asymmetry and Least-Squares Estimation (IDEAL): Reproducibility, Site Variation and Correlation With Age and Menopause. *Br J Radiol* (2016) 89:20150538. doi: 10.1259/bjr.20150538
18. Scheller EL, Doucette CR, Learman BS, Cawthorn WP, Khandaker S, Schell B, et al. Region-Specific Variation in the Properties of Skeletal Adipocytes Reveals Regulated and Constitutive Marrow Adipose Tissues. *Nat Commun* (2015) 6:7808. doi: 10.1038/ncomms8808
19. Tratwal J, Labella R, Bravenboer N, Kerckhofs G, Douni E, Scheller EL, et al. Reporting Guidelines, Review of Methodological Standards, and Challenges Toward Harmonization in Bone Marrow Adiposity Research. Report of the Methodologies Working Group of the International Bone Marrow Adiposity Society. *Front Endocrinol* (2020) 11:65. doi: 10.3389/fendo.2020.00065
20. Leporq B, Lambert SA, Ronot M, Vilgrain V, van Beers BE. Quantification of the Triglyceride Fatty Acid Composition With 3.0 T MRI. *NMR Biomed* (2014) 27:1211–21. doi: 10.1002/nbm.3175
21. Martel D, Leporq B, Bruno M, Regatte RR, Honig S, Chang G. Chemical Shift-Encoded MRI for Assessment of Bone Marrow Adipose Tissue Fat Composition: Pilot Study in Premenopausal Versus Postmenopausal Women. *Magnet Reson Imag* (2018) 53:148–55. doi: 10.1016/j.mri.2018.07.001
22. Martel D, Leporq B, Saxena A, Belmont HM, Turyan G, Honig S, et al. 3T Chemical Shift-Encoded MRI: Detection of Altered Proximal Femur Marrow Adipose Tissue Composition in Glucocorticoid Users and Validation With Magnetic Resonance Spectroscopy. *J Magn Reson Imag: JMRI* (2019) 50:490–6. doi: 10.1002/jmri.26586
23. Leporq B, Lambert SA, Ronot M, Boucenna I, Colinart P, Cauchy F, et al. Hepatic Fat Fraction and Visceral Adipose Tissue Fatty Acid Composition in Mice: Quantification With 7.0T MRI. *Magnet Reson Med* (2016) 76:510–8. doi: 10.1002/mrm.25895
24. Karampinos DC, Melkus G, Baum T, Bauer JS, Rummeny EJ, Krug R. Bone Marrow Fat Quantification in the Presence of Trabecular Bone: Initial Comparison Between Water-Fat Imaging and Single-Voxel MRS. *Magnet Reson Med* (2014) 71:1158–65. doi: 10.1002/mrm.24775
25. Regenboog M, Bohte AE, Akkerman EM, Stoker J, Hollak CEM. Iron Storage in Liver, Bone Marrow and Splenic Gaucheroma Reflects Residual Disease in Type 1 Gaucher Disease Patients on Treatment. *Br J Haematol* (2017) 179(4):635–47. doi: 10.1111/bjh.14915
26. Hamilton G, Yokoo T, Bydder M, Cruite I, Schroeder ME, Sirlin CB, et al. *In Vivo* Characterization of the Liver Fat ^{1}H MR Spectrum. *NMR Biomed* (2011) 24:784–90. doi: 10.1002/nbm.1622
27. Arentsen L, Hansen KE, Yagi M, Takahashi Y, Shanley R, McArthur A, et al. Use of Dual-Energy Computed Tomography to Measure Skeletal-Wide Marrow Composition and Cancellous Bone Mineral Density. *J Bone Min Metab* (2017) 35:428–36. doi: 10.1007/s00774-016-0796-1
28. Kühn J-P, Hernando D, Meffert PJ, Reeder S, Hosten N, Laqua R, et al. Proton-Density Fat Fraction and Simultaneous R2* Estimation as an MRI Tool for Assessment of Osteoporosis. *Eur Radiol* (2013) 23:3432–9. doi: 10.1007/s00330-013-2950-7
29. Baum T, Yap SP, Dieckmeyer M, Ruschke S, Eggers H, Kooijman H, et al. Assessment of Whole Spine Vertebral Bone Marrow Fat Using Chemical Shift-Encoding Based Water-Fat MRI. *J Magnet Reson Imaging* (2015) 42:1018–23. doi: 10.1002/jmri.24854
30. Dieckmeyer M, Ruschke S, Cordes C, Yap SP, Kooijman H, Hauner H, et al. The Need for T2 Correction on MRS-Based Vertebral Bone Marrow Fat Quantification: Implications for Bone Marrow Fat Fraction Age Dependence. *NMR Biomed* (2015) 28:432–9. doi: 10.1002/nbm.3267
31. Baum T, Rohrmeier A, Syvärі J, Diefenbach MN, Franz D, Dieckmeyer M, et al. Anatomical Variation of Age-Related Changes in Vertebral Bone Marrow Composition Using Chemical Shift Encoding-Based Water-Fat

Magnetic Resonance Imaging. *Front Endocrinol* (2018) 9:141. doi: 10.3389/fendo.2018.00141
32. Syed FA, Oursler MJ, Hefferanm TE, Peterson JM, Riggs BL, Khosla S. Effects of Estrogen Therapy on Bone Marrow Adipocytes in Postmenopausal Osteoporotic Women. *Osteo Int* (2008) 19:1323–30. doi: 10.1007/s00198-008-0574-6
33. Limonard EJ, Veldhuis-Vlug AG, van Dussen L, Runge JH, Tanck MW, Endert E, et al. Short-Term Effect of Estrogen on Human Bone Marrow Fat. *J Bone Min Res* (2015) 30:2058–66. doi: 10.1002/jbmr.2557
34. Mistry SD, Woods GN, Sigurdsson S, Ewing SK, Hue TF, Eiriksdottir G, et al. Sex Hormones Are Negatively Associated With Vertebral Bone Marrow Fat. *Bone* (2018) 108:20–4. doi: 10.1016/j.bone.2017.12.009
35. Wang H, Leng Y, Gong Y. Bone Marrow Fat and Hematopoiesis. *Front Endocrinol* (2018) 9:694. doi: 10.3389/fendo.2018.00694
36. Tavassoli M. Marrow Adipose Cells. Histochemical Identification of Labile and Stable Components. *Arch Pathol Lab Med* (1976) 100:16–8.
37. Badr S, Legroux-Gérot I, Vignau J, Chauveau C, Ruschke S, Karampinos DC, et al. Comparison of Regional Bone Marrow Adiposity Characteristics at the Hip of Underweight and Weight-Recovered Women With Anorexia Nervosa Using Magnetic Resonance Spectroscopy. *Bone* (2019) 127:135–45. doi: 10.1016/j.bone.2019.05.033
38. Bao J, Zhuang Y, Chen Z, Cheng J, Zhong J. Detection of Fatty Acid Composition of Trabecular Bone Marrow by Localized iDQC MRS at 3 T: A Pilot Study in Healthy Volunteers. *Magnet Reson Imag* (2021) 77:28–35. doi: 10.1016/j.mri.2020.09.007
39. Lundbom J, Bierwagen A, Bodis K, Apostolopoulou M, Szendroedi J, Müssig K, et al. 1h-MRS of Femoral Red and Yellow Bone Marrow Fat Composition and Water Content in Healthy Young Men and Women at 3 T. *Magma (New York NY)* (2019) 32:591–7. doi: 10.1007/s10334-019-00750-6
40. Yu EW, Greenblatt L, Eajazi A, Torriani M, Bredella MA. Marrow Adipose Tissue Composition in Adults With Morbid Obesity. *Bone* (2017) 97:38–42. doi: 10.1016/j.bone.2016.12.018
41. Wang J, Yi P, Huang Y, Yu Q, Mei Y, Chen J, et al. Quantitative Evaluation of Bone Marrow Fat Content and Unsaturated Fatty Index in Young Male Soccer Players Using Proton Magnetic Resonance Spectroscopy (1H-MRS): A Preliminary Study. *Quanti Imag Med Surg* (2021) 11:4275–86. doi: 10.21037/qims-21-64
42. Yeung DKW, Griffith JF, Antonio GE, Lee FKH, Woo J, Leung PC. Osteoporosis Is Associated With Increased Marrow Fat Content and Decreased Marrow Fat Unsaturation: A Proton MR Spectroscopy Study. *J Magnet Reson Imag* (2005) 22:279–85. doi: 10.1002/jmri.20367
43. Craft CS, Li Z, MacDougald OA, Scheller EL. Molecular Differences Between Subtypes of Bone Marrow Adipocytes. *Curr Mol Biol Rep* (2018) 4:16–23. doi: 10.1007/s40610-018-0087-9
44. Griffith JF, Yeung DKW, Antonio GE, Lee FKH, Hong AWL, Wong SYS, et al. Vertebral Bone Mineral Density, Marrow Perfusion, and Fat Content in Healthy Men and Men With Osteoporosis: Dynamic Contrast-Enhanced MR Imaging and MR Spectroscopy. *Radiology* (2005) 236:945–51. doi: 10.1148/radiol.2363041425
45. Maurin AC, Chavassieux PM, Vericel E, Meunier PJ. Role of Polyunsaturated Fatty Acids in the Inhibitory Effect of Human Adipocytes on Osteoblastic Proliferation. *Bone* (2002) 31:260–6. doi: 10.1016/S8756-3282(02)00805-0
46. Elbaz A, Wu X, Rivas D, Gimble JM, Duque G. Inhibition of Fatty Acid Biosynthesis Prevents Adipocyte Lipotoxicity on Human Osteoblasts *In Vitro*. *J Cell Mol Med* (2010) 14:982–91. doi: 10.1111/j.1582-4934.2009.00751.x
47. Kelly KA, Tanaka S, Baron R, Gimble JM. Murine Bone Marrow Stromally Derived BMS2 Adipocytes Support Differentiation and Function of Osteoclast-Like Cells *In Vitro*. *Endocrinology* (1998) 139:2092–101. doi: 10.1210/endo.139.4.5915
48. Bao M, Zhang K, Wei Y, Hua W, Gao Y, Li X, et al. Therapeutic Potentials and Modulatory Mechanisms of Fatty Acids in Bone. *Cell Prolif* (2020) 53:1–28. doi: 10.1111/cpr.12735
49. Suchacki KJ, Tavares AAS, Mattiucci D, Scheller EL, Papanastasiou G, Gray C, et al. Bone Marrow Adipose Tissue Is a Unique Adipose Subtype With Distinct Roles in Glucose Homeostasis. *Nat Commun* (2020) 11:3097. doi: 10.1038/s41467-020-16878-2
50. Pino AM, Rodríguez JP. Is Fatty Acid Composition of Human Bone Marrow Significant to Bone Health? *Bone* (2019) 118:53–61. doi: 10.1016/j.bone.2017.12.014
51. Diedrich JD, Rajagurubandara E, Herroon MK, Mahapatra G, Hüttemann M, Podgorski I. Bone Marrow Adipocytes Promote the Warburg Phenotype in Metastatic Prostate Tumors *via* HIF-1α Activation. *Oncotarget* (2016) 7:64854–77. doi: 10.18632/oncotarget.11712
52. Shafat MS, Oellerich T, Mohr S, Robinson SD, Edwards DR, Marlein CR, et al. Leukemic Blasts Program Bone Marrow Adipocytes to Generate a Protumoral Microenvironment. *Blood* (2017) 129:1320–32. doi: 10.1182/blood-2016-08-734798
53. Herroon MK, Rajagurubandara E, Hardaway AL, Powell K, Turchick A, Feldmann D, et al. Bone Marrow Adipocytes Promote Tumor Growth in Bone *via* FABP4-Dependent Mechanisms. *Oncotarget* (2013) 4:2108–23. doi: 10.18632/oncotarget.1482
54. Ladanyi A, Mukherjee A, Kenny HA, Johnson A, Mitra AK, Sundaresan S, et al. Adipocyte-Induced CD36 Expression Drives Ovarian Cancer Progression and Metastasis. *Oncogene* (2018) 37:2285–301. doi: 10.1038/s41388-017-0093-z
55. Kakhki VRD, Anvari K, Sadeghi R, Mahmoudian A-S, Torabian-Kakhki M. Pattern and Distribution of Bone Metastases in Common Malignant Tumors. *Nucl Med Rev Cent East Europe* (2013) 16:66–9. doi: 10.5603/NMR.2013.0037
56. Ma W, Peltzer K, Qi L, Xu G, Liu Z, Wang J, et al. Female Sex is Associated With a Lower Risk of Bone Metastases and Favourable Prognosis in non-Sex-Specific Cancers. *BMC Cancer* (2019) 19:1001. doi: 10.1186/s12885-019-6168-1
57. Hussain HK, Chenevert TL, Londy FJ, Gulani V, Swanson SD, McKenna BJ, et al. Hepatic Fat Fraction: MR Imaging for Quantitative Measurement and Display—Early Experience. *Radiology* (2005) 237:1048–55. doi: 10.1148/radiol.2373041639

Conflict of Interest: The authors declare that the research was conducted in the absence of any commercial or financial relationships that could be construed as a potential conflict of interest.

frontiers | Frontiers in Endocrinology

ORIGINAL RESEARCH
published: 06 June 2022
doi: 10.3389/fendo.2022.900816

Effects of Total Flavonoids of Epimedium on Bone Marrow Adipose Tissue in Ovariectomized Rats

Lei Chen[1], Rui Ma[2], Peng Luo[1], Dan Shi[2], Xiao Shi[2], Hua Nian[3], Shi-Xin Chang[1], Wei Yuan[4]* and Guan-Wu Li[1]**

[1] Department of Radiology, Yueyang Hospital of Integrated Traditional Chinese and Western Medicine, Shanghai University of Traditional Chinese Medicine, Shanghai, China, [2] Department of Geriatrics, Yueyang Hospital of Integrated Traditional Chinese and Western Medicine, Shanghai University of Traditional Chinese Medicine, Shanghai, China, [3] Department of Pharmacy, Yueyang Hospital of Integrated Traditional Chinese and Western Medicine, Shanghai University of Traditional Chinese Medicine, Shanghai, China, [4] Department of Orthopaedics, Shanghai Fourth People's Hospital Affiliated to Tongji University School of Medicine, Shanghai, China

OPEN ACCESS

Edited by:
DongMei Wu,
East China Normal University, China

Reviewed by:
Jingzheng Fan,
Tianjin Medical University General Hospital, China
Haiyang Lin,
The Affiliated Wenling Hospital of Wenzhou Medical University, China

***Correspondence:**
Shi-Xin Chang
yy2097@163.com
Wei Yuan
wei95960@126.com
Guan-Wu Li
guanwu.li@shutcm.edu.cn

Specialty section:
This article was submitted to Bone Research, a section of the journal Frontiers in Endocrinology

Received: *21 March 2022*
Accepted: *04 May 2022*
Published: *06 June 2022*

Citation:
Chen L, Ma R, Luo P, Shi D, Shi X, Nian H, Chang S-X, Yuan W and Li G-W (2022) Effects of Total Flavonoids of Epimedium on Bone Marrow Adipose Tissue in Ovariectomized Rats. Front. Endocrinol. 13:900816. doi: 10.3389/fendo.2022.900816

Bone marrow adipose tissue has brown fat characteristics. Several studies have demonstrated that total flavonoids of Epimedium (TFE) could prevent bone loss and reduce the white adiposity in bone marrow induced by ovariectomy (OVX) in rats. However, the effects of TFE on marrow brown fat in OVX rats remain unclear. In this word, we addressed this question expected to provide a new target for preventing and treating osteoporosis. Thirty-six 3-month-old female Sprague-Dawley rats were equally divided into Sham controls, OVX controls, and OVX treated with TFE. Chemical shift coding magnetic resonance was performed to detect marrow fat fraction at the left femur at baseline, 6 and 12 weeks post-OVX. Bone mineral density at the lumbar spine and femur was measured by dual-energy x-ray absorptiometry. Serum bone biomarkers by ELISA, trabecular bone microarchitecture at the proximal tibia by micro-CT, quantitative parameters of marrow adipocyte by hematoxylin, and eosin staining were evaluated. The marrow adipocyte gene and protein expressions profile were determined by real-time quantitative PCR and immunostaining in whole tibiae. We found that TFE treatment could decrease bone turnover rate and improved bone mineral density and trabecular microarchitecture in OVX rats. OVX resulted in marrow adipogenesis as evidenced by increased marrow fat fraction, larger marrow adipocyte size, increased adipocyte number and percentage of adipocyte area, marrow white adipocyte gene, and protein expression, including PPARγ2 and FABP4. These pathological changes induced by estrogen deficiency were restored by TFE treatment. TFE also increased brown adipocyte

expressions of the transcription factor Ucp1 and Prdm16 in whole tibiae. There was no detectible protein expression of brown adipocyte markers in the proximal tibia. Taken together, TFE regulation of bone marrow adiposity in OVX rats is mediated, at least in part, *via* maintaining the reciprocity of white and brown adipose tissue.

Keywords: osteoporosis, total flavonoids of Epimedium, marrow adipocytes, white adipose tissue, brown adipose tissue, ovariectomy

INTRODUCTION

Bone marrow mesenchymal stem cells (MSCs) can differentiate into osteoblasts and adipocytes, which are delicately balanced for osteogenesis and adipogenesis during bone remodeling (1, 2). Growing evidence indicates that an increase in marrow adipogenesis inhibits osteoblastogenesis and promotes osteoclastogenesis. Therefore, a potential therapeutic target for treating estrogen deficiency-induced osteoporosis is to reduce the expansion of marrow adiposity (3, 4). Furthermore, a better understanding of the components of marrow fat tissue and its relationship with neighboring cells can contribute to a reasonable strategy when targeting marrow fat to prevent osteoporosis.

Adipocytes' characteristics and anatomical structure are now widely recognized into three types: white, brown, and beige adipocytes (5). Excessive white adipose tissue in bone marrow is one of the pathogenic mechanisms of osteoporosis (6), while brown fat tissue, as an independent predictor of bone mass, could facilitate osteogenesis *via* regulating bone anabolism (7, 8). Interestingly, animal experiments showed that the brown-like phenotype of adipose tissue was found in the bone marrow cavity of mature mice, where bone remodeling is active (9–12). Moreover, the imbalance of brown and white fat in bone marrow may affect the balance of bone metabolism. It has been demonstrated that peroxisome proliferator-activated receptor-γ coactivator-1α could induce the formation of brown fat in the bone marrow MSCs and promote the browning of white fat (13) indicating the transformation between white and brown phenotypes. Therefore, we suspected that modulating the balance of bone marrow lipid metabolism to increase the brown fat content may provide new insight into preventing and treating osteoporosis.

The total flavonoids of Epimedium (TFE) are active components of Epimedium against osteoporosis (14). Previous studies indicated that TFE could promote osteogenic differentiation and inhibit adipogenic differentiation of MSCs (15–17). Previous *in vivo* studies also confirmed that the early treatment of TFE could prevent bone loss and reduce the white adiposity induced by estrogen deficiency (18). However, the exact mechanism of TFE on marrow adipose tissue, particularly brown fat, remains unclear. Since an association between osteogenesis and adipogenesis has been confirmed, and a mixed brown/white adipose tissue phenotype has been found in marrow adipose tissue, we hypothesized that TFE could maintain the reciprocity of white and brown adipose tissue in a rat model of estrogen deficiency-induced osteoporosis. To verify this hypothesis, in this study, we mainly observed the effects of TFE on bone marrow fat, especially brown fat markers, bone metabolic biomarkers, and bone trabecular microstructures in ovariectomized (OVX) rats, in expected to provide a new target for the prevention and treatment of osteoporosis.

MATERIALS AND METHODS

Experimental Design

Thirty-six female Sprague-Dawley rats (3-month-old; average initial weight, 230 ± 15g) were used and housed in individual cages in an animal room. Room temperature was 22 ± 2°C with a 40-50% relative humidity and a 12 h light and 12 h dark cycle. Food and water were provided ad libitum. The rats were allowed to acclimatize for two weeks before being used for the study and were weighed every week throughout the experimental period. The rats were randomly divided into three groups with 12 per group :(1) sham-operation group (Sham), (2) ovariectomized group (OVX), and (3) OVX treated with TFE group (TFE, 191 mg/kg body weight/day) (Kanion Sunshine Pharmaceutical Co., Ltd., Jiangsu, China). The dosage of TFE was based on previous studies indicating that 191 mg/kg/day was sufficient to restore the bone mass and biomechanical strength to levels of the Sham group (19). All animal procedures followed the National Institutes of Health Guidelines on the Care and Use of Laboratory Animals. To reduce the number of rats used in the current study, we followed the recommendation of the Animal Ethics Committee to use only a standard daily dose of TFE. The Sham and OVX control rats were given the same volume of normal saline as the vehicle. The intervention started 3 days after surgery and lasted for 12 weeks. Administered the substances by daily intragastric gavage 6 times a week and adjusted the dose for the body weight of the rats once a week.

At the end of the 12th week, blood samples were collected by cardiac puncture under anesthesia and put 2mL serum into a sterile EP tube. After standing at 4°C for 24h, the serum was transferred into the sterile EP tube by low-temperature centrifugation (4°C, 3000rpm'5min) and stored at -80°C for biochemical analysis. At the end of treatment, the rats were killed by over injection of pentobarbital sodium. The L4 vertebral body, femur, and tibia were removed and protected by liquid nitrogen for later analysis.

Enzyme-Linked Immunosorbent Assay (ELISA)

Serum 17β-estradiol levels (Kamiya Biomedical Company, Seattle, USA) and biomarkers of bone turnover were analyzed using

enzyme-linked immunosorbent assays. Bone turnover biomarkers included bone formation marker type 1 collagen amino propeptide (P1NP) and bone resorption marker C-terminal telopeptides of type I collagen (CTX-I) (Immunodiagnostic Systems Nordic A/S, Denmark). All analyses were performed according to the manufacturer's protocol.

Dual-Energy X-Ray Absorptiometry (DXA)

The rat's bone mineral density (BMD, g/cm^2) was measured by a dual-energy X-ray absorptiometry (Hologic Inc., Bedford, MA) equipped with specific software for the small animal scanning mode. As previously described (20), the scanning regions were marked with respect to the femur and lumbar spine. Measurements were performed at baseline (before the OVX surgery) and after the interventions (6 and 12 weeks, respectively).

Magnetic Resonance Imaging

MRI scans were conducted using a 3.0T MR scanner (Magnetom Verio, Siemens Healthcare, Germany), equipped with a 4-channel phased-array small animal coil (Shanghai Chenguang, CG-MUC18-H300-AS). In this protocol, A routine T1-weighted VIBE sequence (repetition time 5.91 ms; echo time 2.45/3.675 ms; flip angle 9°; matrix 192 × 192; slice thickness 1.5 mm) covering the entire femur was selected to measure bone marrow fat fraction (**Figure 1**). Fat fraction (FF) was calculated using the following formula as previously described (21, 22): FF (in %) = mean intensity$_{fat\ image}$/(mean intensity$_{fat\ image}$ + mean intensity$_{water\ image}$) ×100%. Imaging scans were performed at baseline (week 0), 6 and 12 weeks postoperatively to obtain the dynamic changes in marrow lipid content.

Micro-Computed Tomography (Micro-CT)

The left tibia in each rat was measured with a micro-CT scanner (Xradia microCT-200A, ZEISS, Pleasanton, CA, USA) at 12.5-μm voxel resolution to assess trabecular microarchitectures. Microstructures of bone trabeculae, including bone volume fraction (BV/TV), trabecular separation (Tb. Sp), trabecular number (Tb. N) and trabecular thickness (Tb. Th), and structure model index (SMI), were determined according to guidelines, as described in detail elsewhere (22).

Hematoxylin and Eosin Staining

After micro-CT scanning, left tibias were fixed in 10% buffered formalin for 24 h and then decalcified in 10% buffered ethylene diamine tetraacetic acid for 4 weeks. Specimens were embedded in paraffin, sectioned in 5 μm thick slices, and stained with hematoxylin and eosin. The photomicrographs were captured at a 200× magnification with five microscopic fields per section using a Leica DM6000B microscopy (Wetzlar, Germany). Image analysis, including adipocyte mean size (μm), adipocyte density (1/mm^2), and percentage of adipocyte area (%) in all analyzed fields, was done using Image-Pro Plus software v6 (Media Cybernetics, Inc, Rockville, MD) as previously described (23). Samples were evaluated in a blinded fashion to avoid investigator bias.

Immunohistochemistry and Immunofluorescence Staining

The bone immunohistochemistry was performed as described in detail elsewhere (24, 25). In brief, fatty acid-binding protein 4 (FABP4) and peroxisome proliferator-activated receptor gamma-2 (PPARγ2) immunostaining in paraffin-embedded 5-μm sections above mentioned were probed using an anti-FABP4 antibody (rabbit monoclonal to FABP4, Abcam) and anti-PPARγ2 antibody (Mouse monoclonal to PPAR gamma 2 + PPAR gamma, Abcam) immunohistochemistry/immunofluorescence Kits. For immunohistochemistry analysis of FABP4, heat-mediated antigen retrieval was performed using

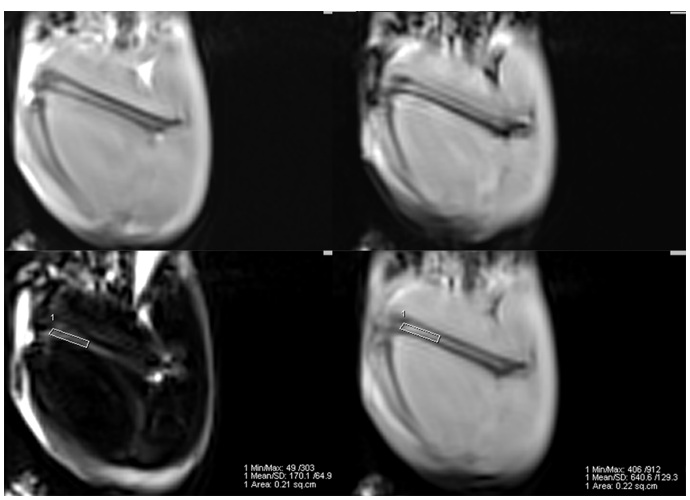

FIGURE 1 | Example of a 2-point Dixon sequence for measuring fat fraction. The region of interest was manually drawn in the distal femur in a fat-only image, avoiding the cortical bone, and directly copied onto a water-only image.

Tris/EDTA buffer. ImmunoHistoProbe one-step HRP Polymer was used as the secondary antibody. Hematoxylin was used as a counterstain. As a negative control, nonimmune mouse immunoglobulin G was used as the primary antibody. Pictures were obtained at a 200×magnification using a Leica DM6000B microscopy (Wetzlar, Germany). For immunofluorescence analysis of PPARγ2, threshold intensities for each analyzed field were determined. Then the number of pixels within the analyzed field above the threshold intensity was calculated and considered positively stained. The positively stained pixels as a percentage of the total pixels in five random fields per sample were calculated for the final analysis (25).

Real-Time Quantitative PCR Analysis

According to the manufacturer's instructions, the total RNA from the right tibiae was extracted with the TRIzol RNA isolation reagent (Invitrogen, Carlsbad, CA). According to the instruction manual, the total RNA (2 μg) was reverse-transcribed to cDNA using the RevertAid First Strand cDNA Synthesis Kit (Thermo). The specific transcripts were quantified by real-time quantitative PCR using a FastStart Universal SYBR Green Master (Roche) and analyzed with an ABI-7500 Step One Plus RT-PCR system (Applied Biosystems) with the following thermal cycling parameters: 95°C for 10 min to activate DNA polymerase, 40 cycles of amplification (95°C for 15 s and 60°C for 60 s). Quantitative analysis was performed according to the ABI protocol. The threshold cycle (Ct) value was calculated from amplification plots. Relative quantification of gene expression was determined using the delta CT (ΔΔCT) method, with each sample being normalized to the expression of the housekeeping gene actin. Each sample was run in triplicate, and the expression level of each gene was expressed relative to the expression level of the gene in BMSCs of the TFE-treated OVX rats. The primers were designed and synthesized by Invitrogen based on the sequence published by GenBank. The primer sequences used in this study are shown in **Table 1**.

Statistical Analysis

All statistical analyses were performed with IBM SPSS Version 26.0 (Armonk, NY). Data were expressed as mean ± SD. Two-way repeated measurement ANOVA was performed to determine the time by group interaction effects and/or time effects for the body weight, BMD, and marrow fat fraction. One-way ANOVA with Bonferroni's multiple comparison test was used to detect the differences in other studied parameters among the three groups. $P < 0.05$ was considered to be statistically significant.

RESULTS

Changes in Body Mass and Uterine Parameters

Of the initial 36 rats, 32 went through the whole study, whereas one rat in the Sham group, two in the OVX group, and one in the TFE group died of an adverse reaction to anesthetics. During the experiment, no adverse gastrointestinal effects (vomiting or diarrhea) or surgical complications (infection or wound dehiscence) were observed. **Figure 2** shows variations in the body weights of the various groups over time. At the beginning of the protocol, the body weights of the three groups of rats were not significantly different. All groups increased body weight across time points; a significant change among rats in the Sham, OVX, and TFE groups was first observed on week 4. On week 12, the body weight of OVX controls was 45.0% higher than at baseline, whereas the body weights of Sham and TFE rats were 22.6% and 28.2% higher, respectively. On week 12, the body weight of OVX controls was 20.6% and 15.2% higher than the body weights of Sham and TFE rats, respectively (all $P<0.001$).

The uterine weight and the uterine index were significantly reduced in the OVX group compared with the Sham group (all $P<0.001$), indicating that estrogen deficiency resulted in atrophy of the uterus of OVX rats. Treatment with TFE did not significantly increase the uterine weight of the OVX rats ($P =0.064$) (**Figure 3**).

Changes in Bone Turnover Biomarkers and 17 β-Estradiol

The serum CTX-I level($P<0.001$) was higher, and estradiol ($P<0.001$) was lower in the OVX rats than that in the Sham rats. There was no significant difference in the level of P1NP ($P>0.05$) between the OVX and Sham controls. The serum estradiol and the P1NP levels were increased when OVX rats were administrated with TFE treatment (all $P<0.05$). In contrast, TFE treatment decreased the serum CTX-I level of OVX rats ($P<0.001$) (**Figure 4**).

TFE Increased BMD and Improved Trabecular Microarchitectures in OVX Rats

Lumbar spine BMD increased over time in the Sham group (+4.8% at week 6, $P >0.05$; +19.5% at week 12, $P <0.001$) and femur BMD (6 weeks +12.6%, $P <0.001$;12 weeks +24.4%, $P<0.001$). TFE treatment increased lumbar spine BMD (6 weeks, +3.6%, $P >0.05$) and (12 weeks, +12.2%, $P <0.001$) and femur BMD (6 weeks, +7.6%, $P >0.05$) and (12 weeks, +15.3%, $P <0.001$). In contrast, the BMD

TABLE 1 | Primer sequences for the quantitative reverse-transcription polymerase chain reaction.

Target genes	Forward (5'-3')	Reverse (5'-3')	Accession Number
Ucp1	CGGGCTTAAAGAGCGAGAGG	CTTGGATCTGAAGGCGGACT	NM_021833.5
Prdm16	CCAAGGCAAGGGCGAAGAA	AGTCTGGTGGGATTGGAATGT	NM_022114.4
FABP4	AAGGTGAAGAGCATCATAACCCT	TCACGCCTTTCATAACACATTCC	NM_001442.3
PPARγ2	ACCATGG TTGACACAGAGATGCCA	AGGAATGCGAGTGGTCTTCCATCA	NM_001145366.1
β-actin	CGAGTACAACCTTCTTGCAGC	CCATATCGTCCCAGTTGGTG	NM_007393.5

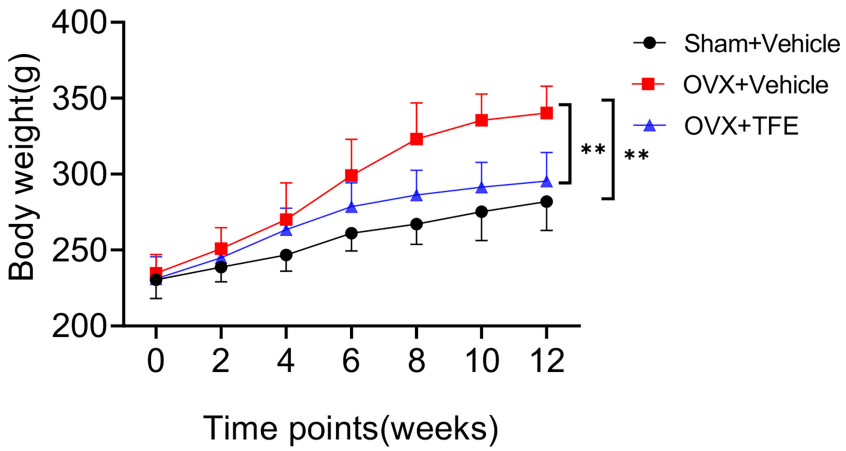

FIGURE 2 | Body weights of rats in all treatment groups throughout the experimental period. Values are presented as mean ± SD (Sham, n = 11; OVX, n = 10; TFE, n = 11). OVX, ovariectomy; Sham, sham-operation; TFE, total flavonoids of Epimedium. *P* values represent Bonferroni-corrected *p*-values (two-way repeated-measures ANOVA). ***P* <0.001 between the OVX and Sham controls and between the OVX controls and TFE-treated group at week 12.

in the OVX control group slightly increased in the lumbar spine (+2.1% at week 6 and +5.9% at week 12 relative to baseline) and femur (6 weeks +6.0%; 12 weeks +7.8%). After OVX, the BMD was significantly decreased than the Sham group (all $P<0.05$). After TFE treatment, the BMD was increased as compared with the OVX but without statistical significance (all $P>0.05$) (**Table 2**).

Trabecular microarchitecture of the tibias was analyzed by micro-CT, and the results are shown in (**Figure 5**). Compared with the Sham group, BV/TV (-36.7%), Tb.N (-56.1%) and Tb.Th (-23.0%) were significantly decreased while Tb.Sp (+135.7%) and SMI (+82.5%, all P <0.001) were increased in the OVX group. Further compared with the OVX group, BV/TV (+35.0%), Tb.N (+70.3%) and Tb.Th (+13.1%) were significantly increased while Tb.Sp (-35.1%) and SMI (-27.4%, all $P<0.05$) were reduced in the TFE-treated rats, which indicated that TFE could restore the deterioration of trabecular microarchitectures.

TFE Lowers Marrow Fat Expansion

After OVX, the marrow fat fraction was rapidly increased over time, by 34.7% at week 6 and 59.9% at week 12 relative to the baseline condition (all P <0.001) (**Table 3**). Compared with week 0, the marrow fat fraction was increased by 8.7% at week 6 (P >0.05) and 19.3% at week12 (P <0.001), respectively, in the OVX+TFE group. In addition, compared with the Sham group, it was found that at 6 weeks and 12 weeks, the marrow fat fraction of the OVX controls was increased by 26.9% (P =0.002) and 45.1% (P <0.001), respectively. The marrow fat fraction of the TFE-treated group was increased by 4.5% at week 6 (P >0.05) and 10.5% at week 12 (P >0.05) in comparison with the Sham controls, indicating that TFE administration significantly inhibited marrow adipogenesis caused by OVX.

Estrogen deficiency leads to marrow adipogenesis, shown as larger adipocyte size, increased adipocyte density, and increased

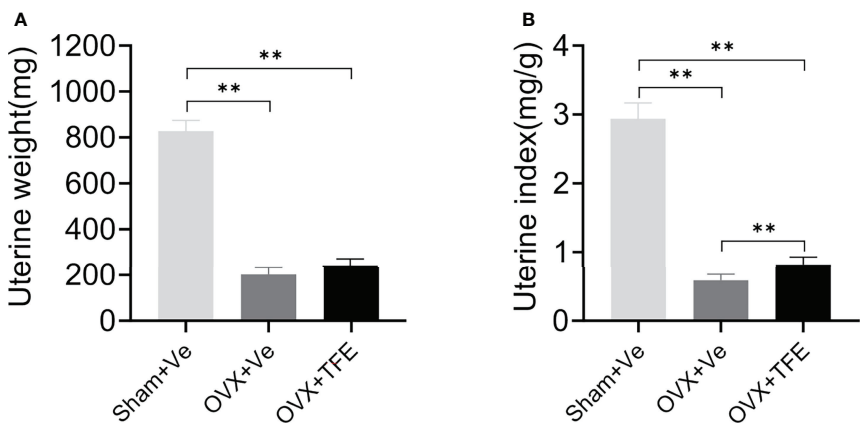

FIGURE 3 | Effects of TFE treatment on **(A)** uterine wet weight and **(B)** uterine index. Data are presented as mean ± SD (Sham, n = 11; OVX, n = 10; TFE, n = 11). OVX, ovariectomy; Sham, sham-operation; TFE, total flavonoids of Epimedium; Ve, vehicle. ***P*<0.001 by One-way ANOVA with Bonferroni-correction.

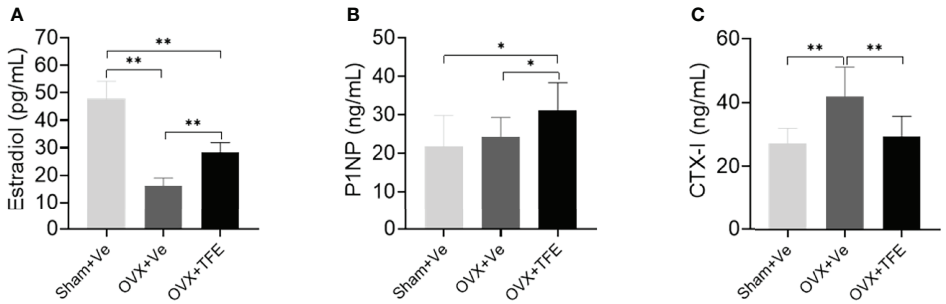

FIGURE 4 | Effects of TFE treatment on **(A)** 17β-estradiol, **(B)** P1NP, and **(C)** CTX-I. Values are presented as mean (SD; Sham, n = 11; OVX, n = 10; TFE, n = 11). CTX-I, C-terminal telopeptides of type I collagen; P1NP, type 1 collagen amino propeptide; OVX, ovariectomy; Sham, sham-operation; TFE, total flavonoids of Epimedium; Ve, vehicle. TFE treatment inhibited bone turnover in OVX rats. Serum 17β-estradiol was significantly reduced while levels of CTX-I were higher in OVX rats than in Sham rats. *P<0.05 and **P<0.001 by One-way ANOVA with Bonferroni-correction.

percentage of adipocyte area. As expected, early TFE supplementation suppresses marrow fat accumulation as evidenced by decreased density (34.7%), mean diameter (16.7%), and area percentage (57.0%; all P <0.001) of adipocytes as compared with the OVX group (**Figure 6**).

TFE Impacted Marrow Adipocyte Gene and Protein Expression

OVX significantly increased white adipocyte transcript expressions of the PPARγ2 and FABP4 in intact tibiae. This effect was inhibited by TFE treatment. OVX significantly decreased brown adipocyte expressions of the transcription factor uncoupling protein 1 (Ucp1) and PR domain-containing 16 (Prdm16) (P < 0.05). TFE treatment for 12 weeks was associated with increased brown adipocyte markers expression in whole tibiae (**Figure 7**).

We next analyzed adipocyte marker expression at the protein level. As shown in **Figure 8**, OVX rats robustly increased PPARγ2 and FABP4 protein expression in proximal tibiae. Both Sham controls and TFE-treated groups had similar PPARγ2 and FABP4 positivity within the marrow space among marrow fat cells. These results suggest suppression of adipogenesis with TFE supplementation compared to the OVX vehicle. However, we could not detect Ucp1 or Prdm16 protein expression in all groups.

DISCUSSION

A series of results showed that TFE could induce bone marrow stromal cells (BMSCs) to differentiate into osteoblasts, enhance their activity, and inhibit bone catabolism and bone resorption produced by osteoclasts (26, 27). In this study, we first evaluated the effects of TFE on bone metabolism. Similar to previous data (17, 19, 28), TFE has an anti-osteoporotic effect as evidenced by bone turnover biomarkers, BMD, and bone trabecular microstructures.

Both osteoblasts and adipocytes are derived from BMSCs, and it is adequate to find agents that promote osteogenesis and inhibit adipogenesis differentiation of BMSCs. Our previous study verified that early TFE treatment could effectively restore marrow adiposity in estrogen-deficient rats (29). The current study further observed that TFE could markedly reduce marrow white fat markers. There are also a series of studies directly targeting bone marrow adipose tissue to treat osteoporosis, such as the antagonization of adipocyte-related transcription factors

TABLE 2 | Changes in vertebral and femoral BMD in three groups of rats.

Parameters	Groups	BMD (g/cm^2)		
		Week 0	Week 6	Week 12
Lumbar spine BMD	Sham+vehicle	0.184 (0.013)	0.193 (0.015)	0.220 (0.017)*#
	OVX+vehicle	0.183 (0.011)	0.187 (0.016)	0.194 (0.014)[a]
	OVX+TFE	0.184 (0.010)	0.191 (0.010)	0.207 (0.013)*#
Femur BMD	Sham+vehicle	0.243 (0.015)	0.273 (0.022)[a]	0.302 (0.016)*#
	OVX+vehicle	0.241 (0.010)	0.255 (0.015)	0.260 (0.028)[a]
	OVX+TFE	0.242 (0.014)	0.261 (0.022)	0.280 (0.021)*

Data are presented as mean (SD); Sham, n = 11; OVX, n = 10; TFE, n = 11.
TFE, total flavonoids of Epimedium; OVX, ovariectomy; Sham, sham-operation.
P values represent Bonferroni-corrected p-values.
[a]P <0.05 vs Sham+ vehicle (Bonferroni post-hoc test).
**P <0.05 vs week 0 and #P <0.05 vs week 6 (paired multiple comparison test).*

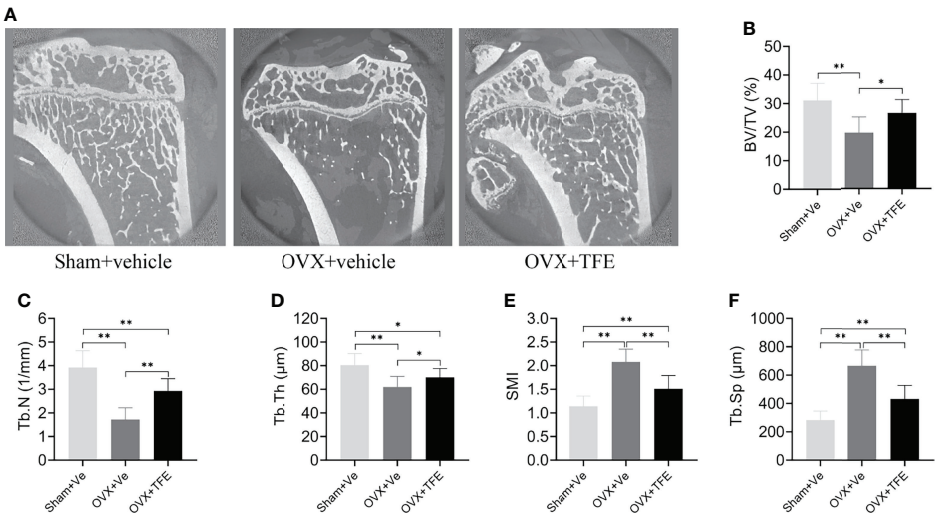

FIGURE 5 | Effects of TFE treatment on bone trabeculae microstructure in the tibia in OVX rats. Sagittal views of micro-CT images at the proximal tibia region **(A)** showed deterioration of trabecular microstructure in OVX rats, and TFE treatment improved bone trabeculae microstructure. TFE-treated rats showed responses to the OVX-induced losses of **(B)** BV/TV, **(C)** Tb.N, **(D)** Tb.Th, **(E)** SMI, and Tb.Sp **(F)**. BV/TV, bone volume fraction; Tb. Sp, trabecular separation; Tb.N, trabecular number; Tb.Th, trabecular thickness; SMI, structure model index; OVX, ovariectomy; Sham, sham-operation; TFE, total flavonoids of Epimedium; Ve, vehicle. Data are shown as mean ± SD (Sham, n = 11; OVX, n = 10; TFE, n = 11). *P<0.05 and **P<0.001 between groups analyzed by One-way ANOVA with Bonferroni-correction.

or targeting cytokines. Bisphenol A diglycidyl ether reduced marrow adiposity and increased bone mass in male C57BL/6 mice (30). Besides, inhibiting sclerostin could significantly reduce marrow fat expansion and improve bone mass in OVX models (31).

Treatment of marrow adipocytes with rosiglitazone, triiodothyronine, or thyroid hormone receptor beta-specific agonist markedly increased expression of several brown/beige adipose markers, indicating bone marrow fat has a mixed brown/white adipose tissue phenotype (9, 32). However, TFE regulation of marrow brown adipose has not previously been examined. In this work, we first analyzed the mRNA expression of adipocyte markers in the total tibia. Marrow brown adipocyte gene markers were upregulated in the total tibia in response to TFE treatment, accompanied by decreased marrow fat fraction, percentage of adipocyte area, and adipocyte density and diameter. Interestingly, the beneficial effect of bone marrow fat on the regulation of bone mass is presented through the expression of brown adipocyte gene markers (Ucp1, Prdm16), and this ability

TABLE 3 | Changes in marrow fat fraction in three groups of rats.

Groups	Week 0	Week 6	Week 12
Sham + vehicle	14.5 (1.8)	15.6 (2.1)	16.2 (2.4)
OVX + vehicle	14.7 (2.5)	19.8 (2.9)[a⋆]	23.5 (3.4)[a⋆#]
OVX + TFE	15.0 (2.2)	16.3 (2.5)[b]	17.9 (2.7)[b⋆#]

Data are presented as mean (SD); Sham, n = 11; OVX, n = 10; TFE, n = 11.
TFE, total flavonoids of Epimedium; OVX, ovariectomy; Sham, sham-operation.
P values represent Bonferroni-corrected P values.
[a]P <0.05 vs Sham+ vehicle and
[b]P <0.05 vs OVX + vehicle (Bonferroni post-hoc test).
**P <0.05 vs week 0 and [#]P <0.05 vs week 6 (paired multiple comparison test).*

diminishes with a decrease in metabolic capacity due to age or diabetes (9). In consistent with our reports, *in vitro* studies have shown that rat bone marrow adipocytes express the adipocyte gene markers PPARγ and CCAAT/enhancer-binding protein-α, but not the brown fat gene markers Ucp1 and Cidea (33). Lineage tracing of Ucp1 expression in mTmG reporter mice was absent in bone marrow fat tissue, and stimulation with β3-agonists could not induce Ucp1-Cre expression in bone marrow fat (34).

At the level of RNA transcript, in solid support of marrow adipose brown potential, adipocytes in the proximal tibia have been reported to express brown fat markers, particularly Ucp1 (9–12). To further evaluate whether the increase in expression of brown transcripts such as Ucp1, Prdm16 in the TFE-treated group supported a corresponding protein expression change, Ucp1 and Prdm16 immunostaining on bone sections were conducted. In consistence with several other studies (3, 35), we were unable to detect expressions of protein related to brown fat markers within the tibia. In contrast, a previous *in vivo* study done by Nishio et al. (36) showed that a multilocular appearing cell in murine vertebral bone marrow expressed Ucp1 protein with immunostaining evidence.

The possible explanations for the significant discrepancies in existing literature might be attributed to the anatomical site of bone specimens, research designs, and methodological differences. First, the marrow adipose composition differs between anatomic sites. In both humans and rodents, marrow adipocytes are composed of two broad subtypes, namely regulated bone marrow adipose and constitutive bone marrow adipose, in which there are some critical differences (3, 37), including the composition of lipid content, response to

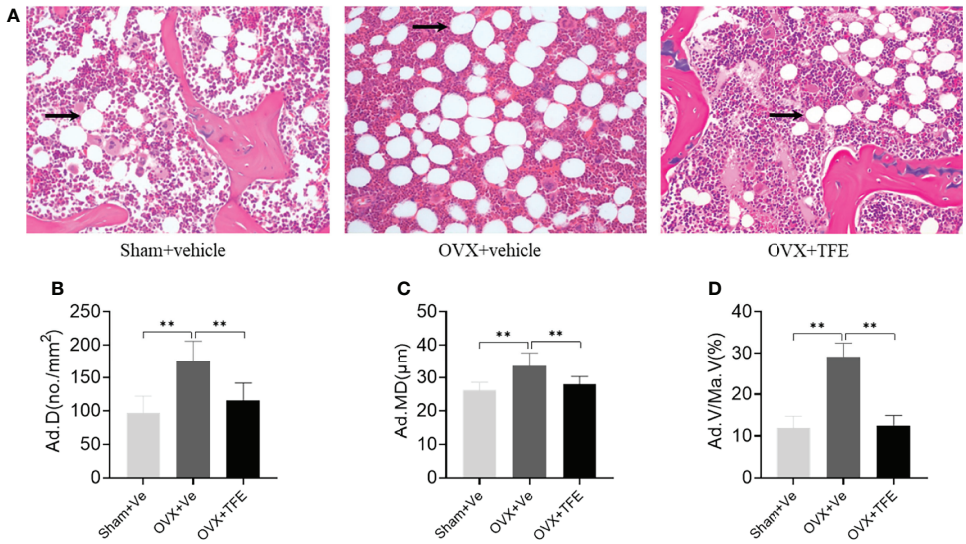

FIGURE 6 | Changes in the marrow adipose **(A)** and adipocyte quantitative parameters **(B–D)**. Sections of decalcified bone were stained with H&E (×200). OVX markedly increased infiltration of marrow fat (arrow). This increase in marrow adiposity was restored by TFE treatment. Ad.D, adipocyte density; Ad.MD, adipocyte mean diameter; Ad.V/Ma.V, percentage adipocyte volume per marrow volume; OVX, ovariectomy; Sham, sham-operation; TFE, total flavonoids of Epimedium; Ve, vehicle. Data are shown as mean ± SD (Sham, n = 11; OVX, n = 10; TFE, n = 11). ***P*<0.001 between groups analyzed by One-way ANOVA with Bonferroni-correction.

pathophysiological stress, and levels of the adipogenic transcription factors. Cold exposure did not induce glucose utilization in the humeral or vertebral marrow adipose tissue compared to brown fat (38, 39), indicating that marrow adipose in humans is a metabolically active, insulin-sensitive fat tissue. Moreover, bone marrow adipose tissue did not express beta3-adrenergic receptor and Ucp1, both characteristic of brown fat (38); however, this result applied only to the mid-diaphysis of tibial and femoral marrow fat, which is mainly composed of constitutive marrow adipose tissue. Consistent with this, recent work by Craft et al. (35) using genetic ablation and lineage tracing of Ucp1 expressing cells has shown that marrow adipocytes do not express Ucp1 during development or after β3-agonist treatment in mice.

Another explanation could be that brown fat transcript was determined by RNA obtained from whole-mount skeletal preparations, which are highly inhomogeneous and especially susceptible to adipose tissue surrounding the skeleton. Furthermore, several studies indicated very low skeletal Ucp1 expression compared to brown adipose tissue (9, 12, 38).

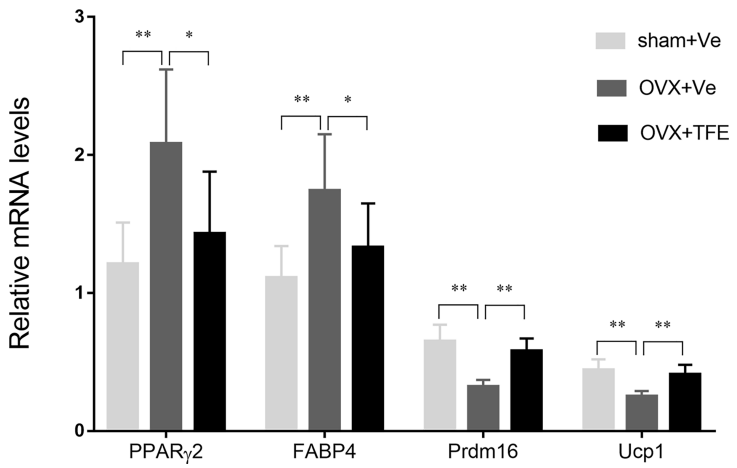

FIGURE 7 | Effects of TFE treatment on marrow white and brown adipocyte gene markers in whole tibiae of OVX rats. Gene expression markers of Prdm16 and Ucp1 were normalized to FABP4 expression in the same sample. OVX, ovariectomy; Sham, sham-operation; TFE, total flavonoids of Epimedium; Ve, vehicle. Results are presented as means ± SD (Sham, n = 11; OVX, n = 10; TFE, n = 11). **P*<0.05 and ***P*<0.001 between groups analyzed by One-way ANOVA with Bonferroni-correction.

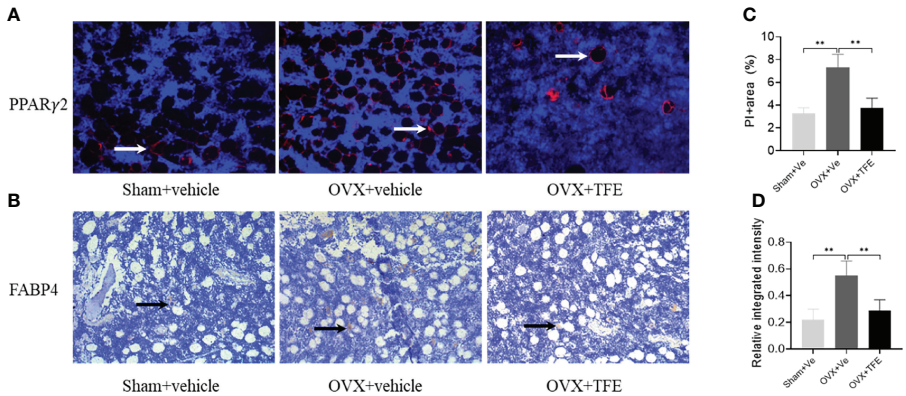

FIGURE 8 | Representative microscopic features of PPARγ2 and FABP4 expression in bone marrow (200x magnification). Quantification of PPARγ2 expression by immunofluorescence **(A)** and FABP4 expression by immunohistochemistry **(B)** in the bone marrow showed a significant increase in PPARγ2 and FABP4 protein expression in proximal tibiae of OVX rats, which were restored to normal levels after TFE treatment. For PPARγ2, the positively staining pixels were presented as a percentage of the total pixels **(C)**; for FABP4, semi-quantification is expressed as the relative integrated intensity of intramarrow staining **(D)**. FABP4, fatty acid-binding protein 4; PPARγ2, peroxisome proliferator-activated receptor gamma-2; OVX, ovariectomy; Sham, sham-operation; TFE, total flavonoids of Epimedium; Ve, vehicle. Data are shown as mean ± SD (Sham, n = 11; OVX, n = 10; TFE, n = 11). $^{**}P<0.001$ between groups analyzed by One-way ANOVA with Bonferroni-correction.

The strength of our study is the characterizations of white and brown fat tissue with multiple methods, including *in vivo* VIBE MRI and gene expression analysis. The current study has some limitations that may need to be addressed by future research. First, our interpretation of this study may be limited by the gene expression analysis of RNA isolated from the whole tibia, mainly due to the difficulty in obtaining and maximizing the retention of bone marrow adipocytes during bone marrow isolation. Therefore, we separate RNA from the whole bone homogenate to represent all adipocytes. Furthermore, because the original cell population is a mixture of different types of cells, there may be deviations in the interpretation of the expression results of gene markers. Second, although our evidence-based *in vivo* VIBE MRI and gene expression analysis showed that TFE induces bone marrow white adipocytes to brown adipocytes, we did not confirm its effect on intact bone as the Sham and OVX rats were treated only with the vehicle and not TFE. Although OVX rats have a high rate of bone loss and prominent trabecular degeneration, their effect on the intact bone should be investigated in future studies. Third, our evidence suggests that the browning effect of TFE was associated with an increase in brown adipocytes. However, we are uncertain whether specific TFE-induced signaling pathways are involved in promoting brown adipocyte generation. In addition to its exclusive signaling pathway, the Wnt/β-catenin signaling pathway, TFE also directly regulates 11 estrogen-related targets and a set of target proteins to exert anti-osteoporosis effects (40). It is essential to determine what factors are involved in the browning effect of TFE on white adipose tissue through a signaling pathway array or gene chips. Finally, we used 3-month-old mice for OVX modeling in this study and started TFE intervention on the third postoperative day. Therefore, we are uncertain about the exact efficacy of TFE in aged mice and chronic osteoporosis.

In conclusion, our data demonstrated that TFE regulation of bone marrow adiposity in a rat model of estrogen deficiency-induced osteoporosis, at least in part, maintained the reciprocity of white and brown adipose tissue. TFE may induce browning of marrow white adipocytes due to increased expressions of brown transcripts Ucp1 and Prdm16 in the whole tibia; however, these results require further confirmation.

DATA AVAILABILITY STATEMENT

The datasets presented in this study can be found in online repositories. The names of the repository/repositories and accession number(s) can be found in the article/supplementary material.

ETHICS STATEMENT

The animal study was reviewed and approved by Yueyang Hospital of Integrated Traditional Chinese and Western Medicine, Shanghai University of Traditional Chinese Medicine.

AUTHOR CONTRIBUTIONS

Study design: LC and G-WL. Study conduct: PL and DS. Data collection: RM and XS. Data analysis: LC and WY. Data interpretation: HN and S-XC. Drafting manuscript: LC and G-WL. All authors critically revised the manuscript and approved the final version of the manuscript to be submitted.

FUNDING

This work was funded by the National Natural Science Foundation of China (No. 81874497).

REFERENCES

1. Hu L, Yin C, Zhao F, Ali A, Ma J, Qian A. Mesenchymal Stem Cells: Cell Fate Decision to Osteoblast or Adipocyte and Application in Osteoporosis Treatment. *Int J Mol Sci* (2018) 19:360. doi: 10.3390/ijms19020360
2. Singh L, Brennan TA, Russell E, Kim JH, Chen Q, Brad Johnson F, et al. Aging Alters Bone-Fat Reciprocity by Shifting *In Vivo* Mesenchymal Precursor Cell Fate Towards an Adipogenic Lineage. *Bone* (2016) 85:29–36. doi: 10.1016/j.bone.2016.01.014
3. Scheller EL, Khandaker S, Learman BS, Cawthorn WP, Anderson LM, Pham HA, et al. Bone Marrow Adipocytes Resist Lipolysis and Remodeling in Response to Beta-Adrenergic Stimulation. *Bone* (2019) 118:32–41. doi: 10.1016/j.bone.2018.01.016
4. Styner M, Pagnotti GM, McGrath C, Wu X, Sen B, Uzer G, et al. Exercise Decreases Marrow Adipose Tissue Through ß-Oxidation in Obese Running Mice. *J Bone Miner Res* (2017) 32:1692–702. doi: 10.1002/jbmr.3159
5. Veldhuis-Vlug AG, Rosen CJ. Clinical Implications of Bone Marrow Adiposity. *J Intern Med* (2018) 283:121–39. doi: 10.1111/joim.12718
6. Li Y, Meng Y, Yu X. The Unique Metabolic Characteristics of Bone Marrow Adipose Tissue. *Front Endocrinol (Lausanne)* (2019) 10:69. doi: 10.3389/fendo.2019.00069
7. Du J, He Z, Xu M, Qu X, Cui J, Zhang S, et al. Brown Adipose Tissue Rescues Bone Loss Induced by Cold Exposure. *Front Endocrinol (Lausanne)* (2021) 12:778019. doi: 10.3389/fendo.2021.778019
8. Lidell ME, Enerback S. Brown Adipose Tissue and Bone. *Int J Obes Suppl* (2015) 5:S23–7. doi: 10.1038/ijosup.2015.7
9. Krings A, Rahman S, Huang S, Lu Y, Czernik PJ, Lecka-Czernik B. Bone Marrow Fat has Brown Adipose Tissue Characteristics, Which Are Attenuated With Aging and Diabetes. *Bone* (2012) 50:546–52. doi: 10.1016/j.bone.2011.06.016
10. Lecka-Czernik B, Stechschulte LA, Czernik PJ, Sherman SB, Huang S, Krings A. Marrow Adipose Tissue: Skeletal Location, Sexual Dimorphism, and Response to Sex Steroid Deficiency. *Front Endocrinol (Lausanne)* (2017) 8:188. doi: 10.3389/fendo.2017.00188
11. Styner M, Pagnotti GM, Galior K, Wu X, Thompson WR, Uzer G, et al. Exercise Regulation of Marrow Fat in the Setting of PPARgamma Agonist Treatment in Female C57BL/6 Mice. *Endocrinology* (2015) 156:2753–61. doi: 10.1210/en.2015-1213
12. Sulston RJ, Learman BS, Zhang B, Scheller EL, Parlee SD, Simon BR, et al. Increased Circulating Adiponectin in Response to Thiazolidinediones: Investigating the Role of Bone Marrow Adipose Tissue. *Front Endocrinol (Lausanne)* (2016) 7:128. doi: 10.3389/fendo.2016.00128
13. Huang PI, Chen YC, Chen LH, Juan CC, Ku HH, Wang ST, et al. PGC-1α Mediates Differentiation of Mesenchymal Stem Cells to Brown Adipose Cells. *J Atheroscler Thromb* (2011) 18:966–80. doi: 10.5551/jat.7401
14. Indran IR, Liang RL, Min TE, Yong EL. Preclinical Studies and Clinical Evaluation of Compounds From the Genus Epimedium for Osteoporosis and Bone Health. *Pharmacol Ther* (2016) 162:188–205. doi: 10.1016/j.pharmthera.2016.01.015
15. Yang A, Yu C, Lu Q, Li H, Li Z, He C. Mechanism of Action of Icariin in Bone Marrow Mesenchymal Stem Cells. *Stem Cells Int* (2019) 2019:5747298. doi: 10.1155/2019/5747298
16. Ye Y, Jing X, Li N, Wu Y, Li B, Xu T. Icariin Promotes Proliferation and Osteogenic Differentiation of Rat Adipose-Derived Stem Cells by Activating the RhoA-TAZ Signaling Pathway. *BioMed Pharmacother* (2017) 88:384–94. doi: 10.1016/j.biopha.2017.01.075
17. Zhang D, Liu L, Jia Z, Yao X, Yang M. Flavonoids of Herba Epimedii Stimulate Osteogenic Differentiation and Suppress Adipogenic Differentiation of Primary Mesenchymal Stem Cells *via* Estrogen Receptor Pathway. *Pharm Biol* (2016) 54:954–63. doi: 10.3109/13880209.2015.1079224
18. Li GW, Xu Z, Chang SX, Zhou L, Wang XY, Nian H, et al. Influence of Early Zoledronic Acid Administration on Bone Marrow Fat in Ovariectomized Rats. *Endocrinology* (2014) 155:4731–8. doi: 10.1210/en.2014-1359
19. Xi HR, Ma HP, Yang FF, Gao YH, Zhou J, Wang YY, et al. Total Flavonoid Extract of Epimedium Herb Increases the Peak Bone Mass of Young Rats Involving Enhanced Activation of the AC10/cAMP/PKA/CREB Pathway. *J Ethnopharmacol* (2018) 223:76–87. doi: 10.1016/j.jep.2018.05.023
20. Govindarajan P, Khassawna T, Kampschulte M, Böcker W, Huerter B, Dürselen L, et al. Implications of Combined Ovariectomy and Glucocorticoid (Dexamethasone) Treatment on Mineral, Microarchitectural, Biomechanical and Matrix Properties of Rat Bone. *Int J Exp Pathol* (2013) 94:387–98. doi: 10.1111/iep.12038
21. Bertheau RC, Lorbeer R, Nattenmuller J, Wintermeyer E, Machann J, Linkohr B, et al. Bone Marrow Fat Fraction Assessment in Regard to Physical Activity: KORA FF4-3-T MR Imaging in a Population-Based Cohort. *Eur Radiol* (2020) 30:3417–28. doi: 10.1007/s00330-019-06612-y
22. Li G, Xu Z, Hou L, Li X, Li X, Yuan W, et al. Differential Effects of Bisphenol A Diglicydyl Ether on Bone Quality and Marrow Adiposity in Ovary-Intact and Ovariectomized Rats. *Am J Physiol Endocrinol Metab* (2016) 311:E922–7. doi: 10.1152/ajpendo.00267.2016
23. Li G, Xu Z, Chen Y, Chang S, Calimente H, Hu J, et al. Longitudinal Assessment of Marrow Fat Content Using Three-Point Dixon Technique in Osteoporotic Rabbits. *Menopause* (2016) 23:1339–44. doi: 10.1097/GME.0000000000000721
24. Wang F-S, Wu R-W, Lain W-S, Tsai T-C, Chen Y-S, Sun Y-C, et al. Sclerostin Vaccination Mitigates Estrogen Deficiency Induction of Bone Mass Loss and Microstructure Deterioration. *Bone* (2018) 112:24–34. doi: 10.1016/j.bone.2018.04.007
25. Elbaz A, Rivas D, Duque G. Effect of Estrogens on Bone Marrow Adipogenesis and Sirt1 in Aging C57BL/6J Mice. *Biogerontology* (2009) 10:747–55. doi: 10.1007/s10522-009-9221-7
26. Zhang S, Feng P, Mo G, Li D, Li Y, Mo L, et al. Icariin Influences Adipogenic Differentiation of Stem Cells Affected by Osteoblast-Osteoclast Co-Culture and Clinical Research Adipogenic. *BioMed Pharmacother* (2017) 88:436–42. doi: 10.1016/j.biopha.2017.01.050
27. Xie L, Liu N, Xiao Y, Liu Y, Yan C, Wang G, et al. *In Vitro* and *In Vivo* Osteogenesis Induced by Icariin and Bone Morphogenetic Protein-2: A Dynamic Observation. *Front Pharmacol* (2020) 11:1058. doi: 10.3389/fphar.2020.01058
28. Zhang DW, Cheng Y, Wang NL, Zhang JC, Yang MS, Yao XS. Effects of Total Flavonoids and Flavonol Glycosides From Epimedium Koreanum Nakai on the Proliferation and Differentiation of Primary Osteoblasts. *Phytomedicine* (2008) 15:55–61. doi: 10.1016/j.phymed.2007.04.002
29. Li GW, Xu Z, Chang SX, Nian H, Wang XY, Qin LD. Icariin Prevents Ovariectomy-Induced Bone Loss and Lowers Marrow Adipogenesis. *Menopause* (2014) 21:1007–16. doi: 10.1097/gme.0000000000000201
30. Duque G, Li W, Vidal C, Bermeo S, Rivas D, Henderson J. Pharmacological Inhibition of Pparγ Increases Osteoblastogenesis and Bone Mass in Male C57BL/6 Mice. *J Bone Miner Res* (2013) 28:639–48. doi: 10.1002/jbmr.1782
31. Li X, Ominsky MS, Villasenor KS, Niu QT, Asuncion FJ, Xia X, et al. Sclerostin Antibody Reverses Bone Loss by Increasing Bone Formation and Decreasing Bone Resorption in a Rat Model of Male Osteoporosis. *Endocrinology* (2018) 159:260–71. doi: 10.1210/en.2017-00794
32. Lindsey RC, Mohan S. Thyroid Hormone Acting *via* TRbeta Induces Expression of Browning Genes in Mouse Bone Marrow Adipose Tissue. *Endocrine* (2017) 56:109–20. doi: 10.1007/s12020-017-1265-x
33. Ambrosi TH, Scialdone A, Graja A, Gohlke S, Jank A-M, Bocian C, et al. Adipocyte Accumulation in the Bone Marrow During Obesity and Aging Impairs Stem Cell-Based Hematopoietic and Bone Regeneration. *Cell Stem Cell* (2017) 20:771–84. doi: 10.1016/j.stem.2017.02.009
34. Horowitz MC, Berry R, Holtrup B, Sebo Z, Nelson T, Fretz JA, et al. Bone Marrow Adipocytes. *Adipocyte* (2017) 6:193–204. doi: 10.1080/21623945.2017.1367881
35. Craft CS, Robles H, Lorenz MR, Hilker ED, Magee KL, Andersen TL, et al. Bone Marrow Adipose Tissue Does Not Express UCP1 During Development or Adrenergic-Induced Remodeling. *Sci Rep* (2019) 9:17427. doi: 10.1038/s41598-019-54036-x
36. Nishio M, Yoneshiro T, Nakahara M, Suzuki S, Saeki K, Hasegawa M, et al. Production of Functional Classical Brown Adipocytes From Human Pluripotent Stem Cells Using Specific Hemopoietin Cocktail Without Gene Transfer. *Cell Metab* (2012) 16:394–406. doi: 10.1016/j.cmet.2012.08.001
37. Piotrowska K, Tarnowski M. Bone Marrow Adipocytes-Role in Physiology and Various Nutritional Conditions in Human and Animal Models. *Nutrients* (2021) 13:1412. doi: 10.3390/nu13051412
38. Suchacki KJ, Tavares AAS, Mattiucci D, Scheller EL, Papanastasiou G, Gray C, et al. Bone Marrow Adipose Tissue Is a Unique Adipose Subtype With

Distinct Roles in Glucose Homeostasis. *Nat Commun* (2020) 11:3097. doi: 10.1038/s41467-020-16878-2
39. Pham TT, Ivaska KK, Hannukainen JC, Virtanen KA, Lidell ME, Enerback S, et al. Human Bone Marrow Adipose Tissue Is a Metabolically Active and Insulin-Sensitive Distinct Fat Depot. *J Clin Endocrinol Metab* (2020) 105:2300–10. doi: 10.1210/clinem/dgaa216
40. Xu F, Ding Y, Guo Y, Liu B, Kou Z, Xiao W, et al. Anti-Osteoporosis Effect of Epimedium *via* an Estrogen-Like Mechanism Based on a System-Level Approach. *J Ethnopharmacol* (2016) 177:148–60. doi: 10.1016/j.jep.2015.11.007

Conflict of Interest: The authors declare that the research was conducted in the absence of any commercial or financial relationships that could be construed as a potential conflict of interest.

Publisher's Note: All claims expressed in this article are solely those of the authors and do not necessarily represent those of their affiliated organizations, or those of the publisher, the editors and the reviewers. Any product that may be evaluated in this article, or claim that may be made by its manufacturer, is not guaranteed or endorsed by the publisher.

frontiers | Frontiers in Endocrinology

REVIEW
published: 21 June 2022
doi: 10.3389/fendo.2022.902033

Distinct Metabolism of Bone Marrow Adipocytes and their Role in Bone Metastasis

Yixuan Li[1†], *Shan Cao*[1,2†], *Anastasia Gaculenko*[2†], *Yifan Zhan*[3], *Aline Bozec*[2] *and Xiaoxiang Chen*[1*]

[1] Department of Rheumatology, Renji Hospital, Shanghai Jiao Tong University School of Medicine, Shanghai, China, [2] Department of Internal Medicine 3, Rheumatology and Immunology, Universitätsklinikum Erlangen, Friedrich-Alexander-Universität (FAU) Erlangen-Nürnberg, Erlangen, Germany, [3] Drug Discovery, Shanghai Huaota Biopharmaceutical Co. Ltd., Shanghai, China

Bone marrow adipocytes (BMAs) represent 10% of the total fat mass of the human body and serve as an energy reservoir for the skeletal niche. They function as an endocrine organ by actively secreting fatty acids, cytokines, and adipokines. The volume of BMAs increases along with age, osteoporosis and/or obesity. With the rapid development of multi-omic analysis and the advance in *in vivo* imaging technology, further distinct characteristics and functions of BMAs have been revealed. There is accumulating evidence that BMAs are metabolically, biologically and functionally unique from white, brown, beige and pink adipocytes. Bone metastatic disease is an uncurable complication in cancer patients, where primary cancer cells spread from their original site into the bone marrow. Recent publications have highlighted those BMAs could also serve as a rich lipid source of fatty acids that can be utilized by the cancer cells during bone metastasis, particularly for breast, prostate, lung, ovarian and pancreatic cancer as well as melanoma. In this review, we summarize the novel progressions in BMAs metabolism, especially with multi-omic analysis and *in vivo* imaging technology. We also update the metabolic role of BMAs in bone metastasis, and their potential new avenues for diagnosis and therapies against metastatic cancers.

Keywords: bone marrow adipocytes, lineage-tracing, metabolism, bone metastasis, multi-omic analysis

OPEN ACCESS

Edited by:
Guanwu Li,
Shanghai University of Traditional Chinese Medicine, China

Reviewed by:
Ren Xu,
Xiamen University, China
Xinfang Huang,
Shanghai East Hospital, China

***Correspondence:**
Xiaoxiang Chen
xiaoxiang0721@126.com

†These authors have contributed equally to this work

Specialty section:
This article was submitted to Bone Research, a section of the journal Frontiers in Endocrinology

Received: *22 March 2022*
Accepted: *06 May 2022*
Published: *21 June 2022*

Citation:
Li Y, Cao S, Gaculenko A, Zhan Y, Bozec A and Chen X (2022) Distinct Metabolism of Bone Marrow Adipocytes and their Role in Bone Metastasis. Front. Endocrinol. 13:902033. doi: 10.3389/fendo.2022.902033

INTRODUCTION

Several types of cancer cells evade clinical treatment by niching into the bone, such as cancer of the breat, prostate, lung and melanoma. Additionally, the bone marrow is a depot for fat-storing adipocytes, which poses a highly dynamic and metabolically active organ. Therefore, the role of bone marrow adipocytes (BMAs) and their effect on niching tumor cells and subsequent tumor growth are of clinical interest. Several studies have demonstrated that BMAs could function as an energy reservoir for the skeletal niche and serve as an endocrine organ secreting fatty acids, cytokines, and adipokines, supporting cancer cells to niche and grow within the bone marrow microenvironment. Because BMAs are deeply embedded in the bone marrow niche, the isolation of sufficient numbers of BMAs from rodent or human bone marrow remains a challenge. In contrast to

white adipose tissues embedded in a matrix consisting of collagen, fibronectin and laminin, BMAs are distributed as single cells or patches in the bone marrow (1). Moreover, their large size and buoyancy do not facilitate their isolation by pelleting or cell sorting. The previous histomorphometric methods could only supply limited descriptions about these cells at the cellular level, such as alterations in structure and organelles, but no further information about molecular changes. Therefore, the characterization of BMA functions in bone metastasis is currently challenging.

Nevertheless, these gaps in understanding the underlying mechanisms have been largely filled in the recent decade due to the rapid development of multi-omic analysis and *in vivo* imaging. Technologies as RNA-seq, single-cell RNA-seq (scRNA-seq), gas chromatography-mass spectrometry (GC-MS), or liquid chromatography-mass spectrometry (LC-MS), gave insights into the transcriptomic, proteomic, and metabolic depth of BMAs. Using lineage tracing, fate mapping technologies and positron emission tomography-computed tomography (PET/CT) with 18F-fluorodeoxyglucose ([^{18}F]FDG), distinct characteristics and functions of BMAs have been revealed in both rodents and humans. Recent findings demonstrate the importance of BMAs as metabolically, biologically, and functionally unique adipocyte subsets distinct from white, brown, beige and pink adipocytes. Here, we summarize the novel research on BMAs, especially the unique metabolic specificity and their potential function in supporting bone metastasis.

ANATOMY

In the human body, BMAs are mainly located in the arms, legs, and sternum but rarely in the clavicle, ribs, and vertebrae (2). Meanwhile BMAs can also be observed in caudal (tail) vertebrae but not in thoracic or lumbar vertebrae (3). Interestingly, in human adults, BMAs represent around 10% of the total adipose tissue mass (4). By the age of 25 years, around 70% of the bone marrow volume in healthy adults is filled with BMAs (5). These cells can mainly be found in long bones in early adulthood. However, around 60 years of age and over, BMAs display age-associated increases in the axial skeleton (6). In long bones, BMAs dwell among the trabecular bone of the epiphysis and metaphysis or close to the endosteal surface of the diaphysis (7). BMAs have been historically overlooked and were considered "fillers" of the inert space for a long time (7). However, with the increasing interest in immunometabolism, they have raised more attention, especially for their distinct metabolic process and the consequent functional alterations.

As early as 1976, Tavassoli has discovered two distinct populations of BMAs in the bone marrow: the performic acid-Schiff (PFAS) – positively stained BMAs in red marrow and the PFAS-negatively stained BMAs in yellow marrow. The two populations also respond differently during the expansion of hematopoiesis (8). In 2015, using the osmium tetroxide staining, Scheller et al. defined for the first time regulated bone marrow adipocytes (rBMAs or red marrow BMAs) and constitutive bone marrow adipocytes (cBMAs or yellow marrow BMAs) (9). cBMAs develop after birth, are large in size and localized in close proximity to each other with a lack of hematopoietic cells in between (10). Their lipid storages mainly contain unsaturated fatty acids. In contrast, the smaller rBMAs develop throughout life and contain mostly saturated fatty acids. In steady state, rBMAs are single cells distributed within areas of active hematopoiesis.

Several environmental factors have been reported to promote the dynamic changes of BMAs. In several publications and our own data, high-calorie feeding such as high-fat diet increases number and size of BMAs. Here, mostly rBMAs localized in the metaphysis of the proximal tibia expand as response to changes in diet and diseases (11, 12). The special location of fat induced expansion of BMAs was confirmed in humans suffering from obesity, diabetes and/or osteoporosis (13, 14). In mice, irradiation and activation of the adipocyte differentiation pathway Peroxisome proliferator-activated receptor gamma (PPARγ) leads to a steady induction of BMA expansion (15). Additionally, expansion of BMAs can be observed in murine models of aging or ovariectomy-induced osteoporosis similar to the observations in patients (16, 17). Intriguingly, caloric deprivation in patients also increases the number of BMAs with gender difference regarding their localization, in L4 vertebra for men and at the femoral metaphysis for women (13). In addition, the psychiatric disease anorexia nervosa paradoxically leads to expanded bone marrow adipose tissue, while other fat depots in the body are reduced in size (18).

ORIGIN

The origin of BMAs has been investigated for decades and is still updating thanks to the development of advanced technologies. In 1976, BMAs were first depicted as derived from a unique progenitor distinct from white adipocytes (19). Nevertheless, due to the limited technical conditions, the differences between BMAs and their extramedullary counterpart were only described roughly according to their morphology. Nowadays, lineage tracing reporter mice and the large-scale, single-cell RNA-sequencing (scRNA-seq) have helped to delineate their features in more details.

BMAs are thought to be derived from Sca1$^+$ CD45$^-$ CD31$^-$ or LepR$^+$ CD45$^-$ CD31$^-$ mesenchymal stem cells (MSCs) in the bone marrow (20, 21). Using *in vivo* cell lineage tracing of the dTomato$^+$ in *Vav1-Cre: mT/mG* mice, BMAs are further confirmed to be originated from MSCs but not hematopoietic stem cells (HSCs) (22, 23). Pathway enrichment analysis also displayed that BMAs are closer to bone marrow mesenchymal stem cells (BMSCs) than to white adipocytes (24). Moreover, in contrast to brown adipocytes, BMAs are all dTomato$^-$ in *Myf5-Cre: mT/mG* mice (25, 26). This indicates that BMAs do not share the same progenitors as brown adipocytes. Further studies demonstrated that BMA progenitors can express Prx1 and Osx1, two markers labelling mesenchymal-osteogenic cells, while white

and brown adipocytes cannot be traced in Osx1-Cre reporter mice (27, 28). In another study, using the lineage tracing of $Adipoq^{Cre+/mTmG+}$ and $UCP1^{Cre+/mTmG+}$ mice, BMAs were demonstrated to not express *UCP1* during development or upon the stimulation of β3-adrenergic agonist CL316,243 (29). These results indicate that BMAs derive from a mesenchymal-osteogenic lineage, and are genetically distinct from white, beige or brown adipocytes. Most recently, with the help of $Adipoq^{Cre+/DTA+/mTmG+}$ triple mutant mice, a defined cluster of adiponectin-negative stromal progenitors has been shown in the bone marrow of fat-free mice. This population was able to differentiate into ectopic BMAs with age and metabolic diseases. These BMAs have increased lipid storage and are not thermogenic as they are unresponsive to cold stress or β3-adrenergic stimulation (30). Despite that adiponectin is an essential adipocyte specific cytokine, the discovery of adiponectin-independent BMA subsets allows to speculate that further origins of BMAs remain to be revealed. Indeed, Zhong et al. have already defined a new population in the bone marrow from their scRNA-seq data, termed marrow adipogenic lineage precursors (MALPs) (31). This subpopulation expresses typical adipocyte markers as *Pparg, Cebpa, Adipoq, Apoe*, and *Lpl*, but not *Plin1*, thus containing no lipid droplets. They are not proliferative precursors for adipocytes but are essential for maintaining marrow vasculature and promoting pathologic bone loss in a RANKL-dependent manner (32, 33). Together, these data have vastly enriched the framework between MSCs and mature adipocytes, bringing more directions for future investigations.

The differentiation fate of BMAs from MSCs is also rigorously regulated by transcriptional cascades (34) (**Figure 1**). The transcription factors CCAAT/enhancer-binding protein CEBPβ and δ are induced primarily during early adipogenesis. Then they activate the expression of two critical adipogenic transcription factors: PPARγ and CEBPα (37). Expression of *Cepba* and *Cebpb* are selectively elevated in cBMAs of rats compared to rBMAs and subcutaneous white adipocytes (9). In addition, the tug-of-war between adipocytes and osteoblast differentiation in the bone marrow is also determined by many pathways such as Wnt/β-catenin and Leptin/LepR signaling. Wnt/β-catenin signaling promotes a cell fate shift from adipocytes to pre-osteoblasts (35, 36), while Leptin/LepR signaling facilitates adipogenesis and inhibits osteogenesis (21) (**Figure 1**).

In addition to the rigorous regulation of transcription cascades of BMA differentiation, the dynamic and complex bone marrow microenvironment could also be an essential contributor. Osteocyte-derived sclerostin, a glycoprotein encoded by *SOst* gene, could promote the expression of the adipogenic

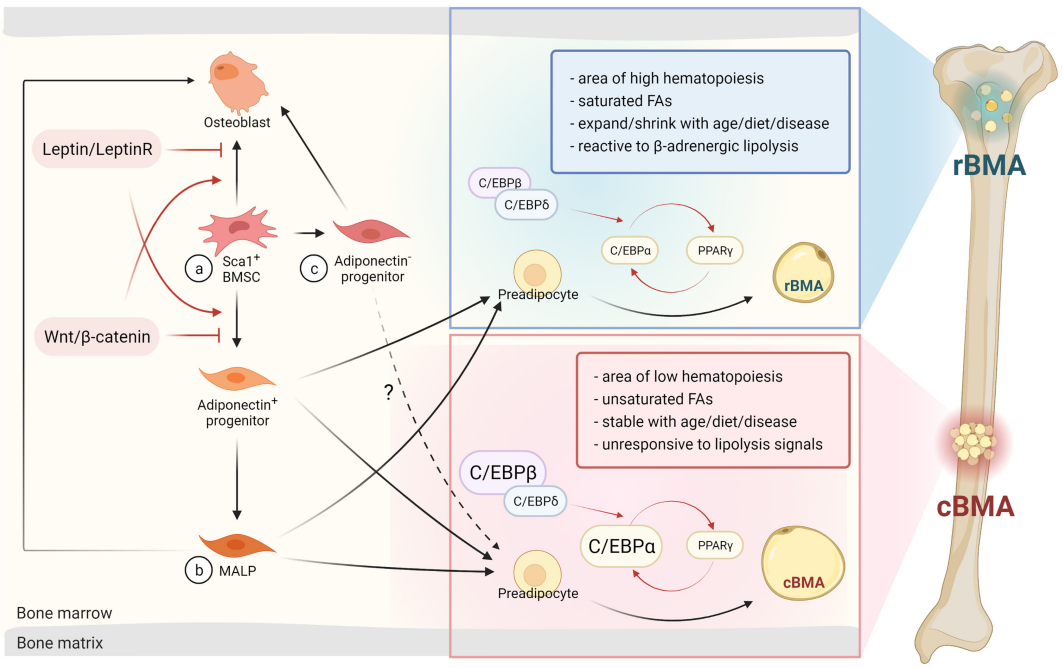

FIGURE 1 | BMAs arise from BMSCs and can differentiate *via* osteogenic or adipogenic progenitors into rBMAs or cBMAs. **(A)** BMAs or osteoblasts originate from Sca1$^+$ BMSCs modulated by the Leptin/LeptinR or Wnt/β-catenin signaling pathways (20–23, 35, 36). **(B)** MALPs are a newly defined primarily adipogenic sub-population that arises from adiponectin$^+$ progenitors. Factors like acute injury and aging can trigger osteogenic differentiation of MALPs (30, 31). **(C)** Adiponectin$^-$ progenitors are predominantly of the osteogenic lineage, but are also able to differentiate into BMAs in metabolic disorders or in aging adults. This population elicits similar properties as cBMAs (30). BMSC, bone mesenchymal stem cells; rBMA, regulated bone marrow adipocyte; cBMA, constitutive bone marrow adipocyte; MALP, marrow adipogenic lineage precursor; C/EBP, CCAAT/enhancer-binding protein; FA, fatty acid; PPARγ, peroxisome proliferator-activated receptor gamma. Red arrows indicate transcription factors and signaling pathways. Dark arrows represent the consecutive stage of differentiation. The dashed arrow emphasizes similarities in cBMAs and adiponectin$^-$ progenitor-derived BMAs. Designed by Biorender.

transcription factors *Pparγ* and *Cebpα* in primary MSCs from both humans and mice *in vitro*. As a consequence, the adipocyte differentiation *via* inhibition of the canonical Wnt signaling pathway was enhanced. *In vivo* studies also found decreased BMA formation in both sclerostin knock-out mouse models and wild-type mice treated with a sclerostin neutralizing antibody (38–40). These studies demonstrated a role for *SOst* and osteocyte-derived sclerostin in regulating fate determination of BMA progenitors. Bone morphogenetic proteins (BMPs) could also promote adipogenesis by promoting the expression of *Pparγ* and *Cebpα* (41). Bajaj and colleagues reported that *BMP4* was highly expressed and secreted especially by T cells and stromal cells in response to irradiation. Thereby, the adipogenic commitment of the M2-10B4 cell line and primary murine MSCs were promoted. This could probably be one of the causes of marrow adipogenesis post-myelosuppression (42). These extrinsic factors generated by the marrow microenvironment may contribute to the distinct metabolic features and function of BMAs compared to white adipocytes, even though much still remains to be further elucidated.

METABOLIC FEATURES

Recent technologies have also unveiled numerous novel metabolic features of BMAs. Attané and colleagues compared the proteomic and lipidomic features of BMAs with subcutaneous fat tissue and concluded that BMAs display a distinct lipid metabolism contrary to classical white adipocytes (45). Pathway enrichment in proteomic results displayed elevated cholesterol metabolism in BMAs, which was further confirmed by a 1.5-fold increase in free cholesterol content and decreased lipolytic activity in BMAs. Moreover, more sphingosine, fewer ceramides and sphingomyelin were observed in the lipid profiles of BMAs compared to subcutaneous white adipocytes. The monoacylglycerol lipase (MGLL) expression is reduced with monoacylglycerol (MG) species elevated in BMAs, implying on an impaired MG hydrolysis compared to subcutaneous fat tissues. The altered lipid metabolism is also corroborated in another study, delineating that human BMAs possess distinct gene expression profiles, especially in regulating lipid metabolism, stemness genes, and browning pathways compared to subcutaneous adipose tissue (24). The overall steady state molecular signature of BMAs was described more comparable to brown adipocytes. In contrast, BMA expansion by aging or diabetes leads to a steady energy storing, white adipocyte-resembling metabolic signature (46). Scheller et al. also reported the diminished lipid hydrolysis in BMAs compared to white adipose tissue in response to β-adrenergic stimulation, mainly in distal regions (47). Transcriptomic analysis in rabbits also revealed decreased glycerol content, insulin resistance, reduced lipid synthesis, and transport, decreased fatty acid metabolism, and decreased thermoregulation in BMAs compared to white adipocytes. Reduction in fatty acid β-oxidation (FAO) and oxidative phosphorylation were also found in BMAs (29).

The glucose metabolism in BMAs and their role in systemic glucose homeostasis are also unique. The transcriptome analysis in rabbits and humans both revealed an altered glucose metabolism and diminished insulin responsiveness in BMAs compared to white adipocytes, while markers of brown or beige adipocytes were enriched. Using PET/CT and [^{18}F] FDG, it was recently demonstrated that BMAs possess high basal glucose uptake both in rodents and humans but are unresponsive to insulin, cold exposure and glucocorticoids (2). However, in another clinical trial, Tam et al. as well used PET/CT and [^{18}F] FDG to characterize the glucose uptake (GU) in human femoral and vertebral BMAs, found that insulin enhances GU in human femoral BMAs (48). These two conflicting results indicate that different species (rodents vs. human) and different sites (distal tibia BMAs vs. femur BMAs) vary significantly in BMA metabolism.

Metabolic programming also plays an important role in regulating BMA differentiation. BMA progenitors display higher insulin-dependent glucose utilization, enhanced capacity for oxidative phosphorylation (OXPHOS) and lipid storage, while osteoblast progenitors exhibit diminished insulin signaling, glycolysis-prone energy production, and reduced lipid storage (49). Moreover, metabolic changes in diseases such as obesity, diabetes and anorexia nervosa could also affect the formation of BMAs. Dyslipidemia caused by overnutrition in obesity facilitates BMA expansion and BMAs could then buffer extra energy in the form of triglycerides (50). The impaired lipid metabolism of type 2 diabetes (T2D) is characterized by the elevated low-density lipoprotein (LDL) cholesterol and free fatty acids, high concentration of plasma triglyceride and decreased high-density lipoprotein (HDL) cholesterol (51). This kind of hyperlipidemia could probably be associated with the enhanced adiposity of the bone marrow, for fatty acids could bind and activate PPARγ (52). In addition, hyperglycemia could induce expression of PPARγ by activating PI3K/Akt pathway and therefore enhance the adipogenicity of MSCs (53). The production of reactive oxygen species (ROS) resulting from the increased glucose levels in T2D could also promote the expression of genes associated with adipogenesis (54, 55). Starvation or fasting caused by anorexia nervosa also leads to hyperlipidemia (56), which could probably partly explain the expanded BMAs mentioned before. Collectively, BMA formation seems to be much closer to serum lipid levels than the type of diseases.

The number of BMAs and osteoblasts might be reciprocal, since they are competing for the same original stem cells. However, BMAs could also interfere with skeletal homeostasis and bone remodeling *via* its metabolic activities (57). The maintenance of bone mass depends on the dynamic and precise coordination of osteoclast-dominated bone resorption and osteoblast-mediated bone formation (58, 59). Studies in rats and dogs indicated reduced osteoblast activity, osteoclast numbers and increased bone loss at sites with higher BMA numbers (57). As osteoblasts are highly dependent on fatty acids for their glycolytic energy production, taking up to 80%, intact BMAs could be of importance for osteoblast function (60, 61). Moreover, Fatty acids, cholesterol, phospholipids and endogenous metabolites have been proven to regulate

numerous signaling pathways mediating the proliferation and function of local osteoclasts and osteoblasts (62). Besides energy resources, BMAs may also protect osteoblasts from lipotoxicity (63). Other studies have shown the existence of BMA-derived exosomes filled with adipogenic factors and anti-osteoblastic miRNAs that are able to alter osteoblast function (64). Nevertheless, the role of BMA metabolism on bone cell survival and function remains poorly understood, and would require further investigation.

METABOLIC ROLE IN BONE METASTASIS

Bone is one of the main organs for metastasis by various tumors. Hernandez et al. have retrospectively analyzed the real world electronic medical record data from oncology practices in the US and estimated the cumulative incidence of bone metastasis among patients with various solid tumors (65). The prostate cohort had the highest risk of bone metastasis with an incidence of 18.0% at one year, 20.4% at two years, 24.5% at five years, and 29.2% at ten years followed by lung (10.4-12.9%), renal (5.8-9.9%), breast (3.4-8.1%), gastrointestinal (2.3-3.6%), malignant melanoma (1.6-3.0%) and other tumors. In addition, the incidence of bone metastasis increased by the stage at diagnosis in all studied tumors. Another retrospective population-based study using data (2010-2015) from Surveillance, Epidemiology, and End Results (SEER) program, has reported that 5.7% of cancer patients suffer from bone metastasis (66). The third most vital factor for cancer is obesity, while smoking and infection pose number 1 and 2, respectively (67). Indeed, approximately 40% of cancers are associated with the excess of body weight (68). Researchers were able to show, that the risk of metastasis formation in obese breast cancer patients is increased by 46% (69). Overall, the link between the expansion of adipose tissue and metastasis formation has become evident in the recent decade, while the mechanism underlying bone metastases and BMAs remains unclear to date.

The novel findings in the metabolism of BMAs could be of vital importance for the understanding of tumor cell niching and growth in the bone marrow (**Figure 2**). In our previous work, we were able to observe that increased numbers of BMAs lead to accelerated melanoma tumor growth in the bone marrow and can be abrogated by inhibiting the adipocyte differentiation *via* PPARγ with the pharmacological compound bisphenol-A-diglycidylether (BADGE) (11, 12). Further experiments demonstrated that increased adipogenic differentiation of pre-adipocytes boosted by melanoma cell-derived factors led to the increase of BMAs at the early stage of bone metastasis, which further favored the tumor cells to niche and proliferate (70). Moreover, it is known that upregulated number of BMAs after chemotherapy and radiotherapy can correlate with tumor evasion (71). Finally, the facts that bone metastasis occurs preferentially in older people who have a higher portion of

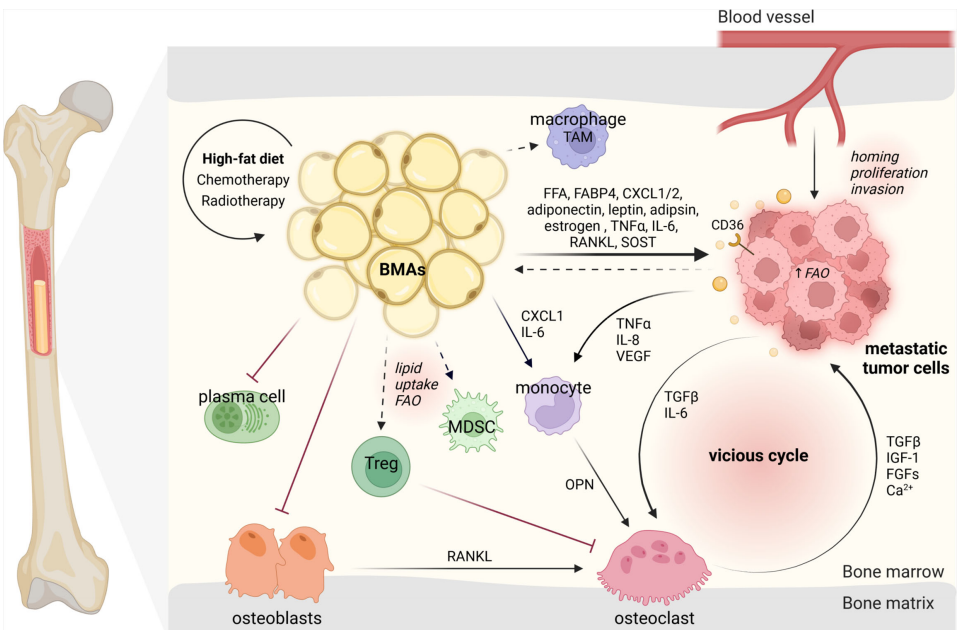

FIGURE 2 | BMAs modulate their surrounding microenvironment and interact with niching tumor cells and bone marrow-resident cells. BMAs, bone marrow adipocytes; TAM, tumor-associated macrophage; FFA, free fatty acid; FABP4, fatty acid-binding protein 4; CXCL1/2, C-X-C motif ligand 1/2; FAO, fatty acid oxidation; TNFα, tumor necrosis factor alpha; VEGF, vascular endothelial growth factor; TGFβ, transforming growth factor beta; IGF-1, insulin-like growth factor-1; FGFs, fibroblast growth factors; OPN, osteopontin; RANKL, receptor activator of NF-κB ligand; Tregs, regulatory T cells. The dark arrows indicate relationships, while dashed arrows represent potential links (43, 44). Designed by Biorender.

adipocytes in the bone marrow, and that BMAs rapidly expand (9-32%) in tumor patients over one year (72) further confirmed the close connection between BMAs and bone metastasis. As a result, the involvement of BMAs in the "vicious cycle" of tumor cells and bone cells seems to accelerate tumor growth. However, recent starving therapies have obtained a gratified result in eliciting an anti-tumor response (73, 74), while BMAs were also observed elevated in these fasting-like conditions. The ambiguous results may depend on the type of the tumor cells and stage of the disease, or the individual state of BMA subsets.

In general, tumor cells metastasize to rBMAs-enriched regions (proximal femur, hip, and lumbar spine) which contain smaller and less stable adipocytes (75). This preference may be directly connected to the distribution of blood vessels allowing distinct distribution of nutrition and oxygen concentration (76). The mechanisms underlying the pro-tumor effects of BMAs have attracted considerable attention. Many publications have discussed the importance of adipokines released by BMAs in bone metastasis, such as adiponectin (71), leptin (77), adipsin (78) and estrogen (79). Others have focused on the pro-inflammatory cytokines released by BMAs like TNFα, IL-6 and RANKL or target on BMAs like sclerostin (75, 80). But the metabolic functions of BMAs during bone metastasis have been less reviewed.

BMAs are a direct power station for tumor cells *via* lipolysis and lipid transfer (81). Using the vibrational spectroscopic technique-Fourier transform infrared (FTIR) microspectroscopy, Ehsan and his colleagues demonstrated that prostate cancer cells take up isotopically labeled FA [deuterated palmitic acid (D(31)-PA)] from human MSC-derived adipocytes (82). Furthermore, they also observed the lipid uptake of prostate cancer cells from nearby BMAs in the bone metastases specimens from patients, providing direct evidence of BMAs inducing tumor growth (83). BMAs could also shape tumor cell metabolism, contributing to their growth and metastasis. Podgorski and colleagues demonstrated that lipids from BMAs could fuel prostate tumor cells by upregulating CD36, FABP4, and Perilipin 2, supporting fatty acid transport (84). They also proved that BMAs drive metabolic reprogramming of tumor cells *via* an oxygen-independent mechanism of HIF-1α activation (85). CD36 is a scavenger receptor found on tumor cells, which was shown to be vital for metastasis formation and is currently considered as a potential therapeutic target (86, 87). It can be activated by free fatty acids secreted by BMAs and thus promote cancer growth (88). For prostate cancer bone metastases, researchers were able to show that the oxidative and endoplasmic reticulum (ER) stress pathways activated in BMAs can upregulate the secretion of survivin and heme oxygenase 1 to facilitate tumor cell survival (89). Other studies have demonstrated BMAs to drive FAO in tumor cells embedded in the bone marrow (88). As a parallel research field, bone cancers show similar indications for BMA mediated FAO. In acute monocytic leukemia, BMAs promote the cell survival by facilitating FAO *via* the stress response-associated AMP-activated protein kinase (AMPK). Thus, FAO in BMAs could also be considered as potential therapeutic target in the fight against bone metastases (90). The investigation of adipocyte-rich tissues revealed that ovarian, pancreatic and breast tumor cells can reprogram adipocytes to cancer-associated adipocytes (CAA). This phenotype aids the tumor growth by adipocyte dedifferentiation and release of their lipids, thereby promoting migration, proliferation, survival and chemoresistance (91–93). In this context, Liu et al. were able to show that BMAs can be reprogrammed to support myeloma-induced bone disease (94). Nevertheless, it remains unclear whether BMAs can dedifferentiate into the same tumor-aiding phenotype as found in other adipose tissues. Regarding overall lipid metabolism, researchers have shown that caprylic acid (C8:0) was increased in prostate cancer patients with diagnosed bone metastases (95). These results open a novel research avenue to study the various fatty acid-influenced molecular actions in the BMA-tumor cell interplays.

BMAs may also shape the microenvironment in the bone marrow in aid of tumor cell colonization (96). An expansion of BMAs with age was shown to be associated with a decreased bone mineral density (BMD) in patients (97). Similarly, experiments in mice demonstrated that high-calorie diets induce a shift from osteoblast to adipocyte differentiation, while increasing parameters for osteoclast activity (12). In addition, BMAs can promote osteoclastogenesis by mediation of osteoblast-secreted RANKL (98). These phenotypes are contributing to the severity of BMA-induced tumor burden, by driving osteoclastogenesis and thereby osteolytic lesion formation *via* IL-6 or indirectly *via* CXCL1 and osteopontin (OPN) (11). The CXCL1 and CXCL2 derived from BMAs were shown to promote prostate cancer survival and stiffen the overall tumor immune response (88, 99). Along this line, these chemokines could potentially attract macrophages and attribute to the distinct BMA-altered microenvironment. Studies in omental adipocytes have demonstrated to induce tumor-associated-macrophage polarization by upregulation of *Pparb* expression (88). Further research is needed to define the specific role of monocyte and macrophage sub-populations dependent on the presence of BMAs on the growth of tumor cells. Concerning the B cell lineage, BMAs were shown to overall impair the function of plasma cells compared to other adipocytes in humans (100). However, B cells in bone tumor niches remain an untouched area of research. Nevertheless, BMAs seem to play a pivotal role in the bone niche allowing the tumor cells to move in and grow.

While the fact that BMA-induced direct metabolic alterations on tumor cells poses a relatively wide scientific base, the effect on the metabolism of other resident cells and metastatic tumor progression remains to be largely under-studied. Researchers have shown the importance of metabolism in various tumor microenvironments. Therefore, it stands to reason that BMAs could influence their microenvironment in a similar way. For instance in other murine tumor tissues, it was shown that lipid uptake and FAO in myeloid-derived suppressor cells (MDSCs) facilitate their inhibitory role on anti-tumor T cells and promote tumor cell growth and migration (101, 102). Researchers could also show that tumor regulatory T cells (Tregs) suppress anti-tumor responses. At the same time the lipid metabolism supports the survival and function of Tregs within the hypoxic tumor

microenvironment (103, 104). As Tregs also modulate osteoclasts, a potential link should be investigated (105). Moreover, in obese mice, creatine is a key metabolite linking adipocytes and breast tumors (106). Even though it is still unknown whether this fits for BMAs and the skeletal metastatic cells, creatine has been reported to promote the antitumor immune activity of $CD8^+$ T cells and reduce the proliferation of subcutaneous tumors (107). Altogether, BMAs and their contribution to bone metastasis growth need to be further elucidated.

LIMITATIONS AND PERSPECTIVES

Taken together, BMAs are distinct from other adipocyte fat depots, especially in the context of transcriptome, metabolism and functions to direct tumor growth. With novel emerging technologies, more information beneath the tip of the BMA iceberg has been unveiled, and BMAs might be considered as potential target to counteract the bone metastasis in a manner of individual treatment. However, their functions are still puzzling and would require further investigation.

While BMAs in their regulated or constitutive form are better characterized in rodents, this topic remains under-studied in patients. As humans have higher bone marrow adiposity than rodents, the role of BMAs in altering the surrounding environment may differ as well. Studies have shown contradicting conclusions regarding GU and insulin response in rodents versus humans. Here, the lack of receptors or other dissimilarities of the different species have to be taken in account. In humans, the insulin-producing beta cells lack a part of the G-protein-coupled receptor as compared to mice (108). Another dissimilarity observed between the species, was the sex-specific increased rBMA content in female versus male mice (9, 109). Overall, it has to be further elucidated whether the sexual dimorphism in rodent BMAs as well as human white adipose tissue is also reflected on human BMAs (110, 111). It is also important to mention that most of the findings are based on *in vitro* co-culture of diverse tumor cells with isolated bone marrow mesenchymal cells-induced adipocytes or differentiated pre-adipocyte cell lines (e.g. 3T3-L1). However, the reduced lipolytic activity in BMAs *in vivo* could not be recapitulated *in vitro* using these bone marrow mesenchymal stem cells (24, 45). It is always questionable to call *in vitro* differentiated adipocytes real BMAs, as the underlying microenvironmental factors distinguishing them from non-BMAs are lacking. Thus, future studies should rely on the direct *in vivo* evidence between BMAs and tumor cells. Also, the different metabolic or functional manners between BMAs and other adipocyte fat depots in supporting tumor cells colonization should be separately delineated.

Nevertheless, the animal models precisely tracing and locating rBMAs and cBMAs *in vivo* are also what we desperately need in future studies. The animal models will be beneficial for the investigations of BMA subpopulations. Exploit of *Ptrf* knockout initiates the first step towards establishing the rBMAs ablation model (9). Simultaneously, we are also confident that more and preciser markers of these adipocyte subpopulations will emerge in the future due to the utilization of large-scale scRNA-seq analyses. Advanced in-depth analyzing strategies may further help eliminate the contamination of BMAs surrounding cells such as osteoblasts and hematopoietic cells (45).

In addition, future studies need to explore the site-dependent lipid types (rBMAs vs. cBMAs) (9), cellular source and subcellular localization of the altered fatty acids. These investigations will help to quantify the impact of BMAs on local and systemic metabolism, and their function in steady-state or with tumor burden. Thus, the pro-tumor and anti-tumor roles of BMAs will be defined further in the future.

AUTHOR CONTRIBUTIONS

XC, YZ and AB designed this review. YL, SC and AG wrote the manuscript. All authors contributed to the article and approved the submitted version.

FUNDING

This study was supported by the National Natural Science Foundation of China (81771729, 81971534). This project was also supported by the German Research Foundation (DFG) priority program SPP2084 μBONE. BO-3811/5–1; BO-3811/6–1, Collaborative Research Centre 1181 project A01, Interdisciplinary Center for Clinical Research grant A77 and J76, The European Research Council consolidator grant ODE.

REFERENCES

1. Ruiz-Ojeda FJ, Mendez-Gutierrez A, Aguilera CM, Plaza-Diaz J. Extracellular Matrix Remodeling of Adipose Tissue in Obesity and Metabolic Diseases. *Int J Mol Sci* (2019) 20(19):4888. doi: 10.3390/ijms20194888
2. Suchacki KJ, Tavares AAS, Mattiucci D, Scheller EL, Papanastasiou G, Gray C, et al. Bone Marrow Adipose Tissue Is a Unique Adipose Subtype With Distinct Roles in Glucose Homeostasis. *Nat Commun* (2020) 11(1):3097. doi: 10.1038/s41467-020-16878-2
3. Naveiras O, Nardi V, Wenzel PL, Hauschka PV, Fahey F, Daley GQ. Bone-Marrow Adipocytes as Negative Regulators of the Haematopoietic Microenvironment. *Nature* (2009) 460(7252):259–63. doi: 10.1038/nature08099
4. Scheller EL, Burr AA, MacDougald OA, Cawthorn WP. Inside Out: Bone Marrow Adipose Tissue as a Source of Circulating Adiponectin. *Adipocyte* (2016) 5(3):251–69. doi: 10.1080/21623945.2016.1149269
5. Fazeli PK, Horowitz MC, MacDougald OA, Scheller EL, Rodeheffer MS, Rosen CJ, et al. Marrow Fat and Bone–New Perspectives. *J Clin Endocrinol Metab* (2013) 98(3):935–45. doi: 10.1210/jc.2012-3634

6. Baum T, Rohrmeier A, Syvari J, Diefenbach MN, Franz D, Dieckmeyer M, et al. Anatomical Variation of Age-Related Changes in Vertebral Bone Marrow Composition Using Chemical Shift Encoding-Based Water-Fat Magnetic Resonance Imaging. *Front Endocrinol (Lausanne)* (2018) 9:141. doi: 10.3389/fendo.2018.00141
7. Morris EV, Edwards CM. Bone Marrow Adipose Tissue: A New Player in Cancer Metastasis to Bone. *Front Endocrinol (Lausanne)* (2016) 7:90. doi: 10.3389/fendo.2016.00090
8. Tavassoli M. Marrow Adipose Cells Histochemical Identification of Labile and Stable Components. *Arch Pathol Lab Med* (1976) 100(1):16–8.
9. Scheller EL, Doucette CR, Learman BS, Cawthorn WP, Khandaker S, Schell B, et al. Region-Specific Variation in the Properties of Skeletal Adipocytes Reveals Regulated and Constitutive Marrow Adipose Tissues. *Nat Commun* (2015) 6:7808. doi: 10.1038/ncomms8808
10. Craft CS, Li Z, MacDougald OA, Scheller EL. Molecular Differences Between Subtypes of Bone Marrow Adipocytes. *Curr Mol Biol Rep* (2018) 4(1):16–23. doi: 10.1007/s40610-018-0087-9
11. Chen GL, Luo Y, Eriksson D, Meng X, Qian C, Bauerle T, et al. High Fat Diet Increases Melanoma Cell Growth in the Bone Marrow by Inducing Osteopontin and Interleukin 6. *Oncotarget* (2016) 7(18):26653–69. doi: 10.18632/oncotarget.8474
12. Gaculenko A, Gregoric G, Popp V, Seyler L, Ringer M, Kachler K, et al. Systemic Ppargamma Antagonism Reduces Metastatic Tumor Progression in Adipocyte-Rich Bone in Excess Weight Male Rodents. *J Bone Miner Res* (2021) 36(12):2440–52. doi: 10.1002/jbmr.4422
13. Fazeli PK, Bredella MA, Pachon-Pena G, Zhao W, Zhang X, Faje AT, et al. The Dynamics of Human Bone Marrow Adipose Tissue in Response to Feeding and Fasting. *JCI Insight* (2021) 6(12):e138636. doi: 10.1172/jci.insight.138636
14. Veldhuis-Vlug AG, Rosen CJ. Clinical Implications of Bone Marrow Adiposity. *J Intern Med* (2018) 283(2):121–39. doi: 10.1111/joim.12718
15. Sebo ZL, Rendina-Ruedy E, Ables GP, Lindskog DM, Rodeheffer MS, Fazeli PK, et al. Bone Marrow Adiposity: Basic and Clinical Implications. *Endocr Rev* (2019) 40(5):1187–206. doi: 10.1210/er.2018-00138
16. Kajkenova O, Lecka-Czernik B, Gubrij I, Hauser SP, Takahashi K, Parfitt AM, et al. Increased Adipogenesis and Myelopoiesis in the Bone Marrow of Samp6, a Murine Model of Defective Osteoblastogenesis and Low Turnover Osteopenia. *J Bone Miner Res* (1997) 12(11):1772–9. doi: 10.1359/jbmr.1997.12.11.1772
17. Kurabayashi T, Tomita M, Matsushita H, Honda A, Takakuwa K, Tanaka K. Effects of a Beta 3 Adrenergic Receptor Agonist on Bone and Bone Marrow Adipocytes in the Tibia and Lumbar Spine of the Ovariectomized Rat. *Calcif Tissue Int* (2001) 68(4):248–54. doi: 10.1007/s002230001203
18. Fazeli PK, Klibanski A. The Paradox of Marrow Adipose Tissue in Anorexia Nervosa. *Bone* (2019) 118:47–52. doi: 10.1016/j.bone.2018.02.013
19. Tavassoli M. Ultrastructural Development of Bone Marrow Adipose Cell. *Acta Anat (Basel)* (1976) 94(1):65–77. doi: 10.1159/000144545
20. Ambrosi TH, Scialdone A, Graja A, Gohlke S, Jank AM, Bocian C, et al. Adipocyte Accumulation in the Bone Marrow During Obesity and Aging Impairs Stem Cell-Based Hematopoietic and Bone Regeneration. *Cell Stem Cell* (2017) 20(6):771–84.e6. doi: 10.1016/j.stem.2017.02.009
21. Yue R, Zhou BO, Shimada IS, Zhao Z, Morrison SJ. Leptin Receptor Promotes Adipogenesis and Reduces Osteogenesis by Regulating Mesenchymal Stromal Cells in Adult Bone Marrow. *Cell Stem Cell* (2016) 18(6):782–96. doi: 10.1016/j.stem.2016.02.015
22. Zmuidzinas A, Fischer KD, Lira SA, Forrester L, Bryant S, Bernstein A, et al. The Vav Proto-Oncogene Is Required Early in Embryogenesis But Not for Hematopoietic Development in Vitro. *EMBO J* (1995) 14(1):1–11. doi: 10.1002/j.1460-2075.1995.tb06969.x
23. Katzav S, Martin-Zanca D, Barbacid M. Vav, a Novel Human Oncogene Derived From a Locus Ubiquitously Expressed in Hematopoietic Cells. *EMBO J* (1989) 8(8):2283–90. doi: 10.1002/j.1460-2075.1989.tb08354.x
24. Mattiucci D, Maurizi G, Izzi V, Cenci L, Ciarlantini M, Mancini S, et al. Bone Marrow Adipocytes Support Hematopoietic Stem Cell Survival. *J Cell Physiol* (2018) 233(2):1500–11. doi: 10.1002/jcp.26037
25. Seale P, Bjork B, Yang W, Kajimura S, Chin S, Kuang S, et al. Prdm16 Controls a Brown Fat/Skeletal Muscle Switch. *Nature* (2008) 454(7207):961–7. doi: 10.1038/nature07182
26. Horowitz MC, Berry R, Holtrup B, Sebo Z, Nelson T, Fretz JA, et al. Bone Marrow Adipocytes. *Adipocyte* (2017) 6(3):193–204. doi: 10.1080/21623945.2017.1367881
27. Chen J, Shi Y, Regan J, Karuppaiah K, Ornitz DM, Long F. Osx-Cre Targets Multiple Cell Types Besides Osteoblast Lineage in Postnatal Mice. *PLoS One* (2014) 9(1):e85161. doi: 10.1371/journal.pone.0085161
28. Logan M, Martin JF, Nagy A, Lobe C, Olson EN, Tabin CJ. Expression of Cre Recombinase in the Developing Mouse Limb Bud Driven by a Prxl Enhancer. *Genesis* (2002) 33(2):77–80. doi: 10.1002/gene.10092
29. Craft CS, Robles H, Lorenz MR, Hilker ED, Magee KL, Andersen TL, et al. Bone Marrow Adipose Tissue Does Not Express Ucp1 During Development or Adrenergic-Induced Remodeling. *Sci Rep* (2019) 9(1):17427. doi: 10.1038/s41598-019-54036-x
30. Zhang X, Robles H, Magee KL, Lorenz MR, Wang Z, Harris CA, et al. A Bone-Specific Adipogenesis Pathway in Fat-Free Mice Defines Key Origins and Adaptations of Bone Marrow Adipocytes With Age and Disease. *Elife* (2021) 10:e66275. doi: 10.7554/eLife.66275
31. Zhong L, Yao L, Tower RJ, Wei Y, Miao Z, Park J, et al. Single Cell Transcriptomics Identifies a Unique Adipose Lineage Cell Population That Regulates Bone Marrow Environment. *Elife* (2020) 9:e54695. doi: 10.7554/eLife.54695
32. Yu W, Zhong L, Yao L, Wei Y, Gui T, Li Z, et al. Bone Marrow Adipogenic Lineage Precursors Promote Osteoclastogenesis in Bone Remodeling and Pathologic Bone Loss. *J Clin Invest* (2021) 131(2):e140214. doi: 10.1172/JCI140214
33. Hu Y, Li X, Zhi X, Cong W, Huang B, Chen H, et al. Rankl From Bone Marrow Adipose Lineage Cells Promotes Osteoclast Formation and Bone Loss. *EMBO Rep* (2021) 22(7):e52481. doi: 10.15252/embr.202152481
34. Rosen ED, MacDougald OA. Adipocyte Differentiation From the Inside Out. *Nat Rev Mol Cell Biol* (2006) 7(12):885–96. doi: 10.1038/nrm2066
35. Matsushita Y, Nagata M, Kozloff KM, Welch JD, Mizuhashi K, Tokavanich N, et al. A Wnt-Mediated Transformation of the Bone Marrow Stromal Cell Identity Orchestrates Skeletal Regeneration. *Nat Commun* (2020) 11(1):332. doi: 10.1038/s41467-019-14029-w
36. Song L, Liu M, Ono N, Bringhurst FR, Kronenberg HM, Guo J. Loss of Wnt/Beta-Catenin Signaling Causes Cell Fate Shift of Preosteoblasts From Osteoblasts to Adipocytes. *J Bone Miner Res* (2012) 27(11):2344–58. doi: 10.1002/jbmr.1694
37. Cao Z, Umek RM, McKnight SL. Regulated Expression of Three C/Ebp Isoforms During Adipose Conversion of 3t3-L1 Cells. *Genes Dev* (1991) 5(9):1538–52. doi: 10.1101/gad.5.9.1538
38. Wang J, Liu R, Wang F, Hong J, Li X, Chen M, et al. Ablation of Lgr4 Promotes Energy Expenditure by Driving White-To-Brown Fat Switch. *Nat Cell Biol* (2013) 15(12):1455–63. doi: 10.1038/ncb2867
39. Fulzele K, Lai F, Dedic C, Saini V, Uda Y, Shi C, et al. Osteocyte-Secreted Wnt Signaling Inhibitor Sclerostin Contributes to Beige Adipogenesis in Peripheral Fat Depots. *J Bone Miner Res* (2017) 32(2):373–84. doi: 10.1002/jbmr.3001
40. Fairfield H, Falank C, Harris E, Demambro V, McDonald M, Pettitt JA, et al. The Skeletal Cell-Derived Molecule Sclerostin Drives Bone Marrow Adipogenesis. *J Cell Physiol* (2018) 233(2):1156–67. doi: 10.1002/jcp.25976
41. Tang QQ, Lane MD. Adipogenesis: From Stem Cell to Adipocyte. *Annu Rev Biochem* (2012) 81:715–36. doi: 10.1146/annurev-biochem-052110-115718
42. Bajaj MS, Kulkarni RS, Ghode SS, Limaye LS, Kale VP. Irradiation-Induced Secretion of Bmp4 by Marrow Cells Causes Marrow Adipogenesis Post-Myelosuppression. *Stem Cell Res* (2016) 17(3):646–53. doi: 10.1016/j.scr.2016.11.015
43. Lamora A, Talbot J, Mullard M, Brounais-Le Royer B, Redini F, Verrecchia F. Tgf-Beta Signaling in Bone Remodeling and Osteosarcoma Progression. *J Clin Med* (2016) 5(11):96. doi: 10.3390/jcm5110096
44. Wang M, Xia F, Wei Y, Wei X. Molecular Mechanisms and Clinical Management of Cancer Bone Metastasis. *Bone Res* (2020) 8(1):30. doi: 10.1038/s41413-020-00105-1
45. Attane C, Esteve D, Chaoui K, Iacovoni JS, Corre J, Moutahir M, et al. Human Bone Marrow Is Comprised of Adipocytes With Specific Lipid Metabolism. *Cell Rep* (2020) 30(4):949–58.e6. doi: 10.1016/j.celrep.2019.12.089
46. Krings A, Rahman S, Huang S, Lu Y, Czernik PJ, Lecka-Czernik B. Bone Marrow Fat Has Brown Adipose Tissue Characteristics, Which Are

Attenuated With Aging and Diabetes. *Bone* (2012) 50(2):546–52. doi: 10.1016/j.bone.2011.06.016
47. Scheller EL, Khandaker S, Learman BS, Cawthorn WP, Anderson LM, Pham HA, et al. Bone Marrow Adipocytes Resist Lipolysis and Remodeling in Response to Beta-Adrenergic Stimulation. *Bone* (2019) 118:32–41. doi: 10.1016/j.bone.2018.01.016
48. Pham TT, Ivaska KK, Hannukainen JC, Virtanen KA, Lidell ME, Enerback S, et al. Human Bone Marrow Adipose Tissue Is a Metabolically Active and Insulin-Sensitive Distinct Fat Depot. *J Clin Endocrinol Metab* (2020) 105 (7):2300–10. doi: 10.1210/clinem/dgaa216
49. Tencerova M, Rendina-Ruedy E, Neess D, Faergeman N, Figeac F, Ali D, et al. Metabolic Programming Determines the Lineage-Differentiation Fate of Murine Bone Marrow Stromal Progenitor Cells. *Bone Res* (2019) 7:35. doi: 10.1038/s41413-019-0076-5
50. Tencerova M, Figeac F, Ditzel N, Taipaleenmaki H, Nielsen TK, Kassem M. High-Fat Diet-Induced Obesity Promotes Expansion of Bone Marrow Adipose Tissue and Impairs Skeletal Stem Cell Functions in Mice. *J Bone Miner Res* (2018) 33(6):1154–65. doi: 10.1002/jbmr.3408
51. Mooradian AD. Dyslipidemia in Type 2 Diabetes Mellitus. *Nat Clin Pract Endocrinol Metab* (2009) 5(3):150–9. doi: 10.1038/ncpendmet1066
52. Varga T, Czimmerer Z, Nagy L. Ppars Are a Unique Set of Fatty Acid Regulated Transcription Factors Controlling Both Lipid Metabolism and Inflammation. *Biochim Biophys Acta* (2011) 1812(8):1007–22. doi: 10.1016/j.bbadis.2011.02.014
53. Chuang CC, Yang RS, Tsai KS, Ho FM, Liu SH. Hyperglycemia Enhances Adipogenic Induction of Lipid Accumulation: Involvement of Extracellular Signal-Regulated Protein Kinase 1/2, Phosphoinositide 3-Kinase/Akt, and Peroxisome Proliferator-Activated Receptor Gamma Signaling. *Endocrinology* (2007) 148(9):4267–75. doi: 10.1210/en.2007-0179
54. Atashi F, Modarressi A, Pepper MS. The Role of Reactive Oxygen Species in Mesenchymal Stem Cell Adipogenic and Osteogenic Differentiation: A Review. *Stem Cells Dev* (2015) 24(10):1150–63. doi: 10.1089/scd.2014.0484
55. Giacco F, Brownlee M. Oxidative Stress and Diabetic Complications. *Circ Res* (2010) 107(9):1058–70. doi: 10.1161/CIRCRESAHA.110.223545
56. Devlin MJ. Why Does Starvation Make Bones Fat? *Am J Hum Biol* (2011) 23 (5):577–85. doi: 10.1002/ajhb.21202
57. Scheller EL, Rosen CJ. What's the Matter With Mat? Marrow Adipose Tissue, Metabolism, and Skeletal Health. *Ann N Y Acad Sci* (2014) 1311:14–30. doi: 10.1111/nyas.12327
58. Hadjidakis DJ, Androulakis II. Bone Remodeling. *Ann N Y Acad Sci* (2006) 1092:385–96. doi: 10.1196/annals.1365.035
59. Wang L, You X, Zhang L, Zhang C, Zou W. Mechanical Regulation of Bone Remodeling. *Bone Res* (2022) 10(1):16. doi: 10.1038/s41413-022-00190-4
60. Kushwaha P, Wolfgang MJ, Riddle RC. Fatty Acid Metabolism by the Osteoblast. *Bone* (2018) 115:8–14. doi: 10.1016/j.bone.2017.08.024
61. Lee WC, Ji X, Nissim I, Long F. Malic Enzyme Couples Mitochondria With Aerobic Glycolysis in Osteoblasts. *Cell Rep* (2020) 32(10):108108. doi: 10.1016/j.celrep.2020.108108
62. During A, Penel G, Hardouin P. Understanding the Local Actions of Lipids in Bone Physiology. *Prog Lipid Res* (2015) 59:126–46. doi: 10.1016/j.plipres.2015.06.002
63. Gunaratnam K, Vidal C, Gimble JM, Duque G. Mechanisms of Palmitate-Induced Lipotoxicity in Human Osteoblasts. *Endocrinology* (2014) 155 (1):108–16. doi: 10.1210/en.2013-1712
64. Martin PJ, Haren N, Ghali O, Clabaut A, Chauveau C, Hardouin P, et al. Adipogenic Rnas Are Transferred in Osteoblasts *Via* Bone Marrow Adipocytes-Derived Extracellular Vesicles (Evs). *BMC Cell Biol* (2015) 16:10. doi: 10.1186/s12860-015-0057-5
65. Hernandez RK, Wade SW, Reich A, Pirolli M, Liede A, Lyman GH. Incidence of Bone Metastases in Patients With Solid Tumors: Analysis of Oncology Electronic Medical Records in the United States. *BMC Cancer* (2018) 18(1):44. doi: 10.1186/s12885-017-3922-0
66. Ryan C, Stoltzfus KC, Horn S, Chen H, Louie AV, Lehrer EJ, et al. Epidemiology of Bone Metastases. *Bone* (2022) 158:115783. doi: 10.1016/j.bone.2020.115783
67. Chan DSM, Vieira AR, Aune D, Bandera EV, Greenwood DC, McTiernan A, et al. Body Mass Index and Survival in Women With Breast Cancer-Systematic Literature Review and Meta-Analysis of 82 Follow-Up Studies. *Ann Oncol* (2014) 25(10):1901–14. doi: 10.1093/annonc/mdu042
68. Steele CB, Thomas CC, Henley SJ, Massetti GM, Galuska DA, Agurs-Collins T, et al. Vital Signs: Trends in Incidence of Cancers Associated With Overweight and Obesity - United States, 2005-2014. *MMWR Morb Mortal Wkly Rep* (2017) 66(39):1052–8. doi: 10.15585/mmwr.mm6639e1
69. Ewertz M, Jensen MB, Gunnarsdottir KA, Hojris I, Jakobsen EH, Nielsen D, et al. Effect of Obesity on Prognosis After Early-Stage Breast Cancer. *J Clin Oncol* (2011) 29(1):25–31. doi: 10.1200/JCO.2010.29.7614
70. Wang J, Chen GL, Cao S, Zhao MC, Liu YQ, Chen XX, et al. Adipogenic Niches for Melanoma Cell Colonization and Growth in Bone Marrow. *Lab Invest* (2017) 97(6):737–45. doi: 10.1038/labinvest.2017.14
71. Cawthorn WP, Scheller EL, Learman BS, Parlee SD, Simon BR, Mori H, et al. Bone Marrow Adipose Tissue Is an Endocrine Organ That Contributes to Increased Circulating Adiponectin During Caloric Restriction. *Cell Metab* (2014) 20(2):368–75. doi: 10.1016/j.cmet.2014.06.003
72. Hui SK, Arentsen L, Sueblinvong T, Brown K, Bolan P, Ghebre RG, et al. A Phase I Feasibility Study of Multi-Modality Imaging Assessing Rapid Expansion of Marrow Fat and Decreased Bone Mineral Density in Cancer Patients. *Bone* (2015) 73:90–7. doi: 10.1016/j.bone.2014.12.014
73. Nencioni A, Caffa I, Cortellino S, Longo VD. Fasting and Cancer: Molecular Mechanisms and Clinical Application. *Nat Rev Cancer* (2018) 18(11):707–19. doi: 10.1038/s41568-018-0061-0
74. Butler M, van der Meer LT, van Leeuwen FN. Amino Acid Depletion Therapies: Starving Cancer Cells to Death. *Trends Endocrinol Metab* (2021) 32(6):367–81. doi: 10.1016/j.tem.2021.03.003
75. Luo G, He Y, Yu X. Bone Marrow Adipocyte: An Intimate Partner With Tumor Cells in Bone Metastasis. *Front Endocrinol (Lausanne)* (2018) 9:339. doi: 10.3389/fendo.2018.00339
76. Gruneboom A, Hawwari I, Weidner D, Culemann S, Muller S, Henneberg S, et al. A Network of Trans-Cortical Capillaries as Mainstay for Blood Circulation in Long Bones. *Nat Metab* (2019) 1(2):236–50. doi: 10.1038/s42255-018-0016-5
77. Maroni P. Leptin, Adiponectin, and Sam68 in Bone Metastasis From Breast Cancer. *Int J Mol Sci* (2020) 21(3):1051. doi: 10.3390/ijms21031051
78. Liu Z, Xu J, He J, Liu H, Lin P, Wan X, et al. Mature Adipocytes in Bone Marrow Protect Myeloma Cells Against Chemotherapy Through Autophagy Activation. *Oncotarget* (2015) 6(33):34329–41. doi: 10.18632/oncotarget.6020
79. Limonard EJ, Veldhuis-Vlug AG, van Dussen L, Runge JH, Tanck MW, Endert E, et al. Short-Term Effect of Estrogen on Human Bone Marrow Fat. *J Bone Miner Res* (2015) 30(11):2058–66. doi: 10.1002/jbmr.2557
80. Liu C, Zhao Q, Yu X. Bone Marrow Adipocytes, Adipocytokines, and Breast Cancer Cells: Novel Implications in Bone Metastasis of Breast Cancer. *Front Oncol* (2020) 10:561595. doi: 10.3389/fonc.2020.561595
81. Diedrich JD, Herroon MK, Rajagurubandara E, Podgorski I. The Lipid Side of Bone Marrow Adipocytes: How Tumor Cells Adapt and Survive in Bone. *Curr Osteoporos Rep* (2018) 16(4):443–57. doi: 10.1007/s11914-018-0453-9
82. Gazi E, Gardner P, Lockyer NP, Hart CA, Brown MD, Clarke NW. Direct Evidence of Lipid Translocation Between Adipocytes and Prostate Cancer Cells With Imaging Ftir Microspectroscopy. *J Lipid Res* (2007) 48(8):1846–56. doi: 10.1194/jlr.M700131-JLR200
83. Gazi E, Dwyer J, Lockyer NP, Gardner P, Shanks JH, Roulson J, et al. Biomolecular Profiling of Metastatic Prostate Cancer Cells in Bone Marrow Tissue Using Ftir Microspectroscopy: A Pilot Study. *Anal Bioanal Chem* (2007) 387(5):1621–31. doi: 10.1007/s00216-006-1093-y
84. Herroon MK, Rajagurubandara E, Hardaway AL, Powell K, Turchick A, Feldmann D, et al. Bone Marrow Adipocytes Promote Tumor Growth in Bone *Via* Fabp4-Dependent Mechanisms. *Oncotarget* (2013) 4(11):2108–23. doi: 10.18632/oncotarget.1482
85. Diedrich JD, Rajagurubandara E, Herroon MK, Mahapatra G, Huttemann M, Podgorski I. Bone Marrow Adipocytes Promote the Warburg Phenotype in Metastatic Prostate Tumors *Via* Hif-1alpha Activation. *Oncotarget* (2016) 7(40):64854–77. doi: 10.18632/oncotarget.11712
86. Wang J, Li Y. Cd36 Tango in Cancer: Signaling Pathways and Functions. *Theranostics* (2019) 9(17):4893–908. doi: 10.7150/thno.36037
87. Liang Y, Han H, Liu L, Duan Y, Yang X, Ma C, et al. Cd36 Plays a Critical Role in Proliferation, Migration and Tamoxifen-Inhibited Growth of Er-Positive Breast Cancer Cells. *Oncogenesis* (2018) 7(12):98. doi: 10.1038/s41389-018-0107-x

88. Cha YJ, Koo JS. Roles of Omental and Bone Marrow Adipocytes in Tumor Biology. *Adipocyte* (2019) 8(1):304–17. doi: 10.1080/21623945.2019.1643189
89. Herroon MK, Rajagurubandara E, Diedrich JD, Heath EI, Podgorski I. Adipocyte-Activated Oxidative and Er Stress Pathways Promote Tumor Survival in Bone *Via* Upregulation of Heme Oxygenase 1 and Survivin. *Sci Rep* (2018) 8(1):40. doi: 10.1038/s41598-017-17800-5
90. Tabe Y, Yamamoto S, Saitoh K, Sekihara K, Monma N, Ikeo K, et al. Bone Marrow Adipocytes Facilitate Fatty Acid Oxidation Activating Ampk and a Transcriptional Network Supporting Survival of Acute Monocytic Leukemia Cells. *Cancer Res* (2017) 77(6):1453–64. doi: 10.1158/0008-5472.CAN-16-1645
91. John B, Naczki C, Patel C, Ghoneum A, Qasem S, Salih Z, et al. Regulation of the Bi-Directional Cross-Talk Between Ovarian Cancer Cells and Adipocytes by Sparc. *Oncogene* (2019) 38(22):4366–83. doi: 10.1038/s41388-019-0728-3
92. Takehara M, Sato Y, Kimura T, Noda K, Miyamoto H, Fujino Y, et al. Cancer-Associated Adipocytes Promote Pancreatic Cancer Progression Through Saa1 Expression. *Cancer Sci* (2020) 111(8):2883–94. doi: 10.1111/cas.14527
93. Dirat B, Bochet L, Dabek M, Daviaud D, Dauvillier S, Majed B, et al. Cancer-Associated Adipocytes Exhibit an Activated Phenotype and Contribute to Breast Cancer Invasion. *Cancer Res* (2011) 71(7):2455–65. doi: 10.1158/0008-5472.CAN-10-3323
94. Liu H, He J, Koh SP, Zhong Y, Liu Z, Wang Z, et al. Reprogrammed Marrow Adipocytes Contribute to Myeloma-Induced Bone Disease. *Sci Transl Med* (2019) 11(494):eaau9087. doi: 10.1126/scitranslmed.aau9087
95. Wang C, Wang J, Chen K, Pang H, Li X, Zhu J, et al. Caprylic Acid (C8:0) Promotes Bone Metastasis of Prostate Cancer by Dysregulated Adipo-Osteogenic Balance in Bone Marrow. *Cancer Sci* (2020) 111(10):3600–12. doi: 10.1111/cas.14606
96. Hofbauer LC, Bozec A, Rauner M, Jakob F, Perner S, Pantel K. Novel Approaches to Target the Microenvironment of Bone Metastasis. *Nat Rev Clin Oncol* (2021) 18(8):488–505. doi: 10.1038/s41571-021-00499-9
97. Hardouin P, Rharass T, Lucas S. Bone Marrow Adipose Tissue: To Be or Not to Be a Typical Adipose Tissue? *Front Endocrinol (Lausanne)* (2016) 7:85. doi: 10.3389/fendo.2016.00085
98. Wu JB, Yin L, Shi C, Li Q, Duan P, Huang JM, et al. Maoa-Dependent Activation of Shh-Il6-Rankl Signaling Network Promotes Prostate Cancer Metastasis by Engaging Tumor-Stromal Cell Interactions. *Cancer Cell* (2017) 31(3):368–82. doi: 10.1016/j.ccell.2017.02.003
99. Hardaway AL, Herroon MK, Rajagurubandara E, Podgorski I. Marrow Adipocyte-Derived Cxcl1 and Cxcl2 Contribute to Osteolysis in Metastatic Prostate Cancer. *Clin Exp Metastasis* (2015) 32(4):353–68. doi: 10.1007/s10585-015-9714-5
100. Miggitsch C, Meryk A, Naismith E, Pangrazzi L, Ejaz A, Jenewein B, et al. Human Bone Marrow Adipocytes Display Distinct Immune Regulatory Properties. *EBioMedicine* (2019) 46:387–98. doi: 10.1016/j.ebiom.2019.07.023
101. Al-Khami AA, Zheng L, Del Valle L, Hossain F, Wyczechowska D, Zabaleta J, et al. Exogenous Lipid Uptake Induces Metabolic and Functional Reprogramming of Tumor-Associated Myeloid-Derived Suppressor Cells. *Oncoimmunology* (2017) 6(10):e1344804. doi: 10.1080/2162402X.2017.1344804
102. Hossain F, Al-Khami AA, Wyczechowska D, Hernandez C, Zheng L, Reiss K, et al. Inhibition of Fatty Acid Oxidation Modulates Immunosuppressive Functions of Myeloid-Derived Suppressor Cells and Enhances Cancer Therapies. *Cancer Immunol Res* (2015) 3(11):1236–47. doi: 10.1158/2326-6066.CIR-15-0036
103. Field CS, Baixauli F, Kyle RL, Puleston DJ, Cameron AM, Sanin DE, et al. Mitochondrial Integrity Regulated by Lipid Metabolism Is a Cell-Intrinsic Checkpoint for Treg Suppressive Function. *Cell Metab* (2020) 31(2):422–37.e5. doi: 10.1016/j.cmet.2019.11.021
104. Lim SA, Wei J, Nguyen TM, Shi H, Su W, Palacios G, et al. Lipid Signalling Enforces Functional Specialization of Treg Cells in Tumours. *Nature* (2021) 591(7849):306–11. doi: 10.1038/s41586-021-03235-6
105. Zhu L, Hua F, Ding W, Ding K, Zhang Y, Xu C. The Correlation Between the Th17/Treg Cell Balance and Bone Health. *Immun Ageing* (2020) 17:30. doi: 10.1186/s12979-020-00202-z
106. Maguire OA, Ackerman SE, Szwed SK, Maganti AV, Marchildon F, Huang X, et al. Creatine-Mediated Crosstalk Between Adipocytes and Cancer Cells Regulates Obesity-Driven Breast Cancer. *Cell Metab* (2021) 33(3):499–512.e6. doi: 10.1016/j.cmet.2021.01.018
107. Di Biase S, Ma X, Wang X, Yu J, Wang YC, Smith DJ, et al. Creatine Uptake Regulates Cd8 T Cell Antitumor Immunity. *J Exp Med* (2019) 216(12):2869–82. doi: 10.1084/jem.20182044
108. Amisten S, Atanes P, Hawkes R, Ruz-Maldonado I, Liu B, Parandeh F, et al. A Comparative Analysis of Human and Mouse Islet G-Protein Coupled Receptor Expression. *Sci Rep* (2017) 7:46600. doi: 10.1038/srep46600
109. Lecka-Czernik B, Stechschulte LA, Czernik PJ, Sherman SB, Huang S, Krings A. Marrow Adipose Tissue: Skeletal Location, Sexual Dimorphism, and Response to Sex Steroid Deficiency. *Front Endocrinol (Lausanne)* (2017) 8:188. doi: 10.3389/fendo.2017.00188
110. Chang E, Varghese M, Singer K. Gender and Sex Differences in Adipose Tissue. *Curr Diabetes Rep* (2018) 18(9):69. doi: 10.1007/s11892-018-1031-3
111. Fuente-Martin E, Argente-Arizon P, Ros P, Argente J, Chowen JA. Sex Differences in Adipose Tissue: It Is Not Only a Question of Quantity and Distribution. *Adipocyte* (2013) 2(3):128–34. doi: 10.4161/adip.24075

Conflict of Interest: Author YZ is employed by company Shanghai Huaota Biopharmaceutical Co. Ltd.

The remaining authors declare that the research was conducted in the absence of any commercial or financial relationships that could be construed as a potential conflict of interest.

Publisher's Note: All claims expressed in this article are solely those of the authors and do not necessarily represent those of their affiliated organizations, or those of the publisher, the editors and the reviewers. Any product that may be evaluated in this article, or claim that may be made by its manufacturer, is not guaranteed or endorsed by the publisher.

frontiers | Frontiers in Endocrinology

ORIGINAL RESEARCH
published: 23 June 2022
doi: 10.3389/fendo.2022.931231

Changes in Vertebral Marrow Fat Fraction Using 3D Fat Analysis & Calculation Technique Imaging Sequence in Aromatase Inhibitor-Treated Breast Cancer Women

Taihu Wan[1], *Yuhang Zhu*[1], *Qinghe Han*[2] *and Lin Liu*[1]*

[1] Department of Radiology, China-Japan Union Hospital of Jilin University, Changchun, China, [2] Radiology of Department, The Second Hospital of Jilin University, Changchun, China

OPEN ACCESS

Edited by:
Guanwu Li,
Shanghai University of Traditional Chinese Medicine, China

Reviewed by:
Jesus Delgado-Calle,
University of Arkansas for Medical Sciences, United States
Haiyang Lin,
The Affiliated Wenling Hospital of Wenzhou Medical University, China

***Correspondence:**
Lin Liu
liulin99@jlu.edu.cn

Specialty section:
This article was submitted to Bone Research, a section of the journal Frontiers in Endocrinology

Received: 28 April 2022
Accepted: 18 May 2022
Published: 23 June 2022

Citation:
Wan T, Zhu Y, Han Q and Liu L (2022) Changes in Vertebral Marrow Fat Fraction Using 3D Fat Analysis & Calculation Technique Imaging Sequence in Aromatase Inhibitor-Treated Breast Cancer Women. Front. Endocrinol. 13:931231. doi: 10.3389/fendo.2022.931231

Aromatase inhibitor (AI) is a cornerstone drug for postmenopausal women with estrogen receptor-positive early-stage breast cancer. Fat-bone interactions within the bone marrow milieu are growing areas of scientific interest. Although AI treatment could lead to deterioration of the skeleton, the association between AI medication and subsequent marrow adiposity remains elusive. A total of 40 postmenopausal, early-staged, and hormone receptor-positive breast cancer patients who underwent treatment with adjuvant AIs and 40 matched controls were included. Marrow proton density fat fraction (PDFF) at the L1–L4 vertebral bodies using 3D Fat Analysis & Calculation Technique imaging (FACT) sequence at 3.0T, bone mineral density (BMD) by dual-energy X-ray absorptiometry, and serum bone turnover biomarkers were determined at baseline and at 6 and 12 months. We found that, in comparison to baseline, an increase of type I collagen cross-linked telopeptide was detected at 12 months (P <0.05). From baseline to 12 months, the PDFF measured using FACT was greatly increased. At 12 months, the median percent change of PDFF (4.9% vs. 0.9%, P <0.05) was significantly different between the AI treatments and controls. The same trend was observed for the marrow PDFF at 6 months relative to the respective values at baseline. Although BMD values were significantly reduced after 12 months in AI-treated women, changes in BMD vs. baseline condition were not significantly different between the AI-treated and control groups [Δ BMD –1.6% to –1.8% vs. –0.3% to –0.6%, respectively, $P > 0.05$]. In the AI-treated group, Δ PDFF was associated with Δ BMD at the lumbar spine ($r = –0.585$, $P <$ 0.001), but not in the controls. Taken together, over a 12-month period, spinal marrow fat content assessed with FACT sequence significantly increased in postmenopausal women with hormone-receptor-positive breast cancer receiving AI treatment.

Keywords: breast cancer, aromatase inhibitor, bone mineral density, chemical shift encoding-based, marrow fat, proton density fat fraction

INTRODUCTION

Aromatase inhibitors (AIs) are widely recommended for use by postmenopausal women who have estrogen receptor-positive early-stage breast cancer. Treatment with AIs provides benefits to breast cancer patients in terms of improved disease-free survival and overall survival (1). However, AI-induced deterioration of bone loss and its management with bisphosphonates is still unclear. In addition, the optimal duration of AI therapy for early breast cancer remains elusive.

Extended use of adjuvant endocrine therapy and persistent deterioration of the skeleton from recent findings emphasized the need to assess bone loss and fracture risk in women with hormone-receptor-positive, early-stage breast cancer initiated on AIs (1, 2). Bone mineral density (BMD) evaluation by dual-energy X-ray absorptiometry (DXA) is actually limited. Accuracy of DXA measurements is influenced by degenerative changes in the spine or aortic mineralization and by the variable proportion of fat in overlying soft tissue since it uses a two-dimensional projectional measurement (3). The use of bone quality assessment by means of a based-DXA trabecular bone score may contribute to identifying those with a higher risk of fracture independent of bone density (4, 5). The use of other imaging techniques, such as high resolution peripheral quantitative computed tomography by capturing more and different information on the properties of bone microstructure, have potential implications for clinical practice in the future (6).

Adipocytes in the bone marrow are highly plastic, and have a distinctive characteristic to secrete an extensive number of cytokines and adipokines such as resistin, leptin, and C-C Motif Chemokine Ligand 2 (CCL2) that exert local and endocrine functions. Additionally, bone marrow adipose tissue has been proposed to have mixed brown and white fat characteristics (7, 8). Both animal and human data supported a clinical association between marrow adipose tissue content and integrity of skeleton (9, 10). The proton density fat fraction (PDFF) as a biomarker for osteopenia and osteoporosis enables discrimination of low bone mass from healthy controls (9, 11). Accumulating evidence also highlights the importance of interactions between marrow adipocytes and tumor cells (12, 13). Although a previous study reported that AI-treated patients maintained vertebral marrow PDFF values with a relatively small sample size, prospective changes of marrow fat content in postmenopausal women with breast cancer at completion of AI treatment remain poorly understood.

Therefore, the current study was designed to evaluate the prospective changes in spinal marrow fat content and bone mass in postmenopausal women with early-staged breast cancer after completing AI treatment using chemical shift encoding–based water-fat magnetic resonance imaging (MRI) at 3.0T.

MATERIALS AND METHODS

Participants

This study was performed in accordance with the ethical standards described in the 1964 Declaration of Helsinki and its later amendments. This study was approved by the Institutional Review Board of China-Japan Union Hospital of Jilin University, and all participants provided informed consent. In this prospective, observational study, we recruited 40 postmenopausal women (age, 51.7-73years) with hormone-receptor-positive early-staged breast cancer (including carcinoma *in situ* and stage I–II breast cancers) who were scheduled to receive treatment with adjuvant AIs (i.e., letrozole, anastrozole, and exemestane) between May 2018 and January 2022. Participants were excluded if they had (1): history of lumbar spinal surgery, known or suspected bone metastases, irradiation and/or chemotherapy, other malignancies, distant metastasis, chronic diseases such as rheumatoid arthritis, diabetes mellitus, liver and kidney dysfunction, severe cardiac, hematological, psycho, and nervous system diseases; 2) use of medications known to interfere with fat/bone metabolism such as glucocorticoids, bisphosphonates, denosumab, teriparatide, strontium ranelate, anticoagulants, anticonvulsants, alcohol abuse; (3) bone mineral density or other missing data. A healthy control group (n = 40; age, 51.5-74years) of age-matched postmenopausal women was also recruited from the community.

At enrollment, all participants completed self-administered questionnaires about demographics, medical history, general risk factors, family history of breast cancer as well as lifestyle factors (e.g., alcohol consumption, current tobacco smoking, and physical activity). Physical activity was assessed with the International Physical Activity Questionnaire short form, with data reported as Metabolic Equivalent of Task hours per week (14). According to standard procedures, body weight and height were measured at baseline. Body mass index (BMI) was calculated as the weight in kilograms divided by the square of the height in meters. All participants were scheduled to undergo chemical shift encoding-based water-fat MRI, DXA, and serum bone turnover marker analysis at baseline condition, and at 6 and 12 months after receiving endocrine therapy. The study flow chart is presented in **Figure 1**.

Biochemical Evaluation

Fasting blood samples were collected after overnight fasting and between 7 a.m. and 9 a.m. on the DXA evaluation day. Biochemical evaluation included 25-hydroxyvitamin D, type I collagen cross-linked telopeptide (CTX-I), N-terminal propeptide of type 1 procollagen (P1NP) and osteocalcin. 25-hydroxyvitamin D was measured by immunoassay. Serum CTX-I, P1NP, and osteocalcin were measured by chemiluminescence (ECLIA) in the analyzer Tesmi-F3999 (Tellgen Super Multiplex Immunoassay System, Shanghai, China).

MRI Acquisition and Analyses

MRI of the lumbar spine was performed on a 3.0 T full-body MRI unit (uMR 780, United Imaging Healthcare, Shanghai, China) to quantify marrow proton density fat fraction (PDFF) at the L1-4 vertebral bodies. Subjects were positioned head-first in the magnet bore in a prone position. Standard clinical MRI protocols, including T1-weighted imaging and T2-weighted imaging (sagittal acquisition), were performed with a built-in 12-channel posterior coil.

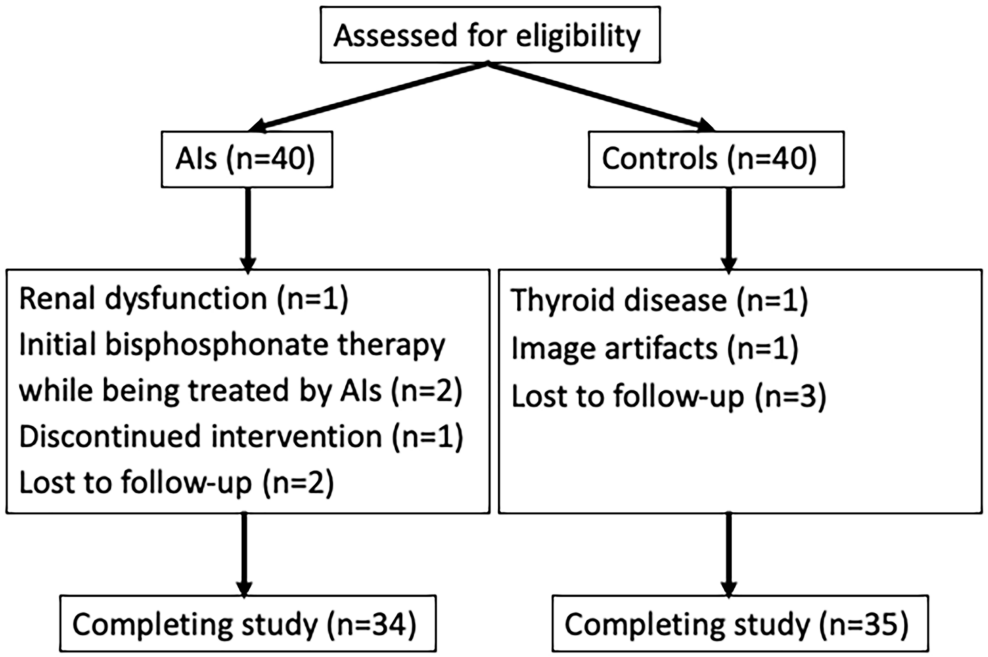

FIGURE 1 | Flow diagram of study subjects. AIs, aromatase inhibitors.

For chemical shift encoding-based water-fat separation at the level of the lumbar spine, a sagittal prescribed 3D Fat Analysis & Calculation Technique (FACT) sequence allowing PDFF quantification, was then acquired with the following parameters: TR= 7.2 ms; six echoes with TE1/ΔTE = 1.21/1.1 ms; flip angle, 3° (low spin flip angle excitation to minimize T1 saturation) (11, 15); slice thickness, 3 mm; interslice gap, 0 mm; acquisition matrix size, 256 × 192; field of view, 380 × 380 mm; 1 average; scan time, 17 seconds. FACT sequence images were transferred to a commercially available workstation (uWS-MR Advanced Postprocess Workstation, United Imaging Healthcare, Shanghai, China). One musculoskeletal radiologist with 5 years' experience quantitatively analyzed PDFF mappings obtained with FACT sequence (**Figure 2**). The coefficient of variation was 3.07% for the repeatability of PDFF measurement.

Evaluation of BMD

Areal BMD values at the lumbar spine (L1-L4), femoral neck, and total hip were assessed using dual energy X-ray absorptiometry (DXA, Hologic Discovery). DXA scans were performed by a certified operator. Precision coefficients were 1.17% for the femoral neck, 1.09% for the total hip, and 1.29% for the lumbar spine. Both MRI and DXA examinations were performed on the same day.

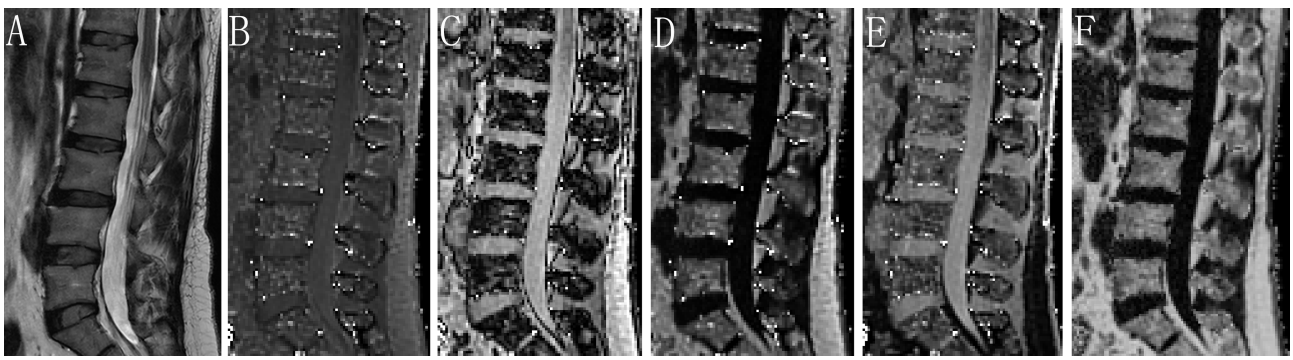

FIGURE 2 | Assessment of PDFF derived from six-echo FACT sequence in image set of a healthy woman. Sagittal T2-weighted **(A)**, in-phase **(B)**, out-of-phase **(C)**, fat-only **(D)**, water-only **(E)**, and the corresponding PDFF map **(F)** with a mean PDFF of 53% at the L1-L4 levels. FACT, Fat Analysis & Calculation Technique imaging; PDFF, proton density fat fraction.

Statistical Analysis

The sample size calculation was performed using G*Power software v3.1, taking into consideration the effect of aromatase inhibitor on fat fraction percentage (16). The effect size of 0.60 showed that with a significance level of 95% and statistical power of 80% (power $1-\beta = 0.80$), the minimum number of participants required was 24. Data are presented as mean ± standard deviation (SD), median (interquartile range, IQR) or n (%) as appropriate. Normality was evaluated by the Shapiro-Wilk test. Student's *t-test* or Mann-Whitney test was performed to compare quantitative variables and Fisher's exact or chi-square test for qualitative analyses between groups. The marrow MRI PDFF, DXA BMD, and serum levels of bone turnover biomarkers at baseline and at 6 and 12 months were assessed using the paired *t* test or Wilcoxon rank-sum test. Statistical analyses were performed using SPSS software version 20.0 for Windows (SPSS Inc, Chicago, IL, USA). All statistical tests were two sided, and significance was set at $P < 0.05$.

RESULTS

Baseline Characteristics of Study Population

A total of 34 postmenopausal women with early breast cancer receiving AI treatment and 35 healthy controls completed the study. As shown in **Figure 1**, 11 participants were excluded from the final analysis: two participants because of initial bisphosphonate therapy while being treated by AIs, two with renal dysfunction and thyroid disease, six with discontinued intervention or lost to follow-up, and the other one because of image artifacts. Over a 12-month period, none of the patients reported any new skeletal-related events. The demographic and clinical characteristics of all participants are shown in **Table 1**. At baseline, no significant differences except for marrow PDFF were observed between the breast cancer women treated with AIs and control groups. Breast cancer patients had higher marrow PDFF than that of the controls.

Changes in Marrow PDFF and BMD

The spinal marrow PDFF, BMD values at the femoral neck, total hip, and lumbar spine from the hormone-receptor-positive early breast cancer patients receiving AI treatment and healthy controls at baseline condition and at 6 and 12 months are shown in **Figure 3**. For the AIs and control groups, changes in marrow PDFF and BMD are shown in **Table 2**. Marrow PDFF at the 6-month follow-up visit (60.8 ± 5.5%) increased significantly compared to PDFF at the initial visit (59.0 ± 6.3%, $P < 0.001$) in the breast cancer patients receiving AIs, but not in the controls (53.7 ± 5.3% vs 53.4 ± 5.9%, $P > 0.05$). Relative to the respective values at baseline, the marrow PDFF value at 6 and 12 months markedly increased by a median of 3.1% and 4.9% (all $P < 0.001$) in the AIs group, respectively, but not in the controls (0.6% and 0.9%, all $P > 0.05$, respectively),

In the breast cancer patients receiving AIs, femoral neck BMD (0.863 ± 0.009 g/cm^2 vs. 0.877 ± 0.007 g/cm^2), total hip BMD (0.945 ± 0.009 g/cm^2 vs. 0.961 ± 0.011g/cm^2), and lumbar spine BMD (1.033 ± 0.014 g/cm^2 vs. 1.052 ± 0.012 g/cm^2, all $P < 0.05$) were decreased at the 12month follow-up visit compared to the initial visit. In contrast, no significant difference was found in the DXA BMD values at the femoral neck, total hip, and lumbar spine, with a median of −0.7%, −0.8%, and −1.0% (all $P > 0.05$), respectively, between baseline condition and at 6 months.

Changes in Serum Biomarkers

At baseline condition, serum biomarkers including 25(OH)D, CTX-I, P1NP, and osteocalcin levels were not significantly different in the breast cancer patients treated with AIs compared with the controls (**Table 1**). Similar results were observed at 6 months. CTX-I level was significantly increased after 12 months in comparison to baseline values in the AI-treated group, and significant differences were found between the AIs and control groups at 12 months (**Table 2**). No significant differences in the 25(OH)D, P1NP, and osteocalcin levels were observed at different timepoints.

TABLE 1 | Baseline characteristics of the study population.

	AIs (n = 34)	Controls (n = 35)
Age, years	59.2 ± 5.2	59.4 ± 5.8
Time since menopause, years	6.0 (4, 9)	6.5 (4.5, 8.5)
Height, cm	158.8 ± 6.1	159.5 ± 7.0
Weight, kg	60.7 ± 7.1	61.6 ± 7.7
BMI, kg/m^2	24.1 ± 3.1	24.4 ± 4.1
Alcohol intake, n (%)	1 (2.9)	2 (5.7)
Smokers, n (%)	2 (5.9)	2 (5.7)
5-hydroxyvitamin D, ng/mL	46.1 (33.5, 67.2)	44.8 (30.2, 63.5)
CTX-I, pg/mL	242 (146, 337)	226 (138, 320)
P1NP, ng/mL	39.6 (29.7, 54.8)	41.0 (30.1, 56.4)
Osteocalcin, ng/mL	15.8 ± 4.9	16.5 ± 5.4
Lumbar spine BMD, g/cm^2	1.052 ± 0.012	1.058 ± 0.009
Total hip BMD, g/cm^2	0.961 ± 0.011	0.958 ± 0.008
Femur neck BMD, g/cm^2	0.877 ± 0.007	0.875 ± 0.008
Spinal PDFF, %	59.0 ± 6.3	53.4 ± 5.9 [a]

Data are presented as mean ± SD, median (IQR) or n (%) as appropriate.

AIs, aromatase inhibitors; BMD bone mineral density; BMI, body mass index; CTX-I, type I collagen cross-linked telopeptide; IQR, interquartile range Q1-Q3; P1NP, N-terminal propeptide of type 1 procollagen; PDFF, proton density fat fraction; SD, standard deviation.

[a] *P <0.05 by independent-sample t-test.*

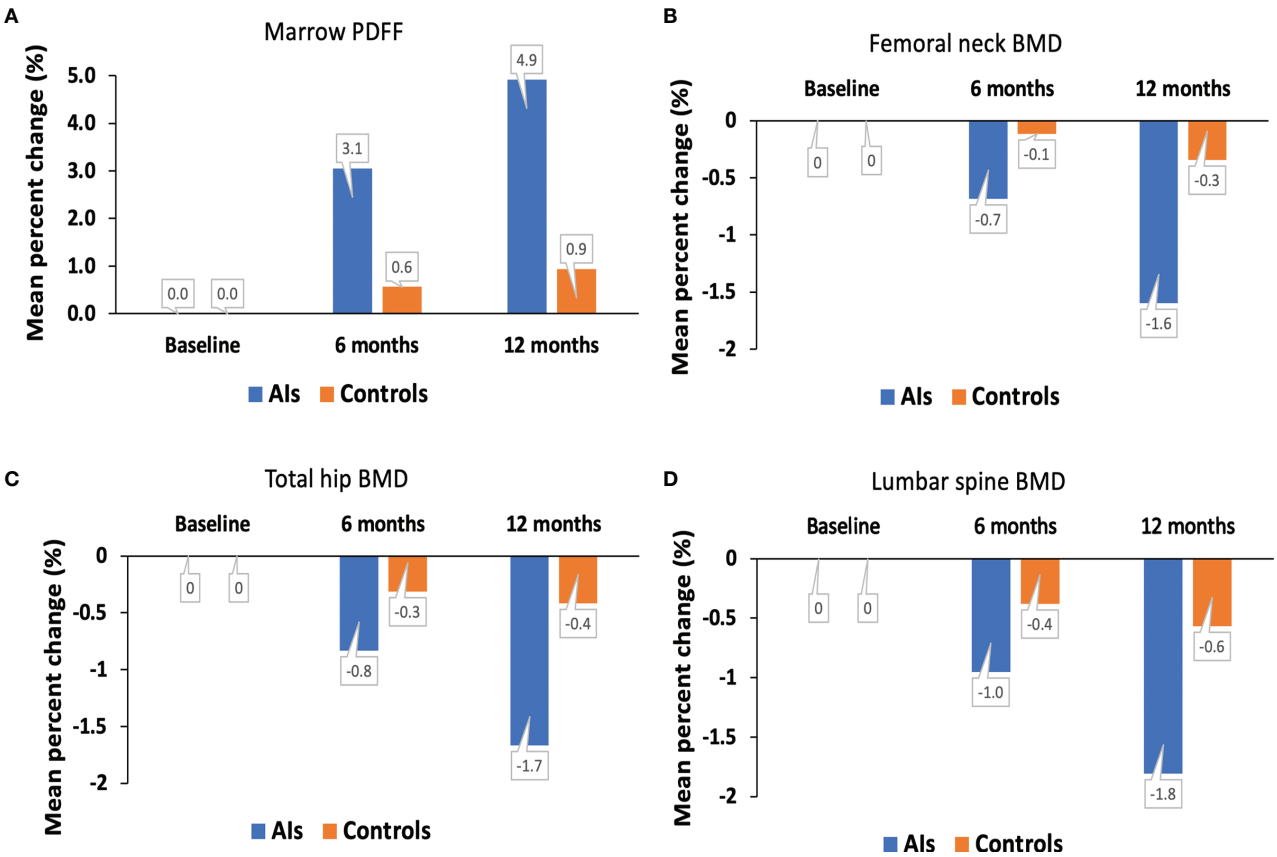

FIGURE 3 | Mean percent change in marrow PDFF **(A)**, BMD at the femoral neck **(B)**, total hip **(C)** and lumbar spine **(D)** over time. AIs, aromatase inhibitors; BMD, bone mineral density; PDFF, proton density fat fraction.

TABLE 2 | Changes in bone turnover biomarkers, BMD and spinal marrow PDFF in AIs-treated group.

Parameters	Groups	At baseline	At 6 months	At 12 months	% change	
					$\Delta_{6\text{-}0m}$	$\Delta_{12\text{-}0m}$
5-hydroxyvitamin D, ng/mL	AIs	46.1(33.5, 67.2)	45.1(29.8, 63.6)	47.7(34.9, 70.1)	−2.2	3.5
	Controls	44.8 (30.2, 63.5)	45.4 (32.0, 68.1)	47.0 (30.0, 70.4)	1.3	4.9
CTX-I, pg/mL	AIs	242 (146, 337)	260 (151, 355)	291 (176, 378)	7.4	20.2 [a]
	Controls	226 (138, 320)	231 (144, 331)	238 (152, 353)	2.2	5.3
P1NP, ng/mL	AIs	39.6 (29.7, 54.8)	40.8 (31.5, 57.3)	42.1 (32.0, 60.9)	3.0	6.3
	Controls	41.0 (30.1, 56.4)	42.0 (28.6, 58.9)	40.1 (29.7, 60,1)	2.4	−2.2
Osteocalcin, ng/mL	AIs	15.8 ± 4.9	15.0 ± 4.5	16.3 ± 5.2	−5.1	3.2
	Controls	16.5 ± 5.4	16.7 ± 5.8	16.0 ± 5.7	1.2	−3.0
Lumbar spine BMD, g/cm^2	AIs	1.052 ± 0.012	1.042 ± 0.011	1.033 ± 0.014	−1.0	−1.8 [b]
	Controls	1.058 ± 0.009	1.054 ± 0.012	1.052 ± 0.013	−0.4	−0.6
Total hip BMD, g/cm^2	AIs	0.961 ± 0.011	0.953 ± 0.010	0.945 ± 0.009	−0.8	−1.7 [b]
	Controls	0.958 ± 0.008	0.955 ± 0.009	0.954 ± 0.012	−0.3	−0.4
Femur neck BMD, g/cm^2	AIs	0.877 ± 0.007	0.871 ± 0.008	0.863 ± 0.009	−0.7	−1.6 [b]
	Controls	0.875 ± 0.008	0.874 ± 0.009	0.872 ± 0.008	−0.1	−0.3
Spinal PDFF, %	AIs	59.0 ± 6.3	60.8 ± 5.5	61.9 ± 6.0	3.1 [b]	4.9 [b]
	Controls	53.4 ± 5.9	53.7 ± 5.3	53.9 ± 5.5	0.6	0.9

Data are presented as mean ± SD, median (IQR) or % as appropriate.

AIs, aromatase inhibitors; BMD bone mineral density; CTX-I, type I collagen cross-linked telopeptide; IQR, interquartile range Q1-Q3; M, month; P1NP, N-terminal propeptide of type 1 procollagen; PDFF, proton density fat fraction; SD, standard deviation.

To detect difference between various time points, [a]P value by Wilcoxon rank-sum test and [b]P value by paired t test (all P <0.05).

Relationships Among Marrow PDFF, BMD, and Serum Biomarkers

In the breast cancer patients receiving AIs group, a significantly negative relationship was found between change of marrow PDFF and change of lumbar spine BMD values ($r = -0.585$, $P < 0.001$) at 12 months relative to the respective values at baseline, but not in the controls group. Spinal marrow PDFF variation over time was not significantly related with changes of BMD at the femoral neck and total hip in both the AI-treated breast cancer patients and healthy controls. In the AIs group, Δ bone turnover biomarkers at 6 months and 12 months versus baseline condition was not associated with Δ spinal marrow PDFF or Δ BMD at the femoral neck, total hip, and lumbar spine.

DISCUSSION

In this prospective observational study, we performed DXA scans, MR FACT sequence, and serological tests to clarify changes in spinal marrow PDFF, BMD at the femoral neck, total hip and lumbar spine, and bone turnover biomarker levels in postmenopausal women with estrogen receptor-positive early-stage breast cancer receiving AIs. We found that vertebral marrow PDFF was significantly increased at 6 and 12 months post-AI treatment onset. We also showed that BMD values at the total hip, femoral neck, and lumbar spine were decreased at the 12-month follow-up visit compared to the initial visit. Changes in marrow PDFF and Δ lumbar spine BMD values were negatively associated in the AIs group.

Bone marrow adipose tissue is now recognized as an endocrine organ. Accumulating evidence indicates that bone marrow fat plays a complex role in bone health, energy metabolism, and hematological diseases like aplastic anemia, multiple myeloma, and leukemia (9, 17). A previous study demonstrated that breast cancer patients had higher marrow fat content in comparison with the age-matched controls. Expansion of marrow fat may be an independent risk factor for postmenopausal breast cancer and clinicopathological characteristics of breast cancer (14). In this present work, as compared with the healthy controls, the hormone-receptor-positive early breast cancer patients receiving AIs showed fat expansion within the bone marrow.

The level of serum β-CTX is used as the reference marker for bone resorption, and P1NP can be measured as one of bone formation biomarkers. During bone formation as well as bone resorption, osteocalcin can be released into the circulation. Several studies indicated that P1NP and β-CTX are the most efficient biomarkers to predict the BMD changes (18). As expected, serum β-CTX markedly elevated at 12 months after AI treatment. Similar to our results, Catalano et al. found that β-CTX levels increased significantly after 9 and 18 months in comparison to baseline values in the AI-treated group (19, 20). In contrast to ours and other studies (19), no significant change was found in serum β-CTX from baseline condition to 12 months in postmenopausal women with early breast cancer at lower and moderate risk of fragility fracture who received AIs (21).

AIs are in widespread use for hormone-receptor-positive breast cancer patients. Several clinical trials have reported AI-related bone loss and fracture risk in both premenopausal and postmenopausal women (4 19, 20, 22). In clinical practice, BMD was used to assess bone strength and risk of fracture. However, in some pathologic conditions such as diabetes mellitus patients, there is an apparent contradiction of elevated bone mass associated with a higher fracture (5), which may be due to poor bone quality assessment with BMD measurement. Seeking imaging methods other than BMD to evaluate bone strength and risk of fracture is of important implication, such as marrow fat fraction, an indirect measure of bone quality (23, 24). The use of chemical shift-encoded MRI or magnetic resonance spectroscopy and bone quality by means of PDFF could additionally help to identify those with bone deterioration or higher risk of fracture independent of BMD (11, 24).

Bone marrow fat tissue composition and quantification may play an important role in bone pathophysiology, but has not been thoroughly studied in AI users. A recent study with a relatively small sample size (n = 8) done by Dieckmeyer et al. (16) showed that over a 12-month period, vertebral bone marrow PDFF was increased by 3.1% in subjects receiving AIs, however it was not significant ($P = 0.52$). Additionally, there was no significant association between PDFF and BMD for the AI treatment group at baseline or follow-up. In our current study with a large sample size and including a group of age-matched healthy controls, we observed that over a 12-month period spinal marrow PDFF was significantly increased in postmenopausal women treated with AIs. *Ex vivo*, estradiol may induce osteogenesis and suppress adipogenesis differentiation of bone marrow mesenchymal stromal cells (25). *In vivo*, estradiol deficiency leads to the increase in bone marrow adipocyte size and number, particularly in postmenopausal osteoporotic women (26). Since treatments with AIs decrease already low endogenous postmenopausal estradiol levels, we found that the PDFF at the lumbar spine was increased by a median of 3.1% at 6 months and 4.9% at 12 months (all $P < 0.05$), respectively. Change of marrow PDFF was associated with change of lumbar spine BMD values at 12 months relative to the respective values at baseline. Thus, marrow PDFF assessed with FACT sequence may be used as a useful early response indicator.

We acknowledge that our study has some limitations. First, the sample size was relatively small, which did not allow to analyze the effects of different AIs (i.e., letrozole, anastrozole, and exemestane) on marrow fat content. This was a single-center study which limits the generalizability of our results. Second, many of the AI-treated breast cancer patients are postmenopausal women who not infrequently have history of multidrug use. Possible interactions between different drugs may affect the bone-fat metabolism that could not be specifically excluded. Third, although we examined both the marrow fat content and BMD, we did not explore their relationships with risk of fractures. Finally, the observation period of AI treatment is typically 5 – 10 years (1), evaluating longitudinal effects over a

longer period of time may help to further elucidate the longer-term effects of AIs on vertebral marrow PDFF.

In conclusion, over a 12-month period, spinal marrow proton density fat fraction as measured by FACT sequence significantly increased in postmenopausal women with early breast cancer receiving AI treatment. Our results demonstrated that healthcare professionals for postmenopausal women who received AIs must pay attention to marrow fat content measurements during and after hormone-receptor-positive early breast cancer treatment.

DATA AVAILABILITY STATEMENT

The original contributions presented in the study are included in the article/supplementary materials. Further inquiries can be directed to the corresponding author.

ETHICS STATEMENT

The studies involving human participants were reviewed and approved by The Institutional Review Board of China-Japan Union Hospital of Jilin University. The patients/participants provided their written informed consent to participate in this study.

AUTHOR CONTRIBUTIONS

Study design: TW, LL Study conduct: YZ; Data collection: QH; Data analysis: TW, YZ; Data interpretation: TW, QH; Drafting manuscript: TW, YZ, QH, LL. All authors contributed to the article and approved the submitted version.

REFERENCES

1. Waqas K, Lima Ferreira J, Tsourdi E, Body JJ, Hadji P, Zillikens MC. Updated Guidance on the Management of Cancer Treatment-Induced Bone Loss (CTIBL) in Pre- and Postmenopausal Women With Early-Stage Breast Cancer. *J Bone Oncol* (2021) 28:100355. doi: 10.1016/j.jbo.2021.100355
2. Chen J, Zhang X, Lu Y, Zhang T, Ouyang Z, Sun Q. Optimal Duration of Endocrine Therapy With Extended Aromatase Inhibitors for Postmenopausal Patients With Hormone Receptor-Positive Breast Cancer: A Meta-Analysis. *Breast Cancer* (2021) 28:630–43. doi: 10.1007/s12282-020-01196-8
3. Tothill P, Weir N, Loveland J. Errors in Dual-Energy X-Ray Scanning of the Hip Because of Nonuniform Fat Distribution. *J Clin Densitom* (2014) 17:91–6. doi: 10.1016/j.jocd.2013.02.008
4. Catalano A, Gaudio A, Agostino RM, Morabito N, Bellone F, Lasco A. Trabecular Bone Score and Quantitative Ultrasound Measurements in the Assessment of Bone Health in Breast Cancer Survivors Assuming Aromatase Inhibitors. *J Endocrinol Invest* (2019) 42:1337–43. doi: 10.1007/s40618-019-01063-0
5. Pechmann LM, Petterle RR, Moreira CA, Borba VZC. Osteosarcopenia and Trabecular Bone Score in Patients With Type 2 Diabetes Mellitus. *Arch Endocrinol Metab* (2021) 65:801–10. doi: 10.20945/2359-3997000000418
6. Shanbhogue VV, Brixen K, Hansen S. Age- and Sex-Related Changes in Bone Microarchitecture and Estimated Strength. A Three-Year Prospective Study Using HR-pQCT. *J Bone Miner Res* (2016) 31(8):1541–9. doi: 10.1002/jbmr.2817
7. Hardaway AL, Herroon MK, Rajagurubandara E, Podgorski I. Bone Marrow Fat: Linking Adipocyte-Induced Inflammation With Skeletal Metastases. *Cancer Metastasis Rev* (2014) 33:527–43. doi: 10.1007/s10555-013-9484-y
8. Krings A, Rahman S, Huang S, Lu Y, Czernik PJ, Lecka-Czernik B. Bone Marrow Fat has Brown Adipose Tissue Characteristics, Which are Attenuated With Aging and Diabetes. *Bone* (2012) 50:546–52. doi: 10.1016/j.bone.2011.06.016
9. Baum T, Rohrmeier A, Syvari J, Diefenbach MN, Franz D, Dieckmeyer M, et al. Anatomical Variation of Age-Related Changes in Vertebral Bone Marrow Composition Using Chemical Shift Encoding-Based Water-Fat Magnetic Resonance Imaging. *Front Endocrinol (Lausanne)* (2018) 9:141. doi: 10.3389/fendo.2018.00141
10. Lecka-Czernik B, Stechschulte LA, Czernik PJ, Sherman SB, Huang S, Krings A. Marrow Adipose Tissue: Skeletal Location, Sexual Dimorphism, and Response to Sex Steroid Deficiency. *Front Endocrinol (Lausanne)* (2017) 8:188. doi: 10.3389/fendo.2017.00188
11. Li G, Xu Z, Gu H, Li X, Yuan W, Chang S, et al. Comparison of Chemical Shift-Encoded Water-Fat MRI and MR Spectroscopy in Quantification of Marrow Fat in Postmenopausal Females. *J Magn Reson Imaging* (2017) 45:66–73. doi: 10.1002/jmri.25351
12. Cha YJ, Koo JS. Roles of Omental and Bone Marrow Adipocytes in Tumor Biology. *Adipocyte* (2019) 8:304–17. doi: 10.1080/21623945.2019.1643189
13. Mukherjee A, Chiang CY, Daifotis HA, Nieman KM, Fahrmann JF, Lastra RR, et al. Adipocyte-Induced FABP4 Expression in Ovarian Cancer Cells Promotes Metastasis and Mediates Carboplatin Resistance. *Cancer Res* (2020) 80:1748–61. doi: 10.1158/0008-5472.CAN-19-1999
14. Li G, Xu Z, Zhuang A, Chang S, Hou L, Chen Y, et al. Magnetic Resonance Spectroscopy-Detected Change in Marrow Adiposity is Strongly Correlated to Postmenopausal Breast Cancer Risk. *Clin Breast Cancer* (2017) 17:239–44. doi: 10.1016/j.clbc.2017.01.004
15. Karampinos DC, Ruschke S, Dieckmeyer M, Eggers H, Kooijman H, Rummeny EJ, et al. Modeling of T2 * Decay in Vertebral Bone Marrow Fat Quantification. *NMR BioMed* (2015) 28:1535–42. doi: 10.1002/nbm.3420
16. Dieckmeyer M, Ruschke S, Rohrmeier A, Syväri J, Einspieler I, Seifert-Klauss V, et al. Vertebral Bone Marrow Fat Fraction Changes in Postmenopausal Women With Breast Cancer Receiving Combined Aromatase Inhibitor and Bisphosphonate Therapy. *BMC Musculoskelet Disord* (2019) 20:515. doi: 10.1186/s12891-019-2916-2
17. Fraczak E, Olbromski M, Piotrowska A, Glatzel-Plucinska N, Dziegiel P, Dybko J, et al. Bone Marrow Adipocytes in Haematological Malignancies. *Acta Histochem* (2018) 120:22–7. doi: 10.1016/j.acthis.2017.10.010
18. Botella S, Restituto P, Monreal I, Colina I, Calleja A, Varo N. Traditional and Novel Bone Remodeling Markers in Premenopausal and Postmenopausal Women. *J Clin Endocrinol Metab* (2013) 98:E1740–8. doi: 10.1210/jc.2013-2264
19. Catalano A, Morabito N, Agostino RM, Basile G, Gaudio A, Atteritano M, et al. Bone Health Assessment by Quantitative Ultrasound and Dual-Energy X-Ray Absorptiometry in Postmenopausal Women With Breast Cancer Receiving Aromatase Inhibitors. *Menopause* (2017) 24:85–91. doi: 10.1097/GME.0000000000000722
20. Catalano A, Gaudio A, Morabito N, Basile G, Agostino RM, Xourafa A, et al. Quantitative Ultrasound and DXA Measurements in Aromatase Inhibitor-Treated Breast Cancer Women Receiving Denosumab. *J Endocrinol Invest* (2017) 40:851–7. doi: 10.1007/s40618-016-0606-6
21. Van Poznak C, Hannon RA, Mackey JR, Campone M, Apffelstaedt JP, Clack G, et al. Prevention of Aromatase Inhibitor-Induced Bone Loss Using Risedronate: The SABRE Trial. *J Clin Oncol* (2010) 28:967–75. doi: 10.1200/JCO.2009.24.5902
22. Kuba S, Watanabe K, Chiba K, Matsumoto M, Yamanouchi K, Fukushima A, et al. Adjuvant Endocrine Therapy Effects on Bone Mineral Density and Microstructure in Women With Breast Cancer. *J Bone Miner Metab* (2021) 39:1031–40. doi: 10.1007/s00774-021-01239-w
23. Patsch JM, Li X, Baum T, Yap SP, Karampinos DC, Schwartz AV, et al. Bone Marrow Fat Composition as a Novel Imaging Biomarker in Postmenopausal Women With Prevalent Fragility Fractures. *J Bone Miner Res* (2013) 28:1721–8. doi: 10.1002/jbmr.1950
24. Karampinos DC, Ruschke S, Gordijenko O, Grande Garcia E, Kooijman H, Burgkart R, et al. Association of MRS-Based Vertebral Bone Marrow Fat Fraction With Bone Strength in a Human *In Vitro* Model. *J Osteoporos* (2015) 2015:152349. doi: 10.1155/2015/152349

25. Niada S, Giannasi C, Ferreira LM, Milani A, Arrigoni E, Brini AT. 17beta-Estradiol Differently Affects Osteogenic Differentiation of Mesenchymal Stem/Stromal Cells From Adipose Tissue and Bone Marrow. *Differentiation* (2016) 92(5):291–7. doi: 10.1016/j.diff.2016.04.001
26. Syed FA, Oursler MJ, Hefferanm TE, Peterson JM, Riggs BL, Khosla S. Effects of Estrogen Therapy on Bone Marrow Adipocytes in Postmenopausal Osteoporotic Women. *Osteoporos Int* (2008) 19:1323–30. doi: 10.1007/s00198-008-0574-6

Conflict of Interest: The authors declare that the research was conducted in the absence of any commercial or financial relationships that could be construed as a potential conflict of interest.

frontiers | Frontiers in Endocrinology

REVIEW
published: 30 June 2022
doi: 10.3389/fendo.2022.898634

Autophagy in Bone Remodeling: A Regulator of Oxidative Stress

Chenyu Zhu[1,2†], *Shiwei Shen*[3†], *Shihua Zhang*[1,4], *Mei Huang*[1], *Lan Zhang*[4*] *and Xi Chen*[2*]

[1] School of Kinesiology, Shanghai University of Sport, Shanghai, China, [2] School of Sports Science, Wenzhou Medical University, Wenzhou, China, [3] The Second School of Medicine, Wenzhou Medical University, Wenzhou, China, [4] College of Sports and Health, Shandong Sport University, Jinan, China

OPEN ACCESS

Edited by:
Guanwu Li,
Shanghai University of Traditional Chinese Medicine, China

Reviewed by:
Chen-he Zhou,
Zhejiang University, China
Elizabeth Rendina-Ruedy,
Vanderbilt University Medical Center, United States
Chaohong Li, Sun Yat-sen University, China

***Correspondence:**
Xi Chen
chenab004@126.com
Lan Zhang
hanglan_sdty@163.com

[†]These authors have contributed equally to this work

Specialty section:
This article was submitted to Bone Research, a section of the journal Frontiers in Endocrinology

Received: 17 March 2022
Accepted: 01 June 2022
Published: 30 June 2022

Citation:
Zhu C, Shen S, Zhang S, Huang M, Zhang L and Chen X (2022) Autophagy in Bone Remodeling: A Regulator of Oxidative Stress. Front. Endocrinol. 13:898634. doi: 10.3389/fendo.2022.898634

Bone homeostasis involves bone formation and bone resorption, which are processes that maintain skeletal health. Oxidative stress is an independent risk factor, causing the dysfunction of bone homeostasis including osteoblast-induced osteogenesis and osteoclast-induced osteoclastogenesis, thereby leading to bone-related diseases, especially osteoporosis. Autophagy is the main cellular stress response system for the limination of damaged organelles and proteins, and it plays a critical role in the differentiation, apoptosis, and survival of bone cells, including bone marrow stem cells (BMSCs), osteoblasts, osteoclasts, and osteocytes. High evels of reactive oxygen species (ROS) induced by oxidative stress induce autophagy to protect against cell damage or even apoptosis. Additionally, pathways such as ROS/FOXO3, ROS/AMPK, ROS/Akt/mTOR, and ROS/JNK/c-Jun are involved in the regulation of oxidative stress-induced autophagy in bone cells, including osteoblasts, osteocytes and osteoclasts. This review discusses how autophagy regulates bone formation and bone resorption following oxidative stress and summarizes the potential protective mechanisms exerted by autophagy, thereby providing new insights regarding bone remodeling and potential therapeutic targets for osteoporosis.

Keywords: autophagy, oxidative stress, osteoblast, osteoclast, osteoporosis

1 INTRODUCTION

Bone is constantly being remodeled to maintain the balance of growth and development of the skeletal system (1). Bone remodeling is essential for the formation and maintenance of bone morphology and the repair of damaged bone (2). Physiological bone remodeling requires a balance between bone formation and bone resorption, while the dynamic balance needs coupling of the activities of different bone cells (e.g., osteoblasts, osteocytes, and osteoclasts) (3). Osteoblasts mainly arise by differentiation of bone marrow mesenchymal stem cells (BMSCs) and play an osteogenic role in the regulation of the synthesis, secretion, and mineralization of the bone matrix (4). At the end stage of bone formation, osteoblasts become encapsulated in the bone matrix and mature into osteocytes, which play a crucial role in bone remodeling (5). Osteoclasts, which are the only bone-resorbing cells in the body, are tissue-specific multinucleated macrophages that arise by the differentiation of monocytes or macrophage precursors on or near the bone surface (6). Bone remodeling consists of four primary stages, including bone resorption, recruitment of osteoblasts

and BMSCs, osteoblast differentiation, and completion of bone mineralization (7). Dysfunction of any cell type involved in this process can lead to the failure of bone remodeling followed by the development of bone-related diseases, especially osteoporosis (8).

Oxidative stress plays a pivotal role in the regulation of the balance of bone remodeling processes (9), including effects on bone formation and bone resorption. Reactive oxygen species (ROS) induced by oxidative stress can lead to apoptosis of osteocytes and osteoblasts and inhibit bone mineralization and osteogenesis, which combine with unbalanced osteoclast formation to lead to enhanced bone loss and progression of osteoporosis (10, 11). At physiological levels, ROS can act as signaling molecules involved in cellular processes such as differentiation, proliferation, apoptosis, autophagy, and redox signaling (12). In contrast, excessive ROS levels result in damage to lipids, proteins, and DNA, which can ultimately lead to cell death (13).

Autophagy is an essential metabolic pathway for cell survival in case of nutrient or energy deficiencies, oxidative stress, infections, or hypoxia (14). The cytoplasm or organelles of the cell itself are engulfed into vesicles to form autophagosomes, which are then transported to the lysosome for degradation to remove damaged or aging organelles and to maintain the basal cellular homeostasis (15, 16). In response to oxidative stress, autophagy is regulated by the level of ROS resulting from cellular injury, and it supports cell survival by a cytoprotective mechanism that mitigates the damage resulting from the oxidative stress (17). However, excessive accumulation of ROS can also exacerbate cellular damage by dysregulation of autophagy, leading to mitochondrial dysfunction and increased levels of ROS (18). It appears that the interaction between ROS and autophagy is critical for cellular homeostasis. Therefore, the mode of interaction between autophagy and oxidative stress during bone remodeling warrants further elucidation. Here, we reviewed the mechanism of autophagy in response to oxidative stress during bone remodeling and discussed potential therapeutic targets of the autophagy process for osteoporosis.

2 ROLE OF OXIDATIVE STRESS IN BONE REMODELING

Cellular oxidative stress is caused by an imbalance of intracellular redox homeostasis or a relative overload of ROS (19). Mitochondrial are rod-shaped or elongated under normal conditions, whereas under conditions of oxidative stress, the length and density of mitochondria are significantly reduced as they become fragmented, resulting in impaired cellular metabolic function and increased ROS production, and potentially even cell death (20). Oxidative stress is an independent risk factor for postmenopausal, glucocorticoid, and diabetic osteoporosis (20). By impairing bone remodeling as a result of disruption of the coupling of osteoblasts and osteoclasts, oxidative stress-induced ROS may underlie the main cellular mechanism of osteoporosis (21, 22).

2.1 Oxidative Stress in Osteoblasts

At physiological levels, ROS help maintain cellular function, whereas uncontrolled levels of ROS are detrimental (23). As osteoblast differentiation requires energy, BMSCs or preosteoblasts undergo a metabolic transformation whereby mitochondrial respiration and ATP production are increased to ensure an adequate energy supply, which is accompanied by an increase in endogenous ROS (24). Additionally, excessive ROS levels reduce osteogenic differentiation in situations of estrogen deficiency, high glucose, diabetes, inflammation, stress, aging, or other pathophysiological factors, which can decrease metabolic enzyme activity or antioxidant production (25, 26). BMSCs cultured long-term *in vitro* exhibit decreased antioxidant capacities and elevated ROS levels, leading to reduction or loss of osteogenic differentiation potential (27). Likewise, hydrogen peroxide (H_2O_2)-induced oxidative stress has been shown to inhibit osteogenic differentiation in rat BMSC as measured by reduction in alkaline phosphatase (ALP) activity and Runx2 and ATF4 expression levels (28) (29). In contrast, reduction in the level of oxidative stress in BMSCs enhanced osteogenic function and restored bone mass and bone microarchitecture in ovariectomized rats (30). In addition, signaling pathways triggered by ROS regulate cell proliferation, growth, differentiation, and even apoptosis, thereby affecting the lifespan of osteoblasts. Mitogen-activated protein kinases (MAPKs) such as c-Jun-N terminal kinase (JNK), extracellular signal-regulated kinase (ERK1/2), and p38 are involved in osteoblasts apoptosis (31–33). High levels of ROS activated the JNK signaling pathway, which increases the transcriptional expression of pro-apoptotic genes such as caspase 3, FASL, and caspase 9 (34). Moreover, ROS induced by H_2O_2 continuously stimulated the ERK signaling pathway in osteoblasts, which then enhances the expression of Bax and the hyperpolarization of the mitochondrial membrane potential, thereby resulting in cell apoptosis (35).

2.2 Oxidative Stress in Osteoclasts

Oxidative stress and the consequent production of ROS promotes osteoclast differentiation and osteoclastogenesis (36). Receptor activator of nuclear factor-κB ligand (RANKL) stimulation has been shown to increase ROS production in bone marrow mesenchymal stem cells (BMMs) through a tumor necrosis factor receptor-associated factor 6 (TRAF6)/RAC1/nicotinamide adenine dinucleotide phosphate oxidase 1 (Nox1) signaling cascade, resulting in enhanced differentiation of osteoclasts. Conversely, exposure to the antioxidant N-acetylcysteine (NAC) has been shown to inhibit the response of BMMs to RANKL, involving ROS production, activation of the MAPK pathway, and osteoclastogenesis (37). Likewise, in the glucose-induced diabetic osteoporosis model in rats, increased ROS production in osteoclasts and subsequently enhanced expression of proteins related to MAPKs [phosphorylated (p)-ERK, p-JNK, and p-p38], NF-κB (NF-κB, p-IκB, and IKK), and NACHT-LRR-PYD domains-containing protein 3 (NLRP3)-related protein expression, which promotes osteoclast differentiation and bone resorption, were observed (38).

ROS production not only directly enhances osteoclast differentiation but also interacts with osteoblasts to regulate the formation and differentiation of osteoclasts. OPG/RANK/RANKL form a molecular triad that links osteoblasts and osteoclasts and thus plays a significant role in osteoclastogenesis (39, 40). High levels of H_2O_2-induced ROS in osteoblasts (including osteoblast-like MG63 cells and primary mice osteoblasts) and BMSCs have been shown to stimulate the expression of RANKL mRNA and protein through ERKs and the PKA-CREB pathway (41). Co-culture of osteoblasts with osteoclast precursor cells has revealed that ethanol (EtOH)-induced RANKL expression depends on intracellular ROS stimulation by NADPH oxidase activity in osteoblast, which promotes osteoclast differentiation (42). These results demonstrate that ROS can promote RANKL secretion by osteoblasts, thereby regulating osteoclast differentiation, thus providing novel insights into the role of ROS production in the regulation of osteoblast-osteoclast communication.

Taken together, these findings suggest that ROS can inhibit osteoblast differentiation and hence also bone formation, in addition to promoting osteoclast differentiation and osteoclastogenesis. The effect of oxidative stress on different cell types and their communication are thought to play an essential role in the development of osteoporosis.

3 ROLE OF AUTOPHAGY IN BONE REMODELING

3.1 Autophagy in Osteoblasts

Autophagy plays a significant role in bone formation, including differentiation of BMSCs into osteoblasts to osteocytes, osteogenesis, differentiation, and the formation of bone matrix. BMSC differentiation requires energy, while the products of autophagosomal degradation can be oxidized by mitochondria to provide a suitable energy supply for their differentiation (43). Optimal differentiation of MSCs into osteoblasts involves an early stage of AMP-activated protein kinase (AMPK)/mTOR signaling axis-mediated autophagy as well as a later stage of Akt/mTOR signaling axis activation (44). Conversely, reduction of the level of autophagy directly inhibits the function of endogenous BMSCs and further promotes the development of osteoporosis (45). When MSCs are fully differentiated into osteoblasts, basal autophagy is completely inhibited, but this does not indicate that the differentiated cells are no longer capable of autophagy (46).

Mesenchymal-derived osteoblasts, which are recognized as specialized mineralizing cells in bone formation, are known to play a critical role in the synthesis, secretion, and mineralization of the bone matrix (47, 48). A previous study *in vitro* found that autophagy defects induced by ablation of FIP200 in osteoblasts led to the dysfunction of osteoblasts differentiation (49). Furthermore, downregulation of the expression of autophagy markers, such as LC3-II and ATG7, has been shown to result in the inhibition of osteoblast differentiation (50, 51). The early stage of osteoblast differentiation requires the activation of AMPK, and the terminal stage is dependent on downregulation of AMPK (52, 53), which is mediated by stimulation of AKT and mTOR (54), and then activates cell autophagy.

Additionally, autophagy is also directly involved in the mineralization process of osteoblasts. Conditional knockdown of ATG7 in osteoblasts led to a reduction of mineralization capacity *in vivo* (55), and knockout of the autophagy-related genes Fip200 or Atg5 in Osterix-Cre transgenic mice also resulted in impaired mineralization and reduced bone mass in mice (56). These results indicated that autophagy is required in the mineralization process of osteoblasts, which can be attributed to autophagic vesicles acting as carriers for the secretion of apatite crystals to the extracellular matrix (55).

3.2 Autophagy in Osteoclasts

Osteoclasts, which differentiate from hematopoietic mononuclear stem cells in the bone marrow, are critical at the beginning of bone remodeling by bone resorption *via* following differentiation into multinucleated osteoclasts which then migrate to the surface of the bone (57, 58). HIF1-α, which is produced in response to hypoxic stress, has been reported to upregulated BNIP3, which increases the level of Beclin-1 and then activates autophagic flux accompanied by the autophagy-related genes ATGs, thereby leading to increased osteoclastogenesis by upregulation of CTSK, NFATC1, and MMP9 (59). Another study showed that a microgravity environment (rotary cell culture system) increased autophagy in osteoclasts, which then stimulated osteoclast differentiation and osteoclastogenesis (60). Moreover, the level of autophagy initiation protein Beclin-1 has been reported to increase during osteoclast differentiation. Ctsk-cell expression conditional Beclin-1 deficient mice exhibited an increase in the thickness of cortical bone *via* attenuated osteoclast function, while overexpression of Beclin-1 in osteoclast precursors has been reported to enhance autophagy-induced osteoclastogenesis *in vitro* and increase bone resorption (61). Mechanistically, it was concluded that TRAF6-mediated K63-linked ubiquitination at Beclin1-K117 is needed for RANKL-induced osteoclast differentiation (61, 62). These findings support the notion that autophagy in osteoclasts is susceptible to environmental factors such as hypoxic stress and microgravity, which results in further regulation of the differentiation of osteoclasts and osteoclastogenesis.

In addition to its role in osteoclast differentiation, autophagy has also been demonstrated to be essential in osteoclast function. Terminally differentiated osteoclasts are tightly attached to the bone surface by pedicles. F-actin, talin, vinculin, and α-actinin are the key anchor targets for osteoclast attachment, and lysosomes then migrate to the bone surface and resorbing bone (57). The autophagy-related proteins ATG4B, ATG5, ATG7, and LC3 have all been shown to play crucial roles in promoting bone resorption activity. For example, knockdown of ATG5 and ATG7 in osteoclasts has been shown to significantly reduce the depth and volume of bone traps and reduce the ability to deliver lysosomes to the fold membrane boundary, although this does not appear to affect osteoclast formation. The lysosomal secretory function requires ATG5-ATG12 coupling to facilitate

LC3 binding to phosphatidylethanolamine. ATG5 deficiency inhibits LC3II production as well as CTSK localization (63, 64).

4 REGULATION OF AUTOPHAGY IN OXIDATIVE STRESS

Oxidative stress is involved in the development of osteoporosis and aging, as evidenced by both ovariectomy and age-increased oxidative stress and reduction of the antioxidant system in rat femurs, which promotes the development of osteoporosis (65). As mentioned above, oxidative stress disrupts the balance of bone formation and resorption by inhibiting osteoblast function and promoting osteoclast activity. In response to oxidative stress-induced autophagy, ROS may act as an antioxidant during dysregulation of bone remodeling to protect from bone loss and osteoporosis. In the following, we describe the regulation of autophagy in response to oxidative stress in osteoblasts, osteocytes, and osteoclasts (**Figure1**).

4.1 Regulation of Autophagy in the Response to Oxidative Stress in Osteoblasts

A high glucose (HG) environment, glucocorticoids or estrogen deficiency cause a pathological increase in ROS levels, thereby impairing the osteoblast function (66–68). In response to ROS, autophagy is activated and promotes osteoblast function as a negative feedback loop. Alberto et al. found that HG increased protein oxidation and the ROS levels, thereby activating autophagy in MC3T3-E1 cells, which reduced damage from HG and protected the cells, whereas inhibition of autophagy increased cell apoptosis (66). In addition, increased ROS levels caused the LC3II/LC3I ratios to increase and p62/SQSTMI to decrease, as observed in advanced glycation end products (AGE)-treated osteoblasts. Furthermore, the autophagy agonist rapamycin (RA) attenuated AGE-induced apoptosis, while the autophagy inhibitor 3-methyladenine (3-MA) increased AGE-induced apoptosis, indicating that autophagy plays a critical role in protecting osteoblasts from AGE-induced apoptosis (69). Likewise, other studies have also demonstrated that osteoblast activity is regulated by glucocorticoids in a dose-dependent manner. Low doses of dexamethasone promoted osteoblast autophagy, protected from damage by ROS, and attenuated apoptosis in osteoblasts. However, as the dose and the duration of the dexamethasone treatment increased, the antioxidant effects of autophagy were overwhelmed, which then lead to apoptosis (67). These results reveal that the protective effect of ROS-induced autophagy is limited and dependent on the dose of ROS level and the duration of stimulation.

Osteoblasts experiencing stress from aging or ovariectomy in mice have been reported to have increased levels of ROS and swollen mitochondria, followed by a 95% decrease in LC3-II levels. Further research has indicated that osteoblast conditional autophagy deficiency in mice results in enhanced aging and estrogen deficiency-related bone loss (68). Conversely, estradiol administration has been shown to increase ULK1, Beclin1, and LC3II protein levels in osteoblasts, decrease oxidative stress levels, and significantly reduced the expression of apoptotic biomarkers through the ER-ERK-mTOR pathway (70). Thus, autophagy can be an important potential target for protection against damage from oxidative stress or ROS, but how autophagy

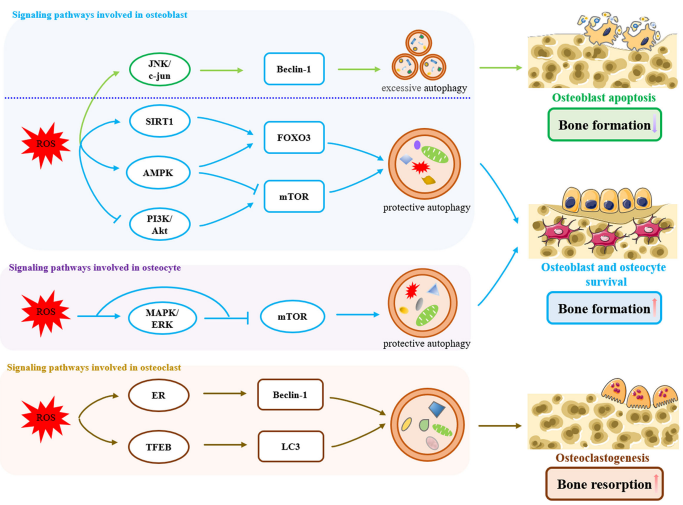

FIGURE 1 | Signaling pathways involved in oxidative stress-induced autophagy in bone remodeling. In osteoblasts, ROS induced an excessive increase in Beclin-1 levels by activation of the JNK/c-jun pathway, which triggered excessive autophagy, exacerbated osteoblasts apoptosis, and reduced bone formation. On the other hand, oxidative stress activates protective autophagy through ROS/SIRT1/FOXO3, ROS/AMPK/FOXO3, ROS/AMPK/mTOR and ROS/PI3K/Akt/mTOR pathways to remove excessive ROS within a certain range, promoting the survival of osteoblasts and increasing bone formation. Likewise in osteoblasts, oxidative stress-induced protective autophagy is also present in osteocytes, which is achieved by ROS/MAPK/ERK/mTOR pathway. In osteoclasts, Oxidative stress-induced autophagy promotes osteoclastogenesis and bone resorption through the ROS/ER and ROS/TFEB pathways.

responds to ROS signaling needs to be further explored. Following is a review of ROS/FOXO3, ROS/AMPK, ROS/Akt/mTOR, and ROS/JNK/c-Jun pathways that are involved in the autophagic response to oxidative stress in osteoblasts.

4.1.1 ROS/FOXO3

Forkhead box O3(FOXO3) protein is a member of the FOXO family, which can be activated by catalase, SOD2, and glutathione peroxide in antioxidant reactions (71). In response to oxidative stress, MAPK8, MAPK14/p38α, and serine/threonine-protein kinase 4 (STK4)/MST1 phosphorylate FOXOs, causing their nuclear translocation as well as transcriptional activation of target genes such as manganese superoxide dismutase (MnSOD) and catalase (72, 73). During BMSC differentiation into osteoblasts, and then osteoblasts differentiation into osteocytes, the increasing level of ROS activates FOXO3 serine 294 phosphorylation, and FOXO3-induced autophagy then downregulates the increased ROS levels as a negative feedback loop to ensure proper differentiation (74). In addition, inhibition of MAPK11/12/14 kinase can reduce the nuclear translocation of FOXO3 by MSC exposure to oxidative stress, while LC3B and GABARAPL1 are significantly upregulated upon FOXO activation, suggesting that MAPK11/12/14 participate in the activation of FOXO3 by ROS and then activate autophagy. PARK2, a ubiquitin ligase that is indispensable for inducing mitochondrial autophagy, was also significantly increased when FOXO3 was induced by ROS, which is an important process for the clearance of ROS, while the process was impaired when FOXO3 was knocked down (74).

SIRT1 is another key factor involved in ROS-mediated FOXO3 activation. Gu et al. found that ROS/SIRT1/FOXO3 may be involved in the survival of the damage from fluoride in MC3T3-E1 osteoblasts. ROS-mediated activation of SIRT1 has been shown to increase the level of FOXO3 deacetylation and to promote the expression of its substrate Bnip3, which promotes the upregulation of autophagy levels and reduces fluoride-induced osteoblast apoptosis. Conversely, inhibition of SIRT1 expression has been shown to impair FOXO3-induced autophagy (75).

4.1.2 ROS/AMPK

AMPK is a heterotrimeric complex comprising a catalytic subunit (α-subunit) and two regulatory subunits (β- and γ-subunits) (76). In addition to its role in energy metabolism, AMPK also acts as an oxidative stress sensor to regulate cell survival under stressful conditions (77). ROS activates AMPK by phosphorylating the AMPK alpha1 threonine 172 (78), and activated AMPK directly phosphorylates the mTORC1 subunit Raptor, which can then suppress the inhibitory effect of mTORC1 on ULK1 to promote autophagy. Moreover, AMPK also directly phosphorylates Ser 317 and Ser 777 of the UKL1 complex to activate autophagy (79). However, inhibition of autophagy enhances ROS-induced cell apoptosis. H_2O_2 can induce phosphorylation of ULK1 and upregulation of LC3B-II *via* activation of AMPK, while treatment with the autophagy inhibitors 3-MA and bafilomycin A1 increases H_2O_2-induced cell death. Furthermore, AMPKα knockdown has been reported to further inhibit ULK1 phosphorylation and LC3B-II upregulation, indicating that ROS/autophagy activation in osteoblasts requires AMPK, which can act as a negative feedback loop in the regulation of ROS levels when exposed to oxidative stress (80). Consistent with these results, the AMPK activators GSK621 or A-769662 enhance the protective autophagic response as evidenced by phosphorylation of ULK1 on Ser-317, upregulation of ATG5 and Beclin-1, and downregulation of p62 (81, 82) in case of H_2O_2-induced oxidative stress in osteoblasts.

4.1.3 ROS/Akt/mTOR

The PI3K/Akt/mTOR pathway plays an essential role in stress responses, autophagy, cell survival, and apoptosis (83). The PI3K/Akt signaling axis activates mTOR by phosphorylation of p70S6K and 4EBP1, thereby inhibiting autophagy (84, 85). ROS initially regulate PI3K/Akt, and the PI3K/Akt pathway in turn regulates ROS homeostasis to promote cell survival (86). It has been reported that ROS levels are significantly elevated under high glucose conditions, and p-Akt and p-mTOR protein expression was significantly downregulated in MC3T3-E1 cells, while the antioxidant NAC reversed their expression and reduced osteoblasts apoptosis, suggesting that high levels of ROS promoted the protective autophagy by inhibition of the Akt/mTOR axis (87). Further study has revealed that the inactivation of phosphatase and tensin homologs (PTEN) when ROS activates PI3K may be the main reason for ROS inhibition of the Akt/mTOR signaling pathway, as PTEN inhibits the synthesis of PIP3 and thus activation of Akt signaling (88). The Chinese traditional medicine monotropein has been reported to protect against the damage from H_2O_2-induced oxidative stress in osteoblasts. Monotropein was found to decrease phosphorylation of Akt, mTOR, p70S6K, and 4EBP1, as well as upregulate Beclin-1 expression and LC3-II/LC3-I ratios, which then activated autophagy to increase osteoblastic bone formation (89). Monotropein, hence, appears to have potential for treatment or prevention of aging or estrogen-deficiency osteoporosis.

4.1.4 ROS/JNK/c-Jun

Fluoride-mediated ROS triggers oxidative cell damage and apoptosis through N-terminal kinase (JNK)/c-Jun signaling. In contrast, the ROS-induced JNK/c-Jun pathway activates SIRT1 and triggers autophagy as an adaptive reaction to protect cells from fluoride damage (90). However, it has also been shown that the ROS-autophagy process mediated by the JNK pathway enhanced osteoblast apoptosis. Glucocorticoids upregulated JNK and c-Jun phosphorylation in osteoblasts, thereby activating JNK/c-Jun signaling pathway-induced autophagy, which then leads to increased apoptosis (91). ROS inhibitors have been reported to downregulate the JNK/c-Jun signaling pathway, but JNK inhibitors did not reduce ROS, indicating that ROS is an upstream signal for JNK, while autophagy and apoptosis occur in response to ROS/JNK/c-Jun signaling (91). Further studies have shown that JNK causes the degradation of the Beclin-1/Bcl-2 complex by phosphorylating Bcl2, and Beclin-1 excessively stimulates the onset of autophagy (92, 93), and a

low level of Beclin-1 promotes autophagy for cell survival, while a high level of Beclin-1 induces autophagic cell death (94, 95). These findings indicated that JNK may be a potential target involved in the balance between oxidative stress-induced autophagy and apoptosis.

In the above studies, autophagy induced by oxidative stress may be a double-edged sword for osteoblasts. On the one hand, in response to aberrant ROS signaling, the MAPK/FOXO3, SIRT1/FOXO3, and AMPK pathways are activated, and the Akt/mTOR pathway is inhibited, leading to activation of autophagy and the scavenging of excessive ROS within a certain range, thereby promoting osteoblast survival and increasing bone formation. On the other hand, when ROS levels are so high as to exceed the clearance effect of protective autophagy, they can activate the JNK pathway and subsequently induce excessive autophagy, thereby enhancing apoptosis of osteoblasts and thus reducing bone formation. A large cascade of interdependent responses between autophagy and JNK-mediated apoptosis has been documented, but how the JNK pathway regulates the balance of autophagy and apoptosis in osteoblasts in response to ROS signaling remains to be fully elucidated.

4.2 Regulation of Autophagy in the Response to Oxidative Stress in Osteocytes

As in osteoblasts, oxidative stress-induced autophagy in osteocytes is also a protective response. Decreased estrogen levels are a prominent cause of postmenopausal osteoporosis. Yang et al. established an ovariectomized rat model that mimics the decrease in estrogen levels *in vivo*. They found a significant decrease in bone mineral density and bone mass in ovariectomized rats, accompanied by a decrease in antioxidant parameters such as the total antioxidant capacity, superoxide dismutase activity, catalase activity, and an increase in the expression level of osteocyte autophagy-related factors such as ATG5, LC3, and Beclin-1. In contrast, estrogen treatment prevented the decrease in bone mass and the abnormal increase in oxidative stress levels, and it restored autophagy to normal levels (96). These data suggest that estrogen deficiency can lead to an increase in oxidative stress levels *in vivo*, which in turn triggers its downstream protective autophagic response, but ultimately leads to the development of osteoporosis due to its limited protective effect. Further exploration of the negative feedback protection mechanism of autophagy in osteocytes has revealed that ROS/MAPK/ERK and ROS/mTOR/ULK1 signaling axes appear to play important roles (97, 98).

4.2.1 ROS/MAPK/ERK

ERK is one of the classical signal transduction components of the MAPK family, and it can directly induce autophagy by upregulation of the expression of autophagy-related proteins such as LC3 and p62 (99). Rekha et al. found that treatment with low doses of glucocorticoids increased oxidative stress levels and basal autophagy levels in osteocytes without increasing osteocyte apoptosis, whereas high doses of glucocorticoids enhanced osteocyte apoptosis. Further studies have revealed that glucocorticoid treatment significantly increases MAPK and ERK phosphorylation in osteocytes, while the ERK-specific inhibitor U0126 completely abolished glucocorticoid-induced elevated LC3 expression. These data suggest that low-dose glucocorticoid-induced oxidative stress activates the MAPK/ERK signaling pathway, which in turn enhances autophagy levels and protects osteocytes from oxidative stress damage, whereas the protective effect of autophagy induced by high levels of glucocorticoids has a range and does not respond to abnormally elevated ROS levels, thus manifesting as excessive apoptosis of osteocytes (97).

4.2.2 ROS/mTOR/ULK1

ULK1 is a key initiator protein in the induction of autophagy, and inhibition of mTOR activity can enhance autophagy levels by binding to and phosphorylating the serine site of ULK1 (100). Bisphenol A (BPA) is an environmental endocrine disruptor that can perturb bone metabolism and bone homeostasis (101). BPA has been reported to increase malondialdehyde and ROS levels in osteocytes and decrease the expression of the antioxidant enzymes nuclear factor E2-related factor 2 (Nrf2) and heme oxygenase-1 (HO-1), leading to oxidative stress. BPA has also been shown to significantly inhibited mTOR phosphorylation and promoted ULK1 phosphorylation, there inducing activation of autophagy. In contrast, treatment with the mTOR activator MHY1485 (MHY) or the ULK1 inhibitor SBI-0206965 (SBI) inhibited BPA-induced autophagy and enhanced apoptosis in osteocytes, but did not reduce ROS levels. Furthermore, NAC treatment attenuated the level of ROS-mediated autophagy. This suggests that the high level of ROS caused by BPA acts upstream of the mTOR/ULK1 signaling axis and that the autophagic response that it triggers is protective against the cytotoxic effects of BPA (98).

4.3 Regulation of Autophagy in the Response to Oxidative Stress in Osteoclasts

ROS acts as intracellular signaling mediators in osteoclast differentiation. RANKL stimulation of osteoclast precursor cells increases intracellular ROS production, and reduction of RANKL-induced ROS by NAC treatment down-regulates of MAPK, ERK, and other signaling pathways, thereby leading to attenuated osteoclast precursor differentiation (102, 103). Unlike autophagy acting as the cytoprotective role in osteoblasts, ROS-induced autophagy even promotes osteoclast differentiation and formation. High levels of ROS induced by glucocorticoids or inflammatory conditions act as a catalyst for osteoclastogenesis. Sul et al. found that lipopolysaccharide promoted autophagy and led to osteoclastogenesis by stimulating ROS production, while reduction of ROS by siNOX1 and siNOX2 dramatically diminished LC3II levels accumulation as well as the expression of osteoclast-specific genes expression (104). Interestingly, osteoclastogenesis was upregulated by glucocorticoids at high doses, but low doses had no effect (105). The accumulation of intracellular ROS in the presence of high glucocorticoid levels

was synchronized with the upregulation of autophagic activity, which was prevented by the ROS scavenger NAC. While 3-MA administration blocked the promotion of osteoclast formation by glucocorticoids, it failed to reduce intracellular ROS accumulation. We further explored how ROS mediates autophagy to enhance osteoclastogenesis and we found that the ROS/ER and ROS/TFEB pathways may be involved in this process.

4.3.1 ROS/ER

Endoplasmic reticulum stress (ER) is induced by the accumulation of misfolded proteins leading to an unfolded protein response. ROS can cause aggregation and misfolding of proteins (106). Activation of ER regulates autophagy, which in turn regulates cell survival and death (107). MCP-1 is an important protein in the differentiation of monocytes into osteoclast precursors, and p47PHOX expression and its membrane translocation expressions induced by MCP-1 have been reported to promote ROS production, which induced ER and subsequently promoted upregulation of the autophagy markers Beclin-1 and LC3II as well as expression of osteoclast-associated markers such as TRAP and Ctsk. 3-MA treatment or knockdown of Beclin-1 significantly suppressed TRAP and Ctsk expression without affecting ER or its upstream ROS levels (108). These results indicate that osteoclast precursor cell differentiation is mediated by ROS production, which leads to ER stress, thereby inducing autophagy and ultimately promoting osteoclastogenesis.

4.3.2 ROS/TFEB

TFEB is a key transcription factor that controls the autophagy-lysosome system. Stress conditions such as lysosomal dysfunction or starvation cause nuclear translocation of TFEB and promote transcription of its target genes (109). ROS can directly oxidize TFEB, reduce its association with RRAG GTPase on lysosomes, and rapidly induce nuclear localization (110). Sul et al. found that high levels of ROS induced by 7-ketocholesterol (7-KC) significantly increased the nuclear translocation of TFEB and upregulated the lipidated form of LC3II in osteoclasts as well as the number and the activity of osteoclasts. In contrast, TFEB knockdown significantly downregulated autophagy levels and osteoclastogenesis. This suggests that 7-KC-mediated ROS induced oxidation of TFEB and promoted its nuclear translocation to enhance autophagy, leading to increased osteoclast numbers and activity (111).

5 CONCLUSION

We have provided an overview of the function of oxidative stress-mediated autophagy in bone remodeling. Oxidative stress-induced ROS impair bone formation by osteoblasts and osteocytes and promote bone resorption by osteoclasts, thereby disrupting the homeostasis of bone and enhancing the progression of osteoporosis. In addition, ROS also activates autophagy and then regulates osteoblasts and osteocytes in a negative feedback loop. However, ROS-mediated autophagy enhances osteoclast differentiation, which can overwhelm the protective effect in osteoblasts and osteocytes, as bone tissue exposed to oxidative stress leads to the development of osteoporosis. Therefore, further studies of the regulatory mechanisms of autophagy in redox signaling during pathological bone remodeling are needed. Furthermore, it may be possible to exploit the potential targets of autophagy for protective or therapeutic strategies against osteoporosis.

AUTHOR CONTRIBUTIONS

XC and LZ designed this review and supervised the whole program; CZ, SS and SZ searched the articles and offered advice; MH prepared the figure; CZ, SS and XC wrote the paper. All the authors reviewed and approved the manuscript.

FUNDING

The work is supported by funding from Wenzhou basic scientific research project (Grant No. 2019Y0848) and the national undergraduate innovation and entrepreneurship training program (Grant No.202110343040).

REFERENCES

1. Feng X, McDonald JM. Disorders of Bone Remodeling. *Annu Rev Pathol* (2011) 6:121–45. doi: 10.1146/annurev-pathol-011110-130203
2. Martin T, Gooi JH, Sims NA. Molecular Mechanisms in Coupling of Bone Formation to Resorption. *Crit Rev Eukaryot Gene Expr* (2009) 19(1):73–88. doi: 10.1615/critreveukargeneexpr.v19.i1.40
3. Wang L, You X, Lotinun S, Zhang L, Wu N, Zou W. Mechanical Sensing Protein Piezo1 Regulates Bone Homeostasis *Via* Osteoblast-Osteoclast Crosstalk. *Nat Commun* (2020) 11(1):282. doi: 10.1038/s41467-019-14146-6
4. Dirckx N, Moorer MC, Clemens TL, Riddle RC. The Role of Osteoblasts in Energy Homeostasis. *Nat Rev Endocrinol* (2019) 15(11):651–65. doi: 10.1038/s41574-019-0246-y
5. Robling AG, Bonewald LF. The Osteocyte: New Insights. *Annu Rev Physiol* (2020) 82:485–506. doi: 10.1146/annurev-physiol-021119-034332
6. Feng X, Teitelbaum SL. Osteoclasts: New Insights. *Bone Res* (2013) 1(1):11–26. doi: 10.4248/BR201301003
7. Martin TJ, Seeman E. New Mechanisms and Targets in the Treatment of Bone Fragility. *Clin Sci (Lond)* (2007) 112(2):77–91. doi: 10.1042/CS20060046
8. Sućur A, Katavić V, Kelava T, Jajić Z, Kovačić N, Grčević D. Induction of Osteoclast Progenitors in Inflammatory Conditions: Key to Bone Destruction in Arthritis. *Int Orthop* (2014) 38(9):1893–903. doi: 10.1007/s00264-014-2386-y
9. Wauquier F, Leotoing L, Coxam V, Guicheux J, Wittrant Y. Oxidative Stress in Bone Remodelling and Disease. *Trends Mol Med* (2009) 15(10):468–77. doi: 10.1016/j.molmed.2009.08.004
10. Manolagas SC. From Estrogen-Centric to Aging and Oxidative Stress: A Revised Perspective of the Pathogenesis of Osteoporosis. *Endocr Rev* (2010) 31(3):266–300. doi: 10.1210/er.2009-0024
11. Baek KH, Oh KW, Lee WY, Lee SS, Kim MK, Kwon HS, et al. Association of Oxidative Stress With Postmenopausal Osteoporosis and the Effects of

Hydrogen Peroxide On Osteoclast Formation in Human Bone Marrow Cell Cultures. *Calcif Tissue Int* (2010) 87(3):226–35. doi: 10.1007/s00223-010-9393-9
12. Finkel T. Signal Transduction by Reactive Oxygen Species. *J Cell Biol* (2011) 194(1):7–15. doi: 10.1083/jcb.201102095
13. Finkel T, Holbrook NJ. Oxidants, Oxidative Stress and the Biology of Ageing. *Nature* (2000) 408(6809):239–47. doi: 10.1038/35041687
14. Dikic I, Elazar Z. Mechanism and Medical Implications of Mammalian Autophagy. *Nat Rev Mol Cell Bio* (2018) 19(6):349–64. doi: 10.1038/s41580-018-0003-4
15. Kim KH, Lee MS. Autophagy–A Key Player in Cellular and Body Metabolism. *Nat Rev Endocrinol* (2014) 10(6):322–37. doi: 10.1038/nrendo.2014.35
16. Klionsky DJ, Emr SD. Autophagy as a Regulated Pathway of Cellular Degradation. *Science* (2000) 290(5497):1717–21. doi: 10.1126/science.290.5497.1717
17. Sridhar S, Botbol Y, Macian F, Cuervo AM. Autophagy and Disease: Always Two Sides to a Problem. *J Pathol* (2012) 226(2):255–73. doi: 10.1002/path.3025
18. Yun HR, Jo YH, Kim J, Shin Y, Kim SS, Choi TG. Roles of Autophagy in Oxidative Stress. *Int J Mol Sci* (2020) 21(9):3289. doi: 10.3390/ijms21093289
19. Yoo BH, Wu X, Derouet M, Haniff M, Eskelinen EL, Rosen K. Hypoxia-Induced Downregulation of Autophagy Mediator Beclin 1 Reduces the Susceptibility of Malignant Intestinal Epithelial Cells to Hypoxia-Dependent Apoptosis. *Autophagy* (2009) 5(8):1166–79. doi: 10.4161/auto.5.8.10167
20. Li Q, Gao Z, Chen Y, Guan MX. The Role of Mitochondria in Osteogenic, Adipogenic and Chondrogenic Differentiation of Mesenchymal Stem Cells. *Protein Cell* (2017) 8(6):439–45. doi: 10.1007/s13238-017-0385-7
21. Cervellati C, Bonaccorsi G, Cremonini E, Bergamini CM, Patella A, Castaldini C, et al. Bone Mass Density Selectively Correlates With Serum Markers of Oxidative Damage in Post-Menopausal Women. *Clin Chem Lab Med* (2013) 51(2):333–8. doi: 10.1515/cclm-2012-0095
22. Fatokun AA, Stone TW, Smith RA. Hydrogen Peroxide-Induced Oxidative Stress in Mc3T3-E1 Cells: The Effects of Glutamate and Protection by Purines. *Bone* (2006) 39(3):542–51. doi: 10.1016/j.bone.2006.02.062
23. Sart S, Song L, Li Y. Controlling Redox Status for Stem Cell Survival, Expansion, and Differentiation. *Oxid Med Cell Longev* (2015) 2015:105135. doi: 10.1155/2015/105135
24. Atashi F, Modarressi A, Pepper MS. The Role of Reactive Oxygen Species in Mesenchymal Stem Cell Adipogenic and Osteogenic Differentiation: A Review. *Stem Cells Dev* (2015) 24(10):1150–63. doi: 10.1089/scd.2014.0484
25. Wang L, Zhao X, Wei BY, Liu Y, Ma XY, Wang J, et al. Insulin Improves Osteogenesis of Titanium Implants Under Diabetic Conditions by Inhibiting Reactive Oxygen Species Overproduction *Via* the PI3K-Akt Pathway. *Biochimie* (2015) 108:85–93. doi: 10.1016/j.biochi.2014.10.004
26. Shi C, Wu J, Yan Q, Wang R, Miao D. Bone Marrow Ablation Demonstrates That Estrogen Plays an Important Role in Osteogenesis and Bone Turnover *Via* an Antioxidative Mechanism. *Bone* (2015) 79:94–104. doi: 10.1016/j.bone.2015.05.034
27. Geissler S, Textor M, Kühnisch J, Könnig D, Klein O, Ode A, et al. Functional Comparison of Chronological and *in Vitro* Aging: Differential Role of the Cytoskeleton and Mitochondria in Mesenchymal Stromal Cells. *PLoS One* (2012) 7(12):e52700. doi: 10.1371/journal.pone.0052700
28. Chen T, Wang H, Jiang C, Lu Y. Pkd1 Alleviates Oxidative Stress-Inhibited Osteogenesis of Rat Bone Marrow-Derived Mesenchymal Stem Cells Through Taz Activation. *J Cell Biochem* (2021) 122(11):1715–25. doi: 10.1002/jcb.30124
29. Tan J, Xu X, Tong Z, Lin J, Yu Q, Lin Y, et al. Decreased Osteogenesis of Adult Mesenchymal Stem Cells by Reactive Oxygen Species Under Cyclic Stretch: A Possible Mechanism of Age Related Osteoporosis. *Bone Res* (2015) 3:15003. doi: 10.1038/boneres.2015.3
30. Chen L, Shi X, Xie J, Weng SJ, Xie ZJ, Tang JH, et al. Apelin-13 Induces Mitophagy in Bone Marrow Mesenchymal Stem Cells to Suppress Intracellular Oxidative Stress and Ameliorate Osteoporosis by Activation of Ampk Signaling Pathway. *Free Radic Biol Med* (2021) 163:356–68. doi: 10.1016/j.freeradbiomed.2020.12.235
31. Fontani F, Marcucci G, Iantomasi T, Brandi ML, Vincenzini MT. Glutathione, N-Acetylcysteine and Lipoic Acid Down-Regulate Starvation-Induced Apoptosis, Rankl/Opg Ratio and Sclerostin in Osteocytes: Involvement of Jnk and Erk1/2 Signalling. *Calcif Tissue Int* (2015) 96(4):335–46. doi: 10.1007/s00223-015-9961-0
32. Plotkin LI, Aguirre JI, Kousteni S, Manolagas SC, Bellido T. Bisphosphonates and Estrogens Inhibit Osteocyte Apoptosis *Via* Distinct Molecular Mechanisms Downstream of Extracellular Signal-Regulated Kinase Activation. *J Biol Chem* (2005) 280(8):7317–25. doi: 10.1074/jbc.M412817200
33. Marathe N, Rangaswami H, Zhuang S, Boss GR, Pilz RB. Pro-Survival Effects of 17β-Estradiol On Osteocytes Are Mediated by Nitric Oxide/Cgmp *Via* Differential Actions of Cgmp-Dependent Protein Kinases I and Ii. *J Biol Chem* (2012) 287(2):978–88. doi: 10.1074/jbc.M111.294959
34. Li X, Han Y, Guan Y, Zhang L, Bai C, Li Y. Aluminum Induces Osteoblast Apoptosis Through the Oxidative Stress-Mediated Jnk Signaling Pathway. *Biol Trace Elem Res* (2012) 150(1-3):502–8. doi: 10.1007/s12011-012-9523-5
35. Park BG, Yoo CI, Kim HT, Kwon CH, Kim YK. Role of Mitogen-Activated Protein Kinases in Hydrogen Peroxide-Induced Cell Death in Osteoblastic Cells. *Toxicology* (2005) 215(1-2):115–25. doi: 10.1016/j.tox.2005.07.003
36. Agidigbi TS, Kim C. Reactive Oxygen Species in Osteoclast Differentiation and Possible Pharmaceutical Targets of Ros-Mediated Osteoclast Diseases. *Int J Mol Sci* (2019) 20(14):3576. doi: 10.3390/ijms20143576
37. Lee NK, Choi YG, Baik JY, Han SY, Jeong DW, Bae YS, et al. A Crucial Role for Reactive Oxygen Species in Rankl-Induced Osteoclast Differentiation. *Blood* (2005) 106(3):852–9. doi: 10.1182/blood-2004-09-3662
38. An Y, Zhang H, Wang C, Jiao F, Xu H, Wang X, et al. Activation of Ros/Mapks/Nf-κb/Nlrp3 and Inhibition of Efferocytosis in Osteoclast-Mediated Diabetic Osteoporosis. *FASEB J* (2019) 33(11):12515–27. doi: 10.1096/fj.201802805RR
39. Yang B, Li S, Chen Z, Feng F, He L, Liu B, et al. Amyloid β Peptide Promotes Bone Formation by Regulating Wnt/β-Catenin Signaling and the Opg/Rankl/Rank System. *FASEB J* (2020) 34(3):3583–93. doi: 10.1096/fj.201901550R
40. Udagawa N, Koide M, Nakamura M, Nakamichi Y, Yamashita T, Uehara S, et al. Osteoclast Differentiation by Rankl and Opg Signaling Pathways. *J Bone Miner Metab* (2021) 39(1):19–26. doi: 10.1007/s00774-020-01162-6
41. Bai XC, Lu D, Liu AL, Zhang ZM, Li XM, Zou ZP, et al. Reactive Oxygen Species Stimulates Receptor Activator of NF-KappaB Ligand Expression in Osteoblast. *J Biol Chem* (2005) 280(17):17497–506. doi: 10.1074/jbc.M409332200
42. Chen JR, Shankar K, Nagarajan S, Badger TM, Ronis MJ. Protective Effects of Estradiol On Ethanol-Induced Bone Loss Involve Inhibition of Reactive Oxygen Species Generation in Osteoblasts and Downstream Activation of the Extracellular Signal-Regulated Kinase/Signal Transducer and Activator of Transcription 3/Receptor Activator of Nuclear Factor-Kappab Ligand Signaling Cascade. *J Pharmacol Exp Ther* (2008) 324(1):50–9. doi: 10.1124/jpet.107.130351
43. Oliver L, Hue E, Priault M, Vallette FM. Basal Autophagy Decreased During the Differentiation of Human Adult Mesenchymal Stem Cells. *Stem Cells Dev* (2012) 21(15):2779–88. doi: 10.1089/scd.2012.0124
44. Pantovic A, Krstic A, Janjetovic K, Kocic J, Harhaji-Trajkovic L, Bugarski D, et al. Coordinated Time-Dependent Modulation of Ampk/Akt/mTOR Signaling and Autophagy Controls Osteogenic Differentiation of Human Mesenchymal Stem Cells. *Bone* (2013) 52(1):524–31. doi: 10.1016/j.bone.2012.10.024
45. Qi M, Zhang L, Ma Y, Shuai Y, Li L, Luo K, et al. Autophagy Maintains the Function of Bone Marrow Mesenchymal Stem Cells to Prevent Estrogen Deficiency-Induced Osteoporosis. *Theranostics* (2017) 7(18):4498–516. doi: 10.7150/thno.17949
46. Priault M, Hue E, Marhuenda F, Pilet P, Oliver L, Vallette FM. Differential Dependence On Beclin1 for the Regulation of Pro-Survival Autophagy by Bcl-2 and Bcl-Xl in Hct116 Colorectal Cancer Cells. *PLoS One* (2010) 5(1):e8755. doi: 10.1371/journal.pone.0008755
47. Wu M, Chen G, Li YP. TGF-β and Bmp Signaling in Osteoblast, Skeletal Development, and Bone Formation, Homeostasis and Disease. *Bone Res* (2016) 4:16009. doi: 10.1038/boneres.2016.9
48. Huitema LF, Vaandrager AB. What Triggers Cell-Mediated Mineralization? *Front Biosci* (2007) 12. doi: 10.2741/2260

49. Liu F, Fang F, Yuan H, Yang D, Chen Y, Williams L, et al. Suppression of Autophagy by Fip200 Deletion Leads to Osteopenia in Mice Through the Inhibition of Osteoblast Terminal Differentiation. *J Bone Miner Res* (2013) 28(11):2414–30. doi: 10.1002/jbmr.1971
50. Chen L, Shi X, Weng SJ, Xie J, Tang JH, Yan DY, et al. Vitamin K2 Can Rescue the Dexamethasone-Induced Downregulation of Osteoblast Autophagy and Mitophagy Thereby Restoring Osteoblast Function *in Vitro* and *in Vivo*. *Front Pharmacol* (2020) 11:1209. doi: 10.3389/fphar.2020.01209
51. Li H, Li D, Ma Z, Qian Z, Kang X, Jin X, et al. Defective Autophagy in Osteoblasts Induces Endoplasmic Reticulum Stress and Causes Remarkable Bone Loss. *Autophagy* (2018) 14(10):1726–41. doi: 10.1080/15548627.2018.1483807
52. Shah M, Kola B, Bataveljic A, Arnett TR, Viollet B, Saxon L, et al. Amp-Activated Protein Kinase (Ampk) Activation Regulates *in Vitro* Bone Formation and Bone Mass. *Bone* (2010) 47(2):309–19. doi: 10.1016/j.bone.2010.04.596
53. Kasai T, Bandow K, Suzuki H, Chiba N, Kakimoto K, Ohnishi T, et al. Osteoblast Differentiation Is Functionally Associated With Decreased Amp Kinase Activity. *J Cell Physiol* (2009) 221(3):740–9. doi: 10.1002/jcp.21917
54. Xi G, Rosen CJ, Clemmons DR. GF-I and IGFBP-2 Stimulate AMPK Activation and Autophagy, Which are Required for Osteoblast Differentiation. *Endocrinology* (2016) 157(1):268–81. doi: 10.1210/en.2015-1690
55. Nollet M, Santucci-Darmanin S, Breuil V, Al-Sahlanee R, Cros C, Topi M, et al. Autophagy in Osteoblasts Is Involved in Mineralization and Bone Homeostasis. *Autophagy* (2014) 10(11):1965–77. doi: 10.4161/auto.36182
56. Thomas N, Choi HK, Wei X, Wang L, Mishina Y, Guan JL, et al. Autophagy Regulates Craniofacial Bone Acquisition. *Calcif Tissue Int* (2019) 105 (5):518–30. doi: 10.1007/s00223-019-00593-2
57. Teitelbaum SL. Bone Resorption by Osteoclasts. *Science* (2000) 289 (5484):1504–8. doi: 10.1126/science.289.5484.1504
58. Shapiro IM, Layfield R, Lotz M, Settembre C, Whitehouse C. Boning Up On Autophagy: The Role of Autophagy in Skeletal Biology. *Autophagy* (2014) 10 (1):7–19. doi: 10.4161/auto.26679
59. Zhao Y, Chen G, Zhang W, Xu N, Zhu JY, Jia J, et al. Autophagy Regulates Hypoxia-Induced Osteoclastogenesis Through the Hif-1α/Bnip3 Signaling Pathway. *J Cell Physiol* (2012) 227(2):639–48. doi: 10.1002/jcp.22768
60. Sambandam Y, Townsend MT, Pierce JJ, Lipman CM, Haque A, Bateman TA, et al. Microgravity Control of Autophagy Modulates Osteoclastogenesis. *Bone* (2014) 61:125–31. doi: 10.1016/j.bone.2014.01.004
61. Arai A, Kim S, Goldshteyn V, Kim T, Park NH, Wang CY, et al. Beclin1 Modulates Bone Homeostasis by Regulating Osteoclast and Chondrocyte Differentiation. *J Bone Miner Res* (2019) 34(9):1753–66. doi: 10.1002/jbmr.3756
62. Lin NY, Stefanica A, Distler JH. Autophagy: A Key Pathway of TNF-Induced Inflammatory Bone Loss. *Autophagy* (2013) 9(8):1253–5. doi: 10.4161/auto.25467
63. Chung YH, Yoon SY, Choi B, Sohn DH, Yoon KH, Kim WJ, et al. Microtubule-Associated Protein Light Chain 3 Regulates Cdc42-Dependent Actin Ring Formation in Osteoclast. *Int J Biochem Cell Biol* (2012) 44(6):989–97. doi: 10.1016/j.biocel.2012.03.007
64. DeSelm CJ, Miller BC, Zou W, Beatty WL, van Meel E, Takahata Y, et al. Autophagy Proteins Regulate the Secretory Component of Osteoclastic Bone Resorption. *Dev Cell* (2011) 21(5):966–74. doi: 10.1016/j.devcel.2011.08.016
65. Muthusami S, Ramachandran I, Muthusamy B, Vasudevan G, Prabhu V, Subramaniam V, et al. Ovariectomy Induces Oxidative Stress and Impairs Bone Antioxidant System in Adult Rats. *Clin Chim Acta* (2005) 360(1-2):81–6. doi: 10.1016/j.cccn.2005.04.014
66. Bartolomé A, López-Herradón A, Portal-Núñez S, García-Aguilar A, Esbrit P, Benito M, et al. Autophagy Impairment Aggravates the Inhibitory Effects of High Glucose On Osteoblast Viability and Function. *Biochem J* (2013) 455 (3):329–37. doi: 10.1042/BJ20130562
67. Zhang S, Liu Y, Liang Q. Low-Dose Dexamethasone Affects Osteoblast Viability by Inducing Autophagy *Via* Intracellular Ros. *Mol Med Rep* (2018) 17(3):4307–16. doi: 10.3892/mmr.2018.8461
68. Camuzard O, Santucci-Darmanin S, Breuil V, Cros C, Gritsaenko T, Pagnotta S, et al. Sex-Specific Autophagy Modulation in Osteoblastic Lineage: A Critical Function to Counteract Bone Loss in Female. *Oncotarget* (2016) 7(41):66416–28. doi: 10.18632/oncotarget.12013
69. Yang L, Meng H, Yang M. Autophagy Protects Osteoblasts From Ages Induced Apoptosis Through. *J Mol Endocrinol* (2016) 56(4):291–300. doi: 10.1530/JME-15-0267
70. Yang YH, Chen K, Li B, Chen JW, Zheng XF, Wang YR, et al. Estradiol Inhibits Osteoblast Apoptosis *Via* Promotion of Autophagy Through the ER-ERK-mTOR Pathway. *Apoptosis* (2013) 18(11):1363–75. doi: 10.1007/s10495-013-0867-x
71. Kops GJ, Dansen TB, Polderman PE, Saarloos I, Wirtz KW, Coffer PJ, et al. Forkhead Transcription Factor Foxo3a Protects Quiescent Cells From Oxidative Stress. *Nature* (2002) 419(6904):316–21. doi: 10.1038/nature01036
72. Ho KK, McGuire VA, Koo CY, Muir KW, de Olano N, Maifoshie E, et al. Phosphorylation of Foxo3a On Ser-7 by P38 Promotes Its Nuclear Localization in Response to Doxorubicin. *J Biol Chem* (2012) 287(2):1545–55. doi: 10.1074/jbc.M111.284224
73. Essers MA, Weijzen S, de Vries-Smits AM, Saarloos I, de Ruiter ND, Bos JL, et al. Foxo Transcription Factor Activation by Oxidative Stress Mediated by the Small Gtpase Ral and Jnk. *EMBO J* (2004) 23(24):4802–12. doi: 10.1038/sj.emboj.7600476
74. Gómez-Puerto MC, Verhagen LP, Braat AK, Lam EWF, Coffer PJ, Lorenowicz MJ. Activation of Autophagy by Foxo3 Regulates Redox Homeostasis During Osteogenic Differentiation. *Autophagy* (2016) 12 (10):1804–16. doi: 10.1080/15548627.2016.1203484
75. Gu X, Han D, Chen W, Zhang L, Lin Q, Gao J, et al. Sirt1-Mediated Foxos Pathways Protect Against Apoptosis by Promoting Autophagy in Osteoblast-Like Mc3T3-E1 Cells Exposed to Sodium Fluoride. *Oncotarget* (2016) 7(40):65218–30. doi: 10.18632/oncotarget.11573
76. Hardie DG. Amp-Activated/Snf1 Protein Kinases: Conserved Guardians of Cellular Energy. *Nat Rev Mol Cell Biol* (2007) 8(10):774–85. doi: 10.1038/nrm2249
77. Mihaylova MM, Shaw RJ. The Ampk Signalling Pathway Coordinates Cell Growth, Autophagy and Metabolism. *Nat Cell Biol* (2011) 13(9):1016–23. doi: 10.1038/ncb2329
78. Wang S, Song P, Zou MH. Amp-Activated Protein Kinase, Stress Responses and Cardiovascular Diseases. *Clin Sci (Lond)* (2012) 122(12):555–73. doi: 10.1042/CS20110625
79. Kim J, Kundu M, Viollet B, Guan KL. Ampk and Mtor Regulate Autophagy Through Direct Phosphorylation of Ulk1. *Nat Cell Biol* (2011) 13(2):132–41. doi: 10.1038/ncb2152
80. She C, Zhu L, Zhen Y, Wang X, Dong Q. Activation of Ampk Protects Against Hydrogen Peroxide-Induced Osteoblast Apoptosis Through Autophagy Induction and Nadph Maintenance: New Implications for Osteonecrosis Treatment? *Cell Signal* (2014) 26(1):1–8. doi: 10.1016/j.cellsig.2013.08.046
81. Liu W, Mao L, Ji F, Chen F, Hao Y, Liu G. Targeted Activation of Ampk by Gsk621 Ameliorates H2O2-Induced Damages in Osteoblasts. *Oncotarget* (2017) 8(6):10543–52. doi: 10.18632/oncotarget.14454
82. Zhu Y, Zhou J, Ao R, Yu B. A-769662 Protects Osteoblasts From Hydrogen Dioxide-Induced Apoptosis Through Activating of Amp-Activated Protein Kinase (Ampk). *Int J Mol Sci* (2014) 15(6):11190–203. doi: 10.3390/ijms150611190
83. Zhao D, Yang J, Yang L. Insights for Oxidative Stress and mTOR Signaling in Myocardial Ischemia/Reperfusion Injury Under Diabetes. *Oxid Med Cell Longev* (2017) 2017:6437467. doi: 10.1155/2017/6437467
84. Hay N, Sonenberg N. Upstream and Downstream of mTOR. *Genes Dev* (2004) 18(16):1926–45. doi: 10.1101/gad.1212704
85. Zhai C, Cheng J, Mujahid H, Wang H, Kong J, Yin Y, et al. Selective Inhibition of PI3K/Akt/ mTOR Signaling Pathway Regulates Autophagy of Macrophage and Vulnerability of Atherosclerotic Plaque. *PLoS One* (2014) 9 (3):e90563. doi: 10.1371/journal.pone.0090563
86. Koundouros N, Poulogiannis G. Phosphoinositide 3-Kinase/Akt Signaling and Redox Metabolism in Cancer. *Front Oncol* (2018) 8. doi: 10.3389/fonc.2018.00160
87. Wang X, Feng Z, Li J, Chen L, Tang W. High Glucose Induces Autophagy of Mc3T3-E1 Cells *Via* Ros-Akt- mTOR Axis. *Mol Cell Endocrinol* (2016) 429:62–72. doi: 10.1016/j.mce.2016.03.036

88. Leslie NR, Downes CP. Pten: The Down Side of PI3-Kinase Signalling. *Cell Signal* (2002) 14(4):285–95. doi: 10.1016/s0898-6568(01)00234-0
89. Shi Y, Liu XY, Jiang YP, Zhang JB, Zhang QY, Wang NN, et al. Monotropein Attenuates Oxidative Stress *Via* Akt/mTOR-Mediated Autophagy in Osteoblast Cells. *BioMed Pharmacother* (2020) 121:109566. doi: 10.1016/j.biopha.2019.109566
90. Suzuki M, Bandoski C, Bartlett JD. Fluoride Induces Oxidative Damage and Sirt1/Autophagy Through Ros-Mediated JNK Signaling. *Free Radic Biol Med* (2015) 89:369–78. doi: 10.1016/j.freeradbiomed.2015.08.015
91. Peng P, Nie Z, Sun F, Peng H. Glucocorticoids Induce Femoral Head Necrosis in Rats Through the ROS/JNK/c-Jun Pathway. *FEBS Open Bio* (2021) 11(1):312–21. doi: 10.1002/2211-5463.13037
92. Zhou F, Yang Y, Xing D. Bcl-2 and Bcl-Xl Play Important Roles in the Crosstalk Between Autophagy and Apoptosis. *FEBS J* (2011) 278(3):403–13. doi: 10.1111/j.1742-4658.2010.07965.x
93. Luo S, Rubinsztein DC. Bcl2L11/Bim: A Novel Molecular Link Between Autophagy and Apoptosis. *Autophagy* (2013) 9(1):104–5. doi: 10.4161/auto.22399
94. Wei Y, Sinha S, Levine B. Dual Role of JNK1-Mediated Phosphorylation of Bcl-2 in Autophagy and Apoptosis Regulation. *Autophagy* (2008) 4(7):949–51. doi: 10.4161/auto.6788
95. Shimizu S, Konishi A, Nishida Y, Mizuta T, Nishina H, Yamamoto A, et al. Involvement of JNK in the Regulation of Autophagic Cell Death. *Oncogene* (2010) 29(14):2070–82. doi: 10.1038/onc.2009.487
96. Yang Y, Zheng X, Li B, Jiang S, Jiang L. Increased Activity of Osteocyte Autophagy in Ovariectomized Rats and Its Correlation With Oxidative Stress Status and Bone Loss. *Biochem Biophys Res Commun* (2014) 451(1):86–92. doi: 10.1016/j.bbrc.2014.07.069
97. Kar R, Riquelme MA, Hua R, Jiang JX. Glucocorticoid-Induced Autophagy Protects Osteocytes Against Oxidative Stress Through Activation of Mapk/Erk Signaling. *JBMR Plus* (2019) 3(4):e10077. doi: 10.1002/jbm4.10077
98. Zhang Y, Yan M, Kuang S, Lou Y, Wu S, Li Y, et al. Bisphenol a Induces Apoptosis and Autophagy in Murine Osteocytes Mlo-Y4: Involvement of ROS-Mediated mTOR/ULK1 Pathway. *Ecotoxicol Environ Saf* (2021) 230:113119. doi: 10.1016/j.ecoenv.2021.113119
99. Lee JJ, Jain V, Amaravadi RK. Clinical Translation of Combined Mapk and Autophagy Inhibition in Ras Mutant Cancer. *Int J Mol Sci* (2021) 22(22):12402. doi: 10.3390/ijms222212402
100. Li Z, Miao Z, Ding L, Teng X, Bao J. Energy Metabolism Disorder Mediated Ammonia Gas-Induced Autophagy *Via* AMPK/mTOR/ULK1-Beclin1 Pathway in Chicken Livers. *Ecotoxicol Environ Saf* (2021) 217:112219. doi: 10.1016/j.ecoenv.2021.112219
101. Wang T, Xu F, Song L, Li J, Wang Q. Bisphenol a Exposure Prenatally Delays Bone Development and Bone Mass Accumulation in Female Rat Offspring *Via* the Erβ/Hdac5/Tgfβ Signaling Pathway. *Toxicology* (2021) 458:152830. doi: 10.1016/j.tox.2021.152830
102. Srinivasan S, Koenigstein A, Joseph J, Sun L, Kalyanaraman B, Zaidi M, et al. Role of Mitochondrial Reactive Oxygen Species in Osteoclast Differentiation. *Ann N Y Acad Sci* (2010) 1192(1):245–52. doi: 10.1111/j.1749-6632.2009.05377.x
103. Kim MS, Yang YM, Son A, Tian YS, Lee SI, Kang SW, et al. Rankl-Mediated Reactive Oxygen Species Pathway That Induces Long Lasting Ca^{2+} Oscillations Essential for Osteoclastogenesis. *J Biol Chem* (2010) 285(10):6913–21. doi: 10.1074/jbc.M109.051557
104. Sul OJ, Park HJ, Son HJ, Choi HS. Lipopolysaccharide (Lps)-Induced Autophagy Is Responsible for Enhanced Osteoclastogenesis. *Mol Cells* (2017) 40(11):880–7. doi: 10.14348/molcells.2017.0230
105. Shi J, Wang L, Zhang H, Jie Q, Li X, Shi Q, et al. Glucocorticoids: Dose-Related Effects On Osteoclast Formation and Function *Via* Reactive Oxygen Species and Autophagy. *Bone* (2015) 79:222–32. doi: 10.1016/j.bone.2015.06.014
106. Malhotra JD, Kaufman RJ. Endoplasmic Reticulum Stress and Oxidative Stress: A Vicious Cycle Or a Double-Edged Sword? *Antioxid Redox Signal* (2007) 9(12):2277–93. doi: 10.1089/ars.2007.1782
107. Fernández A, Ordóñez R, Reiter RJ, González-Gallego J, Mauriz JL. Melatonin and Endoplasmic Reticulum Stress: Relation to Autophagy and Apoptosis. *J Pineal Res* (2015) 59(3):292–307. doi: 10.1111/jpi.12264
108. Wang K, Niu J, Kim H, Kolattukudy PE. Osteoclast Precursor Differentiation by Mcpip *Via* Oxidative Stress, Endoplasmic Reticulum Stress, and Autophagy. *J Mol Cell Biol* (2011) 3(6):360–8. doi: 10.1093/jmcb/mjr021
109. Martini-Stoica H, Xu Y, Ballabio A, Zheng H. The Autophagy-Lysosomal Pathway in Neurodegeneration: A Tfeb Perspective. *Trends Neurosci* (2016) 39(4):221–34. doi: 10.1016/j.tins.2016.02.002
110. Wang H, Wang N, Xu D, Ma Q, Chen Y, Xu S, et al. Oxidation of Multiple Mit/Tfe Transcription Factors Links Oxidative Stress to Transcriptional Control of Autophagy and Lysosome Biogenesis. *Autophagy* (2020) 16(9):1683–96. doi: 10.1080/15548627.2019.1704104
111. Sul OJ, Li G, Kim JE, Kim ES, Choi HS. 7-Ketocholesterol Enhances Autophagy *Via* the Ros-Tfeb Signaling Pathway in Osteoclasts. *J Nutr Biochem* (2021) 96:108783. doi: 10.1016/j.jnutbio.2021.108783

Conflict of Interest: The authors declare that the research was conducted in the absence of any commercial or financial relationships that could be construed as a potential conflict of interest.

Publisher's Note: All claims expressed in this article are solely those of the authors and do not necessarily represent those of their affiliated organizations, or those of the publisher, the editors and the reviewers. Any product that may be evaluated in this article, or claim that may be made by its manufacturer, is not guaranteed or endorsed by the publisher.

frontiers | Frontiers in Endocrinology

ORIGINAL RESEARCH
published: 11 July 2022
doi: 10.3389/fendo.2022.900356

Finite Element Analysis of Osteoporotic and Osteoblastic Vertebrae and Its Association With the Proton Density Fat Fraction From Chemical Shift Encoding-Based Water-Fat MRI – A Preliminary Study

Tobias Greve[1,2], Nithin Manohar Rayudu[3], Michael Dieckmeyer[2], Christof Boehm[4], Stefan Ruschke[4], Egon Burian[2,4], Christopher Kloth[5], Jan S. Kirschke[2,6], Dimitrios C. Karampinos[4], Thomas Baum[2], Karupppasamy Subburaj[3,7] and Nico Sollmann[2,5,6]*

[1] Department of Neurosurgery, University Hospital, Ludwig-Maximilians-University (LMU) Munich, Munich, Germany, [2] Department of Diagnostic and Interventional Neuroradiology, School of Medicine, Klinikum rechts der Isar, Technical University of Munich, Munich, Germany, [3] Engineering Product Development (EPD) Pillar, Singapore University of Technology and Design (SUTD), Singapore, Singapore, [4] Department of Diagnostic and Interventional Radiology, School of Medicine, Klinikum rechts der Isar, Technical University of Munich, Munich, Germany, [5] Department of Diagnostic and Interventional Radiology, University Hospital Ulm, Ulm, Germany, [6] TUM-Neuroimaging Center, Klinikum rechts der Isar, Technical University of Munich, Munich, Germany, [7] Sobey School of Business, Saint Mary's University, Halifax, NS, Canada

OPEN ACCESS

Edited by:
Guanwu Li,
Shanghai University of Traditional Chinese Medicine, China

Reviewed by:
Yanna Si,
Nanjing Medical University, China
Frederic Carsten Schmeel,
University Hospital Bonn, Germany

***Correspondence:**
Tobias Greve
tobias.greve@med.uni-muenchen.de

Specialty section:
This article was submitted to Bone Research, a section of the journal Frontiers in Endocrinology

Received: 20 March 2022
Accepted: 11 May 2022
Published: 11 July 2022

Citation:
Greve T, Rayudu NM, Dieckmeyer M, Boehm C, Ruschke S, Burian E, Kloth C, Kirschke JS, Karampinos DC, Baum T, Subburaj K and Sollmann N (2022) Finite Element Analysis of Osteoporotic and Osteoblastic Vertebrae and Its Association With the Proton Density Fat Fraction From Chemical Shift Encoding-Based Water-Fat MRI – A Preliminary Study. Front. Endocrinol. 13:900356. doi: 10.3389/fendo.2022.900356

Purpose: Osteoporosis is prevalent and entails alterations of vertebral bone and marrow. Yet, the spine is also a common site of metastatic spread. Parameters that can be non-invasively measured and could capture these alterations are the volumetric bone mineral density (vBMD), proton density fat fraction (PDFF) as an estimate of relative fat content, and failure displacement and load from finite element analysis (FEA) for assessment of bone strength. This study's purpose was to investigate if osteoporotic and osteoblastic metastatic changes in lumbar vertebrae can be differentiated based on the abovementioned parameters (vBMD, PDFF, and measures from FEA), and how these parameters correlate with each other.

Materials and Methods: Seven patients (3 females, median age: 77.5 years) who received 3-Tesla magnetic resonance imaging (MRI) and multi-detector computed tomography (CT) of the lumbar spine and were diagnosed with either osteoporosis (4 patients) or diffuse osteoblastic metastases (3 patients) were included. Chemical shift encoding-based water-fat MRI (CSE-MRI) was used to extract the PDFF, while vBMD was extracted after automated vertebral body segmentation using CT. Segmentation masks were used for FEA-based failure displacement and failure load calculations. Failure displacement, failure load, and PDFF were compared between patients with osteoporotic vertebrae versus patients with osteoblastic metastases, considering non-

fractured vertebrae (L1-L4). Associations between those parameters were assessed using Spearman correlation.

Results: Median vBMD was 59.3 mg/cm^3 in osteoporotic patients. Median PDFF was lower in the metastatic compared to the osteoporotic patients (11.9% vs. 43.8%, p=0.032). Median failure displacement and failure load were significantly higher in metastatic compared to osteoporotic patients (0.874 mm vs. 0.348 mm, 29,589 N vs. 3,095 N, p=0.034 each). A strong correlation was noted between PDFF and failure displacement (rho -0.679, p=0.094). A very strong correlation was noted between PDFF and failure load (rho -0.893, p=0.007).

Conclusion: PDFF as well as failure displacement and load allowed to distinguish osteoporotic from diffuse osteoblastic vertebrae. Our findings further show strong associations between PDFF and failure displacement and load, thus may indicate complimentary pathophysiological associations derived from two non-invasive techniques (CSE-MRI and CT) that inherently measure different properties of vertebral bone and marrow.

Keywords: finite element analysis, osteoporosis, metastasis, vertebral fractures, bone mineral density, magnetic resonance imaging, proton density fat fraction, spinal neoplasms

INTRODUCTION

Osteoporosis is a highly prevalent disease that imposes enormous costs on individuals and society (1, 2). The estimated prevalence of osteoporosis worldwide is 23.1% in women and 11.7% in men (3). Osteoporosis-related fragility fractures account for high morbidity and represent a high burden on disability-adjusted years of life (4). The spine is among the most frequent sites for those fragility fractures, and affected patients show a more than 10-fold increased risk for future additional vertebral fractures (VFs) (5–7). Furthermore, the spine is also the most common site of bone metastases, accounting for approximately 50% of cases (8). Spinal metastases occur in approximately 5% to 10% of patients with primary cancer, resulting in about 400,000 new cases of bone metastases each year in the United States alone, underscoring high socioeconomic relevance (9–11). The most common cause of osteoblastic metastases is prostate cancer, but other tumor types such as lung cancer, breast cancer, or bladder cancer can cause these lesions as well (12). Like osteoporosis, vertebral metastases lead to an increased risk of VFs, which can cause severe pain, limb dysfunction, and spinal cord compression, thus markedly affecting the patients' quality of life (1, 13).

The assessment of osteoporosis-related VF risk in routine clinical practice is primarily based on the evaluation of T-scores, which are derived from measurements of areal bone mineral density (aBMD) using dual-energy X-ray absorptiometry (DXA) (14–16). However, DXA is of limited value in identifying patients at high risk of fracture (17–20). Volumetric BMD (vBMD) derived from computed tomography (CT) imaging is only a surrogate measure of bone strength and cannot fully explain fracture incidences (15, 16, 21). In that regard, CT-based finite element analysis (FEA) is a computational approach of generating three-dimensional (3D) patient-specific models that can realistically calculate *in-vivo* material behavior using numerical simulation (22). During biomechanical testing of bones, an increasing strain rate is applied to the bone until failure due to produced deformations or displacements throughout the structure. The load-deformation behavior of the bone is a linear (elastic) region before yield, a post-yield non-linear region containing the maximum (ultimate) load, and the failure point at which bone fracture occurs. During FEA, a simulation is conducted in which a compression loading condition is generated by applying displacement loading on the superior surface. After solving a plotted load versus displacement curve, failure load and failure displacement can be calculated (23). Yeung et al. have observed that using the FEA-predicted failure load and displacement values of the baseline data, it is possible to predict fracture risk in the follow-up fractured vertebrae using CT (24). Specifically, the vertebrae that are going to fail in the future may be characterized by deteriorated bone strength in the baseline data (24). The FEA-derived parameters may have accurately captured the mechanical behavior variation due to the occurrence of follow-up osteoporotic fractures in the vertebrae (24). In osteoporosis, FEA with calculation of the failure load and failure displacement may provide detailed parameters on vertebral bone strength and may more accurately estimate fracture risk than BMD alone (19, 20, 25–28). While being well established in

Abbreviations: 3D, three-dimensional; aBMD, areal bone mineral density; CI, confidence interval; vBMD, volumetric bone mineral density; CSE-MRI, chemical shift encoding-based water-fat MRI; CT, computed tomography; DXA, dual-energy X-ray absorptiometry; FEA, finite element analysis; MRI, magnetic resonance imaging; IQR, inter-quartile range; PDFF, proton density fat fraction; VF, vertebral fracture; PACS, picture archiving and communication system; HU, Hounsfield unit; SINS, Spinal Instability Neoplastic Score.

osteoporosis, only a few studies have presented experimentally validated FEA models for bone strength assessment of vertebrae with metastatic lesions. However, such lesions can also severely impact a vertebral body's structure and resistance to fracture (23, 29).

Besides CT, magnetic resonance imaging (MRI) techniques emerge for assessment of the osteoporotic spine (30, 31). Specifically, the proton density fat fraction (PDFF) of bone marrow as derived from chemical shift encoding-based water-fat MRI (CSE-MRI) provides a map of hydrogen proton density attributable to fat normalized to the total hydrogen proton density and provides an accurate estimate of fat volume fraction (32, 33). The PDFF was shown to facilitate discrimination between benign and malignant lesions because most malignant neoplasms tend to replace the cellular and fatty bone marrow elements, thus resulting in low PDFF values (34–37). In contrast, benign skeletal lesions usually resemble fat in the bone marrow and exhibit higher PDFF values (34–37). In addition, the PDFF has also been implicated as a biomarker for osteoporosis and VF risk (38, 39). In this context, it was shown that PDFF is increased in osteoporosis and negatively correlates with BMD (38, 40–42).

While there is evidence for the applicability of FEA-based parameters derived from CT imaging and PDFF derived from CSE-MRI in osteoporotic and osteoblastic vertebral bodies, the two techniques inherently measure different properties of the vertebral bone and marrow, raising the question of the association between these measures. Therefore, the aim of this study was to compare how accurately osteoporotic and diffuse osteoblastic metastatic changes in lumbar vertebrae can be differentiated based on the abovementioned parameters (vBMD, PDFF, and measures derived from FEA) and how closely these parameters correlate within the same group of patients.

MATERIALS AND METHODS

Study Inclusion and Patient Cohort

This retrospective study was approved by the local institutional review board (ethics committee reference number 5679/13) and was conducted in accordance with the Declaration of Helsinki. Written informed consent was waived due to the study's retrospective design.

Patients who received a CT and MRI examination of the spine from the standard clinical routine protocol between December 2018 and May 2019 were screened for inclusion. They were identified in our hospital's picture archiving and communication system (PACS). Inclusion criteria were (1) acquisition of CSE-MRI and CT of the lumbar spine within 30 days, and (2) osteoporosis with or without osteoporotic fractures in the lumbar vertebral bodies L1 to L4, or, alternatively, diffuse osteoblastic lesions in the vertebral bodies L1 to L4. Exclusion criteria were (1) age below 18 years, (2) motion artifacts in imaging data, (3) previous surgery with instrumentation at the lumbar spine, (4) severe degenerative changes including Schmorl nodes or Modic-type endplate changes (grade 3), (5) inflammatory processes with related bone marrow affection (e.g., spondylodiscitis), and (6) pregnant or breastfeeding women. The presence of VFs in L1 to L4 was not an exclusion criterion, but due to changes in PDFF and/or BMD in vertebral bodies upon acute or old VFs, these vertebral bodies were excluded from averaging and further statistical analysis. Overall, seven patients were eligible and included in this study.

Computed Tomography

Image Acquisition

Image acquisition was performed in supine position using multi-detector CT scanners (Brilliance 64, Ingenuity CT, Philips Healthcare, Best, The Netherlands; Somatom Definition AS+, Somatom Sensation Cardiac 64, Siemens Healthineers, Erlangen, Germany). An initial scout scan was used for planning of the field of view, and subsequent helical scanning was acquired with a peak tube voltage of 120 kVp or 130 kVp and adaptive tube load, without previous application of any intravenous or oral contrast agents. Sagittal reformations of the spine with a slice thickness ≤3 mm were reconstructed with a bone kernel and used for further analysis in this study. The sagittal reformations of the spine were used for VF detection by a board-certified radiologist with 11 years of experience, who used the classification proposed by Genant et al. (43). CT imaging was performed for various indications not related to bone densitometry.

Extraction of Volumetric BMD

Measurements of vBMD were extracted from clinical routine CT scans of the lumbar spine and the median over multiple levels was calculated (L1 to L4, except for fractured vertebrae). Volumetric measures were extracted opportunistically in a semi-automatic multi-step procedure (https://anduin.bonescreen.de) (44–46). First, vertebrae were automatically segmented in CT scans to enclose the entire trabecular compartment using a framework of convolutional neural networks that identifies the spine, labels each vertebral body, and creates segmentation masks, adjusting for the used scanning protocol (120 kVp or 130 kVp) and scanner (44–46). Second, vertebral bodies were separated from posterior elements in these masks using affine and deformable transformations to fit templates of vertebral subregions to each vertebral level (**Figure 1**) (44–46). The vBMD was not extracted from vertebral bodies with fractures or osteoblastic metastases, given that this parameter was previously shown to be falsely elevated in osteoblastic metastases (47). In addition to extraction of vBMD from segmented vertebrae of the lumbar spine, clinical routine CT scans with segmentation masks including the posterior elements were further used for FEA.

Finite Element Analysis

The CT data and segmentation masks were imported to the open-source medical imaging software 3D Slicer (https://www.slicer.org; Surgical Planning Laboratory, Brigham and Women's Hospital, Boston, MA, USA) to reconstruct and generate 3D vertebral models (48). These generated 3D vertebral models were then imported into Abaqus CAE (version 6.10; Dassault

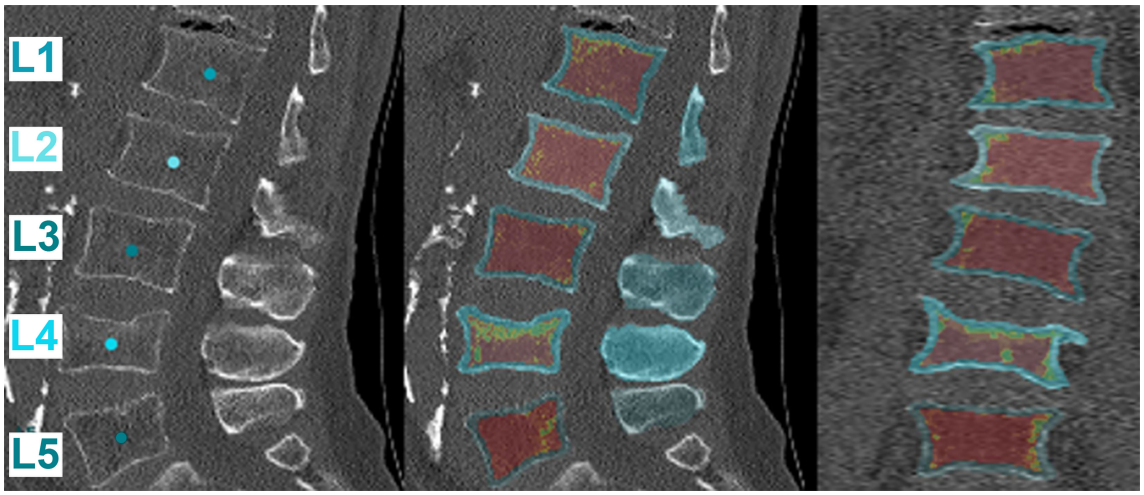

FIGURE 1 | Automatic segmentation and extraction of volumetric bone mineral density (vBMD). The first tile shows the automatic labeling of the vertebral segments. Subsequently, the vBMD is calculated for each vertebral body using different planes (sagittal: middle tile, coronal: right tile). Red marks areas of low vBMD, while green marks areas of high vBMD. Note that fractured vertebrae, in this case L4, have a falsely high vBMD and were excluded from the analysis (https://anduin.bonescreen.de).

Systèmes Simulia Corp., Johnston, RI, USA) for downstream FEA (49). The vertebral models were meshed with linear tetrahedron (C3D4) elements. We used the tetrahedral element for meshing to capture the geometry accurately. The meshed model and CT data were then imported to material mapping software Bonemat (version 3.2; http://www.bonemat.org, Bioengineering and Computing Laboratory, Istituto Ortopedico Rizzoli, Bologna, Italy), which maps on an FEA mesh the bone elastic properties derived from CT images (50). Image attenuation-based material properties were mapped to the meshed vertebral body using Hounsfield unit (HU)-density-modulus relations (**Table 1**). Then, the material mapped model was imported back to Abaqus CAE software for further processing.

In this study, we simulated the compression loading condition by fixing the inferior surface of the vertebrae and applying the normal displacement loading on the superior surface. After solving, the plotted load versus displacement curve was used to calculate failure load and failure displacement. The FEA methodology used in the current study has been validated experimentally in previous studies (**Figure 2**; **Table 2**) (27, 57, 58). To maintain the accuracy of the computational model, a mesh convergence assessment was carried out by varying the element edge length from 1 to 3 mm, with an increment of 0.5 mm. This assessment showed that 2 mm element size gives the mesh independent results, and the same size was chosen to mesh all the vertebral models for downstream analysis.

TABLE 1 | Quantitative paramters for the lumbar spine.

ID	Group	PDFF (%)					Failure Displacement (mm)					Failure Load (N)				
		L1	L2	L3	L4	L1-L4	L1	L2	L3	L4	L1-L4	L1	L2	L3	L4	L1-L4
1	Osteoblastic metastasis	24.1	26.2	27.8	31.8	27.0 [25.7-28.8]	1.027	0.775	0.911	0.724	0.843 [0.762-0.940]	19735	13240	39470	27447	23591 [18111-30453]
2	Osteoblastic metastasis	14.4	10.3	9.4	5.6	9.9 [8.5-11.3]	1.050	0.708	0.804	0.979	0.892 [0.780-0.997]	29731	29447	22665	50760	29589 [27752-34988]
3	Osteoblastic metastasis	7.7	13.4	8.8	9.8	9.3 [8.5-10.7]	0.884	0.841	0.942	0.864	0.874 [0.858-0.899]	45616	53618	53510	27663	49563 [41128-53537]
4	Osteoporosis	46.0	41.4	35.8	49.4	47.7 [46.9-48.6]	0.325	0.978	0.769	0.526	0.426 [0.375-0.476]	4161	3173	10248	3095	3628 [3361-3895]
5	Osteoporosis	33.4	38.0	41.6	26.3	38.0 [35.7-39.8]	0.296	0.369	0.348	0.315	0.348 [0.322-0.359]	3744	4108	4303	5995	4108 [3926-4205]
6	Osteoporosis	41.0	8.1	43.8	38.5	42.4 [41.7-43.1]	0.221	0.224	0.311	0.257	0.266 [0.244-0.289]	3235	6275	2728	6024	2981 [2854-3108]
7	Osteoporosis	43.9	43.0	48.6	45.5	44.7 [43.7-46.2]	0.301	0.502	0.605	0.504	0.503 [0.451-0.529]	2188	2797	2611	2558	2584 [2465-2658]

Grey cells refer to fractured vertebrae. Median and inter-quartile ranges (IQRs) for vertebral bodies L1 to L4 were calculated (without the fractured vertebrae).

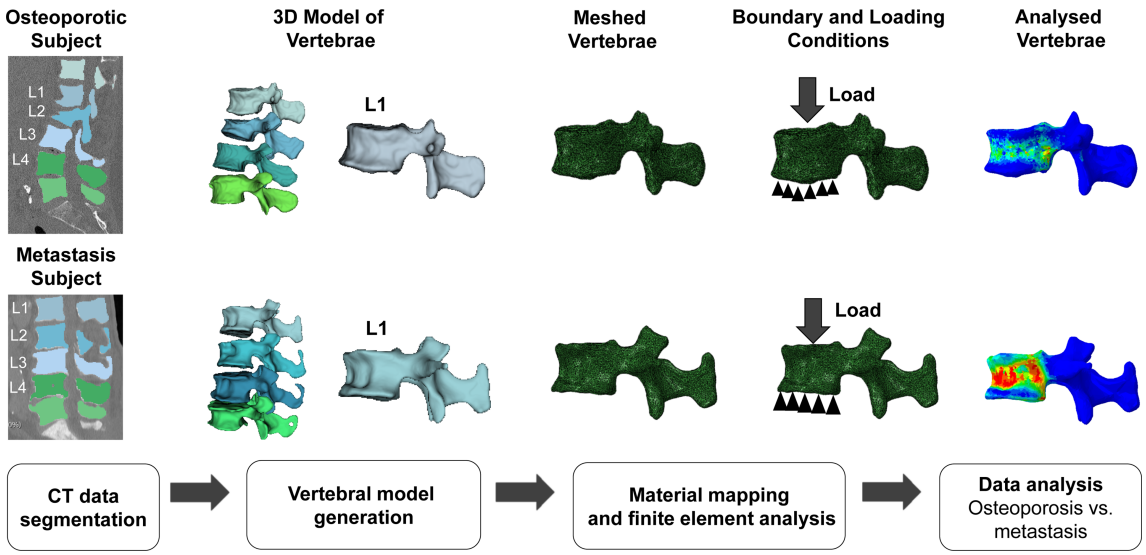

FIGURE 2 | Four-step finite element analysis (FEA) methodology for the calculation of FEA-based failure load and failure displacement in osteoporosis and metastasis models. Schematic representation of the workflow followed for FEA of the models reconstructed from computed tomography (CT) images. The L1 vertebrae model is shown here as a representative example of the analysis of the L1-L4 section. The top and bottom rows of the figure show the analyses for osteoporotic and metastatic vertebrae, respectively. The analysis resulted in the calculation of the FEA-based failure load and displacement for osteoporotic and osteoblastic metastasized vertebrae.

Magnetic Resonance Imaging

Image Acquisition

Acquisition of MRI of the lumbar spine was performed in the supine position on a 3-Tesla scanner (Release 5.4; Ingenia, Philips Healthcare, Best, The Netherlands) using a monopolar time-interleaved multi-echo gradient echo sequence, acquiring 6 echoes in 2 interleaves with 3 echoes per interleave (59). For all patients, the imaging parameters were set to TEmin = 1.12 ms, deltaTE= 0.96 ms, orientation = sagittal, readout direction = anterior-posterior, approximate field of view = 219.6 x 219.6 x 79.2 mm^3, with an isotropic acquisition voxel size of 1.8 mm.

TABLE 2 | Material mapping relations used in the current study for the calculation of failure load and displacement.

Property	Mapping Relations
Apparent density (ρ_{app} in Kg/m^3) (51)	$\rho_{app} = 47 + 1.122 \times HU$ HU-Hounsfield unit
Ash density (ρ_{ash} in Kg/m^3) (52)	$\rho_{ash} = 0.6 \times \rho_{app}$
Elastic modulus (E in MPa) (51, 53)	$E_z = 4730 \times (\rho_{app})^{1.56}$ $E_x = E_y = 0.333\ E_z$ Z-axial direction of the vertebra
Shear modulus (G in MPa) (54)	$G_{xy} = 0.121\ E_z$ $G_{xz} = G_{yz} = 0.157\ E_z$
Poisson ratio (V) (54)	Vxy = 0.381 Vxz = Vyz = 0.104
Maximum principal stress limit (σ in MPa) (55)	$\sigma = 137 \times \rho_{ash}^{1.88}$, $\rho_{ash} < 0.317$ $\sigma = 114 \times \rho_{ash}^{1.72}$, $\rho_{ash} > 0.317$
Plastic strain (ϵ_{AB}) (56)	$\epsilon_{AB} = -0.00315 + 0.0728\ \rho_{ash}$
Minimum principal stress limit (σ_{min} in MPa) (56)	$\sigma_{min} = 65.1 \times \rho_{ash}^{1.93}$

A sagittal T1-weighted turbo spin echo sequence (TR/TE = 600/8 ms) and a sagittal T2-weighted turbo spin echo DIXON sequence (TR/TE: 2,500/100 ms) of the lumbar spine, together with axial acquisitions over selected areas, were added for clinical purposes.

Image Processing

Fat quantification was performed offline using a complex-based water-fat separation, estimating the field map using a variable-layer single-min-cut graph-cut technique (60). The water-fat signal model was solved including a precalibrated seven-peak fat spectrum and a single T2* to model the signal variation with TE (61, 62). The PDFF maps were computed as the ratio of the fat signal over the sum of fat and water signals (32, 33). The vertebral bodies L1 to L4 were included in the analysis and manually segmented by a radiologist with 3 years of experience in spine imaging. Segmentation was performed on the PDFF maps using the open-source software MITK (http://mitk.org/wiki/The_Medical_Imaging_Interaction_Toolkit_(MITK); German Cancer Research Center, Division of Medical and Biological Informatics, Medical Imaging Interaction Toolkit, Heidelberg, Germany) (63). PDFF values were calculated individually for each segmented vertebra from L1 to L4. The median of these PDFF values was calculated without the fractured vertebrae.

Statistics

The statistical analyses were performed with SPSS software (version 26; IBM SPSS Statistics for Windows, IBM Corp., Armonk, NY, USA). Tests were performed using a two-sided level of significance of $\alpha = 0.05$.

Except for descriptive statistics, fractured vertebrae were excluded from further analysis and averaging. According to Shapiro-Wilk tests, the data distribution of the majority of measures of this study was non-parametric. Thus, Friedman's two-way analysis of variance by ranks was performed to test whether there were statistically significant differences among the ≤4 vertebral bodies per patient for the investigated variables. Subsequently, the median and inter-quartile ranges (IQRs) for PDFF, failure displacement, and failure load were calculated from L1 to L4. Mann-Whitney U test was performed to test for differences between patients with osteoblastic metastasis (metastasis group) and low bone density (osteoporosis group) regarding PDFF, failure displacement, and failure load. Spearman's rho with reporting of 95% confidence intervals (CIs) was used to correlate PDFF with failure displacement and failure load. Furthermore, Spearman's rho (with 95% CIs) was also used to investigate associations of vBMD, PDFF, failure displacement, and failure load in osteoporotic patients.

RESULTS

Clinical and Radiographic Characteristics

We included seven patients in the analysis (4 males and 3 females), with a median age of 77.5 years (**Figure 3**). One group consisted of three patients that showed diffuse osteoblastic metastatic changes in the lumbar vertebrae L1 to L4 (metastasis group). None of these patients suffered from fractured vertebrae in these levels. In detail, this group was composed of one 81-year-old female with unilateral breast cancer (initial diagnosis 2006, bone metastases known since 2015, initial treatment with breast-conserving surgery with sentinel lymph node dissection, radiotherapy, and hormonal therapy) and two males (71 and 74 years old) with prostate cancer (initial diagnosis 2015 and 2017, bone metastases known since 2017 in both patients, initial treatment with prostatectomy, chemotherapy, and hormonal therapy in both patients).

The other group consisted of four patients with osteoporosis, with a median vBMD of 59.3 mg/cm^3 (IQR: 56.4 to 64.9 mg/cm^3) according to opportunistic measurements in CT (osteoporosis group). The first of these patients (ID 4) had previous osteoporotic VFs and vertebroplasty of L2 and L3. The second of these patients (ID 5) had an osteoporotic upper endplate fracture of L4. The third patient of this group (ID 6) showed a compression fracture of L2 and an old upper endplate fracture of L4. The last patient of this group (ID 7) did not show any VFs.

Comparison of Metastatic and Osteoporotic Vertebrae

In the metastasis group, the median vertebral PDFF was 11.9% (IQR: 9.3 to 24.7%), while in the osteoporosis group the median PDFF was 43.8% (IQR: 41.3 to 45.7%) (p = 0.032) (**Figure 4**). Outliers in PDFF within the same patient were most evident in the fractured vertebrae, which were already excluded from the analysis a priori. In particular, this was true for vertebral body L2 of patient ID 6, which had a compression fracture for which the PDFF was 8.1%, while it ranged from 38.5% to 43.8% for the other vertebrae (**Table 1**).

Regarding failure displacement, the median value was 0.874 mm (IQR: 0.797 to 0.951 mm) in the metastasis group and 0.348 mm (IQR: 0.306 to 0.503 mm) in the osteoporosis group (p = 0.034) (**Figure 4**). The median failure load was 29,589 N (IQR: 26,252 to 46,902 N) in the metastasis group and 3,095 N (IQR: 2,669 to 3,926 N) in the osteoporosis group (p = 0.034) (**Figure 4**).

Correlation of PDFF and FEA-Based Parameters

A strong negative correlation was noted between PDFF and failure displacement with a Spearman's rho of -0.679 (95% CI: -0.947 to 0.152, p = 0.094). Furthermore, a very strong negative and statistically significant correlation was noted between PDFF and failure load with a Spearman's rho of -0.893 (95% CI: -0.984 to -0.427, p = 0.007) (**Figure 5**).

Correlation of vBMD, PDFF and FEA-Based Parameters in Osteoporotic Patients

In the osteoporotic patients, the correlation of vBMD with PDFF was weak to moderate with a Spearman's rho of -0.400 (95% CI: -0.983 to 0.912, p = 0.600). The correlation of vBMD with failure displacement and failure load was equally weak to moderate with a Spearman's rho of -0.400 (95% CI: -0.983 to 0.912, p = 0.600).

DISCUSSION

This preliminary study used CT for FEA and CSE-MRI to extract vertebral PDFF at the lumbar spine and investigate differences in the quantitative parameters, including failure displacement, failure load, and PDFF between patients with osteoporosis and patients with osteoblastic vertebral lesions. We demonstrated that failure displacement and failure load derived from CT imaging and FEA and PDFF values derived from CSE-MRI showed statistically significant differences between osteoporotic and osteoblastic vertebral bodies. Furthermore, there was a strong correlation between failure displacement and PDFF and a very strong correlation between failure load and PDFF.

PDFF has evolved as a promising non-invasive quantitative marker to assess tissue fat composition. It was shown to be highly accurate and reproducible among MRI vendors, field strengths, and readers, as shown by collinearity and inter-reader agreement (64). Previously, it was shown that the mean PDFF of malignant vertebral bone marrow lesions was significantly lower compared with benign lesions (3.1% vs. 28.2%) (65). A PDFF cutoff of 7.8% demonstrated optimal discriminatory power between benign and malignant lesions (65). In addition, PDFF has been shown to have high accuracy in differentiating acute osteoporotic and neoplastic compression fractures of the spine (66). One other study found an optimal PDFF cutoff to discriminate between benign and malignant lesions of 9% (67). Other previous

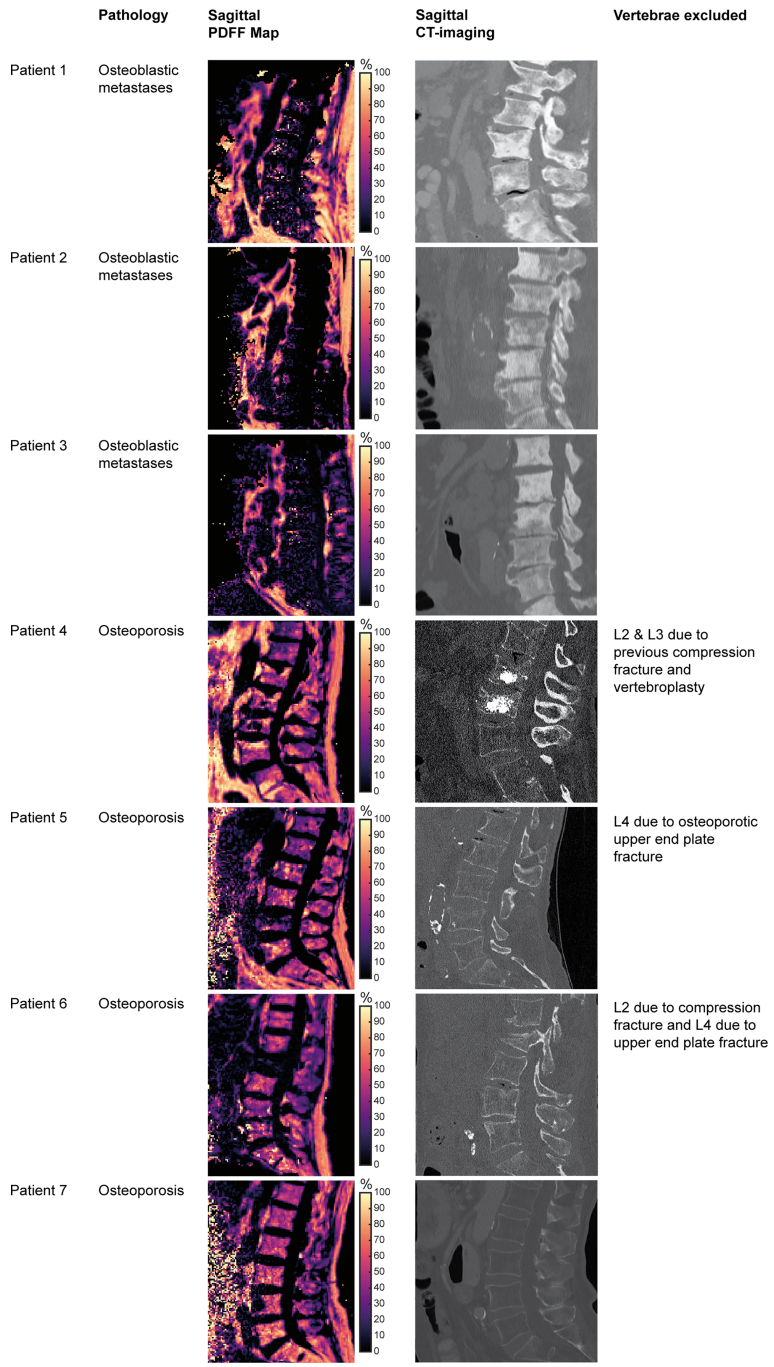

FIGURE 3 | Patient characteristics and imaging. Tiles showing vertebral bodies L1 to S1 on sagittal reformations of proton density fat fraction (PDFF) maps obtained from the six-echo monopolar time-interleaved multi-echo gradient-echo sequence and CT images, respectively.

research applied a preconditioned water-fat total field inversion algorithm that could directly estimate the susceptibility map from complex multi-echo gradient echo data for water-fat regions, which may help to better differentiate between osteoblastic and osteolytic changes in patients with metastatic disease as compared to the local field inversion method and a linear total field inversion method (68). In our study, osteoblastic vertebrae had a median PDFF of 11.9%, which is higher than the PDFF previously described for malignant lesions (67). The likely main reason for the observed measurement differences is probably the different measurement method, as we included the entire trabecular component of the vertebral body in the

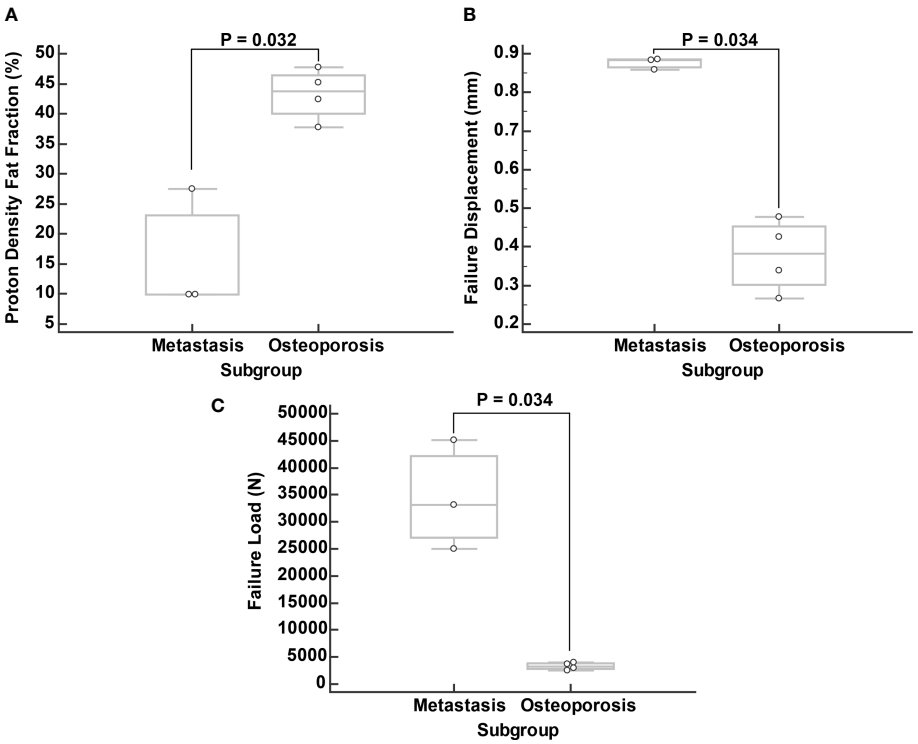

FIGURE 4 | Comparison of proton density fat fraction (PDFF; **A**), failure displacement **(B)**, and failure load **(C)** between subgroups. Boxplots were calculated from median values of vertebral bodies L1 to L4 excluding the fractured vertebrae.

analysis, whereas previous studies mostly evaluated the respective pathology only at individual slices (65, 67). This may explain the higher PDFF in the current study and does not necessarily represent a contradictory result. In addition, diffuse infiltrations have spatial compartments that may have normal cellular and bony structure, which also could result in higher PDFF values on average. In addition, we did not include osteolytic vertebral lesions, which may also partially explain this difference. Another reason could be the small number of subjects in our study, which gives more weight to outliers, especially considering the inherent natural variability of PDFF in spinal lesions and also in healthy individuals, showing a correlation with age and manifesting a fat gradient from cervical to lumbar spinal levels (65, 69, 70). For example, Schmeel and colleagues reported the PDFF in morphologically normal-appearing vertebral bodies to be 55% (mean age 68 years) (65). In contrast, Baum and colleagues reported normal lumbar vertebral body PDFF in young individuals (mean age 26 years) to be 35% (69). Underlining the high variability of PDFF values in different spinal pathologies, it has been recently shown that PDFF was significantly lower in infectious spondylitis compared to erosive endplate changes (4% versus 35%) (71).

In our study, PDFF was markedly increased in patients with osteoporotic vertebrae compared to the metastasis group. This is in line with the literature, which showed that PDFF is negatively correlated to BMD (40, 41). Hence, it might be a useful MRI-derived marker for osteoporosis and bone health (38, 41, 42). However, the correlation between vBMD and PDFF was weak to moderate in our study, which contrasts with the literature, where a stronger correlation (r = 0.64) between both parameters was shown (41). This is most likely explained by the small number of patients in our osteoporotic subgroup. Nevertheless, the median PDFF value in our osteoporosis subgroup was 43.8%, which was lower than the PDFF values of osteoporotic patients in the literature, where a PDFF value of up to 60% is reported (41). In that regard, a recent study showed that PDFF, while correlating with BMD, was significantly higher in patients with osteoporotic/osteopenic vertebrae with VFs than in osteoporotic/osteopenic patients without VFs, even after adjusting for BMD (39). Although correlating with BMD, the authors suggested that PDFF may be an independent predictor for fracture risk in osteoporosis (39). Furthermore, the mean PDFF in osteoporotic/osteopenic vertebrae without VFs was 39% (39), which closely resembles our PDFF values in non-fractured osteoporotic vertebrae.

Considering the complex microstructure of bone, CT imaging and the vBMD calculated from it provide more information for assessing bone quality than the DXA-derived aBMD (44, 72). Notably, DXA is a two-dimensional assessment, thus neglecting the 3D architecture of a vertebral body, and the aBMD only accounts for approximately 60 to 70% of variation in bone strength (73). Yet, patient-specific image-based FEA is considered the reference standard to estimate vertebral strength, having demonstrated to approximate vertebral body compressive

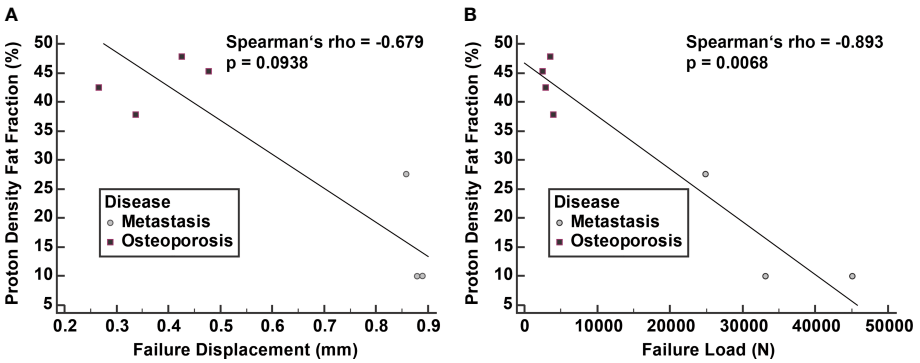

FIGURE 5 | Correlation of proton density fat fraction (PDFF) with failure displacement **(A)** and failure load **(B)**. Spearman correlation was calculated from median values of vertebral bodies L1 to L4 excluding the fractured vertebrae.

strength even better than vBMD according to an *in-vitro* scenario (54). Specifically, vertebral strength measurements derived from FEA have been shown to improve fracture risk calculation and determine treatment efficacy of single segments and functional spinal units (25, 54, 74). Also, the feasibility of performing FEA from routine clinical imaging data to assess fracture risk has been shown (28). In addition, there is evidence that multi-detector CT acquisition with a dose reduction of up to 75% may still enable discriminating between osteoporotic patients with and without VFs (26). One study also showed that the combination of vBMD measurements and FEA derived from routine CT imaging allowed improved prediction of incidental fractures at a vertebral-specific level (24). While the feasibility and utility of FEA for estimating fracture risk of osteoporotic vertebral bodies have been extensively studied, the value of FEA-based parameters in metastatic spinal lesions has been sparsely investigated (23, 29).

However, metastatic changes in vertebral anatomy and structure are of great clinical importance in treating cancer patients, as they are usually the cause of pathological VFs (75, 76). Scores such as the Spinal Instability Neoplastic Score (SINS) have been developed for patients with bone metastases at the spine (77). It categorizes VF risk based on spinal segment, pain, bone quality, radiographic alignment, vertebral body collapse, and postero-lateral involvement of spinal elements (77). However, the reproducibility of its imaging components is suboptimal (78). Thus, its prognostic value in terms of VF risk seems controversial (79). It was shown that FEA-based models provide interesting insights into simulated osteolytic defects (80, 81). However, spinal metastases often present as osteoblastic lesions in prostate and breast cancer (82). Stadelmann et al. investigated osteolytic and osteoblastic metastases in cadaver models and compared FEA models with *in-vitro* compression models (29). They showed that osteoblastic metastases resulted in significantly worse bone tissue properties compared to controls, whereas osteolytic lesions appeared to have a negligible effect, even though osteolytic lesions displayed a lower percentage of mineralized bone tissue in total (29). They mainly attributed these effects to the woven nature of the newly formed bone in osteoblastic lesions and its lower mineralization around the blastic lesions, whereas the material properties of the bone surrounding osteolytic lesions hardly change (29). Another study experimentally measured bone strength (in kN) in cadaveric vertebrae with osteoblastic, osteolytic, and mixed vertebral metastases (83). The authors showed that vBMD was highly variable in osteoblastic and mixed vertebrae while it was generally reduced in osteolytic vertebrae. They also showed that only vBMD, but not lesion type, was an independent predictor of vertebral bone strength (83). Furthermore, *in-vitro* vertebral strength, measured by compression until failure in a laboratory compression model, was strongly associated with FEA-based strength ($r = 0.78$) and only moderately associated with bone mineral content ($r = 0.66$), independent of the lesion type (29). Another preliminary study evaluated FEA models on a vertebra-specific level in three fresh-frozen human donors with multiple myeloma and vertebral compression fractures (23). The authors showed that by applying the same universal loading condition to the vertebral segments T1 to L5, the differences in structural strength highly correlated between *in-vitro* samples and FEA-derived values (23). This study also suggested that absolute fracture load values have little predictive value, while the relative fracture loads provided valuable information on the relative stability between segments (23).

While the PDFF is a quantitative measure of fat content of bone marrow (30, 32, 33), failure load and failure displacement take into account the trabecular morphology including quality factors like bone shape, morphology, critical locations, and bone mass distribution (22, 24). Because these parameters inherently measure different features, it is interesting that they correlate strongly with each other. The most likely reason for this strong correlation is that bone marrow fat content, bone trabecular volume and microarchitecture are in turn also correlated with each other. In this regard, bone marrow fat accumulation is an age-dependent process replacing hematopoietic with fatty bone marrow, but it is also associated with a reduction in BMD (84, 85). Given that adipocytes and osteoblasts share the common precursor mesenchymal stem cells in the bone marrow (86), decreased bone formation observed during aging or osteoporosis may be the result of a disturbance in the equilibrium between adipogenesis versus osteoblastogenesis (84, 87). Increased bone marrow fat deposition

was hypothesized to be linked to lower BMD and increased VF risk through a shift in mesenchymal stem cell lineage allocation that favors adipocytes over osteoblasts, leading to reductions in BMD and changes in bone microarchitecture (84, 88).

Empirical evidence of the increased bone marrow fat content in osteoporosis and its association with VF risk was shown for different modalities, such as CSE-MRI (39), MR spectroscopy (42, 89–91), and in biopsy studies (92). Interestingly, higher marrow fat deposition was found to be associated with VF risk, even after adjusting for trabecular BMD (93). Apart from these pathophysiologic considerations, it is important to conduct further studies with larger patient samples to elucidate the question of whether marrow fat content, trabecular and vertebral morphology and BMD are independent factors relevant to VF risk, or whether one of these parameters might be the dominant explanatory factor in osteoporosis.

The limitations of this study are mainly the small sample size of seven patients, which did not allow for an age- and gender-matched study design. In addition, no osteolytic metastases were included in the cohort, which would have added value to the quantitative parameters derived from CT and MRI. For comparison, a cohort of healthy control subjects would have been helpful, also to assess how FEA-based parameters and PDFF vary between vertebrae within a healthy individual for the herein used setup. Furthermore, inter-reader variability in the generation of segmentation maps is a potential pitfall. In our study, this limitation was circumvented for the calculation of vBMD and FEA-based parameters by using deep learning-based segmentation through our standardized pipeline. Another limitation of FEA itself is the still high computational effort. As a result, this technology has not yet been integrated into everyday clinical practice.

CONCLUSION

The failure displacement and failure load calculated from CT-based FEA were significantly higher in osteoblastic lumbar vertebral bodies than in osteoporotic lumbar vertebral bodies. Conversely, the PDFF calculated from CSE-MRI was significantly lower in diffuse osteoblastic metastatic vertebral bodies than in osteoporotic vertebral bodies. There was a strong correlation between failure displacement and PDFF and a very strong correlation between failure load and PDFF. We were able to show in a preliminary dataset that PDFF and FEA-based failure load and failure displacement are strongly inversely correlated. As a prospect for future diagnostic application of these modalities, a computationally intensive FEA could be performed in a two-stage opportunistic screening approach for those cases found to have significantly reduced PDFF.

DATA AVAILABILITY STATEMENT

The raw data supporting the conclusions of this article will be made available by the authors, without undue reservation.

ETHICS STATEMENT

The studies involving human participants were reviewed and approved by the Ethikkommission der Fakultät für Medizin der Technischen Universität München. Written informed consent was waived due to the study's retrospective design.

AUTHOR CONTRIBUTIONS

Conceptualization was performed by TB, KS, and NS. Methodology involved NR, MD, CB, SR, EB, and NS. Software involved NR, MD, DK, TB, KS, and NS. Formal analysis performed by TG, NR, TB, and NS. Investigation was performed by TG and NS. Resources provided by JK, DK, TB, and KS. Data curation was performed by TG and NS. Writing – original draft preparation was performed by TG and NS. Writing – review and editing was performed by all authors. Visualization was performed by TG, NR, MD, KS, and NS. Supervision was performed by TB, KS, and NS. Project administration was performed by TB and NS. All authors contributed to the article and approved the submitted version.

FUNDING

The present work was supported by the German Research Foundation (Deutsche Forschungsgemeinschaft, DFG, project 432290010, JK and TB) and the German Society of Musculoskeletal Radiology (Deutsche Gesellschaft für Muskuloskelettale Radiologie, DGMSR, MD and NS).

REFERENCES

1. Harvey N, Dennison E, Cooper C. Osteoporosis: Impact on Health and Economics. *Nat Rev Rheumatol* (2010) 6:99–105. doi: 10.1038/nrrheum.2009.260
2. Office of the Surgeon G. Reports of the Surgeon General. Bone Health and Osteoporosis: A Report of the Surgeon General. In: *Reports of the Surgeon General*. Rockville (MD: Office of the Surgeon General US (2004).
3. Salari N, Ghasemi H, Mohammadi L, Behzadi MH, Rabieenia E, Shohaimi S, et al. The Global Prevalence of Osteoporosis in the World: A Comprehensive Systematic Review and Meta-Analysis. *J Orthop Surg Res* (2021) 16:609. doi: 10.1186/s13018-021-02772-0
4. Johnell O, Kanis JA. An Estimate of the Worldwide Prevalence and Disability Associated With Osteoporotic Fractures. *Osteoporos Int* (2006) 17:1726–33. doi: 10.1007/s00198-006-0172-4
5. Compston JE, McClung MR, Leslie WD. Osteoporosis. *Lancet* (2019) 393:364–76. doi: 10.1016/S0140-6736(18)32112-3
6. Melton LJ3rd, Atkinson EJ, Cooper C, O'Fallon WM, Riggs BL. Vertebral Fractures Predict Subsequent Fractures. *Osteoporos Int* (1999) 10:214–21. doi: 10.1007/s001980050218

7. Kanis JA, Johnell O, De Laet C, Johansson H, Oden A, Delmas P, et al. A Meta-Analysis of Previous Fracture and Subsequent Fracture Risk. *Bone* (2004) 35:375–82. doi: 10.1016/j.bone.2004.03.024
8. Greenlee RT, Murray T, Bolden S, Wingo PA. Cancer Statistics, 2000. *CA Cancer J Clin* (2000) 50:7–33. doi: 10.3322/canjclin.50.1.7
9. Siegel RL, Miller KD, Jemal A. Cancer Statistics, 2017. *CA Cancer J Clin* (2017) 67:7–30. doi: 10.3322/caac.21387
10. Aebi M. Spinal Metastasis in the Elderly. *Eur Spine J* (2003) 12 Suppl 2:S202–13. doi: 10.1007/s00586-003-0609-9
11. Parkin DM, Pisani P, Ferlay J. Global Cancer Statistics. *CA Cancer J Clin* (1999) 49:33–64. doi: 10.3322/canjclin.49.1.33
12. Scutellari PN, Antinolfi G, Galeotti R, Giganti M. [Metastatic Bone Disease. Strategies for imaging]. *Minerva Med* (2003) 94:77–90.
13. Jiang W, Rixiati Y, Zhao B, Li Y, Tang C, Liu J. Incidence, Prevalence, and Outcomes of Systemic Malignancy With Bone Metastases. *J Orthop Surg (Hong Kong)* (2020) 28:2309499020915989. doi: 10.1177/2309499020915989
14. Kanis JA. Diagnosis of Osteoporosis and Assessment of Fracture Risk. *Lancet* (2002) 359:1929–36. doi: 10.1016/S0140-6736(02)08761-5
15. Loffler MT, Sollmann N, Mei K, Valentinitsch A, Noel PB, Kirschke JS, et al. X-Ray-Based Quantitative Osteoporosis Imaging at the Spine. *Osteoporos Int* (2019). 31(2):233–250. doi: 10.1007/s00198-019-05212-2
16. Link TM, Kazakia G. Update on Imaging-Based Measurement of Bone Mineral Density and Quality. *Curr Rheumatol Rep* (2020) 22:13. doi: 10.1007/s11926-020-00892-w
17. Schuit SC, van der Klift M, Weel AE, de Laet CE, Burger H, Seeman E, et al. Fracture Incidence and Association With Bone Mineral Density in Elderly Men and Women: The Rotterdam Study. *Bone* (2004) 34:195–202. doi: 10.1016/j.bone.2003.10.001
18. Cody DD, Gross GJ, Hou FJ, Spencer HJ, Goldstein SA, Fyhrie DP. Femoral Strength Is Better Predicted by Finite Element Models Than QCT and DXA. *J Biomech* (1999) 32:1013–20. doi: 10.1016/s0021-9290(99)00099-8
19. Wang X, Sanyal A, Cawthon PM, Palermo L, Jekir M, Christensen J, et al. Prediction of New Clinical Vertebral Fractures in Elderly Men Using Finite Element Analysis of CT Scans. *J Bone Miner Res* (2012) 27:808–16. doi: 10.1002/jbmr.1539
20. Imai K, Ohnishi I, Matsumoto T, Yamamoto S, Nakamura K. Assessment of Vertebral Fracture Risk and Therapeutic Effects of Alendronate in Postmenopausal Women Using a Quantitative Computed Tomography-Based Nonlinear Finite Element Method. *Osteoporos Int* (2009) 20:801–10. doi: 10.1007/s00198-008-0750-8
21. Bailey S, Hackney D, Vashishth D, Alkalay RN. The Effects of Metastatic Lesion on the Structural Determinants of Bone: Current Clinical and Experimental Approaches. *Bone* (2020) 138:115159. doi: 10.1016/j.bone.2019.115159
22. Silva MJ, Keaveny TM, Hayes WC. Computed Tomography-Based Finite Element Analysis Predicts Failure Loads and Fracture Patterns for Vertebral Sections. *J Orthop Res* (1998) 16:300–8. doi: 10.1002/jor.1100160305
23. Anitha D, Baum T, Kirschke JS, Subburaj K. Risk of Vertebral Compression Fractures in Multiple Myeloma Patients: A Finite-Element Study. *Medicine* (2017) 96:e5825. doi: 10.1097/MD.0000000000005825
24. Yeung LY, Rayudu NM, Loffler M, Sekuboyina A, Burian E, Sollmann N, et al. Prediction of Incidental Osteoporotic Fractures at Vertebral-Specific Level Using 3d Non-Linear Finite Element Parameters Derived From Routine Abdominal MDCT. *Diagn (Basel)* (2021) 11(2), 208. doi: 10.3390/diagnostics11020208
25. Allaire BT, Lu D, Johannesdottir F, Kopperdahl D, Keaveny TM, Jarraya M, et al. Prediction of Incident Vertebral Fracture Using CT-Based Finite Element Analysis. *Osteoporos Int* (2019) 30:323–31. doi: 10.1007/s00198-018-4716-1
26. Anitha D, Mei K, Dieckmeyer M, Kopp FK, Sollmann N, Zimmer C, et al. MDCT-Based Finite Element Analysis of Vertebral Fracture Risk: What Dose Is Needed? *Clin Neuroradiol* (2019) 29:645–51. doi: 10.1007/s00062-018-0722-0
27. Anitha D, Subburaj K, Mei K, Kopp FK, Foehr P, Noel PB, et al. Effects of Dose Reduction on Bone Strength Prediction Using Finite Element Analysis. *Sci Rep* (2016) 6:38441. doi: 10.1038/srep38441
28. Rayudu NM, Dieckmeyer M, Loffler MT, Noel PB, Kirschke JS, Baum T, et al. Predicting Vertebral Bone Strength Using Finite Element Analysis for Opportunistic Osteoporosis Screening in Routine Multidetector Computed Tomography Scans-A Feasibility Study. *Front Endocrinol* (2020) 11:526332. doi: 10.3389/fendo.2020.526332
29. Stadelmann MA, Schenk DE, Maquer G, Lenherr C, Buck FM, Bosshardt DD, et al. Conventional Finite Element Models Estimate the Strength of Metastatic Human Vertebrae Despite Alterations of the Bone's Tissue and Structure. *Bone* (2020) 141:115598. doi: 10.1016/j.bone.2020.115598
30. Sollmann N, Loffler MT, Kronthaler S, Bohm C, Dieckmeyer M, Ruschke S, et al. MRI-Based Quantitative Osteoporosis Imaging at the Spine and Femur. *J Magn Reson Imaging* (2021) 54:12–35. doi: 10.1002/jmri.27260
31. Karampinos DC, Ruschke S, Dieckmeyer M, Diefenbach M, Franz D, Gersing AS, et al. Quantitative MRI and Spectroscopy of Bone Marrow. *J Magn Reson Imaging* (2018) 47:332–53. doi: 10.1002/jmri.25769
32. Reeder SB, Hu HH, Sirlin CB. Proton Density Fat-Fraction: A Standardized MR-Based Biomarker of Tissue Fat Concentration. *J Magn Reson Imaging* (2012) 36:1011–4. doi: 10.1002/jmri.23741
33. Ma J. Dixon Techniques for Water and Fat Imaging. *J Magn Reson Imaging* (2008) 28:543–58. doi: 10.1002/jmri.21492
34. Zajick DCJr., Morrison WB, Schweitzer ME, Parellada JA, Carrino JA. Benign and Malignant Processes: Normal Values and Differentiation With Chemical Shift MR Imaging in Vertebral Marrow. *Radiology* (2005) 237:590–6. doi: 10.1148/radiol.2372040990
35. Douis H, Davies AM, Jeys L, Sian P. Chemical Shift MRI can Aid in the Diagnosis of Indeterminate Skeletal Lesions of the Spine. *Eur Radiol* (2016) 26:932–40. doi: 10.1007/s00330-015-3898-6
36. Disler DG, McCauley TR, Ratner LM, Kesack CD, Cooper JA. In-Phase and Out-of-Phase MR Imaging of Bone Marrow: Prediction of Neoplasia Based on the Detection of Coexistent Fat and Water. *AJR Am J Roentgenol* (1997) 169:1439–47. doi: 10.2214/ajr.169.5.9353477
37. Schmeel FC, Luetkens JA, Wagenhauser PJ, Meier-Schroers M, Kuetting DL, Feisst A, et al. Proton Density Fat Fraction (PDFF) MRI for Differentiation of Benign and Malignant Vertebral Lesions. *Eur Radiol* (2018) 28:2397–405. doi: 10.1007/s00330-017-5241-x
38. Kuhn JP, Hernando D, Meffert PJ, Reeder S, Hosten N, Laqua R, et al. Proton-Density Fat Fraction and Simultaneous R2* Estimation as an MRI Tool for Assessment of Osteoporosis. *Eur Radiol* (2013) 23:3432–9. doi: 10.1007/s00330-013-2950-7
39. Gassert FT, Kufner A, Gassert FG, Leonhardt Y, Kronthaler S, Schwaiger BJ, et al. MR-Based Proton Density Fat Fraction (PDFF) of the Vertebral Bone Marrow Differentiates Between Patients With and Without Osteoporotic Vertebral Fractures. *Osteoporos Int* (2022) 33:487–96. doi: 10.1007/s00198-021-06147-3
40. Cheng X, Li K, Zhang Y, Wang L, Xu L, Liu Y, et al. The Accurate Relationship Between Spine Bone Density and Bone Marrow in Humans. *Bone* (2020) 134:115312. doi: 10.1016/j.bone.2020.115312
41. Guo Y, Chen Y, Zhang X, Mei Y, Yi P, Wang Y, et al. Magnetic Susceptibility and Fat Content in the Lumbar Spine of Postmenopausal Women With Varying Bone Mineral Density. *J Magn Reson Imaging* (2019) 49:1020–28. doi: 10.1002/jmri.26279
42. Yeung DK, Griffith JF, Antonio GE, Lee FK, Woo J, Leung PC. Osteoporosis Is Associated With Increased Marrow Fat Content and Decreased Marrow Fat Unsaturation: A Proton MR Spectroscopy Study. *J Magn Reson Imaging* (2005) 22:279–85. doi: 10.1002/jmri.20367
43. Genant HK, Wu CY, van Kuijk C, Nevitt MC. Vertebral Fracture Assessment Using a Semiquantitative Technique. *J Bone Miner Res* (1993) 8:1137–48. doi: 10.1002/jbmr.5650080915
44. Loffler MT, Jacob A, Scharr A, Sollmann N, Burian E, El Husseini M, et al. Automatic Opportunistic Osteoporosis Screening in Routine CT: Improved Prediction of Patients With Prevalent Vertebral Fractures Compared to DXA. *Eur Radiol* (2021) 31:6069–77. doi: 10.1007/s00330-020-07655-2
45. Loffler MT, Sollmann N, Burian E, Bayat A, Aftahy K, Baum T, et al. Opportunistic Osteoporosis Screening Reveals Low Bone Density in Patients With Screw Loosening After Lumbar Semi-Rigid Instrumentation: A Case-Control Study. *Front Endocrinol* (2020) 11:552719. doi: 10.3389/fendo.2020.552719
46. Ruhling S, Scharr A, Sollmann N, Wostrack M, Loffler MT, Menze B, et al. Proposed Diagnostic Volumetric Bone Mineral Density Thresholds for

Osteoporosis and Osteopenia at the Cervicothoracic Spine in Correlation to the Lumbar Spine. *Eur Radiol* (2022). doi: 10.1007/s00330-022-08721-7
47. Tripto-Shkolnik L, Rouach V. A Dramatic Increase in Bone Mineral Density, Enhanced Osteoblast Activity and Malignancy. *QJM* (2020) 113:289–90. doi: 10.1093/qjmed/hcz205
48. Fedorov A, Beichel R, Kalpathy-Cramer J, Finet J, Fillion-Robin JC, Pujol S, et al. 3d Slicer as an Image Computing Platform for the Quantitative Imaging Network. *Magn Reson Imaging* (2012) 30:1323–41. doi: 10.1016/j.mri.2012.05.001
49. Chen G, Schmutz B, Epari D, Rathnayaka K, Ibrahim S, Schuetz MA, et al. A New Approach for Assigning Bone Material Properties From CT Images Into Finite Element Models. *J Biomech* (2010) 43:1011–5. doi: 10.1016/j.jbiomech.2009.10.040
50. Taddei F, Schileo E, Helgason B, Cristofolini L, Viceconti M. The Material Mapping Strategy Influences the Accuracy of CT-Based Finite Element Models of Bones: An Evaluation Against Experimental Measurements. *Med Eng Phys* (2007) 29:973–9. doi: 10.1016/j.medengphy.2006.10.014
51. Rho JY, Hobatho MC, Ashman RB. Relations of Mechanical Properties to Density and CT Numbers in Human Bone. *Med Eng Phys* (1995) 17:347–55. doi: 10.1016/1350-4533(95)97314-f
52. Goulet RW, Goldstein SA, Ciarelli MJ, Kuhn JL, Brown MB, Feldkamp LA. The Relationship Between the Structural and Orthogonal Compressive Properties of Trabecular Bone. *J Biomech* (1994) 27:375–89. doi: 10.1016/0021-9290(94)90014-0
53. Morgan EF, Bayraktar HH, Keaveny TM. Trabecular Bone Modulus-Density Relationships Depend on Anatomic Site. *J Biomech* (2003) 36:897–904. doi: 10.1016/s0021-9290(03)00071-x
54. Crawford RP, Cann CE, Keaveny TM. Finite Element Models Predict *In Vitro* Vertebral Body Compressive Strength Better Than Quantitative Computed Tomography. *Bone* (2003) 33:744–50. doi: 10.1016/s8756-3282(03)00210-2
55. Keller TS. Predicting the Compressive Mechanical Behavior of Bone. *J Biomech* (1994) 27:1159–68. doi: 10.1016/0021-9290(94)90056-6
56. Keyak JH. Improved Prediction of Proximal Femoral Fracture Load Using Nonlinear Finite Element Models. *Med Eng Phys* (2001) 23:165–73. doi: 10.1016/s1350-4533(01)00045-5
57. Anitha DP, Baum T, Kirschke JS, Subburaj K. Effect of the Intervertebral Disc on Vertebral Bone Strength Prediction: A Finite-Element Study. *Spine J* (2020) 20:665–71. doi: 10.1016/j.spinee.2019.11.015
58. Rayudu NM, Baum T, Kirschke JS, Subburaj K. MDCT-Based Finite Element Analysis for the Prediction of Functional Spine Unit Strength—An *In Vitro* Study. *Mater (Basel)* (2021) 14:5791. doi: 10.3390/ma14195791
59. Ruschke S, Eggers H, Kooijman H, Diefenbach MN, Baum T, Haase A, et al. Correction of Phase Errors in Quantitative Water-Fat Imaging Using a Monopolar Time-Interleaved Multi-Echo Gradient Echo Sequence. *Magn Reson Med* (2017) 78:984–96. doi: 10.1002/mrm.26485
60. Boehm C, Diefenbach MN, Makowski MR, Karampinos DC. Improved Body Quantitative Susceptibility Mapping by Using a Variable-Layer Single-Min-Cut Graph-Cut for Field-Mapping. *Magn Reson Med* (2021) 85:1697–712. doi: 10.1002/mrm.28515
61. Karampinos DC, Ruschke S, Dieckmeyer M, Eggers H, Kooijman H, Rummeny EJ, et al. Modeling of T2* Decay in Vertebral Bone Marrow Fat Quantification. *NMR BioMed* (2015) 28:1535–42. doi: 10.1002/nbm.3420
62. Ren J, Dimitrov I, Sherry AD, Malloy CR. Composition of Adipose Tissue and Marrow Fat in Humans by 1H NMR at 7 Tesla. *J Lipid Res* (2008) 49:2055–62. doi: 10.1194/jlr.D800010-JLR200
63. Wolf I, Vetter M, Wegner I, Bottger T, Nolden M, Schobinger M, et al. The Medical Imaging Interaction Toolkit. *Med Image Anal* (2005) 9:594–604. doi: 10.1016/j.media.2005.04.005
64. Schmeel FC, Vomweg T, Traber F, Gerhards A, Enkirch SJ, Faron A, et al. Proton Density Fat Fraction MRI of Vertebral Bone Marrow: Accuracy, Repeatability, and Reproducibility Among Readers, Field Strengths, and Imaging Platforms. *J Magn Reson Imaging* (2019) 50:1762–72. doi: 10.1002/jmri.26748
65. Schmeel FC, Enkirch SJ, Luetkens JA, Faron A, Lehnen N, Sprinkart AM, et al. Diagnostic Accuracy of Quantitative Imaging Biomarkers in the Differentiation of Benign and Malignant Vertebral Lesions : Combination of Diffusion-Weighted and Proton Density Fat Fraction Spine MRI. *Clin Neuroradiol* (2021) 31:1059–70. doi: 10.1007/s00062-021-01009-1
66. Schmeel FC, Luetkens JA, Enkirch SJ, Feisst A, Endler CH, Schmeel LC, et al. Proton Density Fat Fraction (PDFF) MR Imaging for Differentiation of Acute Benign and Neoplastic Compression Fractures of the Spine. *Eur Radiol* (2018) 28:5001–09. doi: 10.1007/s00330-018-5513-0
67. Kwack KS, Lee HD, Jeon SW, Lee HY, Park S. Comparison of Proton Density Fat Fraction, Simultaneous R2*, and Apparent Diffusion Coefficient for Assessment of Focal Vertebral Bone Marrow Lesions. *Clin Radiol* (2020) 75:123–30. doi: 10.1016/j.crad.2019.09.141
68. Boehm C, Sollmann N, Meineke J, Ruschke S, Dieckmeyer M, Weiss K, et al. Preconditioned Water-Fat Total Field Inversion: Application to Spine Quantitative Susceptibility Mapping. *Magn Reson Med* (2022) 87:417–30. doi: 10.1002/mrm.28903
69. Baum T, Yap SP, Dieckmeyer M, Ruschke S, Eggers H, Kooijman H, et al. Assessment of Whole Spine Vertebral Bone Marrow Fat Using Chemical Shift-Encoding Based Water-Fat MRI. *J Magn Reson Imaging* (2015) 42:1018–23. doi: 10.1002/jmri.24854
70. Baum T, Rohrmeier A, Syvari J, Diefenbach MN, Franz D, Dieckmeyer M, et al. Anatomical Variation of Age-Related Changes in Vertebral Bone Marrow Composition Using Chemical Shift Encoding-Based Water-Fat Magnetic Resonance Imaging. *Front Endocrinol* (2018) 9:141. doi: 10.3389/fendo.2018.00141
71. Schmeel FC, Lakghomi A, Lehnen NC, Haase R, Banat M, Wach J, et al. Proton Density Fat Fraction Spine MRI for Differentiation of Erosive Vertebral Endplate Degeneration and Infectious Spondylitis. *Diagn (Basel)* (2022) 12:78. doi: 10.3390/diagnostics12010078
72. Li N, Li XM, Xu L, Sun WJ, Cheng XG, Tian W. Comparison of QCT and DXA: Osteoporosis Detection Rates in Postmenopausal Women. *Int J Endocrinol* (2013) 2013:895474. doi: 10.1155/2013/895474
73. Ammann P, Rizzoli R. Bone Strength and its Determinants. *Osteoporos Int* (2003) 14 Suppl 3:S13–8. doi: 10.1007/s00198-002-1345-4
74. Sollmann N, Rayudu NM, Yeung LY, Sekuboyina A, Burian E, Dieckmeyer M, et al. MDCT-Based Finite Element Analyses: Are Measurements at the Lumbar Spine Associated With the Biomechanical Strength of Functional Spinal Units of Incidental Osteoporotic Fractures Along the Thoracolumbar Spine? *Diagn (Basel)* (2021) 11(3), 455. doi: 10.3390/diagnostics11030455
75. Prasad D, Schiff D. Malignant Spinal-Cord Compression. *Lancet Oncol* (2005) 6:15–24. doi: 10.1016/S1470-2045(04)01709-7
76. Sahgal A, Whyne CM, Ma L, Larson DA, Fehlings MG. Vertebral Compression Fracture After Stereotactic Body Radiotherapy for Spinal Metastases. *Lancet Oncol* (2013) 14:e310–20. doi: 10.1016/S1470-2045(13)70101-3
77. Fisher CG, DiPaola CP, Ryken TC, Bilsky MH, Shaffrey CI, Berven SH, et al. A Novel Classification System for Spinal Instability in Neoplastic Disease: An Evidence-Based Approach and Expert Consensus From the Spine Oncology Study Group. *Spine (Phila Pa 1976)* (2010) 35:E1221–9. doi: 10.1097/BRS.0b013e3181e16ae2
78. Fourney DR, Frangou EM, Ryken TC, Dipaola CP, Shaffrey CI, Berven SH, et al. Spinal Instability Neoplastic Score: An Analysis of Reliability and Validity From the Spine Oncology Study Group. *J Clin Oncol* (2011) 29:3072–7. doi: 10.1200/JCO.2010.34.3897
79. Versteeg AL, Verlaan JJ, Sahgal A, Mendel E, Quraishi NA, Fourney DR, et al. The Spinal Instability Neoplastic Score: Impact on Oncologic Decision-Making. *Spine (Phila Pa 1976)* (2016) 41 Suppl 20:S231–S37. doi: 10.1097/BRS.0000000000001822
80. Whyne CM, Hu SS, Lotz JC. Parametric Finite Element Analysis of Vertebral Bodies Affected by Tumors. *J Biomech* (2001) 34:1317–24. doi: 10.1016/s0021-9290(01)00086-0
81. Costa MC, Campello LBB, Ryan M, Rochester J, Viceconti M, Dall'Ara E. Effect of Size and Location of Simulated Lytic Lesions on the Structural Properties of Human Vertebral Bodies, a Micro-Finite Element Study. *Bone Rep* (2020) 12:100257. doi: 10.1016/j.bonr.2020.100257
82. Buhmann Kirchhoff S, Becker C, Duerr HR, Reiser M, Baur-Melnyk A. Detection of Osseous Metastases of the Spine: Comparison of High Resolution Multi-Detector-CT With MRI. *Eur J Radiol* (2009) 69:567–73. doi: 10.1016/j.ejrad.2007.11.039
83. Alkalay RN, Groff MW, Stadelmann MA, Buck FM, Hoppe S, Theumann N, et al. Improved Estimates of Strength and Stiffness in Pathologic Vertebrae With Bone Metastases Using CT-Derived Bone Density Compared With

Radiographic Bone Lesion Quality Classification. *J Neurosurg Spine* (2022) 36:113–24. doi: 10.3171/2021.2.SPINE202027
84. Moerman EJ, Teng K, Lipschitz DA, Lecka-Czernik B. Aging Activates Adipogenic and Suppresses Osteogenic Programs in Mesenchymal Marrow Stroma/Stem Cells: The Role of PPAR-Gamma2 Transcription Factor and TGF-Beta/BMP Signaling Pathways. *Aging Cell* (2004) 3:379–89. doi: 10.1111/j.1474-9728.2004.00127.x
85. Sheu Y, Cauley JA. The Role of Bone Marrow and Visceral Fat on Bone Metabolism. *Curr Osteoporos Rep* (2011) 9:67–75. doi: 10.1007/s11914-011-0051-6
86. Pittenger MF, Mackay AM, Beck SC, Jaiswal RK, Douglas R, Mosca JD, et al. Multilineage Potential of Adult Human Mesenchymal Stem Cells. *Science* (1999) 284:143–7. doi: 10.1126/science.284.5411.143
87. Savopoulos C, Dokos C, Kaiafa G, Hatzitolios A. Adipogenesis and Osteoblastogenesis: Trans-Differentiation in the Pathophysiology of Bone Disorders. *Hippokratia* (2011) 15:18–21.
88. Gimble JM, Zvonic S, Floyd ZE, Kassem M, Nuttall ME. Playing With Bone and Fat. *J Cell Biochem* (2006) 98:251–66. doi: 10.1002/jcb.20777
89. Devlin MJ. Bone Marrow Composition, Diabetes, and Fracture Risk: More Bad News for Saturated Fat. *J Bone Miner Res* (2013) 28:1718–20. doi: 10.1002/jbmr.2013
90. Verma S, Rajaratnam JH, Denton J, Hoyland JA, Byers RJ. Adipocytic Proportion of Bone Marrow Is Inversely Related to Bone Formation in Osteoporosis. *J Clin Pathol* (2002) 55:693–8. doi: 10.1136/jcp.55.9.693
91. Li X, Kuo D, Schafer AL, Porzig A, Link TM, Black D, et al. Quantification of Vertebral Bone Marrow Fat Content Using 3 Tesla MR Spectroscopy: Reproducibility, Vertebral Variation, and Applications in Osteoporosis. *J Magn Reson Imaging* (2011) 33:974–9. doi: 10.1002/jmri.22489
92. Justesen J, Stenderup K, Ebbesen EN, Mosekilde L, Steiniche T, Kassem M. Adipocyte Tissue Volume in Bone Marrow Is Increased With Aging and in Patients With Osteoporosis. *Biogerontology* (2001) 2:165–71. doi: 10.1023/a:1011513223894
93. Schwartz AV, Sigurdsson S, Hue TF, Lang TF, Harris TB, Rosen CJ, et al. Vertebral Bone Marrow Fat Associated With Lower Trabecular BMD and Prevalent Vertebral Fracture in Older Adults. *J Clin Endocrinol Metab* (2013) 98:2294–300. doi: 10.1210/jc.2012-3949

Conflict of Interest: The authors declare that the research was conducted in the absence of any commercial or financial relationships that could be construed as a potential conflict of interest.

Publisher's Note: All claims expressed in this article are solely those of the authors and do not necessarily represent those of their affiliated organizations, or those of the publisher, the editors and the reviewers. Any product that may be evaluated in this article, or claim that may be made by its manufacturer, is not guaranteed or endorsed by the publisher.

frontiers | Frontiers in Endocrinology

MINI REVIEW
published: 12 July 2022
doi: 10.3389/fendo.2022.903925

Adipocyte-Cancer Cell Interactions in the Bone Microenvironment

*Meredith O. C. Otley and Christopher J. Sinal**

Department of Pharmacology, Dalhousie University, Halifax, NS, Canada

When compared to adipocytes in other anatomical sites, the interaction of bone marrow resident adipocytes with the other cells in their microenvironment is less well understood. Bone marrow adipocytes originate from a resident, self-renewing population of multipotent bone marrow stromal cells which can also give rise to other lineages such as osteoblasts. The differentiation fate of these mesenchymal progenitors can be influenced to favour adipogenesis by several factors, including the administration of thiazolidinediones and increased age. Experimental data suggests that increases in bone marrow adipose tissue volume may make bone both more attractive to metastasis and conducive to cancer cell growth. Bone marrow adipocytes are known to secrete a variety of lipids, cytokines and bioactive signaling molecules known as adipokines, which have been implicated as mediators of the interaction between adipocytes and cancer cells. Recent studies have provided new insight into the impact of bone marrow adipose tissue volume expansion in regard to supporting and exacerbating the effects of bone metastasis from solid tumors, focusing on prostate, breast and lung cancer and blood cancers, focusing on multiple myeloma. In this mini-review, recent research developments pertaining to the role of factors which increase bone marrow adipose tissue volume, as well as the role of adipocyte secreted factors, in the progression of bone metastatic prostate and breast cancer are assessed. In particular, recent findings regarding the complex cross-talk between adipocytes and metastatic cells of both lung and prostate cancer are highlighted.

Keywords: bone, adipocyte, cancer, adipokine, metastasis

OPEN ACCESS

Edited by:
Guanwu Li,
Shanghai University of Traditional Chinese Medicine, China

Reviewed by:
Emily Jane Gallagher,
Icahn School of Medicine at Mount Sinai, United States
Sherri L Christian,
Memorial University of Newfoundland, Canada
Silvia Corvera,
University of Massachusetts Medical School, United States
William Frank Ferris,
Stellenbosch University, South Africa

***Correspondence:**
Christopher J. Sinal
christopher.sinal@dal.ca

Specialty section:
This article was submitted to Bone Research, a section of the journal Frontiers in Endocrinology

Received: *24 March 2022*
Accepted: *15 June 2022*
Published: *12 July 2022*

Citation:
Otley MOC and Sinal CJ (2022) Adipocyte-Cancer Cell Interactions in the Bone Microenvironment. Front. Endocrinol. 13:903925. doi: 10.3389/fendo.2022.903925

INTRODUCTION

Cancer is a leading cause of death worldwide that is attributable for an estimated 14 million incident cases and 8 million deaths annually (1, 2). While obesity is now recognized as a risk factor for several malignancies (3, 4), pathophysiological context and other biological factors modify the magnitude of this effect. Obesity is characterized not only by adipose tissue expansion, but also a progressive adipose tissue dysfunction resulting in profound alterations in the production of lipids, hormones, inflammatory cytokines and adipose derived-signalling molecules termed adipokines (5). These local and systemic physiologic alterations have the potential to impact cancer cells indirectly through immunomodulation or modulation of the tumour microenvironment as well as directly *via* effects on cancer cell growth (6). While considerable study has been devoted to the influence of adipocytes localized in white adipose tissue (WAT) depots (e.g. subcutaneous) on cancer

development and progression, comparatively little attention has been paid to adipocytes resident within bone marrow. This is important, as these adipocytes have unique metabolic and paracrine/endocrine features as well as a developmental origin distinct from peripheral white adipocytes. Moreover, given their location within bone marrow, these adipocytes may be particularly relevant to promoting bone metastases and/or supporting the growth of metastatic cancer cells. This minireview highlights recent findings regarding the role of bone marrow adipocytes in the skeletal metastasis.

ORIGIN AND PHYSIOLOGICAL/ PATHOLOGICAL RELEVANCE OF BONE MARROW ADIPOCYTES

The presence of fat within bone marrow has long been recognized through gross anatomical and histological findings (7). At birth, bone marrow is largely red in appearance owing to the preponderance of hematopoietic and osteogenic cells (8). Beginning in childhood, there is a gradual yellowing of the bone marrow, first in the long bones, and eventually other skeletal sites, due to an accumulation of adipocytes within the marrow (8). While there is considerable individual variation, at the population level there is in general a positive correlation between the volume of bone marrow adipose tissue (BMAT) and age (9). In particular, females experience a marked increase of BMAT between the ages of 55-65 (10). Epidemiological evidence supports a linkage between this increase in BMAT and age-related bone loss (e.g. osteoporosis), particularly in post-menopausal women (11, 12). In addition to age, commonly used drugs such as glucocorticoids and thiazolidinediones have been linked to increased BMAT and bone loss (13). Data regarding the relationship between BMAT and total body fat or specific WAT depots (e.g. visceral, subcutaneous) in humans is somewhat inconsistent with some studies reporting a positive, and others no association with amounts of BMAT (14, 15). Adding to the complexity of this relationship, other studies have reported that conditions characterized by decreased WAT, such as anorexia nervosa and caloric restriction in rodents, are associated with increase BMAT volume (16–18).

It is generally accepted that bone marrow adipocytes derive from a self-renewing population of multipotent progenitor bone marrow stromal cells (BMSCs) (19). Most evidence supports that this developmental origin is distinct from other adipocytes (e.g. subcutaneous white adipocytes) (20, 21) and contributes to the unique role of bone marrow adipocytes in local processes such as hematopoiesis (22) and osteogenesis (23) as well as energy metabolism at both the local and systemic level (24). In addition to adipocytes, BMSCs can also give rise to other bone cell types including chondrocytes, myocytes, and osteoblasts (19) depending upon the nature of the paracrine/endocrine stimulus. Indeed, a shift in BMSC lineage allocation to favour adipogenic versus osteogenic differentiation is believed to contribute to aging and post-menopausal bone loss (25). Similar to white adipocytes, bone marrow adipocytes secrete a variety of biologically active signalling molecules including pro-inflammatory cytokines and adipokines with local and systemic effects. For example, bone marrow adipocytes secrete tumour necrosis factor-alpha and adiponectin, both of which have been shown to inhibit bone marrow hematopoiesis (26). Also, in common with WAT, BMAT serves as an energy reservoir, largely in the form of triglycerides, that can be mobilized through lipolysis and released as free fatty acids (FFAs) into the extracellular environment. While these FFAs may serve as a general energy source that is supportive of normal physiological processes such as hematopoiesis and bone remodelling (24), they may also have unique properties and pathological relevance to the bone marrow microenvironment. For example, elevated levels of certain bone marrow adipocyte-derived saturated FFAs, such as lauric and palmitic acid, inhibit osteoblastic differentiation of BMSCs, promote osteoclast survival and in doing so, may contribute to the potential linkage between BMAT and bone loss (27). Emerging evidence indicates that the pathological relevance of BMAT may also extend to several malignancies and that an adipocyte-rich bone marrow may be both attractive and supportive of metastatic cancer cells (28). This review will focus on prostate, breast and lung cancer and multiple myeloma as the interaction between BMAT and the metastasis of these malignancies has been the most widely studied and thus, most amenable for summation and analysis.

PROSTATE CANCER

Bone is the most common metastatic site in prostate cancer (PCa) (29). Several studies have implicated bone marrow adipocytes as key facilitators of the progression and exacerbation of these bone metastases, as summarized in **Figure 1** (30–34). Two recent preclinical trials have emphasized the association between an increased number bone marrow adipocytes, volume of BMAT and the progression of PCa cells in the bone marrow niche (32, 33). High fat diet, caprylic acid treatment and androgen depletion (castration) enhanced the BMSC-to-adipocyte transition *in vitro* and in mouse models (32, 33). Androgen deprivation therapy (ADT) is a common treatment for prostate cancer. Clinical studies have demonstrated an increase in BMAT and decrease of bone mineral density in lower spinal vertebral bodies (35) as well as an increased risk for the development of castrate-resistant bone metastases for patients undergoing this treatment (36). Pan et al. (32) found that the bone marrow of castrated mice compared to controls had increased bone marrow adipocytes as well as increased levels of adipocyte markers, most notably adiponectin, perilipin and peroxisome proliferator-activated receptor-γ (PPARγ). Moreover, treatment of BMSCs *in vitro* with androgens suppressed adipogenesis and transient knockdown of the androgen receptor inhibited this suppression (32). These findings are consistent with previous clinical findings of increased marrow fat fraction after ADT (35, 37). Interestingly, treatment with statins, inhibitors of cholesterol biosynthesis, suppressed adipogenesis *in vitro* and *in vivo* and reduced bone

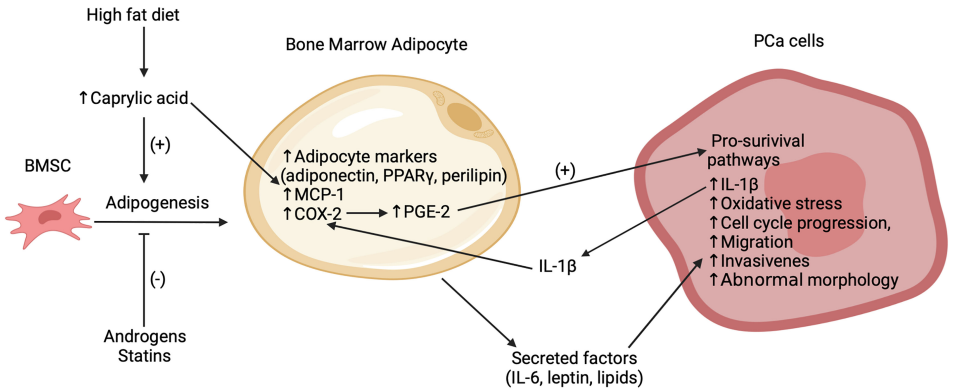

FIGURE 1 | Summary of recent findings regarding the interactions between bone marrow adipocytes and PCa cells in the bone marrow microenvironment. Bone marrow adipogenesis promoted by high fat diet, caprylic acid and inhibited by statins and androgens. Caprylic acid increases adipocyte markers (adiponectin, PPARγ, perilipin), MCP-1 and COX-2 expression in the bone marrow adipocytes. COX-2 subsequently increases PGE-2 which activates pro-survival pathways in the bone metastatic PCa cells. Secreted factors, which potentially include leptin and lipids, stimulate oxidative stress, cell cycle progression, migration, invasion, abnormal morphology, and secretion of IL-1β in the PCa cells. This IL-1β acts to further increase COX-2. While this figure highlights empirical findings from PCa studies, it is likely that several of these mechanisms are also relevant to the interaction of bone marrow adipocytes with other cancer cell types.

metastatic PCa progression in a 22RV1/LT xenograft model with castrated mice (32). These effects were found to be mediated in part through a reduced expression of both PPARγ - a pro-adipogenic transcription factor – and leptin – an adipokine that was shown to promote cell-cycle progression and proliferation of PCa cells – after statin treatment. These data suggest the potential therapeutic utility of agents that interrupt the BMSC-to-adipocyte transition as a novel approach to reduce PCa metastasis.

Previous studies have suggested that high fat diets can promote adipogenesis in bone and thereby contribute to a pro-tumor environment (31, 38). However, the mechanisms underlying this effect remain unclear. Wang et al. (33) found that mice on a high fat diet exhibited increased marrow adiposity and FFA levels. Following from this, they identified caprylic acid as a specific FFA with levels higher in the blood of patients with PCa bone metastasis *versus* that of PCa patients without bone metastasis or that of healthy controls. However, it should be noted that these data are derived from a relatively small sample size with 16 controls, 8 patients with PCa and 8 patients with PCa bone metastasis. While it is unclear as to whether the relationship of the elevated caprylic acid levels in patients was causative or correlational with PCa bone metastasis, *in vivo* treatment of BMSCs with caprylic acid increased the adipocyte differentiation and the protein expression of PPARγ, while subsequently reducing the number of osteoblasts. Treatment of bone marrow adipocytes with caprylic acid also induced higher expression of cyclooxygenase 2 (COX-2) (33), which has been implicated in several pro-tumor pathways (39). Thus, elevated levels of caprylic acid may support PCa bone metastasis through the promotion of adipogenesis over osteoblastogenesis. Similar results have been reported for arachidonic acid (40), suggesting that elevated FFA levels due to high fat diets may contribute to PCa bone metastasis by promoting a pro-tumor environment *via* increased bone marrow adipocytes and BMAT volume.

It is well established that certain factors secreted by white adipocytes, such as interleukin-6 (IL-6), contribute to primary PCa progression (41). Less well defined is the contribution of adipocyte secreted factors to the pro-tumor microenvironment within bone marrow. Both bone marrow adipocyte-derived lipids (38) and certain adipokines (42) have been shown to have several pro-tumor actions with respect to PCa cells including stimulating cell cycle progression, proliferation (32), migration, invasion (30, 33), abnormal morphology (43) and promoting oxidative stress (30). For example, in a 3D *in vitro* co-culture model of bone marrow adipocytes and PCa cells, inhibitors of fatty acid-binding protein 4 and adipocyte triglyceride lipase, used in combination, reduced the invasiveness of PCa cells (43). While it is unclear if the effect of fatty acid-binding protein 4 inhibition was a consequence of effects in the adipocytes and/or PCA cells, given the high levels of adipocyte triglyceride lipase expression in adipocytes, it is likely that reduced PCa invasiveness was indirectly liked to inhibition of adipocyte lipolysis. Overall, these data are consistent with previous findings from a 2D co-culture model that lipolysis and subsequent uptake of bone marrow adipocyte-derived lipids by PCa cells may be a key mediator of the interaction between these cell types (38). The adipokine leptin was found to be increased in bone marrow adipocyte-conditioned media and treatment with recombinant leptin stimulated PCa cell cycle progression and proliferation, possibly mediated by activation of STAT3, a transcription factor that has been implicated in promoting the survival, growth and metastasis of cancer cells (32, 44). While these initial findings are informative, the identities and mechanisms of action of secreted factors that mediate the interactions between bone marrow adipocytes and PCa cells require further investigation.

Although increased levels of reactive oxygen species are generally detrimental to cells, persistent activation of oxidative

stress pathways by bone marrow adipocytes, may promote tumor progression in a tissue-selective manner (30, 45). For example, heme oxygenase 1 (HO-1) was reported to be upregulated in PCa bone tumors but not in subcutaneous tumors of mice with diet induced marrow adiposity, indicating an effect specific to the bone marrow environment (30). Upon review of ONCOMINE, a cancer microarray database, Herroon et al. subsequently reported (30) that HO-1 is elevated in metastatic human PCa tumors compared to primary tumors. However, they were not able to distinguish between bone metastases and other metastatic sites using that database. Based on investigation of metastatic PCa cells in co-culture with bone marrow adipocytes, HO-1 overexpression was linked to pro-survival pathways in PCa cells, an effect which was significantly reduced by treatment with an HO-1 inhibitor (30). Moreover, consistent with other findings (38), bone marrow adipocytes increased the invasive potential of PCa cells. This effect was reduced by antioxidant treatment and subsequently recovered by forced overexpression of HO-1 in PCa cells (30). While these data point to antioxidants as a potential strategy for treating bone metastasis in PCa, a recent systematic review indicated that the efficacy of antioxidant supplements taken by cancer patients remains unclear (46). In addition to oxidative stress, two recent studies from Heroon et al. (30, 34) have examined the upregulation of markers of endoplasmic reticulum (ER) stress in PCa cells upon interaction with bone marrow adipocytes. Their findings suggest that ER chaperone glucose regulated protein 78 (BIP), may be involved in facilitating bone marrow adipocyte-mediated ER stress in metastatic PCa cells which may help them survive in the bone marrow environment.

Emerging evidence indicates that the interaction between PCa cells and bone marrow adipocytes is not one sided, but rather entails a complex cross talk involving multiple paracrine factors. Interleukin 1β (IL-1β) was reported to be upregulated in bone metastatic PCa cells in mice with diet induced bone marrow adiposity (38). Another study found that this cytokine upregulated the expression of COX-2, as was also observed with caprylic acid treatment (33), and macrophage chemoattractant protein (MCP-1) in bone marrow adipocytes (31). This COX-2 upregulation was further linked to an increase in the production of prostaglandin-2 (PGE-2) by bone marrow adipocytes which was proposed to reciprocally act on PCa to activate pro-survival pathways (31, 33). Interestingly, PCa cells co-cultured with bone marrow adipocytes exhibited a reduced sensitivity to docetaxel, a drug used to treat metastatic PCa (31). The response to docetaxel was partially restored by inhibition of IL-1β or lipolysis, suggesting that BMA-PCa cross talk may be linked to drug resistance. Further investigation is needed in order to determine the implications of these findings.

BREAST CANCER

Similar to PCa, bone is the most common metastatic site for breast cancer (47). The primary site of breast cancer growth is in close vicinity to the mammary fat pad and there is a well-established link between these local white adipocytes and breast cancer development (48). It has been proposed that this connection also holds true with respect to the interaction between bone marrow adipocytes and bone metastatic breast cancer cells (48). However, this notion is challenged somewhat by known phenotypic distinctions between white adipocytes and bone marrow adipocytes (49), as well as the limited number of bone marrow adipocyte-specific studies addressing this relationship. Recent data has demonstrated that there is preferential migration of breast cancer cells towards bone marrow adipocytes occupied components when compared to the mineralized component of bone in a human bone tissue explant model (50). This behaviour was exhibited by two different breast cancer cell lines (MCF-7 and MDA-MB-231) and there was extensive direct contact between the breast cancer cells and the bone marrow adipocytes (50). MDA-MB-231 cells, a bone-trophic line, were found to overexpress HO-1 after co-culture with bone marrow adipocytes (30). Similarly, increased proliferation and invasion of MDA-MB-231 cells after exposure to bone marrow adipocyte-conditioned media was also associated with HO-1 induction in a previous study (38).While there is evidence that HO-1 upregulation led to the activation of pro-survival pathways in PCa cells, a similar mechanism remains to be demonstrated in breast cancer cells. In an analysis of 56 breast cancer patients and 56 controls, high BMAT volume was found to be an independent risk factor for breast cancer (51). However, while it was strongly associated with lymph node metastasis, the study did not include bone metastasis as a parameter (51).

While bone marrow adipocyte-secreted factors have been suggested as mediators of the interaction between this cell type and breast cancer cells, empirical evidence to support this is currently limited. Cytoplasmic lipid accumulation and upregulation of lipid transport proteins was reported for MDA-MB-231 cells exposed to either bone marrow adipocyte-conditioned media or in transwell co-culture with bone marrow adipocytes (38). Increased uptake of bone marrow adipocyte-derived FFAs by *via* fatty acid binding protein-4 was proposed as a means of energy provision to support the increased proliferation and invasiveness of breast cancer cells observed under these conditions (38). However, there have been no further studies supporting this hypothesis. Breast cancer cells have been observed to exhibit increased migration toward the bone marrow adipocytes in an explant model in which MCF-7 or MDA-MB-231 cells were co-cultured with cancellous bone tissue fragments isolated from hip arthroplasties (50). Analysis of the supernatants of the explants revealed a significant association between increasing levels of IL-1β and leptin with MDA-MB-231 migration in the bone microenvironment and implicate these factors as potential mediators by which bone marrow adipocytes encourage breast cancer cell migration to bone marrow (50). However, there are some limitations to this conclusion, as it was assumed that bone marrow adipocytes were the main source of leptin and IL-1β in the bone marrow environment. These findings, support that increased BMAT volume in post-menopausal women (10) may contribute to breast cancer bone

metastasis and other clinical findings indicative of a poorer prognosis for post- versus pre-menopausal breast cancer patients (52). However, other clinical data suggests that there is a lower incidence of bone metastasis in post- versus pre-menopausal women (53). As such, this relationship remains unclear at present and further clinical investigation of the impact of increased post-menopausal marrow adiposity on bone metastasis of breast cancer is needed.

LUNG CANCER

As bone metastasis is less common in lung cancer than in breast and prostate cancer, there has been little investigation regarding the role of bone marrow adipocytes in the progression of lung cancer (47). However, a recent study investigated the cross talk between bone marrow adipocytes and small cell lung carcinoma cells (54). Rosiglitazone maleate, a thiazolidinedione, was used to induce increased BMAT volume in mice. Compared to controls that did not receive rosiglitazone treatment, the treated mice exhibited augmented osteolytic destruction when SBC-5 cells, a small cell lung carcinoma cell line with bone metastatic potential, were injected into their femurs (54). S100A8/A9 is a heterodimeric calcium binding protein that is highly expressed in several cancer types and is involved in the regulation inflammatory processes and immune response (54, 55). In comparing SBC-5 to SBC-3 (a small cell lung carcinoma cell line without bone metastatic potential), increased S100A8/A9 expression was the predominant difference identified in the SBC-5 versus -3 transcriptome (54). These data suggest that S100A9/A8 expression levels may be a determinant of the bone tropism of certain lung cancers. Moreover, co-culture of bone marrow adipocytes and SBC-5 cells, was associated with elevated expression of IL-6 in the former and the cognate receptor (IL-6R) in the latter. Conditioned media from BMSCs enhanced the migration of both SBC-3 and SBC-5 cells, whereas conditioned media from bone marrow adipocytes enhanced the invasion of SBC-5 cells only. Reciprocally, SBC-5 conditioned media inhibited the adipogenic differentiation of BMSCs and promoted de-differentiation and decreased adipogenic marker expression in mature bone marrow adipocytes. This effect was reduced when toll-like receptor 4, which can be activated by S100A8/A9 (56), was inhibited, further implicating S100A8/A9 in this cross talk. More research is required to better understand these findings and their implications for the progression and maintenance of bone metastatic lung cancer.

MULTIPLE MYELOMA

Oncolytic bone loss is a frequent occurrence with multiple myeloma and while several comprehensive reviews (57–59) have addressed and summarized findings regarding the complex cross-talk between marrow adipocytes and myeloma cells, recent studies further characterizing this relationship are worth highlighting. For example, while it has been variously reported that multiple myeloma cells can promote the adipogenic versus osteoblastogenic differentiation of MSCs, the mechanisms underlying this effect have been unclear. Liu et al. (60, 61) recently described a mechanism by which the integrin alpha4 subunit expressed on the surface of multipole myeloma cells stimulated vascular cell adhesion molecule 1 on MSCs leading to repression of muscle ring-finger protein-1 mediated ubiquitination of PPARγ. The resultant stabilization and accumulation of PPARγ levels in turn promoted adipogenesis and reduced osteoblastogenesis of MSCs, suppressing bone formation *in vitro* and *in vivo*. Another recent study (60) reported that conditioned media prepared from adipocytes isolated from bone marrow aspirates collected from myeloma patients (newly diagnosed or in complete remission) promoted the development of prominent osteolytic lesions in a humanized murine fetal bone chip model when compared to media prepared from adipocytes of normal subjects. Interestingly, co-culture of multiple myeloma cells with MSC-derived adipocytes resulted in the development of a "senescence-associated secretory" phenotype characterized by alterations in the release of adipose-derived cytokines, adipokines and other signalling molecules associated the promotion and survival of tumour cells (62). Consistent with a tumour supportive relationship between BMAT and multiple myeloma, clinical studies have found that inclusion of bone marrow fat fraction improved both the discrimination of healthy controls from multiple myeloma patients by MRI and further, those patients with diffuse versus focal lesions (63). Taken together, these findings are consistent with a complex cross-talk between multiple myeloma cells and adipocytes. This may entail a reprogramming of MSCs and adipocytes, that persists even with remission, to repress bone formation and promote oncolytic lesions as well as to support tumour growth and survival.

DISCUSSION

The prognosis for cancer patients with bone metastasis remains poor. Currently, most research investigating the interactions between bone marrow adipocytes and bone metastasis has focused on prostate cancer and multiple myeloma. However, given the high incidence of bone metastasis in breast cancer patients, as well as the clear relationship between white adipocytes and primary breast tumors, this is an important area of future study. Despite the lower incidence of bone metastasis in lung cancer compared to that seen in breast and prostate cancer, it has a shorter median survival (47), illustrating the need for a greater understanding of the role of bone marrow adipocytes in lung cancer bone-tropism. In addition to further research into specific cancer types, identification of which secreted factors mediate these interactions and the elucidation of the underlying mechanisms is needed. Based on the current research, there could be potential therapeutic implications if strategies to reduce the BMSC-to-adipocyte transition or to interrupt adipocyte-tumor cross talk are more clearly defined.

AUTHOR CONTRIBUTIONS

MO and CS contributed equally to the conception and preparation of this manuscript.

FUNDING

The authors' work was supported by funding from Research Nova Scotia.

REFERENCES

1. Sung H, Ferlay J, Siegel RL, Laversanne M, Soerjomataram I, Jemal A, et al. Global Cancer Statistics 2020: GLOBOCAN Estimates of Incidence and Mortality Worldwide for 36 Cancers in 185 Countries. *CA Cancer J Clin* (2021) 71:209–49. doi: 10.3322/caac.21660
2. Ferlay J, Colombet M, Soerjomataram I, Mathers C, Parkin DM, Pineros M, et al. Estimating the Global Cancer Incidence and Mortality in 2018: GLOBOCAN Sources and Methods. *Int J Cancer* (2019) 144:1941–53. doi: 10.1002/ijc.31937
3. Avgerinos KI, Spyrou N, Mantzoros CS, Dalamaga M. Obesity and Cancer Risk: Emerging Biological Mechanisms and Perspectives. *Metabolism* (2019) 92:121–35. doi: 10.1016/j.metabol.2018.11.001
4. Lega IC, Lipscombe LL. Review: Diabetes, Obesity, and Cancer-Pathophysiology and Clinical Implications. *Endocr Rev* (2020) 41:33–52. doi: 10.1210/endrev/bnz014
5. Matafome P, Santos-Silva D, Sena CM, Seica R. Common Mechanisms of Dysfunctional Adipose Tissue and Obesity-Related Cancers. *Diabetes Metab Res Rev* (2013) 29:285–95. doi: 10.1002/dmrr.2395
6. Choi J, Cha YJ, Koo JS. Adipocyte Biology in Breast Cancer: From Silent Bystander to Active Facilitator. *Prog Lipid Res* (2018) 69:11–20. doi: 10.1016/j.plipres.2017.11.002
7. Horowitz MC, Berry R, Holtrup B, Sebo Z, Nelson T, Fretz JA, et al. Bone Marrow Adipocytes. *Adipocyte* (2017) 6:193–204. doi: 10.1080/21623945.2017.1367881
8. Moore SG, Dawson KL. Red and Yellow Marrow in the Femur: Age-Related Changes in Appearance at MR Imaging. *Radiology* (1990) 175:219–23. doi: 10.1148/radiology.175.1.2315484
9. Singhal V, Bredella MA. Marrow Adipose Tissue Imaging in Humans. *Bone* (2019) 118:69–76. doi: 10.1016/j.bone.2018.01.009
10. Griffith JF, Yeung DK, Ma HT, Leung JC, Kwok TC, Leung PC. Bone Marrow Fat Content in the Elderly: A Reversal of Sex Difference Seen in Younger Subjects. *J Magn Reson Imaging* (2012) 36:225–30. doi: 10.1002/jmri.23619
11. Yeung DK, Griffith JF, Antonio GE, Lee FK, Woo J, Leung PC. Osteoporosis is Associated With Increased Marrow Fat Content and Decreased Marrow Fat Unsaturation: A Proton MR Spectroscopy Study. *J Magn Reson Imaging* (2005) 22:279–85. doi: 10.1002/jmri.20367
12. Shen W, Chen J, Gantz M, Punyanitya M, Heymsfield SB, Gallagher D, et al. MRI-Measured Pelvic Bone Marrow Adipose Tissue is Inversely Related to DXA-Measured Bone Mineral in Younger and Older Adults. *Eur J Clin Nutr* (2012) 66:983–8. doi: 10.1038/ejcn.2012.35
13. Sadie-Van Gijsen H, Hough FS, Ferris WF. Determinants of Bone Marrow Adiposity: The Modulation of Peroxisome Proliferator-Activated Receptor-Gamma2 Activity as a Central Mechanism. *Bone* (2013) 56:255–65. doi: 10.1016/j.bone.2013.06.016
14. Yu EW, Greenblatt L, Eajazi A, Torriani M, Bredella MA. Marrow Adipose Tissue Composition in Adults With Morbid Obesity. *Bone* (2017) 97:38–42. doi: 10.1016/j.bone.2016.12.018
15. Kim TY, Schwartz AV, Li X, Xu K, Black DM, Petrenko DM, et al. Bone Marrow Fat Changes After Gastric Bypass Surgery Are Associated With Loss of Bone Mass. *J Bone Miner Res* (2017) 32:2239–47. doi: 10.1002/jbmr.3212
16. Ecklund K, Vajapeyam S, Feldman HA, Buzney CD, Mulkern RV, Kleinman PK, et al. Bone Marrow Changes in Adolescent Girls With Anorexia Nervosa. *J Bone Miner Res* (2010) 25:298–304. doi: 10.1359/jbmr.090805
17. Bredella MA, Fazeli PK, Miller KK, Misra M, Torriani M, Thomas BJ, et al. Increased Bone Marrow Fat in Anorexia Nervosa. *J Clin Endocrinol Metab* (2009) 94:2129–36. doi: 10.1210/jc.2008-2532
18. Devlin MJ, Cloutier AM, Thomas NA, Panus DA, Lotinun S, Pinz I, et al. Caloric Restriction Leads to High Marrow Adiposity and Low Bone Mass in Growing Mice. *J Bone Miner Res* (2010) 25:2078–88. doi: 10.1002/jbmr.82
19. Hu L, Yin C, Zhao F, Ali A, Ma J, Qian A. Mesenchymal Stem Cells: Cell Fate Decision to Osteoblast or Adipocyte and Application in Osteoporosis Treatment. *Int J Mol Sci* (2018) 19:360–79. doi: 10.3390/ijms19020360
20. Krings A, Rahman S, Huang S, Lu Y, Czernik PJ, Lecka-Czernik B. Bone Marrow Fat has Brown Adipose Tissue Characteristics, Which are Attenuated With Aging and Diabetes. *Bone* (2012) 50:546–52. doi: 10.1016/j.bone.2011.06.016
21. Chen J, Shi Y, Regan J, Karuppaiah K, Ornitz DM, Long F. Osx-Cre Targets Multiple Cell Types Besides Osteoblast Lineage in Postnatal Mice. *PloS One* (2014) 9:e85161. doi: 10.1371/journal.pone.0085161
22. Zhou BO, Yu H, Yue R, Zhao Z, Rios JJ, Naveiras O, et al. Bone Marrow Adipocytes Promote the Regeneration of Stem Cells and Haematopoiesis by Secreting SCF. *Nat Cell Biol* (2017) 19:891–903. doi: 10.1038/ncb3570
23. Ambrosi TH, Scialdone A, Graja A, Gohlke S, Jank AM, Bocian C, et al. Adipocyte Accumulation in the Bone Marrow During Obesity and Aging Impairs Stem Cell-Based Hematopoietic and Bone Regeneration. *Cell Stem Cell* (2017) 20:771–784 e6. doi: 10.1016/j.stem.2017.02.009
24. Lecka-Czernik B. Marrow Fat Metabolism is Linked to the Systemic Energy Metabolism. *Bone* (2012) 50:534–9. doi: 10.1016/j.bone.2011.06.032
25. Yu W, Zhong L, Yao L, Wei Y, Gui T, Li Z, et al. Bone Marrow Adipogenic Lineage Precursors Promote Osteoclastogenesis in Bone Remodeling and Pathologic Bone Loss. *J Clin Invest* (2021) 131:1–15. doi: 10.1172/JCI140214
26. Iversen PO, Wiig H. Tumor Necrosis Factor Alpha and Adiponectin in Bone Marrow Interstitial Fluid From Patients With Acute Myeloid Leukemia Inhibit Normal Hematopoiesis. *Clin Cancer Res* (2005) 11:6793–9. doi: 10.1158/1078-0432.CCR-05-1033
27. Oh SR, Sul OJ, Kim YY, Kim HJ, Yu R, Suh JH, et al. Saturated Fatty Acids Enhance Osteoclast Survival. *J Lipid Res* (2010) 51:892–9. doi: 10.1194/jlr.M800626-JLR200
28. Clezardin P, Coleman R, Puppo M, Ottewell P, Bonnelye E, Paycha F, et al. Bone Metastasis: Mechanisms, Therapies, and Biomarkers. *Physiol Rev* (2021) 101:797–855. doi: 10.1152/physrev.00012.2019
29. Gandaglia G, Abdollah F, Schiffmann J, Trudeau V, Shariat SF, Kim SP, et al. Distribution of Metastatic Sites in Patients With Prostate Cancer: A Population-Based Analysis. *Prostate* (2014) 74:210–6. doi: 10.1002/pros.22742
30. Herroon MK, Rajagurubandara E, Diedrich JD, Heath EI, Podgorski I. Adipocyte-Activated Oxidative and ER Stress Pathways Promote Tumor Survival in Bone *via* Upregulation of Heme Oxygenase 1 and Survivin. *Sci Rep* (2018) 8:40. doi: 10.1038/s41598-017-17800-5
31. Herroon MK, Diedrich JD, Rajagurubandara E, Martin C, Maddipati KR, Kim S, et al. Prostate Tumor Cell-Derived IL1beta Induces an Inflammatory Phenotype in Bone Marrow Adipocytes and Reduces Sensitivity to Docetaxel *via* Lipolysis-Dependent Mechanisms. *Mol Cancer Res* (2019) 17:2508–21. doi: 10.1158/1541-7786.MCR-19-0540
32. Pan T, Lin SC, Lee YC, Yu G, Song JH, Pan J, et al. Statins Reduce Castration-Induced Bone Marrow Adiposity and Prostate Cancer Progression in Bone. *Oncogene* (2021) 40:4592–603. doi: 10.1038/s41388-021-01874-7
33. Wang C, Wang J, Chen K, Pang H, Li X, Zhu J, et al. Caprylic Acid (C8:0) Promotes Bone Metastasis of Prostate Cancer by Dysregulated Adipo-Osteogenic Balance in Bone Marrow. *Cancer Sci* (2020) 111:3600–12. doi: 10.1111/cas.14606
34. Herroon MK, Mecca S, Haimbaugh A, Garmo LC, Rajagurubandara E, Todi SV, et al. Adipocyte-Driven Unfolded Protein Response is a Shared Transcriptomic Signature of Metastatic Prostate Carcinoma Cells. *Biochim Biophys Acta Mol Cell Res* (2021) 1868:119101. doi: 10.1016/j.bbamcr.2021.119101
35. Martin J, Arm J, Smart J, Palazzi K, Capp A, Ainsworth P, et al. And DEXA Changes Over Time in Men With Prostate Cancer Treated With Androgen Deprivation Therapy: A Potential Imaging Biomarker of Treatment Toxicity. *Eur Radiol* (2017) 27:995–1003. doi: 10.1007/s00330-016-4434-z

36. Hotte SJ, Saad F. Current Management of Castrate-Resistant Prostate Cancer. *Curr Oncol* (2010) 17 Suppl 2:S72–9. doi: 10.3747/co.v17i0.718
37. Bandara V, Capp A, Ahmed G, Arm J, Martin J. Assessment and Predictors of Fatigue in Men With Prostate Cancer Receiving Radiotherapy and Androgen Deprivation Therapy. *J Med Imaging Radiat Oncol* (2019) 63:683–90. doi: 10.1111/1754-9485.12922
38. Herroon MK, Rajagurubandara E, Hardaway AL, Powell K, Turchick A, Feldmann D, et al. Bone Marrow Adipocytes Promote Tumor Growth in Bone *via* FABP4-Dependent Mechanisms. *Oncotarget* (2013) 4:2108–23. doi: 10.18632/oncotarget.1482
39. Hashemi Goradel N, Najafi M, Salehi E, Farhood B, Mortezaee K. Cyclooxygenase-2 in Cancer: A Review. *J Cell Physiol* (2019) 234:5683–99. doi: 10.1002/jcp.27411
40. Brown MD, Hart C, Gazi E, Gardner P, Lockyer N, Clarke N. Influence of Omega-6 PUFA Arachidonic Acid and Bone Marrow Adipocytes on Metastatic Spread From Prostate Cancer. *Br J Cancer* (2010) 102:403–13. doi: 10.1038/sj.bjc.6605481
41. Nieman KM, Romero IL, Van Houten B, Lengyel E. Adipose Tissue and Adipocytes Support Tumorigenesis and Metastasis. *Biochim Biophys Acta* (2013) 1831:1533–41. doi: 10.1016/j.bbalip.2013.02.010
42. Hardaway AL, Herroon MK, Rajagurubandara E, Podgorski I. Bone Marrow Fat: Linking Adipocyte-Induced Inflammation With Skeletal Metastases. *Cancer Metastasis Rev* (2014) 33:527–43. doi: 10.1007/s10555-013-9484-y
43. Herroon MK, Diedrich JD, Podgorski I. New 3d-Culture Approaches to Study Interactions of Bone Marrow Adipocytes With Metastatic Prostate Cancer Cells. *Front Endocrinol (Lausanne)* (2016) 7:84. doi: 10.3389/fendo.2016.00084
44. Vlahopoulos SA. Aberrant Control of NF-kappaB in Cancer Permits Transcriptional and Phenotypic Plasticity, to Curtail Dependence on Host Tissue: Molecular Mode. *Cancer Biol Med* (2017) 14:254–70. doi: 10.20892/j.issn.2095-3941.2017.0029
45. Khandrika L, Kumar B, Koul S, Maroni P, Koul HK. Oxidative Stress in Prostate Cancer. *Cancer Lett* (2009) 282:125–36. doi: 10.1016/j.canlet.2008.12.011
46. Yasueda A, Urushima H, Ito T. Efficacy and Interaction of Antioxidant Supplements as Adjuvant Therapy in Cancer Treatment: A Systematic Review. *Integr Cancer Ther* (2016) 15:17–39. doi: 10.1177/1534735415610427
47. Svensson E, Christiansen CF, Ulrichsen SP, Rorth MR, Sorensen HT. Survival After Bone Metastasis by Primary Cancer Type: A Danish Population-Based Cohort Study. *BMJ Open* (2017) 7:e016022. doi: 10.1136/bmjopen-2017-016022
48. Liu C, Zhao Q, Yu X. Bone Marrow Adipocytes, Adipocytokines, and Breast Cancer Cells: Novel Implications in Bone Metastasis of Breast Cancer. *Front Oncol* (2020) 10:561595. doi: 10.3389/fonc.2020.561595
49. Sebo ZL, Rendina-Ruedy E, Ables GP, Lindskog DM, Rodeheffer MS, Fazeli PK, et al. Bone Marrow Adiposity: Basic and Clinical Implications. *Endocr Rev* (2019) 40:1187–206. doi: 10.1210/er.2018-00138
50. Templeton ZS, Lie WR, Wang W, Rosenberg-Hasson Y, Alluri RV, Tamaresis JS, et al. Breast Cancer Cell Colonization of the Human Bone Marrow Adipose Tissue Niche. *Neoplasia* (2015) 17:849–61. doi: 10.1016/j.neo.2015.11.005
51. Li G, Xu Z, Zhuang A, Chang S, Hou L, Chen Y, et al. Magnetic Resonance Spectroscopy-Detected Change in Marrow Adiposity Is Strongly Correlated to Postmenopausal Breast Cancer Risk. *Clin Breast Cancer* (2017) 17:239–44. doi: 10.1016/j.clbc.2017.01.004
52. Coleman RE. How can We Improve the Treatment of Bone Metastases Further? *Curr Opin Oncol* (1998) 10 Suppl 1:S7–13. doi: 10.1017/S1049023X00038103
53. Braun S, Vogl FD, Naume B, Janni W, Osborne MP, Coombes RC, et al. A Pooled Analysis of Bone Marrow Micrometastasis in Breast Cancer. *N Engl J Med* (2005) 353:793–802. doi: 10.1056/NEJMoa050434
54. Luo G, Tang M, Zhao Q, Lu L, Xie Y, Li Y, et al. Bone Marrow Adipocytes Enhance Osteolytic Bone Destruction by Activating 1q21.3(S100A7/8/9-IL6R)-TLR4 Pathway in Lung Cancer. *J Cancer Res Clin Oncol* (2020) 146:2241–53. doi: 10.1007/s00432-020-03277-9
55. Wagner NB, Weide B, Gries M, Reith M, Tarnanidis K, Schuermans V, et al. Tumor Microenvironment-Derived S100A8/A9 is a Novel Prognostic Biomarker for Advanced Melanoma Patients and During Immunotherapy With Anti-PD-1 Antibodies. *J Immunother Cancer* (2019) 7:343. doi: 10.1186/s40425-019-0828-1
56. Schiopu A, Cotoi OS. S100A8 and S100A9: DAMPs at the Crossroads Between Innate Immunity, Traditional Risk Factors, and Cardiovascular Disease. *Mediators Inflamm* (2013) 213:828354. doi: 10.1155/2013/828354
57. Falank C, Fairfield H, Reagan MR. Signaling Interplay Between Bone Marrow Adipose Tissue and Multiple Myeloma Cells. *Front Endocrinol (Lausanne)* (2016) 7:67. doi: 10.3389/fendo.2016.00067
58. Morris EV, Edwards CM. Bone Marrow Adiposity and Multiple Myeloma. *Bone* (2019) 118:42–6. doi: 10.1016/j.bone.2018.03.011
59. Morris EV, Edwards CM. Adipokines, Adiposity, and Bone Marrow Adipocytes: Dangerous Accomplices in Multiple Myeloma. *J Cell Physiol* (2018) 233:9159–66. doi: 10.1002/jcp.26884
60. Liu H, He J, Koh SP, Zhong Y, Liu Z, Wang Z, et al. Reprogrammed Marrow Adipocytes Contribute to Myeloma-Induced Bone Disease. *Sci Transl Med* (2019) 11:1–24. doi: 10.1126/scitranslmed.aau9087
61. Morris EV, Suchacki KJ, Hocking J, Cartwright R, Sowman A, Gamez B, et al. Myeloma Cells Down-Regulate Adiponectin in Bone Marrow Adipocytes *Via* TNF-Alpha. *J Bone Miner Res* (2020) 35:942–55. doi: 10.1002/jbmr.3951
62. Fairfield H, Dudakovic A, Khatib CM, Farrell M, Costa S, Falank C, et al. Myeloma-Modified Adipocytes Exhibit Metabolic Dysfunction and a Senescence-Associated Secretory Phenotype. *Cancer Res* (2021) 81:634–47. doi: 10.1158/0008-5472.CAN-20-1088
63. Berardo S, Sukhovei L, Andorno S, Carriero A, Stecco A. Quantitative Bone Marrow Magnetic Resonance Imaging Through Apparent Diffusion Coefficient and Fat Fraction in Multiple Myeloma Patients. *Radiol Med* (2021) 126:445–52. doi: 10.1007/s11547-020-01258-z

Conflict of Interest: The authors declare that the research was conducted in the absence of any commercial or financial relationships that could be construed as a potential conflict of interest.

Publisher's Note: All claims expressed in this article are solely those of the authors and do not necessarily represent those of their affiliated organizations, or those of the publisher, the editors and the reviewers. Any product that may be evaluated in this article, or claim that may be made by its manufacturer, is not guaranteed or endorsed by the publisher.

Advantages of publishing in Frontiers

OPEN ACCESS
Articles are free to read for greatest visibility and readership

FAST PUBLICATION
Around 90 days from submission to decision

HIGH QUALITY PEER-REVIEW
Rigorous, collaborative, and constructive peer-review

TRANSPARENT PEER-REVIEW
Editors and reviewers acknowledged by name on published articles

Frontiers
Avenue du Tribunal-Fédéral 34
1005 Lausanne | Switzerland

Visit us: www.frontiersin.org
Contact us: frontiersin.org/about/contact

REPRODUCIBILITY OF RESEARCH
Support open data and methods to enhance research reproducibility

DIGITAL PUBLISHING
Articles designed for optimal readership across devices

FOLLOW US
@frontiersin

IMPACT METRICS
Advanced article metrics track visibility across digital media

EXTENSIVE PROMOTION
Marketing and promotion of impactful research

LOOP RESEARCH NETWORK
Our network increases your article's readership